TESIS DE LA UNIVERSIDAD
DE ZARAGOZA

2024

452

Laura García Mendívil

Ex vivo, in vitro and in silico characterization of human cardiac aging and its impact on Arrhythmic risk.
Caracterización ex vivo, in vitro e in silico del envejecimiento cardiaco humano y su impacto en

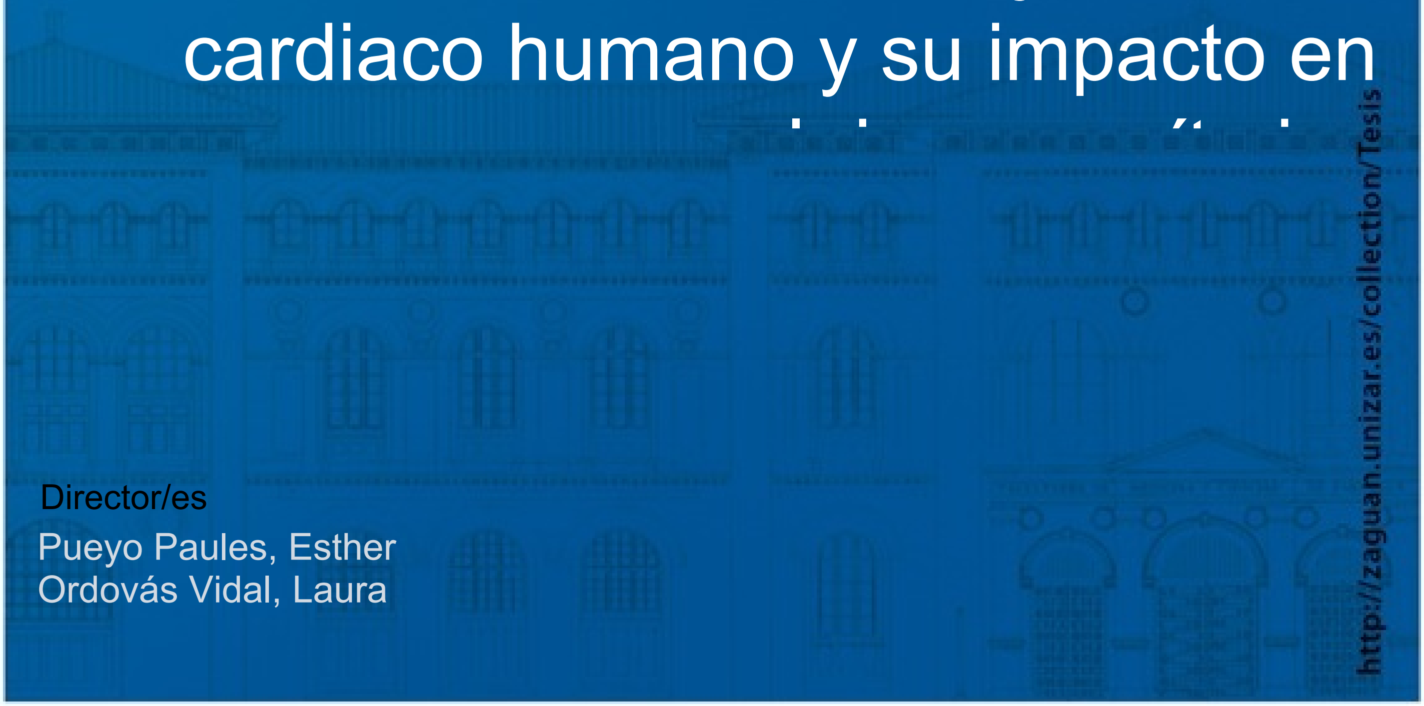

Director/es

Pueyo Paules, Esther
Ordovás Vidal, Laura

ISSN 2254-7606

Prensas de la Universidad
Universidad Zaragoza

Universidad de Zaragoza
Servicio de Publicaciones

ISSN 2254-7606

Tesis Doctoral

EX VIVO, IN VITRO AND IN SILICO CHARACTERIZATION OF HUMAN CARDIAC AGING AND ITS IMPACT ON ARRHYTHMIC RISK. CARACTERIZACIÓN EX VIVO, IN VITRO E IN SILICO DEL ENVEJECIMIENTO CARDIACO HUMANO Y SU IMPACTO EN EL RIESGO ARRÍTMICO

Autor

Laura García Mendívil

Director/es

Pueyo Paules, Esther
Ordovás Vidal, Laura

UNIVERSIDAD DE ZARAGOZA
Escuela de Doctorado

Programa de Doctorado en Ingeniería Biomédica

2023

Tesis Doctoral

Ex vivo, in vitro and *in silico* characterization of human cardiac aging and its impact on arrhythmic risk

Caracterización *ex vivo*, *in vitro* e *in silico* del envejecimiento cardiaco humano y su impacto en el riesgo arrítmico

Laura García Mendívil

Esther Pueyo Paules
Laura Ordovás Vidal

Universidad de Zaragoza
Instituto de Investigación en Ingeniería (I3A)
2023

A mis padres y a mi hermano

Funding

This thesis has been developed in the frame of the following scientific projects:

- European Research Council through grant ERC G.A. 63828
- Ministerio de Ciencia e Innovación (Spain) (PID2019-105674RB-I00)
- Ministerio de Ciencia e Innovación (Spain) (TED2021-130459B-I00)
- Gobierno de Aragón (LMP124_18)
- Gobierno de Aragón (LMP94_21)
- Gobierno de Aragón (LMP128_21)
- Ibercaja (JIUZ-2017-TEC-07)
- European Social Fund and by Gobierno de Aragón (Reference Group BSICoS T39-20R) cofounded by FEDER 2014–2020 “Building Europe from Aragon.”

I was supported by a predoctoral fellowship from the Departamento de Ciencia, Universidad y Sociedad del Conocimiento from the Gobierno de Aragón 2016-2020 cofounded by Programa Operativo del Fondo Social Europeo Aragón (C150/2016).

The research stays were supported by EMBO Short-Term fellowship (7710) and Ibercaja-CAI Estancias de Investigación IT18/18.

Abstract

Cardiovascular diseases (CVDs) are the leading cause of death in the world. A relevant proportion of patients with CVDs develop arrhythmias and some of these arrhythmias can lead to sudden cardiac death. Aging is a major risk factor for CVDs, in general, and arrhythmias, in particular. In the heart, aging is associated with molecular and cellular changes that eventually lead to structural and functional remodeling. Numerous mechanisms are involved in age-related alterations of the heart, including genomic instability, loss of proteostasis, cellular senescence, extracellular matrix remodeling, altered intercellular communication and gene expression, among others. Most studies on cardiac aging have been conducted in animal models of limited translational value, being human research scant and mostly cross-sectional in nature due to inherent limitations associated with human research.

In addition, cardiac aging is mostly addressed in relation to chronological age (CA), a mere time index that does not account for the individual aging rate and, thus, does not necessarily explain the biological condition of an individual or an organ. The biological age (BA) of an organ, perceived as its actual structural and functional state, comprises both genetic and environmental factors acting together over time. An improvement in the knowledge regarding the molecular and cellular mechanisms involved in human cardiac aging along with the development of longitudinal human-based models of cardiac aging could advance the development of non-invasive tools for the early detection and the prevention of age-related arrhythmias.

This thesis investigates aging hallmarks in the human left ventricle (LV) by combining molecular and histological analysis of LV samples from living donors with *in vitro* and *in silico* methodologies. The studied age-related cardiac mechanisms are gene expression, with a focus on miRNAs (key pleiotropic post-transcriptional regulators), fibrosis deposition and CX43 remodeling. Taking the conducted experimental characterizations as a basis, *in vitro* and *in silico* models are created to further investigate the impact of aging on the human heart.

Chapter 2 studies the transcriptional dynamics of the aging myocardium in relation to CA and BA, with a focus on miRNAs as key regulators of gene expression. This thesis proves the potential of *CDKN2A* and AppAge as LV transcriptomic BA descriptors and shows they perform better than CA to unveil age-related changes in a cross-sectional study. Based on *CKDN2A*-related results, a bioinformatics LV-specific gene regulation network controlled by BA-related miRNAs provides new insights into the potential mechanisms regulated by miRNAs in age-induced LV impairments. Also, two LV-enriched BA-related miRNAs present in plasma are proposed as potential non-invasive blood biomarkers of the aging myocardium.

Chapter 3 characterizes *LMNA* and *LMNA Δ50* expression in human myocardium from midlife onwards and develops and characterizes an *LMNA Δ50* inducible-expression hiPSC line under the hypothesis that *LMNA Δ50*-induced premature aging can recapitulate fundamental aspects of natural cardiac aging. This thesis rules out *LMNA Δ50* as a major contributor to natural cardiac aging, while the *LMNA Δ50* inducible expression in hiPSC-derived cardiomyocytes recapitulates the hallmarks of aging and gene expression changes observed in physiological aging.

Chapter 4 analyzes collagen remodeling (amount, aggregation and spatial distribution) beyond midlife in human LV tissue in relation to CA and BA. Complementarily, the same analysis is performed in a clinically relevant animal model, namely the pig, from adulthood to elder age. From midlife onwards, changes in collagen characteristics are shown to have a poor relationship with CA but to be more closely related to the values of the age pigment lipofuscin. Consistency between pig and human results supports the pig as a relevant and translational model to study age-related LV remodeling. The outcomes of the experimental analysis are integrated into *in silico* models of human LV electrophysiology to assess the arrhythmic effect of fibrosis remodeling. Alterations in both the amount and the organization of fibrosis to the degrees observed in old individuals are shown to enhance arrhythmia vulnerability.

Chapter 5 characterizes CX43 remodeling (content, expression level, heterogeneity and lateralization) and its relationship with fibrosis in the human LV beyond midlife. Characterizations are conducted in relation to CA and BA. Non-significant CX43 remodeling beyond midlife either by CA or BA is found in the analyzed population. Also, there is absence of correlation between CX43 characteristics and fibrosis deposition. *In silico* LV tissue models of human ventricular electrical activity are built, which account for the CX43 and fibrosis characteristics quantified in the study population. Simulation results show that a reduction in the amount of CX43 and/or an increment in CX43 spatial heterogeneity combined with higher levels of fibrosis, as quantified in some individuals, lead to increased proarrhythmic risk, with increased spatial dispersion of repolarization and widening of the temporal window for reentrant arrhythmias triggered by premature beats.

In conclusion, this thesis provides: a thorough experimental characterization of human cardiac aging hallmarks in relation to CA and BA; quantification of the risk for ventricular arrhythmias associated with the analyzed hallmarks based on biophysically detailed *in silico* modeling and simulation; and the creation and characterization of an *in vitro* model of cardiac cellular aging. This thesis illustrates the importance of using integrative interdisciplinary research to generate new insights into human cardiac aging, which can be the basis for future strategies towards healthy cardiac aging.

Resumen y Conclusiones

Las enfermedades cardiovasculares (ECV) son la principal causa de muerte a nivel mundial. Una proporción relevante de pacientes con ECV desarrollan arritmias, algunas de las cuales pueden conducir a la muerte cardiaca súbita. El envejecimiento es uno de los principales factores de riesgo de las ECV, en general y de las arritmias en particular. En el corazón, el envejecimiento se asocia a cambios moleculares y celulares que acaban provocando un remodelado estructural y funcional. Entre las alteraciones cardiacas asociadas a la edad se encuentran la inestabilidad genómica, la pérdida de proteostasis, la senescencia celular, el remodelado de la matriz extracelular, la alteración de la comunicación intercelular y la expresión génica, entre otros. La mayoría de los estudios de envejecimiento cardiaco se han realizado en modelos animales, de limitado valor traslacional, siendo la investigación en humanos escasa y de naturaleza mayoritariamente transversal debido a las limitaciones inherentes asociadas a la investigación en humanos.

Además, el envejecimiento cardiaco se realiza sobre todo en relación a la edad cronológica (EC), un índice temporal que no tiene en cuenta la tasa de envejecimiento individual y, por tanto, no explica necesariamente el estado biológico de un individuo o un órgano. La edad biológica (EB) de un órgano, percibida como su estado estructural y funcional real, comprende factores genéticos y ambientales que actúan conjuntamente a lo largo del tiempo. Un conocimiento más profundo sobre los mecanismos moleculares y celulares implicados en el envejecimiento cardiaco humano, junto con el desarrollo de modelos longitudinales de envejecimiento cardiaco humano, podrían impulsar el desarrollo de herramientas no invasivas para la detección precoz y la prevención de arritmias asociadas a la edad.

Esta tesis investiga los rasgos distintivos del envejecimiento en el ventrículo izquierdo (VI) humano mediante el análisis molecular e histológico de muestras de VI de donantes vivos combinado con metodologías *in vitro* e *in silico*. Los mecanismos cardiacos relacionados con la edad estudiados en la tesis son la expresión génica, con especial atención a los miRNAs (reguladores pleiotrópicos postranscripcionales) y el remodelado de la fibrosis y CX43, siendo esta última un componente principal de las uniones GAP en el VI humano. Tomando como base las caracterizaciones experimentales realizadas, se han creado modelos *in vitro* e *in silico* para avanzar en el estudio del impacto que el envejecimiento tiene en el corazón humano.

El capítulo 2 estudia de manera transversal la dinámica transcripcional del miocardio envejecido en relación con la EC y la EB, centrándose en los miRNAs como reguladores clave de la expresión génica. Esta tesis demuestra el potencial de *CDKN2A* y AppAge como descriptores transcriptómicos de EB del VI además de su capacidad para revelar cambios asociados a la edad de una forma más precisa que la EC. Sobre la base de los resultados relacionados con *CKDN2A*, se ha construido una red bioinformática de regulación génica específica del VI controlada por miRNAs relacionados con la EB (BIO-AGEmiRNA) que proporciona nuevos conocimientos sobre los posibles mecanismos regulados por miRNAs en el deterioro del VI inducido por la edad. Además, se proponen dos BIO-AGEmiRNAs relacionados con el VI que están presentes en plasma y son, por tanto, posibles biomarcadores sanguíneos no invasivos del miocardio envejecido.

El capítulo 3 caracteriza la expresión de *LMNA* y *LMNA Δ50* en el miocardio humano a partir de la mediana edad y desarrolla y caracteriza una línea hiPSC de expresión inducible de *LMNA Δ50* bajo la hipótesis de que el envejecimiento prematuro inducido por *LMNA Δ50* puede recapitular aspectos fundamentales del envejecimiento cardiaco natural. Esta tesis descarta que la *LMNA Δ50* intervenga en el envejecimiento cardiaco natural, mientras que la expresión inducible de *LMNA Δ50* en cardiomiocitos derivados de hiPSC recapitula rasgos distintivos del envejecimiento y cambios en la expresión génica observados en el envejecimiento fisiológico del corazón humano.

El capítulo 4 analiza el remodelado del colágeno (cantidad, agregación y distribución espacial) a partir de la mediana edad en el VI humano en relación a la EC y la EB. De forma complementaria, se realiza el mismo análisis en un modelo animal clínicamente relevante, el cerdo, desde la edad adulta hasta la vejez. A partir de la mediana edad, los cambios en las características del colágeno muestran una escasa relación con la EC, pero están estrechamente relacionados con la cantidad de lipofuscina o pigmento de la edad. La consistencia entre los resultados en cerdos y en humanos destaca el valor del cerdo como modelo relevante y traslacional para estudiar el remodelado del VI en función de la edad. Los resultados de la caracterización experimental se han integrado en modelos *in silico* de electrofisiología del VI humano de manera paciente-específica para evaluar el efecto arrítmico de la fibrosis. Esta tesis demuestra que las alteraciones con la edad tanto en la cantidad como en la organización de la fibrosis aumentan la vulnerabilidad a las arritmias.

El capítulo 5 caracteriza el remodelado de la CX43 (contenido, nivel de expresión, heterogeneidad y lateralización) y su relación con la fibrosis en el VI humano a partir de la mediana edad en función de la EC y la EB. En la población analizada, no se observa un remodelado significativo de las características relativas a CX43 a partir de la mediana edad, ni por EC ni por EB. Además, no existe correlación entre las características de la CX43 y la deposición de fibrosis, en contraste con observaciones en modelos animales. Se han construido modelos tisulares computacionales de la actividad eléctrica ventricular humana, que representan los datos obtenidos. Los resultados de la simulación muestran que una reducción en la cantidad de la CX43 y/o un incremento en su heterogeneidad espacial combinados con mayores niveles de fibrosis, como se cuantifica en algunos individuos, conducen a un aumento del riesgo proarrítmico determinado por un incremento de la dispersión espacial de la repolarización y una ampliación de la ventana temporal en la que se producen arritmias por reentrada desencadenadas por latidos prematuros.

En conclusión, esta tesis aporta una caracterización experimental exhaustiva de los rasgos distintivos del envejecimiento cardiaco humano en relación con la EC y la EB; la cuantificación del riesgo de arritmias ventriculares asociado a los rasgos distintivos analizados, basada en modelizaciones y simulaciones computacionales biofísicamente detalladas; y la creación y caracterización de un modelo *in vitro* de envejecimiento celular cardiaco que recapitula cambios observados experimentalmente en humanos. Además, esta tesis demuestra la importancia de la investigación interdisciplinar e integradora para generar nuevo conocimiento sobre el envejecimiento cardiaco humano, que puede ser la base para futuras estrategias que lleven a un envejecimiento cardiaco saludable.

Contents

List of Acronyms

µg	Microgram
AP	Action potential
APD	Action potential duration
AppAge	Apparent age
ATP	Adenosine triphosphate
AV	Atrioventricular
BA	Biological age
BIO-AGEmiRNAs	BA-related miRNAs
CA	Chronological age
CaMK	Calcium/calmodulin-dependent protein kinase II
CD	Cardiac-related causes
cm	Centimeter
CMRI	Cardiac magnetic resonance imaging
CV	Conduction velocity
CVDs	Cardiovascular diseases
Cx43	Connexin 43
DAD	Delayed afterdepolarizations
DSBs	Double-strands DNA breaks
EAD	Early afterdepolarization
ECG	Electrocardiogram
ECM	Cardiac extracellular matrix
EGM	Intracardiac electrogram
FRT	Flippase recognition target
FS	Forward scatter
FS-H	Forward scatter height
GJs	Gap junctions
GO	Gene ontology group
HGPS	Hutchinson-Gilford progeria syndrome
HGR	High Repolarization Gradient
hiPSCs	Human induced pluripotent stem cells
iCMs	hiPSC-derived cardiomyocytes
kDa	Kilo Daltons
LV	Left ventricle
LVEF	Left ventricular ejection fraction
MEF	Mechano-electrical feedback
MFI	Median Fluorescence Intensity
miRNAs	MicroRNAs
mL	Milliliter
mm	Millimeter
MMPs	Metalloproteinases
ms	Milliseconds
NCD	Non-cardiac-related cause of death

NP	Number of pixels
ODE	Ordinary differential equation
PDF	Probability density function
PI	Pixel intensity
RISC	RNA-induced silencing complex
ROS	Reactive oxygen species
RyR	rryanodine receptors
s	Seconds
SASP	Senescence-associated secretory phenotype
SHG	Second harmonic generation
SR	Sarcoplasmic reticulum
SS	Side scatter
SS-H	Side scatter height
TA	Transcriptomic age
TIMPs	Tissue inhibitors of metalloproteinases
VI	Ventrículo izquierdo
VW	Vulnerability window
Years old	y.o.
β-gal	β-galactosidase

Chapter 1

1. Introduction

1.1 Aging and cardiovascular diseases

Cardiovascular diseases (CVDs) are the leading cause of death in the world. CVDs cause 3.9 million deaths in Europe every year. In 2015, more than 85 million people in Europe were living with CVDs. The estimated cost of CVDs to the European Union economy is approximately €210 billion per year, with 53% of this cost being due to healthcare expenditure, 26% to productivity losses and 21% to the informal care of CVD patients [1]. CVDs include valve disease, coronary artery disease, heart failure or stroke, among others. A relevant proportion of patients with CVDs develop arrhythmias and some of these arrhythmias can lead to sudden cardiac death. Cardiac arrhythmias comprise different disorders altering heart rate and rhythm and are due to abnormalities in electrical impulse generation, impulse propagation or both. Based on their origin, arrhythmias are classified as either supraventricular (originating at or above the atrioventricular (AV) node) or ventricular (originated in the ventricles). Reentrant arrhythmias are self-sustaining cardiac rhythm abnormalities in which the electrical signal propagates in a way analogous to a closed-loop circuit. These reentries occur when the impulse cannot follow its normal propagation route and re-excites the heart after the refractory period, i.e. the time interval during which the cardiac cell cannot initiate another action potential (AP), with the AP being is the electrical response of cardiac cells to a stimulus [2], [3].

The most relevant behavioral factors for developing CVDs are unhealthy eating, smoking, sedentarism and alcohol. The effects derived from these factors lead to increased blood pressure, augmented blood glucose, higher blood lipids, overweight and obesity [4]. Aging is a principal risk factor for many human diseases including cancer, neurodegenerative disorders, diabetes or CVDs [5]. Aging is the accumulation of molecular and cellular damage over time that leads to a progressive loss of functional integrity. Age-associated changes are not constant and are only partially related to a person's age, since aging is also influenced by other factors such as environment, genetics and lifestyle [4].

In particular, cardiac aging is associated with molecular and cellular changes that eventually lead to structural and functional remodeling of the heart. Aging involves multiple mechanisms, including mitochondrial dysfunction and increased production of reactive oxygen species (ROS), genomic instability, epigenetic changes, loss of proteostasis, cellular senescence, cardiac extracellular matrix remodeling, altered intercellular communication and gene expression deregulation (**Figure 1**) [5], [6].

Most studies addressing cardiac aging have been conducted in animal models with the difficulties of subsequently translating results to humans. A better understanding of the molecular and cellular mechanisms involved in human cardiac aging could help in the development of non-invasive tools for the early identification of risk for age-related cardiac disease or to create preventive treatments of age-associated effects. On this basis, this thesis characterizes hallmarks of aging in the human left ventricle (LV) and uses the experimental characterizations to build and calibrate computational models of human cardiac electrophysiology and assess the effects on ventricular function of the characterized age-related alterations. Also, this thesis develops and validates an *in vitro* model of human cardiac accelerated aging to allow translational mechanistic research. The final goal is to generate new insights into human cardiac aging and new tools to improve diagnosis, prevention and treatment of age-related CVDs. To contribute to this goal, this thesis proposes an integrative interdisciplinary approach that combines *ex vivo*, *in vitro* and *in silico* methodologies.

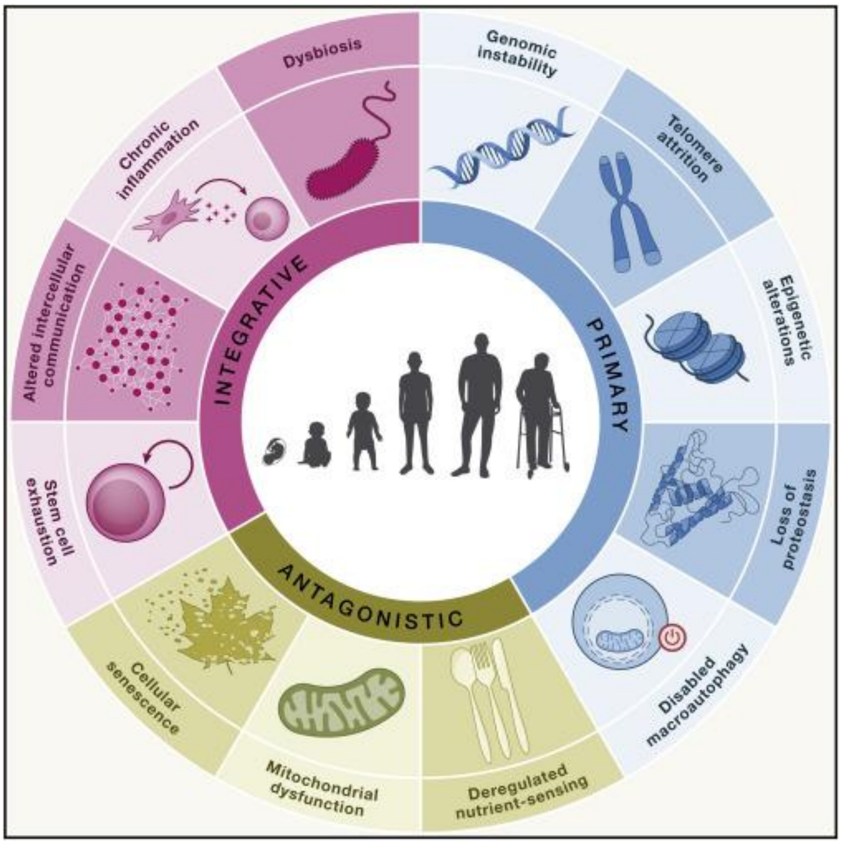

Figure 1. Hallmarks of aging. Extracted from [7].

In the following sections, a general introduction to the general mechanisms underlying aging and the specific ones associated with cardiac aging is presented. Next, the heart and its electrical activity are described. Subsequently, an overview of *in silico* electrophysiological models is presented, with details provided for the two AP models used in this PhD thesis: the O'Hara-Virág-Varró-Rudy human ventricular cardiomyocyte model [8] and the MacCannell mammalian ventricular fibroblast model [9]. These two *in silico* models are used here to assess the effects that age-related hallmarks of cardiac aging have on conduction velocity (CV), AP duration (APD) and proarrhythmicity. A general review of other natural and induced *ex vivo* and *in vitro* models of aging and the description of biological age and the indicators used to determine it are provided next. The chapter ends with the goals and the outline of the thesis.

1.2 Aging mechanisms

1.2.1 Mitochondrial dysfunction and reactive oxygen species

Mitochondria are fundamental in numerous cellular processes such as fatty acid oxidation, regulation of programmed cell death, biosynthetic pathways, cellular redox homeostasis, urea cycle or adenosine triphosphate (ATP) production via oxidative phosphorylation [10]. They are dynamic organelles that continuously experience fusion and fission mechanisms, whose rate depends on cellular stress levels and energy demands. Mitochondria are the main ATP supplier for cardiomyocyte contraction and homeostasis maintenance, which makes the heart particularly susceptible to mitochondrial malfunctioning. In addition to this role, mitochondria are also fundamental for regulating cardiomyocyte survival and death [11]. Animal models have shown contradictory results regarding the age-dependent evolution of the quantity of cardiac mitochondria. Some studies reported an unaltered quantity [12], whereas others reported a reduction [13], [14]. The characterization of cardiac mitochondria morphology in aged animals has shown them to be rounder and to have a reduced inner membrane with respect to young animals [15].

Several theories have postulated a distinct cause for aging beyond inflammation [16] and the immune system [17], with mitochondria malfunctioning being one of the main candidates, featuring in the so-called free radical theory [18] and the mitochondrial DNA theory [19], [20]. Many studies have focused on the free radical theory, particularly the mitochondrial free radical theory, which associates ROS production and the resulting damage with aging [18]. The other mitochondrial theory also postulates increased ROS production, but mutations in mitochondrial DNA are considered the aging inductor. Mitochondrial DNA has a high mutation rate, but limited repair capacity. Therefore, these mutations accumulate with age and alter mitochondrial genome integrity, leading to impaired mitochondrial function and ultimately to augmented ROS synthesis [19], [20]. Although further investigation of these aging theories is warranted, it is unquestionable that mitochondria are essential, particularly in the heart, to maintain homeostasis. During cardiac aging, mitochondrial dysfunction is usually associated with augmented production of ROS, decreased mitochondrial activity, altered mitochondrial quality control processes and reduced mitophagy [10].

Cells produce ROS such as superoxide anion or hydrogen peroxide at low levels, but constantly since they are necessary for several physiological functions. In the mammalian heart, aging and age-related diseases cause an increase in ROS generation [21], [22], which paves the way for malfunctions and a higher cell-susceptibility to injure, diminished stress tolerance or decreased energy deposit [23]. Besides, oxidative stress is profibrotic in cardiac tissue as NOX2-derived ROS are fundamental in cardiac fibrosis development. ROS are particularly relevant in the progression of myocardial infarction, atherosclerosis and heart failure [24].

1.2.2 Genomic instability and telomere damage

Endogenous components (e.g., reactive oxygen and nitrogen species) and environmental factors (e.g., carcinogens, chemical mutagens and radiation) trigger DNA damage. Cells are constantly exposed to many of them. DNA damage from deamination, alkylation, spontaneous hydrolysis of glycosidic bonds or oxidation is corrected by the base excision repair machinery. For bulky DNA lesions in mammal cells caused by chemical mutagens or ultraviolet light, nucleotide excision repair machinery is the foremost pathway involved. The most genotoxic DNA lesions encompass single and double-strand DNA breaks (DSBs) [25].

DSBs take place when the two DNA strands are broken with enough closeness to affect the linear continuity of the genome [26]. DSBs can be originated from genotoxic compounds, ionizing radiation, replication stress or ROS, and they can activate senescence, death or both processes as they are associated with genomic instability and chromosomal rearrangements [25]. Wherever a DNA lesion takes place, the DNA damage response is activated to fix it. The phosphorylation of the C-terminal of the core histone protein H2AX, named γ-H2AX when phosphorylated, is one of the first responses to these DNA breaks [27]. The phosphorylation of H2AX has broadly been used as a marker of DNA damage and reported in many aging studies [26]–[28].

Using natural and accelerated mice models of aging, De Majo and colleagues reported that in natural aging the heart is not associated with accumulation of mutations in contrast to other organs such as liver or spleen [29]. These results support the idea than tissues accumulate mutations at different rates. Besides, in transgenic mice, it has been shown that the old heart is associated with large genome rearrangements rather than point mutations [30]. Studies in humans, and particularly regarding human aging, are scarce. Nevertheless, increased DNA damage and DNA damage response in CVDs has been reported. In particular, DNA damage accumulation was reported to be positively correlated with the severity of atherosclerosis in human coronary artery disease [31] and atherosclerotic plaques showed increased DNA damage, including DSBs, and DNA damage response proteins [32], [33].

Telomeres are repetitive DNA sequences that do not encode for any gene and that protect the ends of eukaryotic chromosomes. Telomeres shorten with each successive cell division, ultimately altering the protective cap, paving the way for sustained DNA damage response and triggering the senescence program [29], [30]. Replication-induced telomere attrition is an aging hallmark, however, shortly after birth the heart loses its proliferative capacity. Thus, other mechanisms than replication might cause telomeric damage in the heart. Indeed, Anderson and colleagues [29] demonstrated that in seldom dividing post-mitotic cells, like cardiomyocytes, the damage induced in telomeres is length-independent.

1.2.3 Epigenetic modifications

Epigenetic alterations comprise all the modifications in gene expression without changing the DNA sequence. The main mechanisms are DNA methylation and histone post-transcriptional modifications: ubiquitination, methylation, phosphorylation and acetylation. Mammal DNA methylation implies the addition of a methyl group to the 5-carbon of the cytosine ring. These CpG dinucleotides are not frequently found in the genome, but they are mainly present in specific gene promoters and their surrounding areas. The presence of the methyl group blocks transcription [31]. DNA methylation is vital in many functions such as genomic imprinting, differentiation, development and X-chromosome inactivation. For that reason, it is one of the most studied epigenetic modifications. Over the last few years several studies have suggested a relation between DNA methylation and different pathologies [32], [33], cancer being the most studied one [34].

Chromatin is a complex composed of DNA and proteins. The fundamental chromatin unit is the nucleosome, which is formed by eight histones (each of them being either H2A, H2B, H3 or H4) surrounded by 147 base-pairs of DNA [35]. The degree of chromatin condensation and therefore gene expression is defined by the interaction between histones and DNA. Each nucleosome has at least 30 possible sites to be modified and there are six different modifications: sumoylation, methylation, proline isomerization, phosphorylation, acetylation and ubiquitination, so the number of regulatory combinations is high [31]. Chromosomes have two structural and functional different states: heterochromatin and euchromatin. Heterochromatin is a transcriptionally silent, highly condensed packaging of a low number of genes; euchromatin is easily transcribed, less condensed packing of a high number of genes. Heterochromatin and euchromatin entail different nucleosome modifications. Heterochromatin has increased hypoacetylated histones and H3K9 methylation. On the other hand, euchromatin is characterized by acetylation of H3 and H4 histones and H3K4 methylation [36] (**Figure 2**).

Aging has been associated with some epigenetic marks such as decreased H3K27 trimethylation and H3K9 methylation or augmented H3K4 trimethylation, H4K16 acetylation and H4K20 trimethylation [5], [37], [38]. In cardiac aging, loss of repressive marks and gain of active marks have been reported. Some studies suggested that these effects might lead to activation of genes promoting aging programs, deleterious activation of repetitive sequence and augmented transcriptional noise [39]. Cardiomyocytes isolated from failing mouse hearts shared methylation patterns with neonatal mice [40]. However, it is unclear whether changes in the epigenetic patterns return to an embryonic stage or merely shift to open chromatin. This is because the knowledge of epigenetic regulation in cardiac aging is still incomplete. Furthermore, many investigations have concentrated on epigenetic changes associated with CVDs and not with the aging process itself, therefore further studies are required to elucidate this process [39].

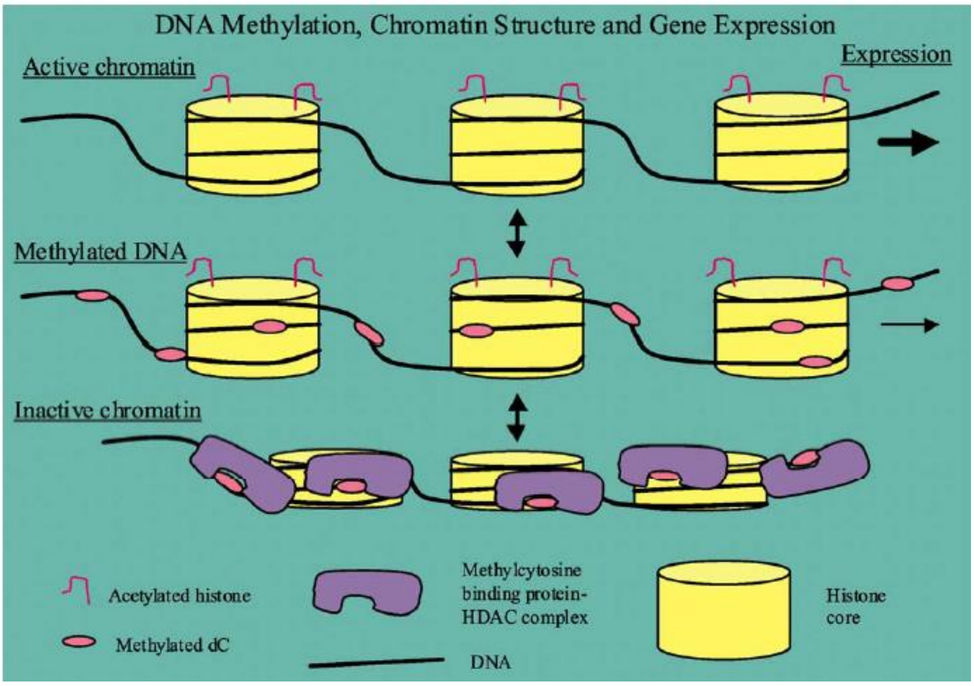

Figure 2. Chromatin inactivation by DNA methylation and histone deacetylation. Extracted from [32].

1.2.4 Loss of cellular proteostasis

Cellular components are constantly being renewed, with damaged organelles and biomolecules being replaced with new functional structures. Correct cell functioning requires a balance between the synthesis of new proteins and the degradation of the misfolded and old ones. This balance is known as proteostasis [41]. A series of processes regulates proteostais by controlling protein concentration, folding, interaction and localization from synthesis to degradation. Proteasome and autophagy are the main clearance mechanisms to maintain proteostasis. The ubiquitin-proteasome system is a complex machinery that uses ubiquitination to target unfolded and proteolyzed proteins for degradation. In the proteolysis mediated by autophagy, proteins are cleared in the lysosome. At first, this process was considered to be non-selective, but chaperons and other cargo-recognition proteins, including ubiquitins, are also responsible for specifically identifying and degrade proteins. Keeping this balance during aging is challenging as these mechanisms decline and give rise to the accumulation of damaged proteins [42]. This altered proteostasis is common to numerous age-related diseases: Parkinson [43], Huntington [44] or Alzheimer [45].

Cellular components that more frequently accumulate with age are damaged mitochondria, protein aggregates and lipofuscin. Lipofuscin is a fluorescent pigment composed of proteins, lipids and carbohydrates which cannot be degraded and accumulate during aging, particularly in brain and cardiac tissues [41]. Different studies have reported its relation with age in animal [46], [47] and human cardiac tissue [48], [49]. For that reason lipofuscin is considered an age pigment [50].

1.2.5 Cellular senescence

Cellular senescence implies cell cycle arrest that reduces the tissue regeneration capacity and leads to inflammation and pathological tissue remodeling. This process is mediated by cell cycle inhibitory tumor suppressor pathways p53-p21 and p16 [51], [52]. Cellular senescence is believed to have developed to avoid accumulation of damaged cells that can therefore become cancerous. Nevertheless, senescent cells accumulation is detrimental as these cells directly and indirectly harm the neighboring cells [53]. Senescent cells have a specific senescence-associated secretory phenotype (SASP) that secretes proteins, cytokines, chemokines, growth factors and proteases to the tissue microenvironment. SASP cells act autocrinally by reinforcing their own cellular senescence and paracrinally by triggering the senescence of nearby cells [54], [55]. It has been reported that senescent cells briefly emerge during organ development in mammals, in which SASP factors participate in the activation of the differentiation of the surrounding cells and elimination of unnecessary cells [56]. The repair of damaged tissues is another important physiological function performed by SASP. For example, SASP factors secreted by fibroblasts in harmed tissues enlist immune cells to remove damaged tissue and trigger skin progenitor proliferation to generate new skin [57]. However, SASP factors have also pernicious effects as they contribute to inflammation and cancer [56].

As cardiomyocytes are terminally differentiated cells, cell cycle arrest is not the main hallmark of senescence. However, cardiac senescent cells express SASP (tumor growth factor beta, tumor necrosis factor alpha, growth and differentiation factor 15 and interleukins, among others) for controlling non-myocyte cells of the surrounding microenvironment as well as promoting cardiac malfunctioning and remodeling. Senescent cardiomyocytes accumulate with age and result in chronic inflammation and functional abnormalities as well as in altered intercellular communication [51], [52].

1.2.6 Cardiac extracellular matrix remodeling

The cardiac extracellular matrix (ECM) is an intricate structure that accommodates various cell types, including cardiomyocytes, cardiac fibroblasts, cardiac vascular cells and smooth muscle cells. The principal components of the ECM are: i) adhesive proteins: fibronectin, collagen IV and laminin; ii) anti-adhesive proteins: osteopontin, thrombospondin and tenascin; iii) proteoglycans; and iv) structural proteins: elastin and collagen [58]. ECM has a structural function conferring strength, stiffness and support, but it also accommodates several proteins, transfers mechanical forces to myocardial fibers and takes part in effective cardiac activity by myocyte alignment and blood flow control during contraction and compliance [59], [60]. ECM homeostasis depends on the equilibrium between metalloproteinases (MMPs) and tissue inhibitors of metalloproteinases (TIMPs). Alterations in this balance can lead to abnormal cardiac function [59], [60]. MMPs comprise more than 20 proteins. Most of them are inactive enzymes that are activated in the ECM to degrade proteins. Four kinds of TIMPs that hinder the excessive MMP degradation of proteins have been identified [59].

The different ECM components are synthesized by different heart cells: collagen IV, by cardiomyocytes and endothelial cells; collagen I, collagen III and fibronectin, by fibroblasts and smooth muscle cells; laminin, by endothelial cells, cardiomyocytes and smooth cells. Cardiac structure and functionality are highly dependent on the ratio of ECM proteins, and therefore affected by any changes thereto. Among other ECM fundamental functions, proteoglycans and glycoproteins maintain the geometry of the heart. Collagen is the most abundant element [59].

Five collagen types have been identified so far in the heart (I, III, IV, V, and VI). All except collagen V are highly relevant for the cardiac system. Collagen I and III prevent blood vessels deformation, maintain tissue structure and constitute more than the 90% of the total collagen. The basal lamina is comprised of collagen IV and VI [58]. Collagen is fundamental for the proper function of the heart and its remodeling can trigger cardiac malfunctioning. In multiple organs, such as pancreas [61], kidney [62], [63], lung [64] and liver [65], [66], progressive fibrosis is a hallmark of aging. In the heart, there is an age-related accumulation of collagen in the cardiac interstitial and perivascular space as well as in the vascular wall that paves the way for myocardial and arterial compliance [67]. Studies using animals have reported increased cardiac fibrosis accumulation in mice [68]–[70] and dog [71]. This age-related deposition has also been reported in humans, namely in LV [72], [73] and in the right atrium [74], [75].

Excessive fibrosis accumulation hinders electrical coupling and can contribute to arrhythmia generation [76]. Both collagen amount and texture are relevant for the electrical impulse propagation [77]. Fibrosis is classified as replacement fibrosis or reactive fibrosis [78]. Replacement fibrosis takes place to maintain the structure of the myocardium after removal of dead myocytes. It is normally associated with compact or patchy fibrosis and usually occurs due to chronic pressure overload or after an infarct. Compact fibrosis refers to whole areas being replaced by fibrosis, and patchy fibrosis to areas where fibrosis is intermingled with myocardial cells. Surprisingly, compact fibrosis is less arrhythmogenic as re-entries can only occur around the fibrosis area [79], which is not often observed, whereas patchy fibrosis can cause large conduction delays due to zig-zag conduction between bundles, thus more frequently leading to arrhythmias [80]. The term reactive fibrosis is used when fibrosis synthesis is faster than its degradation, but there is not a loss of viable cardiomyocytes. It can be classified as diffuse and interstitial. Several factors can activate this process such a phenotypical switch from fibroblast to myofibroblast, changes in gene expression or aging, among others. Diffuse fibrosis resembles the patchy one, but collagen strands are shorter and its degree of arrhythmogenicity is also lower, whereas interstitial fibrosis is located between individual cells and its excess results in reduced electrical coupling [81], [82].

1.2.7 Altered intercellular communication

Gap junctions (GJs) are intercellular structures that connect two adjacent cells allowing electrical coupling and the exchange of small molecules, ions or metabolites with a size of approximately 1 kDa. A GJ is comprised of two hemi-channels, named connexons, each of them belonging to one of the two adjoining cells. Each connexon consists of six proteins, called connexins, and connects with the connexon of the neighboring cell to assemble a functional channel in the intercellular space (**Figure 3**). There are three main connexin isoforms expressed in cardiomyocytes: Connexin 40, Connexin 45 and Connexin 43 (Cx43), the latter being the most expressed one in ventricular cardiomyocytes [83]. GJs along with adherens junctions and desmosomes are placed in the intercalated disks at the longitudinal cell edges between two cells [82]. A reduction in CX43 between intercalated disks has been reported in patients with different cardiac pathologies including coronary artery disease, idiopathic dilated cardiomyopathy or Naxos disease [84]–[88]. Besides, other studies have reported a redistribution of CX43 in t patients with cardiac diseases [89]–[91].

Little is known about the relationship between aging and Cx43 quantity and spatial remodeling in the heart. The few available studies have been conducted mostly in small animal models. These studies have shown divergent results depending on animal species and age groups. In mice, a significant decrease of Cx43 in the LV was reported for old animals as compared to young ones [92]. Also, a decrease in Cx43 at the LV was described in middle-aged mice compared to young mice [93]. In rabbits, the proportion of lateral membranes of ventricular myocytes positively stained for Cx43 was significantly larger in aged versus young rabbits, which was accompanied by a non-significant increase in the percentage of polar membranes positively stained for Cx43 [94]. In hamsters, Cx43 content showed to be low in young animals, significantly higher in adults and low in old animals [95]. In rats, studies reported a decrease in Cx43 content in aged versus adult animals [96] and diminished Cx43 content in adult versus young animals [97]. In humans, however, studies on the effect of age on CX43 amount and location are lacking.

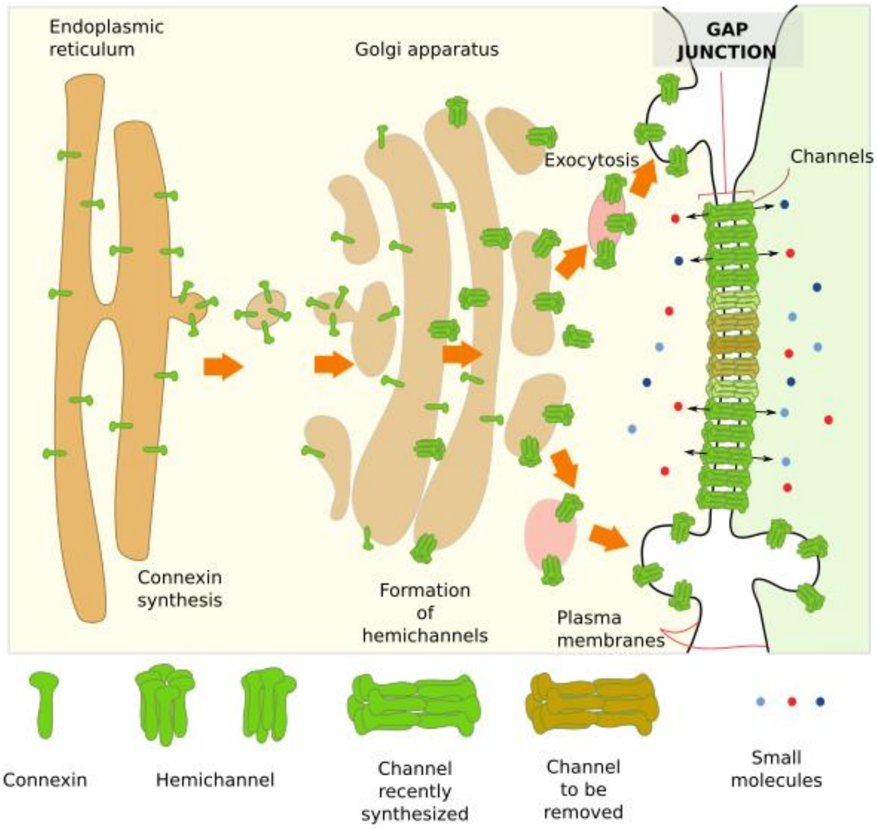

Figure 3. Synthesis, assembly and formation of gap junctions. Extracted from [98].

1.2.8 Gene expression deregulation

Aging is associated with changes at gene expression level in all tissues and organs. Particularly, cardiomyocytes must adapt to the changes and demands of the organism, which leads to alterations at functional, structural and gene level. Mouse models have been used to characterize age-associated changes at gene and protein level. Among other gene expression changes, cardiac aging has been associated with reduced expression of both skeletal and cardiac sarcomeric α-actin isoforms [99], [100] and SERCA, the sarco/endoplasmic reticulum Ca^{2+}-ATPase [100]–[102]. Bodyak *et al* [100] reported also decreased expression of different genes related to the sarcomere: cardiac myosin light chain 2 (*MYL2*), α-myosin heavy chain (*MYH6*), tropomyosin 1 (*TPM1*), troponin I type 3 (*TNNI3*) and troponin C (*TNNC1*) as well as genes of the complex 1 and 3 of the mitochondria respiratory complex.

MicroRNAs (miRNAs) are single-strand non-coding RNAs sequences of approximately 18-25 nucleotides that regulate gene expression at the post-transcriptional level. They are largely conserved during evolution and control numerous biological functions in physiological conditions (differentiation, metabolism, cell proliferation, apoptosis, development and aging) and pathological ones (neurological disorders, cancer or CVDs). A miRNA can regulate multiple genes, controlling full mechanisms, and a gene can be regulated by multiple miRNAs. miRNAs inhibit the expression of a gene by complementary binding to the target mRNA transcript [103]. miRNAs are transcribed by the RNA polymerase II as primary transcripts (pri-miRNA) that are further processed in the nucleus by the Drosha to form a stem-loop double strand RNA (pre-miRNA) that it is exported to the cytoplasm for Dicer endonucleases to generate a short miRNA duplex. After argonauta (Ago) processing, the guide strands are loaded into the RNA-induced silencing complex (RISC) to bind to the target mRNA to degrade it or pause translation. The passenger strand is frequently degraded [104] (**Figure 4**).

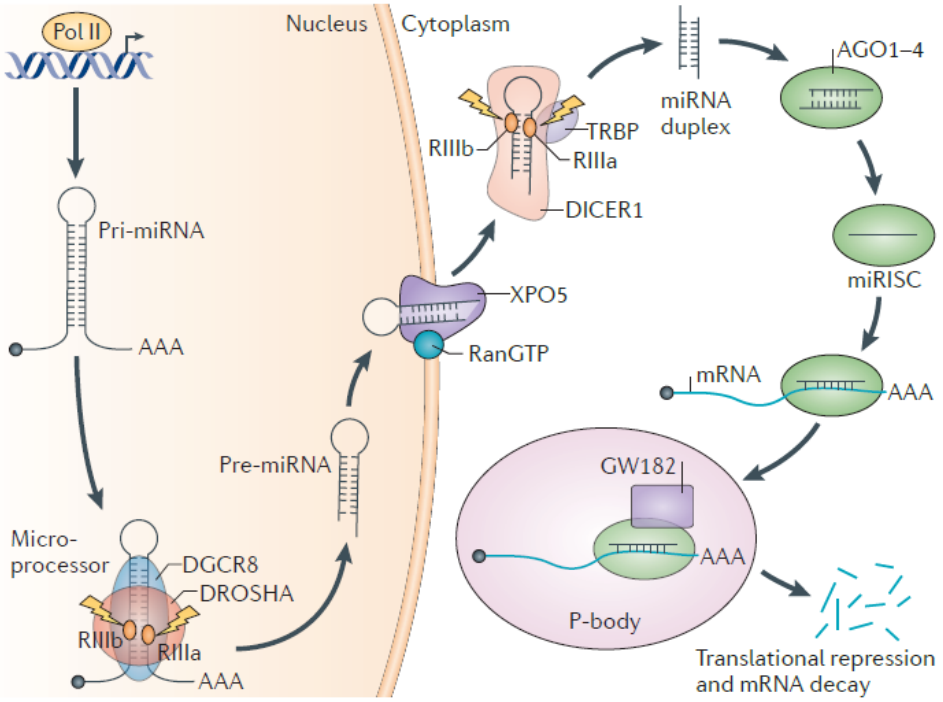

Figure 4. The biogenesis of miRNAs. Extracted from [105].

During the last years, miRNAs have been proposed as key regulators of CVDs and aging. Using animal models some genes regulated by miRNA have been described in relation to cardiac aging [6]. For example, miR-18a and miR-19b are associated with age-related ECM remodeling as they regulate the expression of the connective tissue growth factor and thrombospondins, being both genes related to the ECM [6], [106]. Another example is the increased expression of miR-22 which regulates cardiac fibroblast senescence [107] or the augmented expression of miR-34a whose silencing *in vivo* alleviates the increased cardiomyocyte cell death observed in mice [108]. Further studies are required to characterize the role that miRNAs play on human cardiac aging.

miRNAs are actively and passively released to blood, thus circulating miRNAs are avidly being investigated as biomarkers in age and disease. Rusanova *et al* [109] proposed three miRNAs associated with frailty in the elderly: miRNA-21 and miRNA223 are related to inflammation and miRNA-483 to the regulation of melatonin synthesis. Considering that all organs do not age at the same rate [110], it would be necessary to find organ-specific circulating miRNAs to estimate cardiac aging.

1.3 Biological aging

Chronological age (CA) is a main risk factor for many human diseases. Nevertheless, there is large inter-individual heterogeneity in health outcomes of elder individuals. Some individuals are frail and need continuous assistance, whereas others are independent and exhibit good health until extreme ages [111]. Studies investigating human aging are mainly conducted transversally in relation to CA. But CA is a mere time index that does not necessarily explain the biological condition of an individual or an organ. The biological age (BA) of an organ, perceived as its actual structural and functional state, is a composite of both genetic and environmental factors acting together over time. Traditional aging research in humans is performed cross-sectionally and its outcomes are conditioned to the masking effects of this inter-individual variability, which could be accounted for by BA but not by CA.

BA is a complex parameter that can be scored by different approximations such as clinical markers, functional tests or molecular indicators. Measures of the physical ability are relevant indicators of present and future health. Some of the physical function measurements that are commonly used include grip strength, chair stand, walking speed or standing balance. Poor performance in these tests is related to higher mortality rates [112]–[114]. Since body composition changes with age, some anthropometrical indexes are also used as aging markers such as body mass index, muscle mass and waist circumference. Risk mortality increases with high abdominal adiposity, loss of skeletal muscle mass and augmented body mass index [115]–[117]. As imaging technology is improving, new methodologies are being developed based on magnetic resonance imaging or peripheral quantitative computer tomography to analyze body composition and muscle mass with greater accuracy. Besides, wearable devices will provide precise and real-time data in future studies. Some aging biomarkers are measured in blood and are related to glucose metabolism, inflammation, cardiovascular function, nutritional status or endocrinology [118]. For example, there is strong evidence that the lipid profile correlates with morbidity and mortality [119], [120]. Besides, tumor necrosis factor α, interleukin 6, interleukin 1β and C-reactive protein are collectively named inflammaging and its increase is associated with mortality [121], [122]. Furthermore, centenarians have reduced presence of this inflammaging [123]. Although there is evidence of these blood measurements as aging predictors, it is necessary to establish standards and reference ranges[118].

As epigenetic alterations are an aging hallmark, some DNA methylation clocks have been developed [124], [125]. These clocks are based on DNA methylation being a dynamic modification that changes with age. They are mainly focused on cytosine methylation in CpG dinucleotides [126]. DNA methylation clocks are capable of precisely predicting age across a wide range of tissue types, on top of the tissue for which they were developed, suggesting that they measure aging signals that are common between cell types. Nevertheless, mortality risk, the broadly used BA indicator, has shown inconstant association with these clocks, thus raising doubts about their applicability. RNA expression levels have also been used to develop aging clocks. As they are more related to genes, their interpretation and experimental validation is augmented [127], [128]. Even though great efforts have been made in this field to overcome noise associated with transcriptomic data, it is not clear how reproducible these methods are in large human cohorts. Most methods have been conducted in reduced populations and not tested in independent cohorts or are based on older microarray technology which is not as precise and reproducible as recent RNA sequencing technology. Based on RNA, organ-specific BA indicators calculated as an index of apparent age have been also developed [128]. Furthermore, BA indicators based on proteomics of plasma samples have been proposed. Although in principle they have many advantages, they have shown some drawbacks too. Plasma protein composition is affected by kidneys, but this process remains substantially unknown. Besides, proteomic technology is more recent than DNA technology and, consequently, these proteomic clocks are not as validated as methylation ones. Some studies have used multiple targeted and untargeted mass spectrometry and nuclear magnetic resonance methods to generate metabolomic clocks from plasma and urine metabolites. These methods have advantages, as they can detect many metabolites, although the structure of most of them is still not characterized [129].

As the accumulation of senescent cells is another aging hallmark, some aging biomarkers are based on this mechanism. The most broadly used are β-galactosidase (β-gal) and P16. Increased β-gal activity reflects augmented lysosomal mass, but this marker can yield false positives, so it is usually combined with other indicators [53], [130]. Cellular senescence is tightly related to the expression of the cell-cycle regulator and cell senescence marker *P16*, expressed from the *CDKN2A* locus [131]. *P16/CDKN2A* is considered a BA marker in human skin and peripheral blood cells [132], [133].

There are organ-specific markers that correlate with organ dysfunction such as markers for the diagnosis and prognosis of heart failure (cardiac troponin, brain natriuretic peptide and N-terminal pro-brain natriuretic peptide), indicator of kidney chronic disease (cystatin C), the neurodegenerative disease marker (apolipoprotein E level in cerebrospinal fluid) or indicators of liver dysfunction (alkaline phosphatase or albumin). However, its application as long-term risk prediction is yet not established [134].

The significance of BA on top of CA in CVD has been studied. BA has been associated with improved prognosis capacity after ischemic stroke as compared to CA [135] and with higher risk of CVD [136].

1.4 The heart

1.4.1 Cardiac anatomy and function

The heart is the most important organ of the circulatory system. It is divided in two sides: the right side pumps blood to the lungs and the left side pumps blood to the peripheral organs. Each side is divided in two chambers: the atrium (upper chamber) and the ventricle (lower chamber) (**Figure 5**). Under physiological conditions, oxygen-poor blood reaches the heart through the right atrium, which contracts after its electrical excitation and ejects the blood to the right ventricle. From there, ventricular contraction pumps blood to the lungs for it to be oxygenated. Meanwhile, on the left side, oxygen-rich blood enters the left atrium from the lungs. The electrical activation of the left atrium triggers its contraction and the blood passes to the LV. The contraction of the LV is responsible for oxygen-rich blood to be pumped to all organs in the body. Appropriate blood circulation requires a fine interplay between the electrical and mechanical function of the heart, with the electrical activation being the trigger for the mechanical contraction [137].

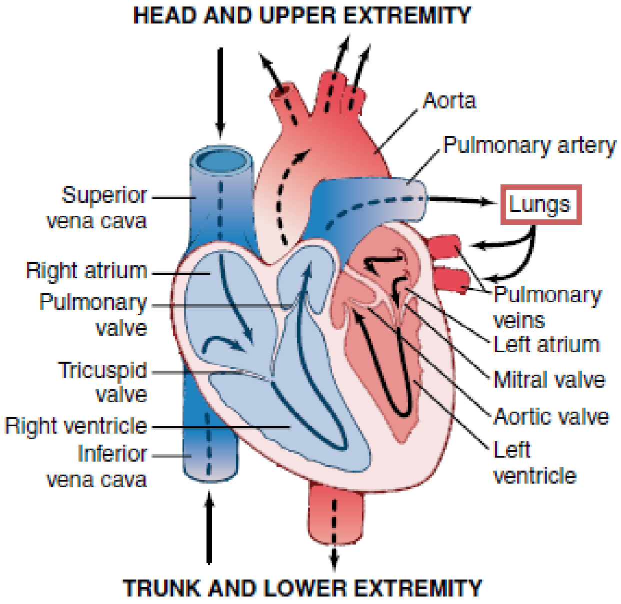

Figure 5. Structure of the heart. Extracted from [137].

1.4.2 Cardiac electrical activity

Three main types of proteins in the cellular membrane of the cardiomyocytes are involved in their electrical activity: ion channels, exchangers and pumps. Ion channels, i.e., pore-forming proteins embedded in the membrane, allow the selective exchange of ions between the inside and outside of the cell through protein conformational changes, which cause the channel to open and conduct the ions or to close and, thus, restrict their movement across the membrane.

Sodium (Na^+), potassium (K^+), calcium (Ca^{2+}), and chloride (Cl^-) are the main ions in the intracellular and extracellular media. Two forces control their passive movement through ion channels: the electrical gradient (i.e., the difference in the potential between the inside and outside of the cell) and the chemical gradient (i.e., the difference in the ion concentrations between the two media). The Na^+-Ca^{2+} exchanger is an important element for Ca^{2+} regulation in the cell. The Na^+- K^+ pump is responsible for maintaining the concentrations of Na^+ and K^+ at both sides of the cell membrane [138].

The sinoatrial (SA) node is the natural pacemaker of the heart. It generates the electrical stimuli that are transmitted throughout the heart to the atria and ventricles. When a stimulus has a magnitude above the minimum required threshold and excites the atrial and ventricular cardiomyocytes, it causes the transmembrane potential of these cells to rapidly grow (activation or depolarization phase). This is followed by a slower decrease during which the cell returns to its resting state (relaxation or repolarization phase). The change in the transmembrane potential over time corresponding to a heartbeat, i.e., the AP of the cell, is generated by ion exchanges between the intracellular and extracellular spaces through ion channels. These exchanges are associated with inward and outward ionic currents. While AP depolarization is fundamentally associated with the entry of Na^+ ions through the Na^+ channels, the return of the transmembrane potential to its resting value corresponds to different ions passing through different ion channel families [137]. The AP of atrial and ventricular cells is divided into the following 5 different phases (**Figure 6**):

Phase 0. Fast depolarization. The upstroke characteristic of this phase is due to the fast inflow of Na^+ through voltage-gated Na^+ channels. These Na^+ channels are open for a short period of time and generate the fast Na^+ current (I_{Na}). During this phase the transmembrane potential varies from -85 mV to 20 mV in about 3-5 ms [139], [140].
Phase 1. Early repolarization. The decline in the transmembrane potential is due to the inactivation of Na^+ channels, while the outward transient K^+ current (I_{to}) begins to repolarize the cell [139], [140].
Phase 2. Plateau. The equilibrium in this phase is due to the balance between the influx of Ca^{2+} ions through the slow L-type Ca^{2+} channels (I_{CaL}), the slow opening of outward K^+ channels (I_{Ks}). Other involved ionic currents are the late Na^+ inward current (I_{NaL}) and the current associated with the activity of the Na^+/Ca^{2+} exchanger (I_{NaCa}) [139], [140].
Phase 3. Repolarization. During this phase the transmembrane potential goes back to the resting potential due to the inactivation of Ca^{2+} channels while K^+ channels are open. These K^+ currents are the rapid delayed rectifier current (I_{Kr}), the slow delayed rectifier current (I_{Ks}) and the inwardly rectifier current (I_{K1}) [139], [140].
Phase 4. Resting potential. The transmembrane potential is reached (approximately -85 mV) mainly due to the outward K^+ currents (I_{K1}) and the current associated with the activity of the Na^+/K^+ pump (I_{NaK}) [139], [140].

Some cardiac arrhythmias have been associated to secondary voltage depolarizations known as early afterdepolarizations (EADs) and delayed afterdepolarizations (DADs). Voltage fluctuations during repolarization are the primary source of EADS. EADs can augment the dispersion of refractoriness by locally prolonging the APD, making the tissue susceptible to reentry. In addition, EADs can act as reentry-inducing triggers if they reach the threshold for propagation out of this region as premature ventricular contractions. During diastole, spontaneous Ca^{2+} generates DADs. DADs can lead to conduction block by locally depolarizing the resting membrane potential. If they reach the threshold for Na^+ channel activation, they can lead to premature ventricular contractions and trigger reentry [141].

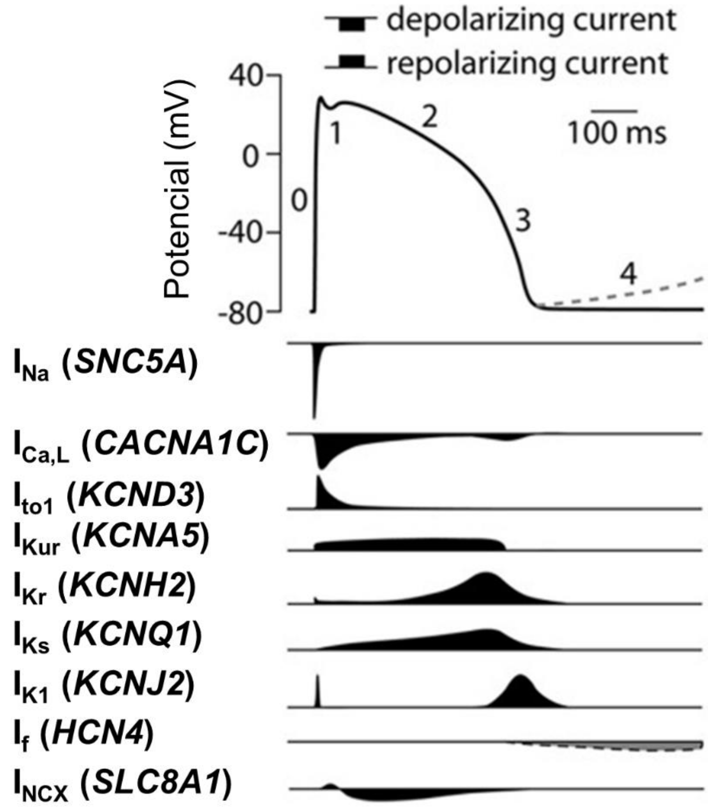

Figure 6. Schematic representation of a human ventricular AP with the ionic currents (genes encoding the ionic channels in brackets) involved in each AP phase and their time course. Extracted from [142].

1.4.3 Cardiac electromechanical coupling

The cardiac contraction-relaxation cycle is possible due to cardiac electromechanical coupling. Specifically, the depolarization of the cardiac cell membrane causes the opening of L-type Ca^{2+} channels resulting in an inward Ca^{2+} current that increases the intracellular Ca^{2+} concentration in the dyadic space of cardiomyocytes. This triggers the opening of Ca^{2+}-sensitive ryanodine receptors (RyR) in the sarcoplasmic reticulum (SR), which induces the Ca^{2+} release from the SR, augmenting even further the Ca^{2+} levels in the cytosol. Part of this released Ca^{2+} binds to troponin, allowing the interaction of the two contractile proteins actin and myosin, which leads to the mechanical contraction of the cardiomyocyte. After contraction, the SERCA pump restores cytoplasmic Ca^{2+} concentration by introducing Ca^{2+} into the SR [143].

In addition to how electrical excitation affects mechanical contraction, the so-called mechano-electrical feedback (MEF) also explains how the deformation of the heart affects cellular excitation. MEF has been demonstrated to have a significant impact on cardiac arrhythmias. One of the MEF mechanisms is associated with the effect that myofilament length has on Ca^{2+} dynamics, as the buffer ability of troponin augments when myofilaments are stretched [144], which impacts the AP [145]. Another relevant MEF mechanism is through mechano-sensitive ion channels, like the stretch-activated channels in the cell membrane, whose activity contributes to electrical features such as rate dependence, refractory period, AP duration or resting membrane potential [146].

1.4.4 Cardiac electrical propagation

Under physiological conditions, the spontaneous AP generated in the SA node initiates each cardiac cycle. The SA node is situated in the superior lateral wall of the right atrium, close to the opening of the superior vena cava. The AP propagates from the sinus node to both atria. It first activates the right atrium and then the left one. Next, the electrical impulse travels to the ventricles through the AV node. The AV node, which is part of the specialized cardiac conduction system, causes a transmission delay to allow atria to contract and pump blood into the ventricles. The electrical propagation from the AV node to the ventricles occurs through the His bundle and the Purkinje fibers, which facilitate a rapid spread of the cardiac impulse throughout the ventricles. After their electrical depolarization, the ventricles contract and pump blood to the rest of the body (**Figure 7**).

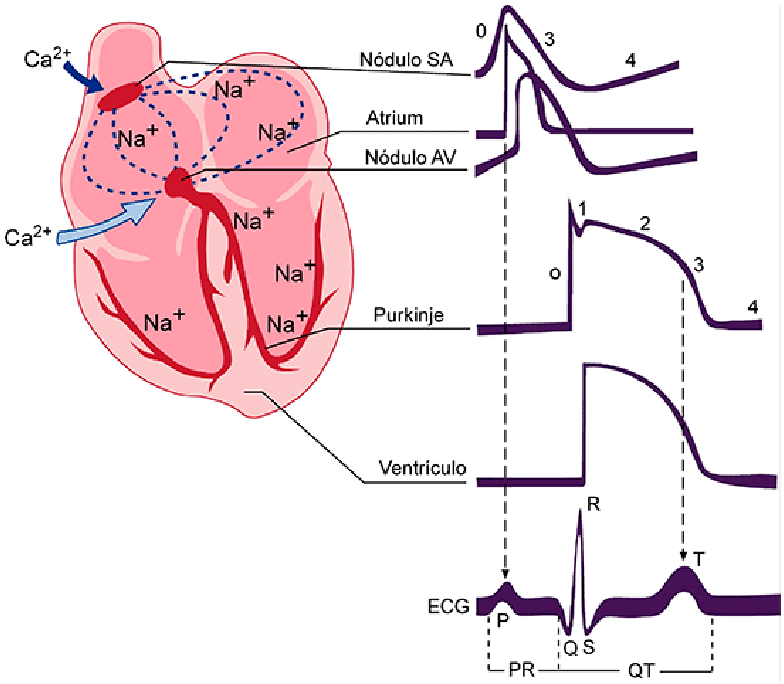

Figure 7. Schematic representation of the APs recorded in various cardiac tissues and the correspondence with the electrocardiogram waves and intervals. Extracted from https://www.itaca.edu.es/cardiac-action-potential.htm#potential2

Electrical conduction in the heart is highly dependent on cellular connectivity, in addition to the specialized cardiac conduction system. Individual cardiac muscle cells are separated by intercalated discs. GJs form when adjoining cell membranes fuse at each intercalated disc. Ions preferentially move along the longitudinal axes of the cardiac muscle fibers and the electrical impulse travels from one cardiac cell to the next one through intercalated discs. Thus, cardiac muscle is a syncytium of closely interconnected cardiac cells and, when one of these cells excites, the AP propagates to the rest of them [137].

The elapsed time since the last depolarization and the duration of the repolarization determine the ability of cardiac cells to respond to a stimulus. Over the course of the AP, four states of refractoriness can be distinguished: 1) the absolute refractory period is the time during which, regardless the strength of the stimulus, it will not produce an AP because the membrane is not sufficiently repolarized and the Na^+ channels are in their inactivated state; 2) the relative refractory period, which requires a larger strength of the stimulus to trigger an AP; 3) the supernormal period, when the threshold on the stimulus strength to produce an AP is lower than usual; and 4) normal excitability [147].

1.4.5 Electrograms and electrocardiograms

An intracardiac electrogram (EGM) is a signal obtained by placing electrodes directly on the surface of the heart to measure the electrical activity in the region where the electrodes are placed. EGMs are invasive recordings that quantify the difference between the electrical signals captured by two electrodes. If the two electrodes are intracardiac, the acquired signals is a bipolar EGM. If one electrode is intracardiac and the other one is remotely positioned, the acquired signals is a unipolar EGM.

The standard 12-lead electrocardiogram (ECG) is recorded from 12 different views using 10 surface electrodes. The ECG signal measures the electrical activity of the heart on the body surface. To acquire the standard 12-lead ECG, four limb electrodes and six chest electrodes are used. The limb electrodes are located in each of the arms and legs and allow recording standard limb leads I, II and III and the augmented limb leads aVR, aVL and aVF. The chest electrodes are located at specific locations on the chest and are used to record precordial leads V1, V2, V3, V4, V5 and V6. The standard limb leads are bipolar as they measure differences between a positive and a negative electrode in the limbs. The augmented and precordial leads are unipolar as they measure differences between a positive electrode and a combination of electrodes that acts as a negative electrode.

Each cardiac cycle is represented in the ECG by P and T waves and the QRS complex. The QRS complex is usually, but not always, composed of Q, R and S waves. The P wave and the QRS complex are related to depolarization: the P wave corresponds to the atrial depolarization and the QRS complex to the ventricular depolarization. Atrial repolarization is masked within the QRS complex, which is considered to represent almost exclusively the ventricular repolarization, as the mass of the ventricles is considerably larger and, thus, will have greater contribution to the ECG signal. Ventricular repolarization is associated with the T wave. Other segments and intervals in the ECG signal include the QT interval, which comprises the duration of ventricular depolarization and repolarization. The time interval between ventricular depolarization and repolarization is, under physiological conditions, an isoelectric period, which is represented in the ECG by the ST segment. The RR interval is the elapsed time between two consecutive heartbeats. [148] (**Figures 7-8**). **Figure 7** shows the correspondence between the ECG waveforms and the APs of cells from different regions of the heart. As can be observed, the electrical activities of all cells in the heart contribute to the ECG. A close relationship exists between the cardiac electrical activities at different scales, covering ion channels, cells, tissues, the whole heart and the ECG measured on the body surface.

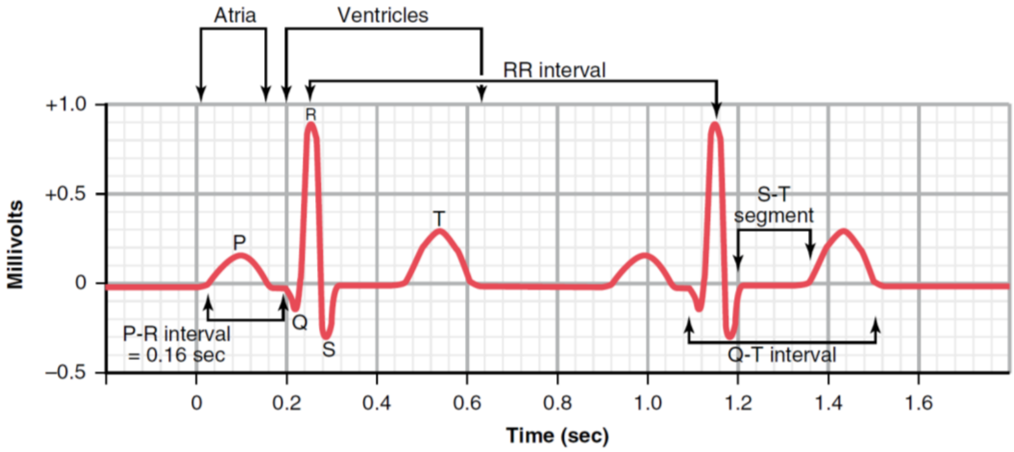

Figure 8. Normal electrocardiogram. Extracted from [137].

1.5 *In silico* electrophysiological models

Computational models have become very powerful tools to complement *in vivo* an *in vitro* research, since they do not entail ethical restrictions, and allow almost unlimited hypotheses to be tested, even unfeasible ones for *in vivo* an *in vitro* studies, in a time and cost-effective manner. *In silico* models have been used to model physiological processes, diseases or to develop drugs by studying the mode of action or derived adverse cardiac effects, among other applications. The huge development of computational models has been fueled by the increase in computational power at continuously decreasing costs available to researchers nowadays [149].

1.5.1 The Hodgkin & Huxley cellular model

In 1952, Hodgkin and Huxley [150] proposed the first electrophysiological model of an excitable cell, which in their case was a squid giant axon. In their model, called the HH model in the following, Hodgkin and Huxley formulated the equations for the temporal evolution of the transmembrane voltage and the ionic currents on the basis that the cell membrane is selectively permeable to K^+ and Na^+ ions in a voltage and time dependent manner. They depicted the electrical activity of the squid giant axon considering that this can be represented by an electrical circuit composed of resistors (ion channels), a capacitor (cell membrane) and voltage sources (**Figure 9**). In the HH model, four different ionic currents were included: the Na^+ current (I_{Na}), the K^+ current (I_K), the leak current generated by all other types of ions (I_L) and the capacitive current (I_c) [151].

The movement of ions through the cell membrane is determined by electrical and diffusion forces. Each type of ion reaches an equilibrium when these two forces are equal in magnitude and opposite in sign. The potential equilibrium of an ion x is known as the Nernst potential and is defined as:

$$V_X = -\frac{RT}{Z_x F}\log\left(\frac{[x]_i}{[x]_e}\right) \tag{1}$$

where V_x is the Nernst potential for the ion x, R is the gas constant, T is the absolute temperature, Z_x is the ion valence, F is Faraday's constant, $[x]_i$ is the ion intracellular concentration and $[x]_e$ is the ion extracellular concentration.

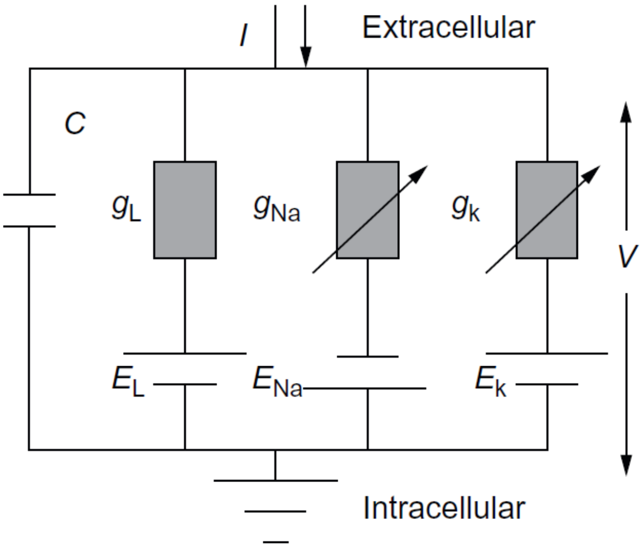

Figure 9. **Schematic diagram of Hodgkin-Huxley model.** Extracted from [151].

The diffusion force is modeled as a voltage source using the V_x potential calculated with the above equation. Also, using Ohm's law, the conductance per unit area, g_x, for the ion x is calculated as:

$$g_x = \frac{I_x}{V - V_x} \tag{2}$$

where I_x is the current through the ion channels of type x, V is the transmembrane potential and V_x is the Nernst potential for the ion x. Considering that ion channels are selective for a particular ion type and that ions pass through them only when the channels are open, the conductance g_x is calculated as:

$$g_x = G_{x,max}\, p_{x,o} \tag{3}$$

where $G_{x,max}$ is the maximum current when all channels are open and $p_{x,o}$ is the proportion of channels of type x that are open, with this proportion being dependent on the transmembrane potential V [151].

At the time Hodgkin and Huxley proposed their model, little was known regarding the structure of the ion channels, and they defined their behavior using a set of hypothetical activation and inactivation gates. In the HH model, each of the gates could be in the open or the closed states and transitioned between these two states along time, with the opening and closing transition rates being dependent on transmembrane voltage. For the Na^+ channels, Hodgkin and Huxley defined three activation gates (called m gates), which became open when voltage increased and remained closed during the resting AP phase, whereas inactivation gates (named h gates) were open during the resting AP phase and became closed when transmembrane potential increased. In the HH model, K^+ channels were composed of four activation gates (named n gates). Assuming that each of the gates open and close independently of the others, the proportion of open channels is equal to the product of the proportions of open gates for the different types of gates the channel is composed of [151]. For Na^+ and K^+ channels this can be written as:

$$p_{Na,O} = m^3 h \tag{4}$$

$$p_{K,O} = n^4 \tag{5}$$

Based on the above equations, the K^+ and Na^+ currents in the HH model are defined by the following equations:

$$I_{Na} = g_{Na} (V - V_{Na}) = G_{Na,max}\ m^3 h (V - V_{Na}) \tag{6}$$

$$I_K = g_K (V - V_K) = G_{K,max}\ n^4 (V - V_K) \tag{7}$$

where G_{Na} and G_K correspond to the maximum conductance of Na^+ and K^+, respectively, when all channels are open.

The opening and closing of ionic gates are defined by the following ordinary differential equation (ODE):

$$\frac{d_y}{d_t} = a\,(1 - y) + b\,y \tag{8}$$

where a is the transition rate from the closed to the open state, b is the transition rate from the open to closed state and y is the proportion of open channels.

Taking all the above into account and denoting by **u** the vector that contains all the state variables defined by ODEs, the total current in the HH model is defined as the sum of the ionic currents (K^+, Na^+ and leak currents) and the capacitive current, as described in the following equation:

$$I_{tot}(\mathbf{u}, V) = C_m \frac{dV}{dt} + I_K(\mathbf{u}, V) + I_{Na}(\mathbf{u}, V) + I_{leak}(\mathbf{u}, V) \tag{9}$$

where C_m is the membrane capacitance.

1.5.2 Human cardiomyocyte and fibroblast models

Since the 1950s, when the first AP model for an excitable cell was developed by Hodgkin and Huxley, *in silico* electrophysiological modeling has significantly progressed. Based on the HH model, Denis Noble and coworkers proposed the first mathematical model for mammalian cardiac cells in the 1960s. The Noble model reproduced the electrical activity of Purkinje fiber cells [152]. As reported in a review of models representing cell types of the heart in various species (Noble et al., 2012), the first ventricular cell model was proposed by Krause and coworkers in 1966 [153]. Currently, there are cardiac electrophysiological models for ion channels, cells, tissues and whole cardiac cavities and for many different species [154], [155].

For the purposes of this thesis, the O'Hara-Virág-Varró-Rudy (ORd) model [8] is used to define the electrophysiology of human epicardial and midmyocardial cells. To model fibrosis in ventricular tissues, the MacCannell [9] model is used to describe the electrophysiology of fibroblasts.

1.5.2.1 The O'Hara-Virág-Varró-Rudy human ventricular cell model

The ORd model [8] (**Figure 10**) is a highly detailed mathematical model of the undiseased human ventricular electrophysiology. It was developed based on experimental data from more than 100 undiseased human hearts. It provides descriptions for the electrical activity of human ventricular cells in the epicardium, mid-myocardium and endocardium. This mathematical model reproduces a broad range of physiological behaviors and is validated over a large set of physiological frequencies. The performance of the ORd model has been compared with those of previous human ventricular cell models like the Ten Tusscher-Panfilov [156] model and the Grandi-Bers [157] model [8].

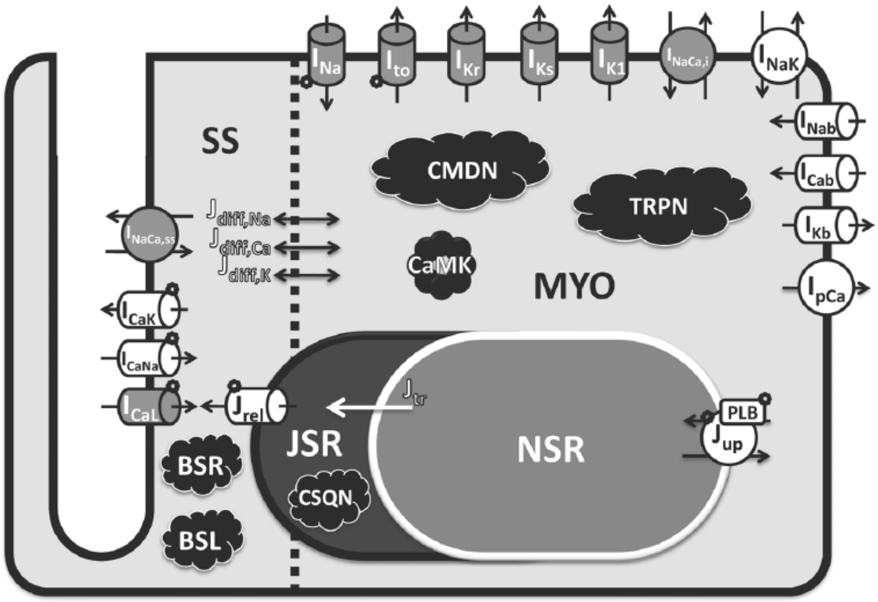

Figure 10. Schematic representation of the ORd model with ionic currents and fluxes. Extracted from [8].

The K^+ currents in the ORd model are I_{ks}, I_{to}, I_{K1} and I_{kr}. In this model, I_{Ks} has less effects on the AP than in other previous *in silico* models. Na^+ currents in the ORd model include I_{NaL} and I_{Na}. Regarding Ca^{2+} currents, the I_{CaL}, the K^+ current through L-type channels (I_{CaK}) and the Na^+ current through L-type channels (I_{CaNa}) are described in the model.

The ORd model uses the HH formulation for some ion channels whereas others are formulated using Markov models (MM). The HH formulation describes the behavior of ion channels by considering that these contain gates that open and close independently along time. The MM formulation considers that the channel can be in different possible states and transitions between them along time. Although the MM formulation can more accurately describe the actual behavior of ion channels, models based on this formulation are computationally much more demanding and mathematically more complex in terms of parameter estimation and identifiability than those based on HH formulations. The dramatic increase in computational time can be affordable for single cell simulations, but may become prohibitive for large-scale simulations [158].

The ORd model also comprises the Na^+- Ca^{2+} exchanger current (I_{NaCa}), the Na^+- K^+ ATPase pump current (I_{NaK}) and the following background currents: K^+ (I_{Kb}), Ca^{2+} (I_{Cab}) and Na^+ (I_{Nab}). Some of the innovations of the ORd model are the accurate kinetics of I_{Ks}, I_{to}, I_{k1}, I_{Kr}, I_{NaL}, I_{Na} and I_{NaCa}, the replication of APD behavior at all physiological pacing rates with and without blocking the major currents and the effects of the Ca^{2+}/calmodulin-dependent protein kinase II (CaMK), which plays an important role in Ca^{2+} cycling. Besides, this model reproduces EADs, described above [159], and alternans, a beat-to-beat alternation in the APD or Ca^{2+} cycling, being both fundamental arrhythmic events that a model should replicate to study cardiac arrhythmias [8].

1.5.2.2 The MacCannell mammalian ventricular fibroblast model

MacCannell and colleagues developed mathematical models to describe the electrophysiological properties of ventricular fibroblasts. Two different fibroblast models were presented: passive and active. In this thesis, the active model is used, which includes four membrane ionic currents: time- and voltage-dependent “delayed-rectifier” K^+ current (I_{Kv}), inward rectifying K^+ current (I_{K1}), Na^+-K^+ pump current (I_{NaK}) and background Na^+ current ($I_{b,Na}$). The MacCannell model for ventricular fibroblasts renders novel insights into the functional consequences of the electrotonic coupling between adult ventricular myocytes and fibroblasts. When the I_{K1} and I_{Kv} currents are considered in the active fibroblast model, there is a significant shortening of the APD and a decrease in the height of the plateau phase of ventricular myocytes.

1.5.3 Propagation of the electrical impulse through the tissue

To mathematically model the electrical propagation in the cardiac tissue, the bidomain and the monodomain models are commonly used. The bidomain equations are defined as a coupled system of equations describing the electrical potential in the intracellular and extracellular domains along the cardiac tissue. The tissue is composed by two continuous domains: the intracellular and the extracellular ones, which coexist in space but are separated by the cell membrane. This is in contrast to real cardiac tissues, where each of the domains physically occupies a fraction of the total volume. In the bidomain model, the two domains act as conducting volumes with different conductivity tensors and electric potential and there is an ionic current flow between them through the cell membrane [160].

The system defined by the bidomain equations consists of two partial differential equations (PDEs) coupled at each point in space with a system of ODEs. The PDEs describe the electric field in the intracellular and extracellular spaces using a reaction-diffusion model, whereas ODEs defined ion concentrations and the proportion of ion channels in the different states for each family of ion channels at the cellular level [160].

The parabolic-parabolic form of the bidomain equations in the region occupied by the cardiac tissue, Ω, is:

$$\nabla\bullet(\mathbf{D}_i \nabla \phi_i) = \chi\left(C_m \frac{\partial V}{\partial t} + I_{ion}(\mathbf{u}, V)\right) - I_i^{(vol)} \tag{10}$$

$$\nabla\bullet(\mathbf{D}_e \nabla \phi_e) = -\chi\left(C_m \frac{\partial V}{\partial t} + I_{ion}(\mathbf{u}, V)\right) - I_e^{(vol)} \tag{11}$$

$$\frac{\partial \mathbf{u}}{\partial t} = \mathbf{f}(\mathbf{u}, V) \tag{12}$$

where $\mathbf{D}_i$ is the intracellular conductivity tensor, $\mathbf{D}_e$ is the extracellular conductivity tensor, ϕ_i is the intracellular electric potential, ϕ_e is the extracellular electric potential, χ is the surface-area-to-volume ratio and C_m is the membrane capacitance per unit area. The vector **u** contains the state variables defined at the cellular level, including the ion concentrations and the gate variables or proportion of channels in different states. I_{ion} (**u**,V) is the ionic current per unit surface area and it is calculated, together with **f**, according to the mathematical model used to represent the cellular electrophysiology at each point in space. The source terms $I_i^{(vol)}$ and $I_e^{(vol)}$ are the intracellular and extracellular stimuli per unit volume. The equations (10) and (11) describe the local conservation of current in the intracellular and extracellular spaces, respectively [160].

The parabolic-elliptic form of the bidomain equations is obtained by combining equation (10) with the sum of equations (10) and (11).

$$\chi\left(C_m\frac{\partial V}{\partial t}+I_{ion}(\mathbf{u},V)\right)-\nabla\bullet\left(\mathbf{D}_i\nabla(V+\phi_e)\right)=I_i^{(vol)} \tag{13}$$

$$\nabla\bullet\left((\mathbf{D}_i+\mathbf{D}_e)\nabla\phi_e+\mathbf{D}_i\nabla V\right)=-I_{total}^{(vol)} \tag{14}$$

$$\frac{\partial\mathbf{u}}{\partial t}=\mathbf{f}(\mathbf{u},V) \tag{15}$$

$$I_{total}^{(vol)}=I_i^{(vol)}+I_e^{(vol)} \tag{16}$$

The boundary conditions for equations (13) and (14) specify the current applied along the border:

$$\mathbf{n}\bullet\left(\mathbf{D}_i\nabla(V+\phi_e)\right)=I_i^{(surf)} \tag{17}$$

$$\mathbf{n}\bullet(\mathbf{D}_e\nabla\phi_e)=I_e^{(surf)} \tag{18}$$

where n is the outward pointing unit normal vector to the tissue and $I_i^{(surf)}$ and $I_e^{(surf)}$ are the intracellular and extracellular currents per unit area applied along the boundary. The group of equations (13)-(18) completely define the system by specifying the initial conditions for the transmembrane potential V and all the variables defined by the vector **u** at all points of the cardiac tissue Ω [160].

If proportionality is considered between the intracellular and extracellular conductivity tensors, $\mathbf{D}_i = \alpha\mathbf{D}_e$, where α is a scalar, the previous expressions can be simplified to lead to the monodomain equations. The parabolic PDE has only one unknown variable, i.e., the transmembrane potential. Subsequently, the second equation of the model is solved to calculate the extracellular potential.

The parabolic PDE dependent on the transmembrane potential is:

$$\chi\left(C_m\frac{\partial V}{\partial t}+I_{ion}(\mathbf{u},V)\right)-\nabla\bullet(\mathbf{D}\nabla V)=I^{(vol)} \tag{19}$$

$$\frac{\partial\mathbf{u}}{\partial t}=\mathbf{f}(\mathbf{u},V) \tag{20}$$

where **D** is the conductivity tensor and $I^{(vol)}$ is the stimulation current. This equation models a reaction-diffusion phenomenon, where the term that contains the ionic current I_{ion}, defined from the cell model, represents the reaction and the term that contains the spatial derivatives of the transmembrane potential describes the propagation of the AP and represents the diffusion. In most situations in which the transmission of the electrical impulse in the heart is simulated, the monodomain model can reproduce the phenomena observed experimentally and is, therefore, the chosen model. However, in particular situations, as when simulating defibrillation through the injection of current in the extracellular space, the different anisotropy of the intracellular and extracellular domains gives rise to electrical patterns that can only be reproduced using the bidomain model [161].

1.6 Aging models

1.6.1 Human aging research

Human aging is a complex and multifactorial process in which many mechanisms are altered. Human studies are constricted by ethical and practical reasons. On top of that, most of them are cross-sectional, which can veil aging features due to the high inter-individual variability. Other studies are based on twin couples, unrelated centenarians, families with many long-living members and longitudinal studies. Twins have been used to analyze genetic and non-genetic factors related to longevity [162]. Centenarians have been analyzed to find causes of their healthy aging and longevity, with studies investigating their genetics, immune system and environment. Research on centenarians is useful to find putative genes and common polymorphisms associated with longevity [163]–[165]. Furthermore, population genetic studies have been performed to identify genetic associations with human lifespan applying Genome-Wide Association analysis. These studies found that some loci are associated with longevity-related phenotypes. However, these studies have some limitations as sometimes replication between studies is limited due to different definitions for cases and controls [166]. There are different regions in the world with families having many long-living members (Netherlanders from Leiden, Mormons from Utah, White Americans from New England, Japanese from Okinawa, Askhenazi Jews living in the USA and Icelanders). Studies of these populations have reported that first-degree family members of these long-live individuals have higher probability to be also a long-lived individual, but not their partners even if they spend most of their adulthood together [167]–[169]. Thus, these results suggest that there is a genetic factor in human longevity. Some studies try to find the genes responsible for this longevity, which may or may not exist. Finally, a longitudinal study is an investigation of the same individuals repeatedly over the years. These studies are time-consuming and expensive, but they can be also enlightening as they can be used to identify gene polymorphisms associated with longevity or with a protective role for disease onset. The three principal longitudinal studies regarding aging and longevity are the Danish 1905 Cohort Survey [170], the Leiden 85-Plus Study [171] and the Invecchiare in Chianti 'InCHIANTI' study [172]. The Leiden 85-Plus Study reported changes in genetics, decreased frequency of HLA-B40 and increased frequency of HLA-DR5 with age. Regarding disability, although women have been found to have higher lifespan, they tend to be more handicapped and perform worse in physical tests [162], [171].

1.6.2 *In vivo* animal models of physiological and accelerated aging

Aging research is fundamentally developed in animal models. Natural aging models were recently reviewed by Brunet and colleagues [173].The different categories of experimental models include non-vertebrate models, traditional vertebrate models and the use of species more related to humans. Non-vertebrate models (worm, fly and yeast) can be genetically modified easily and their lifespan is short. These models have improved the knowledge about genetic pathways involved in longevity and previously unknown chromatin regulators. Despite being useful in some applications, these models lack some organs and systems, which are fundamental in human aging, such as a closed circulation system, blood or an adaptive immune system, among others [174]–[176]. Mice [177] and zebrafish [178] models, the so-called traditional vertebrate models, have been used as they more closely resemble humans. Mouse models have been useful, among other applications, to validate drugs and anti-aging interventions, confirm genes and pathways from non-vertebrate models or unveil genes from the growth hormone axis associated with the regulation of lifespan. Non-human primates (marmosets and rhesus monkeys) are evolutionary more linked to humans, but they are time- and money-wise costly. Also, their environmental and genetic features are difficult to control [179], [180]. Lately, some studies have used companion dogs as they share environmental factors with humans and their genetics are easier to control [181], [182]. Since these dog and non-human primate models are money and time consuming, they are mainly used for validation rather than for discovery investigations.

Aside of natural aging models, there are also accelerated aging models that have greater animal rate survival and briefer experimental time. Mouse and rat are the most commonly used species to induce aging due to its similarity to human, high reproducibility, short lifespan, amenability for transgenesis and reduced costs. However, large animal models of accelerated aging also exist [183]–[185]. This accelerated aging can be induced in the whole animal, thus obtaining systemic aging models, or specific to an organ or tissue. The systemic-induced aging models can be obtained by drug treatment, genetic engineering or irradiation, among others [186]. Some studies have used sub-lethal body irradiation to generate accelerated mouse aging models. This methodology causes tissue and cellular damage by the ionization as well as free radicals' generation due to water radiolysis [187], [188]. An example of transgenic model is the homozygous knock-in mice that express a proofreading-deficient version of PolgA, the catalytic subunit of mtDNA polymerase, are one example of genetic modifications used to induce accelerated aging. Point mutation rates are increased and deleted mtDNA content is augmented in these mice. All of this results in shorter lifespan and the premature onset of the aging phenotype including alopecia, obesity and osteoporosis [189].

Progeria syndrome mice are another example of genetic engineering models. Progeroid syndromes comprise human genetic disorders characterized by reduced lifespan and premature development of symptoms associated with advanced age [186], [190]. The progeroid mice are a useful tool to study aging due to their high similarity to normal aging. Between the non-genetic approaches, D-galactose administration is the preferred method to induce aging due to its fewer side effects and greater survival rate. D-galactose is a reducing sugar present naturally in the body, but at high levels it generates an increase in ROS production leading to mitochondrial dysfunction, apoptosis and oxidative stress, which leads to many organs, like liver, lung, kidney, heart, or the gastrointestinal system, evidencing aging phenotypes [191]–[193]. As per the organ-specific aging models, they have been developed for several organs including brain or nerve system (by e.g., obtaining transgenic mice with amyloid deposition [194]–[196]), muscle (by e.g., generating knockout mice with altered ECM proteins [197]) or liver (by e.g., feeding animals with a high fat diet [198]), among others. With respect to cardiac-specific models of aging, there are mouse models of age related cardiac disease like heart failure with reduced ejection fraction or preserved ejection fraction. The most frequent method used for generating this cardiac model is the long-term infusion of angiotensin II, as this treatment is associated with hypertension, fibrosis, aldosterone secretion and cardiac hypertrophy [199]. Withaar *et al* [200] combine angiotensin II treatment with a high fat diet, obtaining a model with more severe diastolic dysfunction and greater cardiac hypertrophy and fibrosis than with the use of only high fat diet or angiotensin II treatment.

The limitations of translating results from animal species to humans, the shortage of human samples and the difficulties of performing longitudinal aging studies in humans have led to the development of other models to study cardiac aging: *in silico* and *in vitro* models.

1.6.3 *In vitro* aging models

Induced pluripotent stem cells (iPSCs) were derived from embryonic and adult fibroblasts mouse cells by Takahashi and Yamanaka in 2006 [201] and from human fibroblasts subsequently in 2007 [202]. This groundbreaking discovery yielded Yamanaka the Nobel Prize in Physiology or Medicine in 2012 jointly to John B. Gourdon. iPSCs can be differentiated into any cell type of the body and have unlimited replicative capacity without senescence. The revolutionary aspect of this technology is that reprogramming enables the generation of patient-specific iPSC and, thus, the *in vitro* modelling of human conditions in what is called “the patient in a dish” approach. So, iPSCs are a cutting-edge tool than can be used for drug discovery, screening and toxicity evaluation, development of disease-specific autologous cell therapy and modeling human conditions and diseases, among other personalized approaches [203].

hiPSCs can be used to develop *in vitro* models of human cardiac development as well as CVDs, as these models allow studying the physiology and pathology of the human heart *In vitro* differentiation of hiPSCs into cardiomyocytes (iCMs) mimics the known signals occurring at different stages of development Different protocols have been used for this, such as embryoid bodies, inductive co-culture and monolayer differentiation [204]. The latter is preferred due to its simplicity as well as greater efficiency. Improvements in monolayer differentiation protocols have led to obtaining cardiomyocytes differentiation efficiencies of 85% and even 95% when selection based on medium with sodium lactate [205], [206] or SIRPA and VCAM1 surface markers [207], [208] is applied. The obtained cardiomyocytes express ion channels and sarcomeric proteins and they beat spontaneously and show AP and Ca^{2+} transients, although iCMs are functionally immature [209]. Although some improvements in costs and batch-to-batch differences can still be applied, nowadays robust cardiac differentiation is possible and even hiPSCs-CM are commercially available [204].

Human iCMs have been extensively used to characterize molecular mechanisms in many cardiac diseases by mainly using three different strategies: innate, engineered and induced models (**Table 1 and Figure 11**). Innate models are based on the generation of patient-specific disease lines using somatic cells from patients with familial mutations associated with cardiac disease. The introduction or correction of pathogenic mutations in healthy or patient derived iCM, respectively, via genome editing approaches is used for the generation of the engineered model with isogenic backgrounds. The induced model is based on the induction of cardiac disease in iCMs from healthy individuals via exposure to stress-inducing conditions, pathogen infection or drug treatment [210].

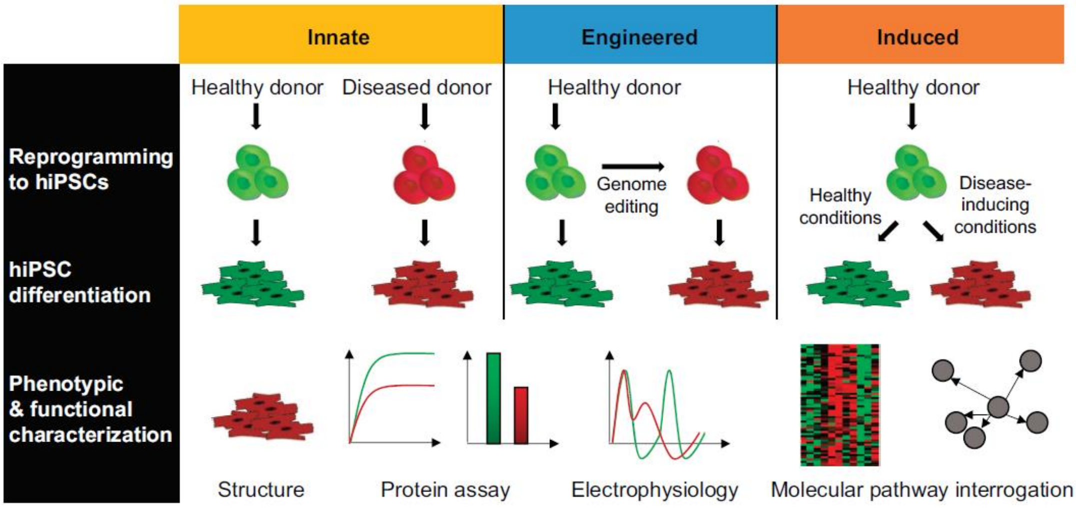

Figure 11. Schematic representation of strategies used for hiPSC-based disease modeling. Extracted from [210]

Table 1. hiPSC-based models of cardiac disease.

Disease	Gene	Modeling approach	References
LQT1	*KCNQ1*	Innate	[211], [212]
	KCNQ1	Engineered	[213]
LQT2	*KCNH2*	Innate	[214]–[217]
	KCNH2	Engineered	[218], [219]
Pompe disease	*GAA*	Innate	[220]–[223]
Fabry	*GLA*	Innate	[224]–[227]
Danon	*LAMP-2*	Innate	[228]
Familial hypertrophic cardiomyopathy	MYH7	Innate	[229]
Catecholaminergic polymorphic ventricular tachycardia type 1	*RYR2*	Innate	[230]–[235]
Dilated cardiomyopathy	*TTN*	Innate	[236]
	TNNT2	Innate	[237], [238]

The main disadvantage of hiPSCs-CM is its immaturity in comparison with human adult cardiomyocytes, which sometimes hampers its application on drug testing or disease modeling. Different approaches have been applied to promote maturation, including metabolic, biophysical, epigenetic or electromechanical cues [239]. Feeding cells with hormones such as dexamethasone, triiodohyronine or glucocorticoid analog improves their maturation [240], [241]. Another strategy is to use glucose-free medium supplemented with fatty acid (particularly carnitine, palmitate, linoleic acid and oleic acid) as cardiomyocyte maturation is associated with a metabolic change from glycolysis to fatty acid oxidation [242]. Other approaches have modified substrate stiffness and/or extracellular matrices to mimic cellular interactions observed *in vitro* or to recreate the augmented cardiac stiffness due to collagen deposition [243], [244]. Also, epigenetic priming [245], biophysical stimulation [246], [247], electromechanical stimulation [248] and tissue engineering including co-culture [249], [250] enhance maturity [239]. Great efforts are being made in this regard, but further investigations are still required.

On the basis of the above observations, there is a paucity of *in vitro* aging models. Acun *et al.* for the first-time showed human aged hiPSCs-CMs by keeping cells in culture for a long time. After approximately 55 days of culture hiPSCs-CM reach a mature phenotype, but after 100 days they evidence malfunctioning with similarities to aged human cardiomyocytes. These aged hiPSCs-CM have prolonged Ca^{2+} transient decay, reduced beat frequency and velocity, lipofuscin granules or augmented expression of the p21 aging marker, among others [251]. Other approaches are based on doxorubicin treatment [252], [253], a highly genotoxic chemotherapeutic whose main side effect in oncologic patients is a dose-dependent life-threatening cardiotoxicity [254]. Topoisomerase II, a crucial regulator of genomic integrity, is the molecular target of doxorubicin. Nevertheless, doxorubicin also causes cardiac energy deprivation, cell death and increased ROS generation, which results in cardiac muscle dysfunction and heart failure [255]. Based on doxorubicin therapy, Lazzarini's model [252] replicated aging landmarks and age-related cardiac characteristics.

Miller *et al* [256] proposed a strategy based on inducing progerin expression in hiPSCs-derived fibroblasts and mid-brain dopamine neurons to obtain aged cells and to generate a model for studying late onset traits of Parkinson’s disease. Hutchinson-Gilford progeria syndrome (HGPS) is a rare and fatal disease caused by progerin, a mutant variant of lamin A, that leads to premature aging. Although there is variability in some signs and symptoms, patients share clinical features and they are phenotypically similar. Progerin is a truncated form of the *lamin A* gene (*LMNA*) originated by a mutation within exon 11 (classic form) or at the exon 11 intronic border (atypical form). The nuclear lamina is mainly composed of lamin proteins, and it is located between the inner membrane of the nuclear envelope and chromatin. Lamina integrity is fundamental for many cellular processes: DNA replication, RNA transcription, mitosis, nuclear pore assembly, cell cycling or apoptosis, among others. The twelve *lamin A* exons are transcribed to generate prelamin A. This precursor suffers four post-translational modifications: farnesylation, cleavage of the last three amino acids residues of the C-terminal, methyl esterification and, ultimately, proteolysis of the 18 amino acids of the C-terminal including the farnesyl group to become the mature lamin A. In all HGPS mutations, the transcription and post-translational modifications lead to the deletion of 50 amino acids near the C-terminal end, resulting in a truncated abnormal protein. The resulting protein maintains the farnesyl group added during the post-translational modifications, which causes a stronger interaction with the membrane and leads to instability in the nuclear membrane and alterations in the heterochromatin [257]. The approach followed by Miller and colleagues is based on previous studies that suggest common mechanisms between the HGPS and natural aging [258]. In the heart, HGPS leads to cardiovascular features observed in natural aging like, for example, endothelial dysfunction, ventricular hypertrophy or atherosclerosis regarding cardiac aging [259].

To progress beyond current knowledge in *in vitro* human cardiac aging, this thesis characterizes the molecular and structural changes occurring over natural human cardiac aging to generate and validate a human *in vitro* model of cardiac cell aging based on human iPSC and inducible expression of progerin in iCM (Chapter 3).

1.6.4 *In silico* aging models

As described in previous sections, nowadays there are computational models for most cardiac regions and species due to the existence of extensive experimental data available for model development, calibration and validation. However, regarding cardiac aging, the number of *in silico* models that reproduce this process is reduced. Nesterova *et al* [260] used data from atrial aging in canines and mice to feed the Courtemanche model [261]and represent the effects of age on human atria. Because of the scarcity of knowledge relative to age-related ionic remodeling that occurs in human atria, they used experimental atrial data from aged mouse and dogs. Such *in silico* aging model was used to predict the effects that dofetilide, one of the antiarrhythmic drugs most widely prescribed for atrial fibrillation, has on human atria in aged individuals.

Dokuchaev *et al* [262] used the *in silico* model resulting from coupling the human ventricular electrophysiology model developed by Ten Tusscher et al. [156], [263] with the Ekaterinburg model of the mechanical activity and Ca^{2+} handling in ventricular cardiomyocytes [264]. To generate a control population, they varied 9 parameters of the coupled model (8 parameters representing the ionic conductance for main ionic currents and 1 parameter describing the maximal velocity of the SERCA pump) and obtained 20,000 randomly generated models. They calibrated this population to discard those whose AP and Ca^{2+} transient properties were outside the physiological ranges reported experimentally, thus reducing the population to 240 models. Subsequently, they generated age-related models by reducing the density of the K^+ transient outward current (I_{to}) and the maximal velocity of SERCA and augmenting the density of the Na^+-Ca^{2+} exchanger current (I_{NCX}) and L-type Ca^{2+} current (I_{CaL}). Two protocols of age-related change in the model parameters were performed. First, the authors gradually modified each parameter individually by 20, 50, 70% in every model of the control population to evaluate the sensitivity of the entire population to the parameter variation and to compare the contribution of the parameters to the age-related abnormalities. Next, the authors generated 60 age-related sets of these four parameters using normal distributions for parameter deviation from the reference value with 25% mean and 10% of standard deviation and applied each set of the aging parameters to every model in the control population. The authors evaluated 60 aged sub-populations, each consisting of 240 models. In total, approximately 15,000 age-related models were assessed in the study. Their approach allowed the authors to assess the contribution to arrhythmogenesis of different excitation-contraction mechanisms present in cardiac aging.

To go further in the generation of *in silico* models of cardiac aging that allow assessing the effects of age on human ventricular electrophysiology, this thesis proposes new two-dimensional models of human ventricular electrophysiology built on the basis of experimental characterizations in healthy donors. For that purpose, the experimental characterization of fibrosis deposition and CX43 age-related remodeling is carried out and translated into the computational model to assess age-related changes on CV, APD and arrhythmogenesis, as detailed in Chapters 4 and 5.

1.7 Hypothesis and Goals

The **hypothesis** of this thesis is that the characterization of the human cardiac remodeling with age will generate new fundamental knowledge to ground the development of novel tools to investigate its functional effects and allow longitudinal investigations to be conducted. Additionally, the research proposed in this thesis is hypothesized to set a basis for future studies that improve the diagnosis, prevention and treatment of age-related heart diseases. Based on this, **this thesis aims at** characterizing the molecular, cellular and structural changes that occur with age in the human LV and integrating the novel data into *in silico* and *in vitro* models that support arrhythmic risk assessment and longitudinal mechanistic research, respectively. The ultimate goal is to contribute to the development of novel therapeutic solutions to promote healthy cardiac aging and of non-invasive tools for the early identification and prevention of age-related arrhythmic risk.

The specific objectives of this thesis are:

1. *Analysis of age-related transcriptome dynamics in the human LV and role of miRNAs*

Mechanisms associated with human cardiac aging are scarcely characterized. Most studies are cross-sectional and based on chronological age, thus, age-related remodeling may be obscured by the effect of the individual aging rate, which is determined by the influence of environment and genetics. The aim in this chapter is to study the transcriptional dynamics of the aging myocardium in relation to chronological and biological age, with a focus in miRNAs as key regulators of gene expression. This thesis pursues the generation of a miRNA-based regulation network of genes related to cardiac function to obtain the landscape of miRNAs contribution in the control of cardiac aging.

2. *Characterization of LMNA Δ50 expression in the human myocardium and development of a model of human cardiac cell aging*

Cardiac aging at the cellular and molecular levels is scarcely characterized in humans due to ethical and practical reasons. Knowledge comes mainly from human cross-sectional studies based on chronological age and from animal models whose translational applicability is unknown. hiPSCs have been used to investigate the molecular and functional mechanisms of cardiac physiology and disease, but they have been barely used to model cardiac cell aging. *LMNA A50*-mediated accelerated aging shares phenotypic features with natural aging. This thesis aims at deciphering the potential contribution of *LMNA Δ50* to cardiac physiological aging and at developing a cardiac cell aging model based on *LMNA Δ50* inducible expression.

3. *Characterization of collagen remodeling in the human LV associated with age and its role in cardiac arrhythmia generation*

Age-associated changes in collagen have been mainly studied in animals, fundamentally regarding collagen amount, and from a chronological point of view. In this thesis, the aim is to characterize collagen features (amount, aggregation and spatial distribution) beyond midlife in human LV tissue from a chronological and biological point of view. Also, the thesis aims at conducting the same characterizations in a clinically relevant animal model, namely the pig, from adulthood to elder age. Using *in silico* models of human LV electrophysiology and the outcomes from the experimental characterizations, another goal of the thesis is to determine the arrhythmic potential of the age-related remodeling in the fibrosis features.

4. *Analysis of CX43 structural dynamics with age in the human LV and its implication on cardiac electrophysiology*

Cx43 remodeling has mainly been studied in the context of disease, using animal models and considering only Cx43 expression levels. The goal in this thesis is to characterize CX43 remodeling and its relation with fibrosis in human LV tissue beyond midlife by chronological and biological age. Importantly, the thesis seeks to ultimately determine the influence that CX43 characteristics in individuals from middle-to-old age have on conduction, repolarization duration and dispersion and arrhythmicity.

1.8 Structure of the thesis

The thesis is organized as follows:

- Chapter 2 presents the research conducted to show that biological age markers, *CDKN2A* and a highly complex transcriptional index named apparent age, allow to better describe the transcriptomic LV dynamics than chronological age in a large population of young-to-old individuals. The fundamental role of miRNAs in the regulation of genes involved in functional and structural changes during cardiac aging of the human LV is established by describing a bioinformatics miRNA-gene regulatory network that is partially validated experimentally.

The research described in this chapter generated the following journal publication and congress communications:

- E. Ramos-Marquès* **& L. García-Mendívil***, M. Pérez-Zabalza, H. Santander-Badules, S. Srinivasan, J.C. Oliveros, R. Torres-Pérez, A. Cebollada, J.M. Vallejo-Gil, P.C. Fresneda-Roldán, J. Fañanás-Mastral, M. Vázquez-Sancho, M. Matamala-Adell, F. Sorribas-Berjón, J.A. Bellido-Morales, F.J. Mancebón-Sierra, A.S. Vaca-Núñez, C. Ballester-Cuenca, M. Jiménez-Navarro, J.M. Villaescusa, E. Garrido-Huéscar, M. Segovia-Roldán, A. Oliván-Viguera, C. Gómez-González, G. Muñiz, E. Diez, L. Ordovás, E. Pueyo. "Chronological and biological aging of the human left ventricular myocardium: Analysis of microRNAs contribution". *Aging Cell* 2021. 20(7):e13383. **Corresponding Author (*Equal contribution)**

- **L. García-Mendívil**, N. Smisdom, K.A. Mountris, A. Olivan-Viguera, J.M. Vallejo-Gil, PC. Fresneda-Roldán, J. Fañanás-Mastral, M. Matamala-Adell, F. Sorribas-Berjón, M. Vázquez-Sancho, C. Ballester-Cuenca, E. Wolfs, RB. Driesen, L. Ordovás, E. Pueyo. "Histological characterization of age-related remodeling in human left ventricle by second harmonic generation and lipofuscin content". Myocardial Function & Cellular Biology of the Heart 2019 Naples (Italy). Poster

- **L. García-Mendívil,** E. Ramos-Marquès, J.C. Oliveros, R. Torres-Pérez, J. Fernández-Bes, A. Oliván-Viguera, E. Pueyo, L. Ordovás. "Transcriptional analysis of human cardiac aging by chronological and biological age". Myocardial Function & Cellular Biology of the Heart 2019 2019 Naples (Italy). **Oral communication**

- E. Ramos-Marquès, **L. García-Mendívil**, J.C. Oliveros, R. Torres-Pérez, A. López-Ruiz, A. Olivan-Viguera, J.M. Vallejo-Gil, P.C. Fresneda-Roldán, J. Fañanás-Mastral, M. Matamala-Adell, F. Sorribas-Berjón, M. Vázquez-Sancho, C. Ballester-Cuenca, L. Ordovás, E. Pueyo. "The role of microRNAs in age-related remodeling of the human left ventricle". Myocardial Function & Cellular Biology of the Heart 2019 Naples (Italy). Poster

- **L. García-Mendívil,** E. Ramos-Marquès, J.C. Oliveros, R. Torres-Pérez, J. Fernández-Bes, A. Oliván-Viguera, E. Pueyo, L. Ordovás. "Transcriptional analysis of human cardiac aging by chronological and biological age". Cell Symposia: Aging & Metabolism 2018 Sitges (Spain). Poster

- E. Ramos-Marquès, **L. García-Mendívil,** J.C. Oliveros, R. Torres-Pérez, A. Oliván-Viguera, L. Ordovás, E. Pueyo. "Analysis of the role of microRNA in age-related heart electrophysiological remodeling". Cell Symposia: Aging & Metabolism 2018 Sitges (Spain). Poster

- Chapter 3 shows that *LMNA* processing does not shift towards the pathological *Δ50* isoform in natural aging in the human LV. However, *LMNA Δ50* expression in committed iCMs leads to the recapitulation of aging hallmarks and age-related transcriptomic changes observed in natural aging of the human heart.

The research described in this chapter generated the following journal manuscript and congress communications:

- **L. García-Mendívil**, N. Hernández-Bellido, M. Sánchez-Barat, M. Pérez-Zabalza, E. Garrido-Huéscar, J.M. Vallejo-Gil, M. Matamala-Adell, J.F. Sorribas-Berjón, J.A. Bellido-Morales, A.S. Vaca-Núñez, C.M. Verfaillie, C. Ballester-Cuenca, E. Pueyo, L. Ordovás. "Natural and Induced Human Cardiac Aging: *Lamin A Δ50* does not accumulate naturally, but accelerates aging *in vitro*". Submitted. **Corresponding author**

- **L. García-Mendívil**, N. Hernández-Bellido, M. Sánchez-Barat, M. Pérez-Zabalza, E. Garrido-Huéscar, J.C. Oliveros, R. Torres-Pérez, E. Ramos-Marquès, E. Pueyo, L. Ordovás. "Envejecimiento cardiaco humano: transcriptómica y desarrollo de modelos celulares". II International Congress of PhD students Miguel Hernández University of Elche (Spain) 2022. **Oral communication**

- **L. García Mendívil**, N. Hernández Bellido, M. Sánchez Barat, M. Pérez Zabalza, E. Garrido Huéscar, J.C. Oliveros, R. Torres Pérez, E. Ramos Marquès, E. Pueyo, L. Ordovás. "*In vivo* and *in vitro* cardiac aging: developing of cellular aging models". XIX Congress of the Spanish Society of Cellular Biology Bohadilla del Monte (Spain) 2021. Poster

- **L. García Mendívil**, N. Hernández Bellido, M. Sánchez Barat, M. Pérez Zabalza, E. Garrido Huéscar, J.C. Oliveros, R. Torres Pérez, E. Ramos Marquès, E. Pueyo, L. Ordovás. "Envejecimiento cardiaco humano: transcriptómica y desarrollo de modelos celulares de envejecimiento". X Congress of Young researchers of the I3A Institute Zaragoza (Spain) 2021. **Oral communication**

- Chapter 4 shows the suitability of characterizing collagen features by SHG microscopy and automated image analysis. Collagen remodeling with chronological age was not observed beyond midlife in humans or in adult-to-old pigs. However, collagen features correlated in humans with the biological age marker, lipofuscin. By *in silico* modeling and simulation of human LV electrophysiology, the alterations in the amount and organization of fibrosis with age are shown to play a major role in arrhythmogenesis.

The research described in this chapter generated the following journal publication and congress communications:

- **L. García-Mendívil**, M. Pérez-Zabalza, K. Mountris, S. Duwé, N. Smisdom, M. Pérez, L. Luján, E. Wolfs, R.B. Driesen, J.M. Vallejo-Gil, P.C. Fresneda-Roldán, J. Fañanás-Mastral, M. Vázquez-Sancho, M. Matamala-Adell, J.F. Sorribas-Berjón, J.A. Bellido-Morales, F.J. Mancebón-Sierra, A.S. Vaca-Núñez, C. Ballester-Cuenca, A. Oliván-Viguera, E. Diez, L. Ordovás, E. Pueyo. "Analysis of age-related left ventricular collagen remodeling in living donors: implications in arrhythmogenesis". *iScience* 2022. 5(2):103822 **Corresponding Author**

- **L. García-Mendívil**, M. Pérez-Zabalza, K. Mountris, F.J. Mancebón-Sierra3 A.S. Vaca-Núñez, S. Duwé, L. Ordovás, E. Pueyo. "Caracterización del remodelado del colágeno asociado a la edad en el ventrículo izquierdo humano de donantes vivos y sus implicaciones en la generación de arritmias". XI Congress of Young researchers of the I3A Institute Zaragoza (Spain) 2022. Poster
- **L. García-Mendívil**, N. Smisdom, S. Duwe, K. Mountris, S. Srinivasan, M. Pérez, L. Luján, E. Wolfs, R.B. Driesen, A. Oliván-Viguera, J.M. Vallejo-Gil, P.C. Fresneda-Roldán, J. Fañanás-Mastral, M. Matamala-Adell, F. Sorribas-Berjón, M. Vázquez-Sancho, C. Ballester-Cuenca, E. Diez, L. Ordovás, E. Pueyo. "Characterization of cardiac remodeling associated with aging in the human left ventricle". I Congress of PhD students Miguel Hernández University of Elche (Spain) 2021. **Oral communication**

- Chapter 5 shows that CX43 dynamics barely changes from midlife onwards in humans, with these changes being slightly better explained by the biological age marker lipofuscin than by chronological age. CX43 remodeling is shown to be unrelated to fibrosis alterations with age. At an individual level, characteristics of CX43 amount and heterogeneity like those observed in certain individuals of the studied middle-to-old age population increase arrhythmic risk, particularly when combined with enhanced fibrosis deposition.

The research described in this chapter generated the following manuscript and congress communication:

- **L. García-Mendívil**, M. Pérez-Zabalza, J.M. Vallejo-Gil4, J. Fañanás-Mastral, M. Vázquez-Sancho, J.A. Bellido-Morales, A.S. Vaca-Núñez, C. Ballester-Cuenca, E. Diez, L. Ordovás, E. Pueyo. "Inter-individual age-independent differences in human CX43 impact ventricular arrhythmic risk". Submitted **Corresponding author**

- **L. García-Mendívil.** "Characterization of age-related cardiac remodeling in the human left ventricle. *In vitro* and *in silico* modeling". PhD students of Biomedical Research in Aragon (Spain) 2021. **Oral communication**

Chapter 2

Chronological and biological aging of the human left ventricular myocardium: analysis of microRNAs contribution

This chapter has been partially adapted from the publication "Chronological and biological aging of the human left ventricular myocardium: analysis of microRNAs contribution" by Ramos-Marques & García-Mendívil✉ and colleagues [265].

2.1 Introduction

As described in Chapter 1, age is a major risk factor for CVDs. Aged hearts undergo structural and functional changes at multiple levels that contribute to the pathogenesis of the disease. Changes at the molecular level have been scarcely characterized in humans. This lack of knowledge is inherent to the associated limitations of human research, namely difficulties in discerning between aging and disease effects, in conducting longitudinal studies and in obtaining cardiac samples.

Studies investigating human aging are mainly conducted transversally in relation to CA, but CA is merely a time index that does not necessarily describe an individual or organ's biological condition. In contrast, the BA of an organ is the result of the interaction of genetic and environmental factors over time. The significance of accounting for BA on top of CA in CVDs has been reported. BA has been associated with improved prognosis capacity after ischemic stroke as compared to CA [135] and with higher risk of CVDs [136]. However, the transcriptional dynamics of the aging heart, and specifically of the LV, have not been investigated from a biological point of view yet.

BA is a complex parameter that can be scored by different approximations such as clinical markers, functional tests or molecular indicators. Cellular senescence is a fundamental mechanism of aging tightly related to the expression of the cell-cycle regulator and cell senescence marker *P16* (expressed from the *CDKN2A* locus) [131]. *P16/CDKN2A* is considered a BA marker in human skin and peripheral blood cells [132], [133]. The number of *P16/CDKN2A*$^+$ senescent cells increases with age in various human tissues [266], including the heart [267]. In the mouse heart, the pool of p16/Cdkn2a$^+$ senescent cells also increases with age [268], [269] and their clearance reverts age-related phenotypes in cardiovascular disorders and improves heart function in chronologically aged mice [270]–[272]. Yet, to the best of my knowledge, *CDKN2A* expression has not been distinctly used as a cardiac BA marker. Other highly complex transcriptomic indices could also account for the aging rate variability of an organ. Apparent age

(AppAge) is an unbiased BA index computed from age-related transcriptional indicators [273] that adjusts the CA of an individual by his/her aging rate.

As described in Chapter 1, miRNAs are relevant regulators of biological processes that inhibit expression of their target genes [103]. miRNAs seem to have a role in the regulation of heart aging. For example, miR-22, miR-18, miR-19a, and miR-19b and miR-17-3p have been associated with senescence, apoptosis, autophagy, hypertrophy and fibrosis in the heart, mainly in animal models [107], [274], and miR-34 is a master regulator of cardiac aging in mice with age-related expression in human right atrium [108]. Little is known, though, about their role in humans. Circulating miRNAs have been described as biomarkers of aging and frailty [109], but since not all organs seem to age at the same rate [275], organ-specific circulating biomarkers should be used to estimate heart aging.

This chapter describes gene and miRNA expression changes in the human LV induced by CA and transcriptomic BA through transcriptomic analysis of LV samples of the extensive GTEx RNA-seq dataset. The potential of simple (*CDKN2A* expression) and highly complex (AppAge) transcriptomic age (TA) markers to uncover cardiac-specific age-related processes is assessed and the relation of TA markers to an aging phenotype is demonstrated. Also, this chapter deciphers the potential contribution of miRNAs in modulating age-related transcriptional changes and establishes and partially validates a downstream regulation network of genes involved in myocardial function. Finally, the presence of cardiac-enriched BA-regulated miRNAs in plasma is assessed.

2.2 Methods

2.2.1 Donors and sample selection

RNA-seq data (for both messenger RNAs and microRNAs) from a total of 318 RNA samples of 202 male and 116 female, were obtained from LV specimens of the GTEx study Version 7 [276]. By using the keywords “cardiac arrest”, “acute myocardial infarction”, “cardiovascular”, “heart disease”, “cardiovascular collapse”, “cardiac failure”, “atherosclerotic cardiovascular disease”, “heart failure”, “cardiopulmonary arrest” and “cardiopulmonary failure” on the cause of death, individuals who died of cardiac-related causes (CD) were identified and removed from the study. This work is focused on the non-cardiac-related cause of death (NCD) donors. Considering the reported gender-related differences in gene expression with aging [277] and the smaller number of female NCD donors, this study focused on the male gender. The 132 male NCD samples were classified in decades (20-30, 31-40, 41-50, 51-60 and 61-70 y.o.) (**Table 2**) or fifths according to *CDKN2A* expression or AppAge (P20/40/60/80/100).

RNA samples of the 132 samples included in the study showed a median [Interquartile range, IQR] RIN (RNA integrity number) value of 7.50 [6.50-8.10]. Post-ischemic time, meaning the time between death and tissue preservation, had median values of 304.5 [148.25-659.75] minutes. Previous studies on the effect of postmortem interval on RNA quality suggest only minor expression changes within the first 24 hours postmortem when stored in cold conditions [278].

Table 2. Left ventricle samples from GTEx consortium.

		Number of donors
Total		**202**
Non-cardiac death (NCD)		132
NCD age range	20-30	12
	31-40	13
	41-50	25
	51-60	50
	61-70	32

2.2.2 Hierarchical clustering and age sample distribution analysis

Normalized expression values were obtained from raw expression (read counts) of RNA-seq samples by normalization using the DESeq2 R package (version 1.10.1) [279] and log2-transformation (zero values were converted to 1 prior to log2 calculation) (**Table 3**, available in the online publication as Table S2). For all tables shown in this study, symbol and description of each gene were retrieved using BioMart (NCBI) with assembly GRCh37.p13.

AppAge, defined as the sum of CA and Δ-aging, was calculated according to the method described in [128]. AppAge of each individual was calculated in this study cohort from 2863 age-related genes (**Figure 12**).

Hierarchical clustering was performed by using MeV (MultiExperiment Viewer) [280]. Samples were hierarchically clustered by normalized expression values of the whole transcriptome. Sample trees were obtained by selecting Euclidean distance and average linkage clustering. EvolView was used to display the dendrogram [281]. Histograms and kernel smoothing function fits were calculated for each of the two main groups of the dendrogram (defined by the two earliest separated branches), according to three aging variables (**Table 4**, available in the online publication as S3): AppAge, *CDKN2A* expression and CA.

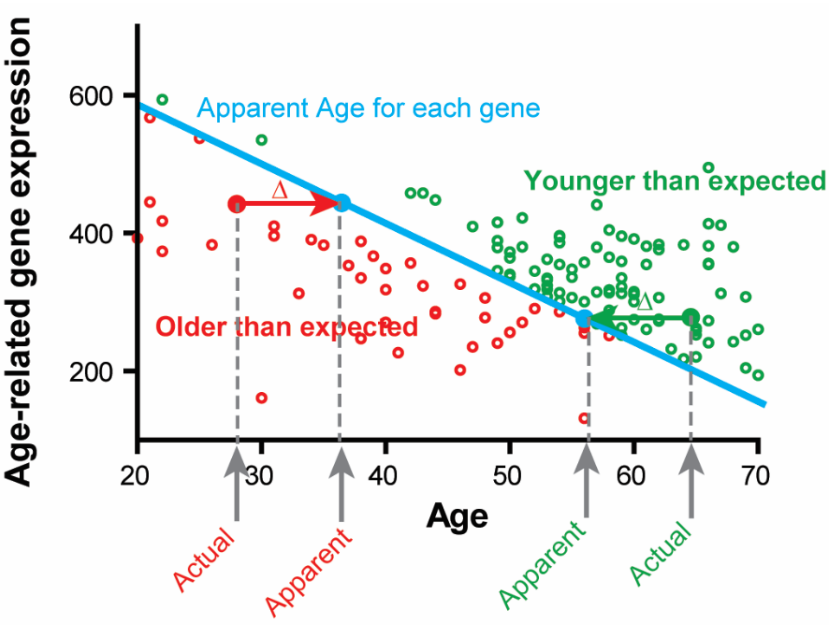

Figure 12. Representation of Apparent age. Age-related genes are identified by Pearson correlation analysis (FDR<0.05). Delta-aging (Δ) is calculated for each gene by linear regression as the difference between the actual gene expression value and the expected (regressed) one. The image represents an individual whose age-related gene expression corresponds to and older apparent age than the actual one (red) and the opposite (green). The aging rate of the individual (Δ-aging) is computed as the aggregate of Δ values of all the age-related genes. Then, the apparent age (AppAge) of the individual is calculated as the sum of CA and the aging-rate factor.

2.2.3 Quantification of myocardial fibrosis

Histology images of hematoxylin-eosin staining corresponding to the 132 NCD donors were downloaded in svs format from the GTEx database and transformed to TIFF. Images were analyzed with in-house software tool (MATLAB R2020a, The MathWorks Inc., USA) which works via a graphical user interface (GUI). After loading and displaying the TIFF image to analyze, the custom software performs automatic masks extraction for the tissue (myocytes) or the extracellular matrix and quantifies the percentage of the fibrotic tissue. Masks were generated obtaining first the representative RGB color of each component, the tissue and the extracellular matrix, by exploring interactively the pixel color values through the image. Once defined, the tissue and the matrix masks were identified as those pixels whose absolute RGB value minus the representative RGB value were less than 20 and 10, respectively. A black mask was created for such pixels and the rest of values were included in a white mask. For visualization purposes, the tissue mask was depicted as red, the extracellular matrix mask as blue and the merge as black (**Figure 13**). RGB values were adjusted when necessary to eliminate merge. The percentage of cardiac fibrosis was calculated by dividing the number of black pixels of the extracellular matrix mask over the sum of white pixels of both masks.

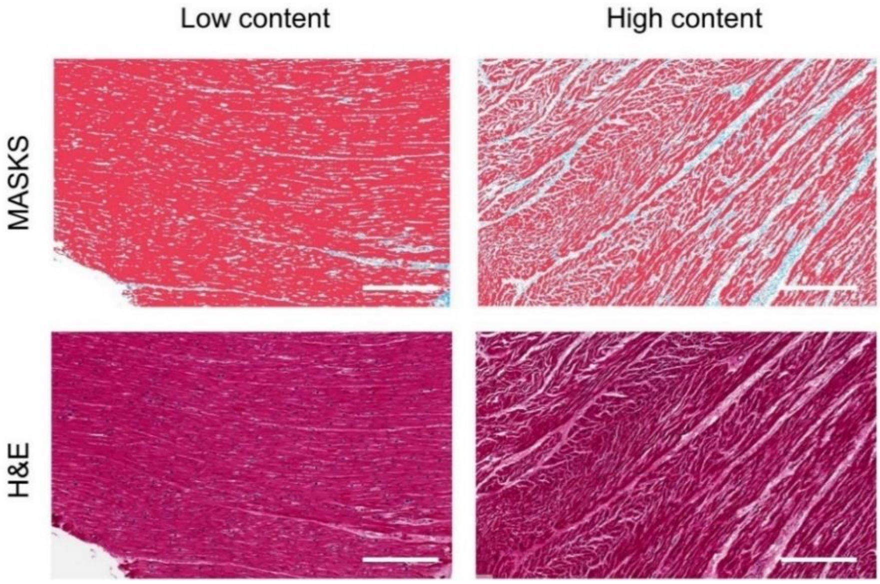

Figure 13. Quantification of fibrotic tissue in samples of the GTEx study. Representative hematoxylin-eosin images of individuals with low and high content of fibrosis in LV (bottom). The corresponding masks of each image depict myocytes in red and extracellular matrix in blue (top). Scale bars are 300 µm.

2.2.4 Differential gene expression and whole transcriptome gene set enrichment analysis

GSEA software version 3.0 software [282], [283] was used to define functional groups (Gene Ontology of biological processes, from MSigDB v6.2) of genes enriched or depleted in individuals having high AppAge values, high *CDKN2A* expression and CA-old. Settings used in the GSEA are the following: group size was limited from 3 to 500 genes and the number of permutations was set to 1000. GSEA pre-ranked option was used to evaluate the 54320 genes annotated in the RNA-seq whole transcriptome analysis. The differential expression values (LogRatio) for each gene were obtained by using DESeq2 R package in donors with high/low AppAge (P100 and P20), high/low *CDKN2A* expression (P100 and P20) or old/young CA (61-70 and 20-30 y.o.) (**Table 5**, available in the online publication as Table S4). Venn diagrams were created using Venny 2.1.0: (https://bioinfogp.cnb.csic.es/tools/venny/index.html) [284].

2.2.5 miRNA expression profile calculation

To obtain gene expression profiles along aging, the RNA-seq samples were normalized using the quantiles (normalizeQuantiles) method of the R limma package [285] and the values were log2-transformed as indicated above. For each gene, the average of the normalized log2-expression in each interval (*CDKN2A* expression or AppAge quintile) was computed (interval average). A baseline expression was calculated for each gene as the average of the five interval averages. The ratio of gene expression for each *CDKN2A* quintile was computed by subtracting the baseline value (**Table 6**, available in the online publication as Table S7).

2.2.6 Identification of age-related miRNAs

The human LV miRNome consisted of 1314 annotated miRNAs, although miRNAs with no reads in any of the studied individuals were removed, thus leaving 608 miRNAs and only those miRNAs with RNA-seq normalized expression values (**Table 3**, available in the online publication as Table S2) in at least 30% of individuals were included in the analysis, rendering a total of 93 miRNAs for further analysis (**Table 7**, available in the online publication as Table S5). Since aging is a continuous process in time, BA-related miRNAs (BIO-AGEmiRNAs) were identified not only as those being differentially expressed (DEG) between the highest/lowest *CDKN2A* expressing groups (**Table 5**, available in the online publication as Table S4), but also showing significant Spearman correlation with *CDKN2A* expression (**Table 8**, available in the online publication as Table S6).

2.2.7 Selection of mirror targets for BIO-AGEmiRNAs

The miRWalk database (http://zmf.umm.uni-heidelberg.de/apps/zmf/mirwalk2/index.html) [286] was used to identify BIO-AGEmiRNA targets. The predicted targets were filtered to mirror the expression profile of their associated BIO-AGEmiRNA. Specifically, the expression patterns obtained above (**Table 6**, available in the online publication as Table S7) were used to calculate the slopes between consecutive *CDKN2A* quintiles. For steep BIO-AGEmiRNA slopes (above 0.15 or below -0.15), predicted target genes were required to present slopes of opposite and, particularly for very steep BIO-AGEmiRNA slopes (above 0.5 or below -0.5), corresponding target slopes were required to be of at least half its magnitude. For flat BIO-AGEmiRNA slopes (absolute value below 0.15), target slopes were required not to exceed 0.25 in absolute value. In addition, these identified targets were further assessed for correlation with *CDKN2A* expression, this being of opposite sign to the corresponding BIO-AGEmiRNA, and significant differential expression. The predicted target genes meeting all the above-described criteria were defined as mirror targets.

2.2.8 Establishment of LV-specific BIO-AGEmiRNA downstream gene regulation network

Cardiac-related gene ontology groups (GOs) were selected from the full GO list (**Table 9**, available in the online publication as Table S11) by including those with any of the following keywords in their group name: “heart”, “cardiac”, “ion”, “cytoskeleton”, “action potential”, “actin” or “catecholamine”. All the mirror targets were functionally annotated into GO groups. BIO-AGEmiRNAs and their associated mirror targets present in cardiac GOs were used to construct the network. For ease and simplicity, cardiac Gos were grouped into five functional categories with direct contribution to “Action potential”, “Heart rate”, “Cardiac contraction”, “Cardiac conduction” and “Autonomic Nervous System” divided in turn into sections (**Table 10**, available in the online publication as Table S8). It should be noted that some genes belonged to several cardiac GOs and could thus be represented in more than one functional category.

2.2.9 Luciferase reporter assay

The vector used, pmirGLO-P2A-3fLAG-MCS, was a modification of pmirGLO (Promega, USA). Briefly, downstream of Firefly luciferase, the autocatalytic peptide P2A, the tag 3xFlag and a MCS were inserted. The 5'UTR, coding region and 3'UTR were cloned form most of genes in the MCS. For *DSP*, only the coding region was cloned. Regions of each gene cloned, and primers used for cloning are included in **Table 11** (available in the online publication as Table S9).

HEK-293 cells were transfected with plasmid (1ng/ul) and miRNA mimic (1uM) (M-00202, Ribbox, Germany) or negative control N1 (K-01000, Riboxx, Germany) with Lipofectamine 2000 (11668027, Invitrogen, USA). After 24h, the luciferase assay was conducted with Dual-Glo Luciferase Assay Kit (E2940, Promega, USA) according to the manufacturer's instruction.

2.2.10 Gene expression analysis on human LV samples from living donors

Blood and transmural tissue were collected from patients undergoing valve replacement surgery or coronary artery bypass at University Hospital Miguel Servet (Zaragoza, Spain) and Hospital Universitario Virgen de la Victoria (Málaga, Spain). The tissue samples were obtained with a 14 G tru-cut biopsy needle during cardiac arrest, immediately after the patient was placed on cardiopulmonary bypass, from an area of the anterior wall of the LV, near the base of the heart, with no evidence of ischemia or any other macroscopic pathology [287]. All biopsies were obtained from nonischemic ventricular myocardium of patients with absent LV hypertrophy, absence of dilated cardiomyopathy and with normal LV systolic function (LV ejection fraction above 50%). Immediately upon collection, tissue specimens were placed in freshly prepared ice-cold preoxygenated 30mM BDM-Tyrode's solution as described in [287] and split in approximately 3 mm^3 pieces for either molecular (snap frozen in liquid nitrogen) or histological (see Chapter 4) analysis.

For this study, a total of 29 LV and 10 blood samples were obtained in age ranges from 50 to 83 years old (y.o.) with median value 68 and IQR [60-73] (**Table 12**, available in the online publication as Table S14). Plasma was isolated right after blood extraction and stored at -80ºC. LV samples were immediately processed and snap frozen in liquid nitrogen. Collection and analysis of human LV samples conformed to the principles outlined in the Declaration of Helsinki and were approved by the local ethics committee (CEICA, reference number PI17/0023 and CEI from 28/09/2017), with all patients giving written informed consent before surgery and prior to their inclusion in the study.

Total RNA was extracted from snap frozen tissue using the AllPrep DNA/RNA/miRNA Universal Kit (50980224, Qiagen, Germany)) and retrotranscribed with PrimeScript RT Master Mix (RR036B, Takara Bio, Japan). Plasma RNA was extracted with miRNeasy Serum/Plasma Kit (217184, Qiagen, Germany). miRNA was retrotranscribed from total LV RNA or plasma RNA using the qScript microRNA cDNA Synthesis Kit (95091-025, Quanta Biosciences, USA). Real time PCR was carried out with Power SYBR Green PCR Master Mix (4309155, Thermo Fisher, USA) using the oligonucleotides listed in **Table 13** (available in the online publication as Table S15) in a Viia7 instrument (Thermo Fisher, USA). mRNA expression was normalized to *YHWAZ*, *POLR2A* and *IPO8* reference genes [288]. miRNA expression was normalized to *RNU6* and *cel-miR-39-5p* (spiked in plasma samples before RNA isolation) in LV or plasma, respectively. After the PCR run, individuals were classified for *CDKN2A* expression (based on ΔCt) and grouped in fifths. Relative gene expression was calculated according to the $2^{-\Delta\Delta Ct}$ method between the first (low *CKDN2A*) and fifth (high *CDKN2A*) quintiles using as reference sample the individual with the lowest ΔCt value for each gene. Non-relative gene expression was calculated as $2^{-\Delta Ct}$. For comparison purposes, a CA-matched subset of GTEx donors was selected, individuals were categorized by *CDKN2A* expression (RPKM) and grouped into fifths. Relative expression between low (P20) and high (P100) *CDKN2A*-expressing individuals of each gene was calculated in this case by dividing the RPKM value of each sample by the reference sample (the one with lowest RPKM value).

2.2.11 Tissue specificity assessment

LV expression specificity of each of the BIO-AGEmiRNAs was determined by calculating the Specificity Measure SPM [289]. SPM of BIO-AGEmiRNA was calculated using the reads per kilobase per million mapped reads (RPKM) values of all individuals from GTEx V7 (GTEx_Analysis_2016-01-15_v7_RNASeQCv1.1.8_gene_reads.gct.gz). The following tissues were excluded from the analysis: transformed cells (EBV-transformed lymphocytes and transformed fibroblasts), female tissues (ovary, uterus, vagina, cervix and fallopian tubes) and whole blood, to include in the detection LV-specific BIO-AGEmiRNAs secreted to the bloodstream. 44 tissues, including LV, remained. Since not all of them had samples for all individuals, only those with available samples for at least 30% of the NCD individuals were included in the analysis, rendering a total of 26 tissues in the P20 group (young BA) and 25 tissues in the P100 group (old BA). When all individuals were analyzed, the analysis rendered 27 tissues. SPM values calculated for LV (**Table 14**, available in the online publication as Table S16) can range from 0 to 1, with 1 indicating that a gene is specifically expressed in LV. Statistical differences in the expression levels of BIO-AGEmiRNAs between LV and each of the other analyzed tissues were determined by Mann-Whitney tests.

2.2.12 Statistical analysis

SPSS version 22 was used for statistical analyses. Spearman correlation analysis was used to test the strength and direction of association between two variables. Mann-Whitney test was used to assess differences between two independent groups. The significance threshold was established at $p = 0.05$ for Mann-Whitney test and FDR = 0.05 for the rest of analyses.

2.3 Results

2.3.1 *CDKN2A* expression and AppAge represent LV transcriptomic age

Firstly, the capacity of CA and TA (*CDKN2A* expression, AppAge) markers to represent gene expression differences with age in the 132 male individuals of the GTEx consortium with NCD cause of death was assessed to understand whether age was embodied in the transcriptome.

Hierarchical clustering using the whole transcriptome categorized individuals into two main groups (**Figure 14A**). Group 1 (83 individuals) contained a larger proportion of individuals with low CA, AppAge and *CDKN2A* expression while group 2 (49 individuals) had a larger number of individuals with high CA, AppAge and *CDKN2A* expression values. Sample distributions according to the age markers were significantly different between group 1 and group 2, with the overlapping area between the two groups being 31% for AppAge, 61% for *CDKN2A* expression and 76% for CA (**Figure 14A**). These results indicated that aging was represented in the whole LV transcriptome and that AppAge, a highly complex TA marker, better aligned with the hierarchical clustering classification followed by *CDKN2A* expression and CA.

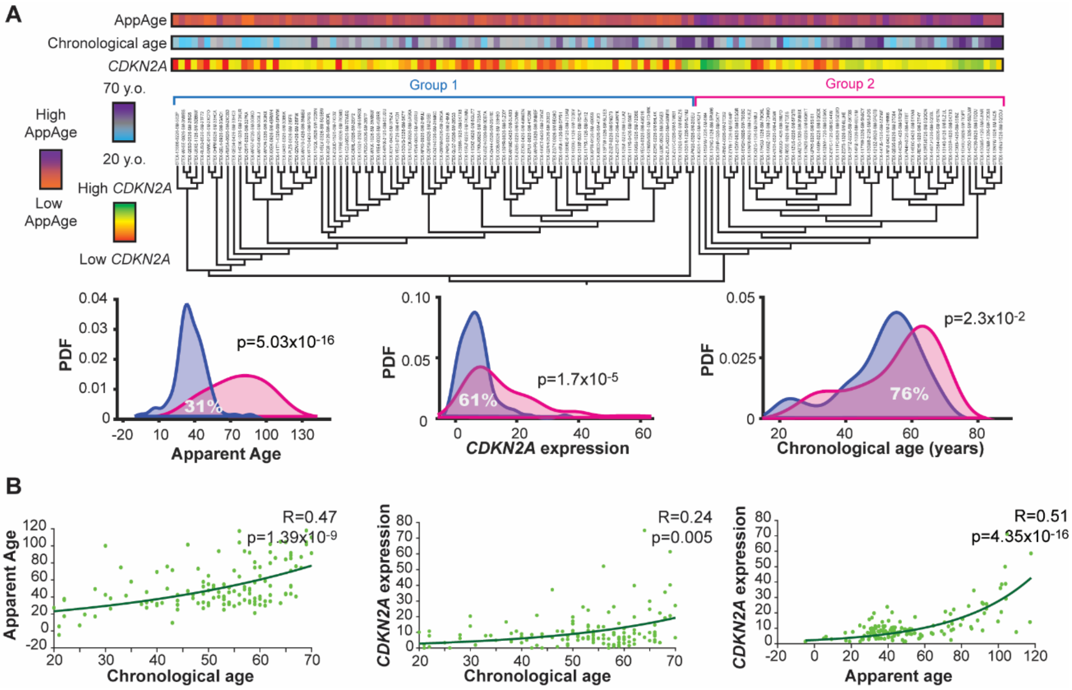

Figure 14. Relationship between human LV transcriptome and aging. **A)** Dendrogram representing hierarchical clustering classification of individuals based on the whole transcriptome analysis. Groups 1 (blue) and 2 (pink) are determined by early separated branches. Color bars on top of the dendrogram represent CA, AppAge or CDKN2A expression of each individual according to the indicated color scales on the left. Below, the histograms show the distributions of CA, AppAge or *CDKN2A* expression levels for the two groups of the dendrogram. Y-axes show the probability density function (PDF). Percentages of overlap and p-values (Mann-Whitney test) are shown. **B)** Correlation between aging markers (CA, AppAge, and *CDKN2A* expression). Dots indicate individual data, while the line represents the fitted function. Correlation coefficient HAS and p-values (Spearman) are shown.

Subsequently, the biological significance of TA markers was assessed by correlation analysis with CA. AppAge and *CDKN2A* presented significant correlation with CA, with Spearman R coefficients being 0.47 and 0.24, respectively (**Figure 14B**). Interestingly, although they were independently calculated and they relied on a largely different number of genes (1 vs 2863), a clear correlation was found between the two TA markers, AppAge and *CDKN2A*, with a Spearman R coefficient of 0.51 **(Figure 14B)**. Thus, the TA markers, AppAge and *CDKN2A*, are correlated and represent the transcriptomic characteristics of the analyzed population better than CA for the human LV.

2.3.2 TA markers are associated with a cardiac aging phenotype linked to heart dysfunction

To provide biological validation for the age markers, their relation with myocardial fibrosis, a feature of structural remodeling of the aging heart that is related to impaired function, was investigated [72], [290]. The amount of fibrosis found in the LV was significantly correlated with all age markers with Spearman R being 0.27, 0.32 and 0.58 for CA, *CDKN2A* expression and AppAge, respectively (**Figure 15A and Table 15,** available in the online publication as Table S10). Looking closer at the mechanism, the expression of genes involved in the pro-fibrotic *TGF-β* pathway showed that most of the *TGF-β* factors, receptors and downstream signaling molecules, were associated with all three aging markers (**Figure 15B**). Instead, genes encoding extracellular matrix (ECM) proteins, final effectors of the fibrotic phenotype, were all significantly associated with both TA markers, but not with CA (except for Elastin, *ELN*) (**Figure 15B**). This is in line with the results exposed above, where CA shows the weakest correlation to the percentage of fibrosis. Altogether, the results show that both TA markers, AppAge and *CDKN2A* expression, are not only good descriptors of transcriptomic age but also explain, better than CA, the age-related fibrotic phenotype, and its main mechanisms at the single gene level.

2.3.3 Biological and chronological age-based analysis reveals differentially altered functions in the aged human LV

Next, the potential of the three age markers to uncover age-related genes by differential gene expression analysis was examined. Samples were classified in CA decades (20-30, 31-40, 41-50, 51-60 and 61-70 y.o.) or fifths according to *CDKN2A* expression and AppAge (P20/40/60/80/100). CA identified 657 differentially expressed genes (DEGs) between young (20-30 y.o.) and old individuals (61-70 y.o.), substantially much less than the 14,437 and 15,670 discovered by *CDKN2A* and AppAge-based analysis comparing young (P20) and old (P100) BA individuals, respectively. More than 70% of the CA-upregulated or downregulated genes in old as compared to young donors were also retrieved by *CDKN2A* and AppAge, once again confirming their link to age **(Figure 16)**. Moreover, there was more than 93% overlap of DEGs between TA markers.

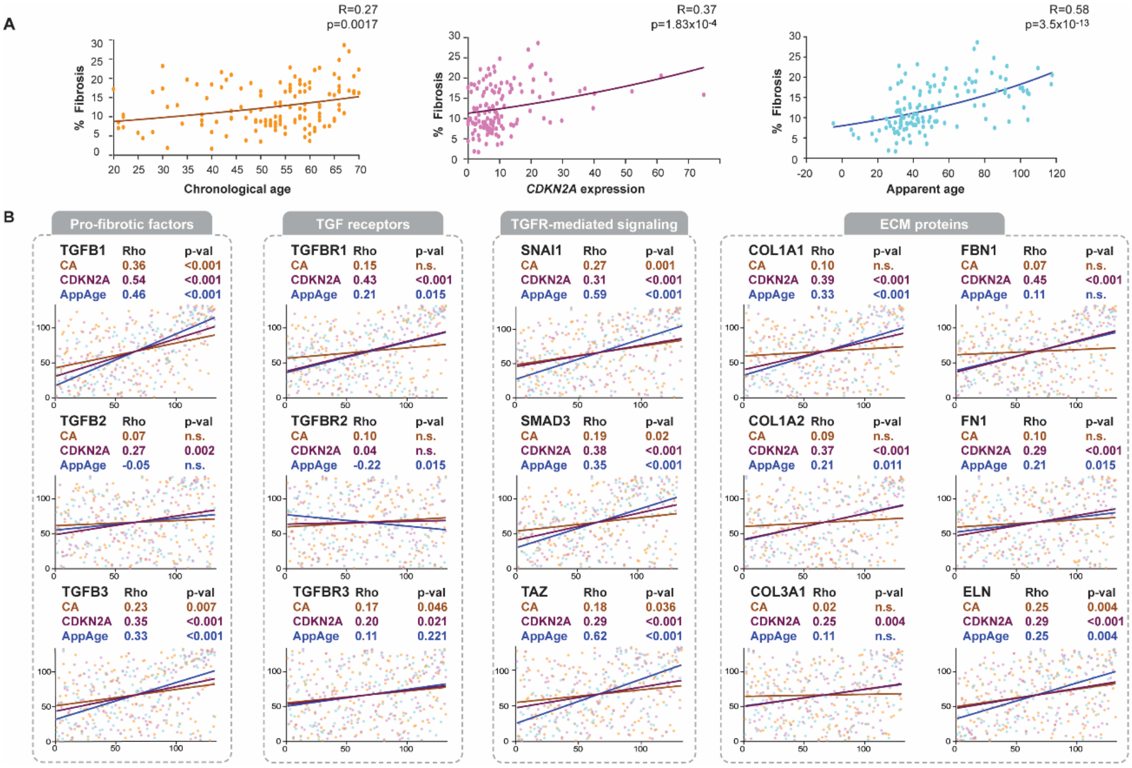

Figure 15. Correlations between aging markers and fibrosis. A) Correlation between interstitial fibrosis percentage and age markers (CA, *CDKN2A*, and AppAge). Dots indicate individual data, while the line represents the fitted function. Correlation coefficient (Rho) and p-values (Spearman) are shown. **B)** Correlation between fibrosis-related genes and age markers (CA, *CDKN2A*, and AppAge). Correlation coefficient (Rho) and p-values (Spearman) are shown (*p < 0.05; **p < 0.01; ***p < 0.001). Axes show the 132 samples ordered by the three age markers (X axis) and each gene expression level (Y axis).

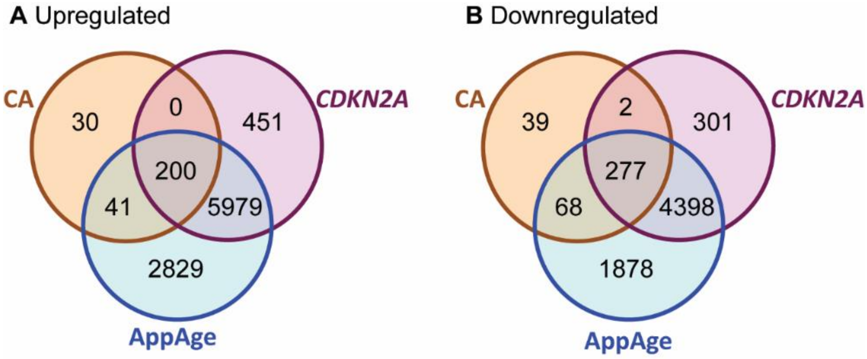

Figure 16. Differentially expressed genes according to the three aging parameters. Venn diagrams show the number upregulated **(A)** or downregulated **(B)** differentially expressed genes according to CA, *CDKN2A* and AppAge. “Upregulated” and “downregulated” indicate old > young and old < young, respectively.

These findings led to evaluate enrichment or depletion of functional processes in old individuals using gene set enrichment analysis (GSEA) (**Table 9**, available in the online publication as Table S11). A total of 64, 895 and 1,684 GOs were significantly enriched by CA, *CDKN2A* or AppAge, respectively. The top 20 depleted and enriched GOs in old versus young (**Table 16**, available in the online publication as Table S12) were classified into wider categories to understand which general functions were altered according to the three age markers. In the CA-, AppAge- and *CDKN2A*-classified samples, functions related to immunity, inflammation and chemotaxis were enriched (**Figure 17A**), while those related to mitochondrial respiration, metabolism and protein metabolism and translation were depleted (**Figure 17B**). These functional groups belong to the aging landmarks 'inflammation', 'mitochondrial dysfunction' and 'loss of protein homeostasis' [5].

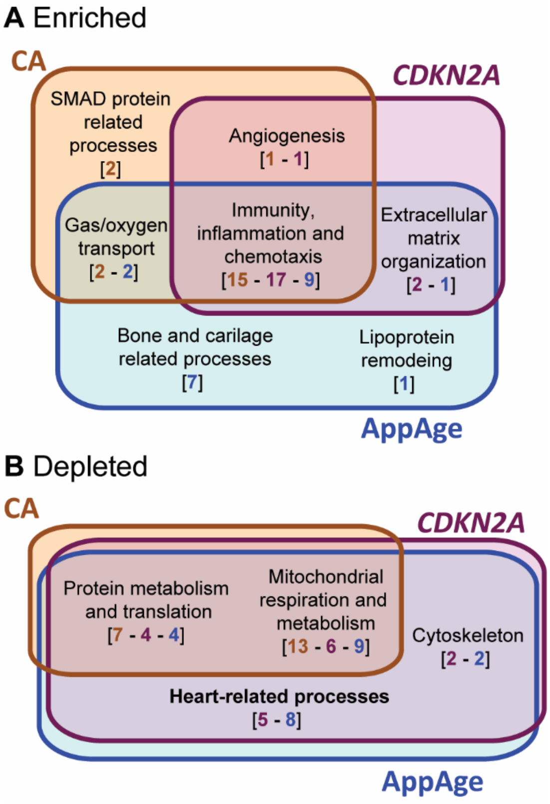

Figure 17. Analysis of enriched and depleted functions in biologically and chronologically old individuals. A) Enriched functions in CA-, AppAge-, or *CDKN2A*-classified samples, and the overlapping between them. **B)** Depleted functions in CA-, AppAge-, or *CDKN2A*-classified samples, and the overlapping between them. Colored numbers in brackets indicate the number of GOs gathered into the broader biological functions in each age-based analysis (orange, blue, and purple for CA, CDKN2A, and AppAge, respectively).

A functional group enriched in high CA- and high *CDKN2A*-classified samples was related to angiogenesis. Also, groups related to gas and oxygen transport, in line with the angiogenic process, were enriched both in high CA- and high AppAge-classified samples. Groups related to ECM organization emerged in high *CDKN2A* and high AppAge donors only, while SMAD processes appeared enriched in CA-old individuals only. Another substantial difference between all the age markers was the identification by only high AppAge of 7 enriched GOs involved in bone and cartilage processes.

Of note, despite *CDKN2A* being a cell cycle regulator, only two enriched groups out of 795 were related to cell cycle-related processes (“Regulation of cell cycle arrest” and “Negative regulation of cell cycle arrest”), but they had low normalized enrichment score (**Table 9**, available in the online publication as Table S11).

Depleted functional groups related to heart function showed up in high AppAge- (8 GOs) and high *CDKN2A*- (5 GOs) classified samples. These included processes such as “Heart process”, “Cardiac muscle contraction”, “Cardiac muscle cell action potential” or “Cell communication involved in cardiac conduction” (**Table 16**, available in the online publication as Table S12). Also, GOs related to cytoskeleton processes (“Regulation of actin filament-based movement”, “Myofibril assembly” or “Actin-mediated cell contraction”) were present in the TA-based analysis. None of these heart- or cytoskeleton- related processes were retrieved in CA-old individuals.

Altogether, both TA markers demonstrated to represent age in the human LV transcriptome **(Figure 14)**, proved association with an aging phenotype **(Figure 15)**, and unveiled depleted heart-related processes **(Figure 17)** with overall higher sensitivity than CA, being AppAge more precise and containing most of the information retrieved by *CDKN2A*. The TA markers significantly correlate among them, but the use of AppAge has relevant drawbacks. Its high complexity (computed from 2863 genes in this data set) would preclude the validation of RNA-seq data on new LV specimens at the single gene level. In addition, AppAge computation is cohort-dependent, what would prevent comparison between studies. Therefore, results with AppAge allowed to confirm the findings observed for *CDKN2A* in the GTEx NCD cohort, but, for the subsequent analysis, BA is estimated with the TA marker *CDKN2A* expression.

2.3.4 miRNAs are involved in biological aging of the human LV

Next, this chapter investigated whether miRNAs could contribute to the transcriptomic regulation of cardiac functions altered with BA. BIO-AGEmiRNAs were identified as those differentially expressed and presenting significant correlation with *CDKN2A* expression. In total, 20 BIO-AGEmiRNAs were identified, 14 were upregulated and 6 downregulated **(Table 17)**. Subsequently, a total of 18,679 putative targets of BIO-AGEmiRNAs were found in the miRWalk database [286]. Of these, only 10,561 fitted mirror expression pattern to their corresponding regulating miRNAs **(Figure 18)**. Additional filters based on differential expression between BA-young and old groups and significant correlation with *CDKN2A*-expression led to the final number of 5,879 mirror targets: 3,658 from upregulated and 2,221 from downregulated BIO-AGEmiRNAs. In conclusion, this approach identifies a number of BIO-AGEmiRNAs and their mirror targets with a clear BA-related profile.

Table 17. List of up/down-regulated BIO-AGEmiRNAs in elder versus young individuals.

BIO-AGEmiRNAs

Upregulated			**Downregulated**
MIR4435-1HG	MIR3911	hsa-mir-7162	MIR600HG
hsa-mir-6080	MIR155HG	MIR4461	hsa-mir-490
MIR24-2	MIR1304		MIR3936
MIR497HG	MIR3648		MIR635
MIR3916	MIR296		MIR22HG
MIR503HG	MIR210HG		MIR17HG

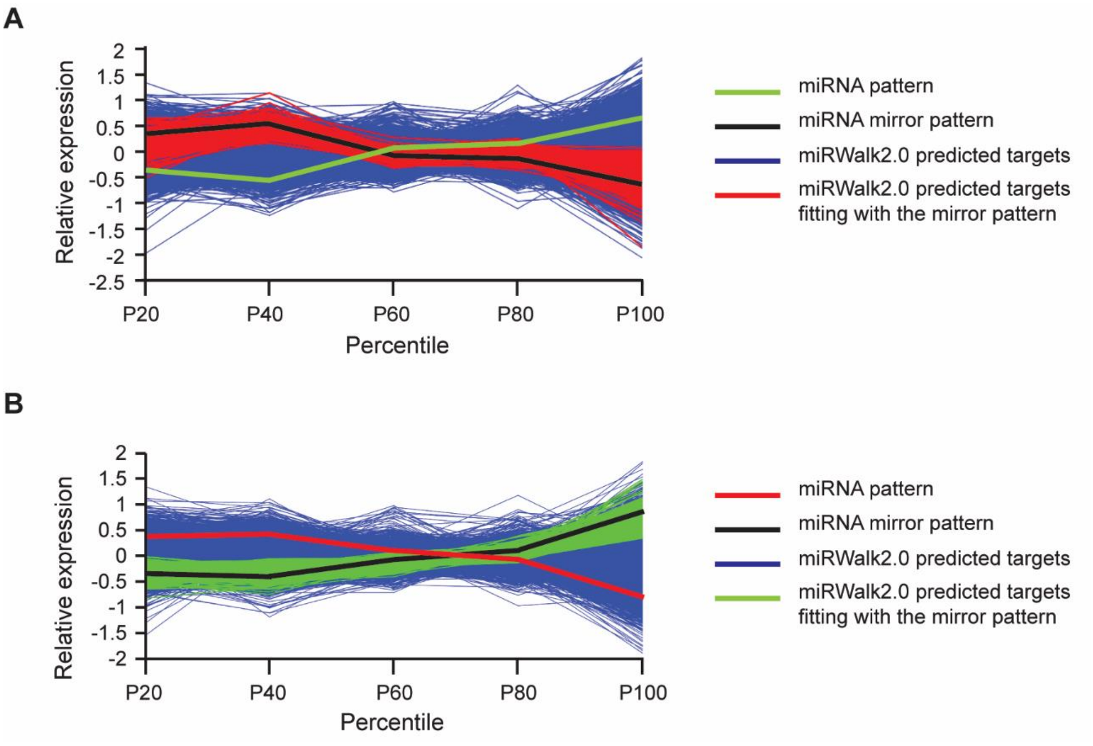

Figure 18. Identification of BIO-AGEmiRNAs mirror targets. A) Representative image of the procedure used to mirror targets identification. Upregulated miRNA expression pattern (green) is used to outline an exact mirror pattern (black). The expression profiles of all predicted targets are shown in blue, while those fitting the mirror pattern (mirror genes) are shown in red. **B)** Idem as in **(A)** for downregulated miRNA (red) and upregulated mirror targets (green).

2.3.5 Biological (*CDKN2A*) age-related miRNAs are predicted to orchestrate heart-related processes during aging

To understand how LV function along aging could be modulated by miRNAs, a downstream gene regulation network of heart-related functions was established. Mirror targets belonging to cardiac GOs (**Table 18**, available in the online publication as Table S13) were selected and represented in five functional categories. Due to space limitations, only the top 5 induced and repressed BIO-AGEmiRNAs were represented in the networks **(Figure 19)**. The top 5 upregulated BIO-AGEmiRNAs had 3,524 mirror targets and 72 of them belonged to cardiac GOs **(Figure 19A)**. MIR3916 had the largest contribution in the network potentially regulating 63% of the cardiac genes all over the functional categories. Although the majority of cardiac mirror targets were linked to one or two BIO-AGEmiRNAs, some genes such as *CAMK2D*, *CACNA2D1*, *CACNA1C* or *TMOD1* were modulated by 4 out of the 5 BIO-AGEmiRNAs. Out of the 2,213 mirror targets of downregulated BIO-AGEmiRNAs, 34 of them were annotated into cardiac GOs. *MIR22HG* had the largest contribution to the network (**Figure 19B**), regulating 52% of the genes. In this case too, most of these genes were linked to only one BIO-AGEmiRNA.

To validate the bioinformatics approach used to construct the network, some of the predicted interactions were assessed *in vitro*. Two BIO-AGEmiRNAs (hsa-miR-24-2 and hsa-miR-4435) and ten of their cardiac targets were chosen based on their highest correlation coefficient with *CDKN2A* expression **(Figure 20)**. hsa-mir-24-2-5p significantly interacted with *ADRA1A*, *POPDC2*, *SERCA2*, *TMOD* and *ACTN2* gene sequences as compared to a non-targeting miRNA control. *ACTN2* also showed positive interaction with hsa-miR-24-2-3p, but *CASQ2* and *DMD* did not respond to the treatment with any branch of hsa-miR-24-2 mimics. As per hsa-miR-4435, only the vector containing the *DSP* target sequence yielded interaction. In total, 6 out of 10 tested interactions proved positive indicating the high predictable value of the network.

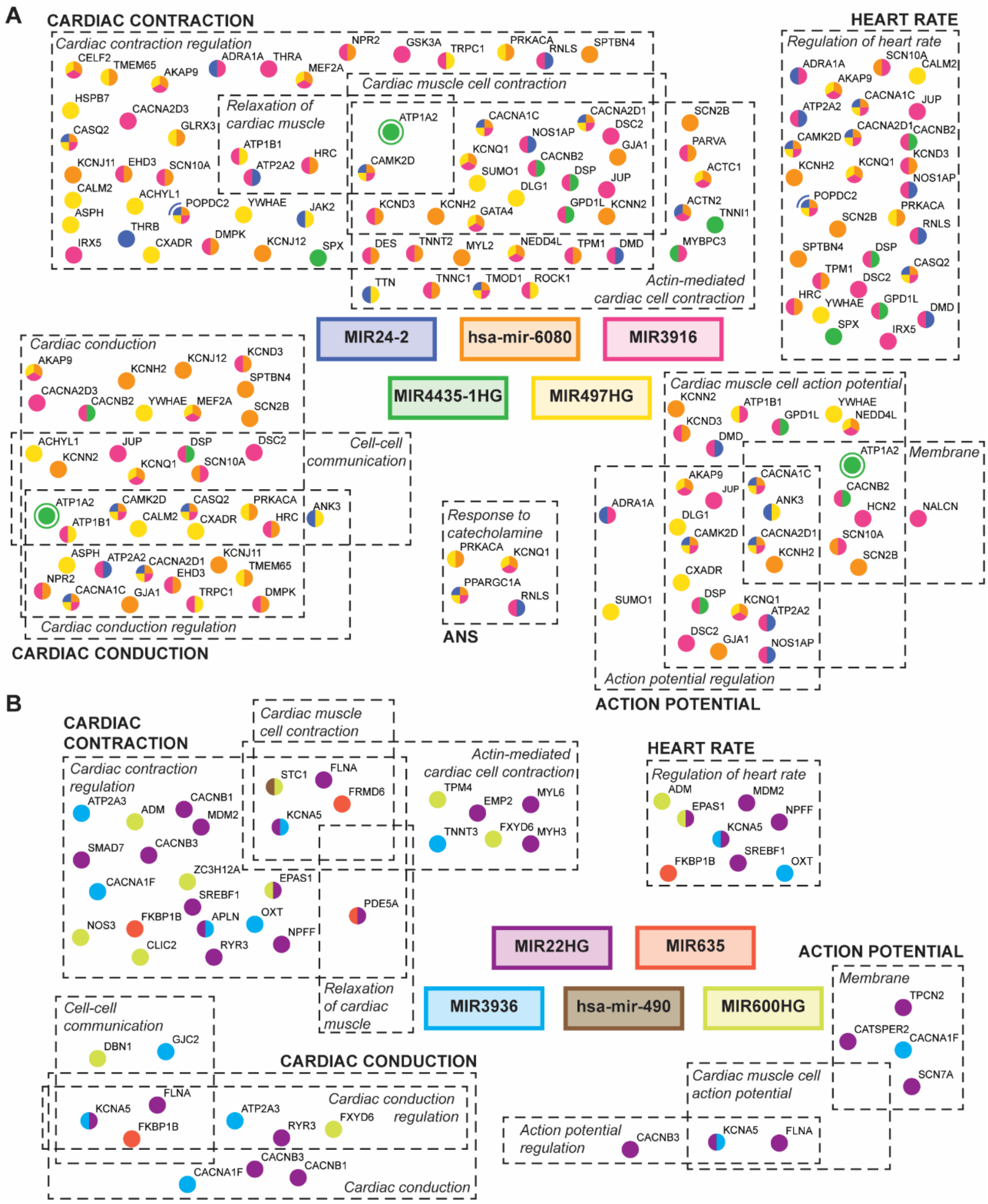

Figure 19. Predicted BIO-AGEmiRNAs gene regulatory networks of cardiac-related functions. Network for the top 5 upregulated **(A)** or downregulated **(B)** BIO-AGEmiRNAs. Mirror targets are shown as color-coded dots according to their putative regulating miRNA. Sections of cardiac GOs are delimited by dashed lines and functional categories are shown in capital letters.

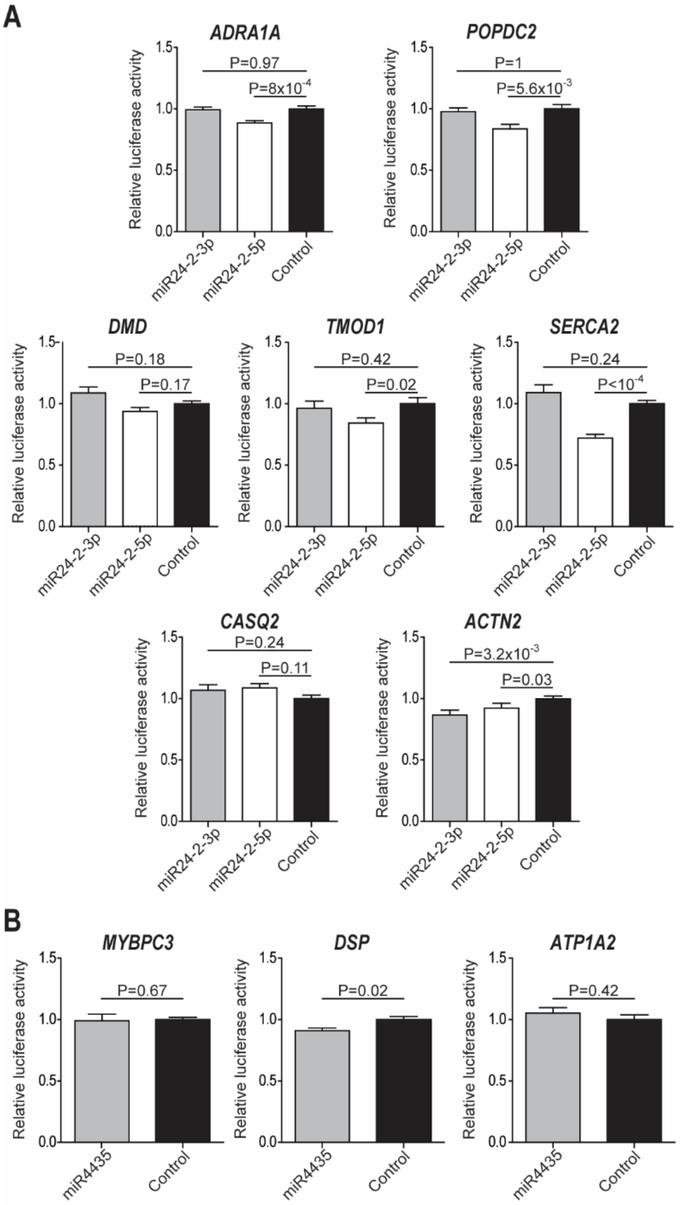

Figure 20. BIO-AGEmiRNAs and cardiac target interactions. Luciferase expression assay performed for miR24-2-3p or miR24-2-5p **(A)** and miR4435 **(B)**. Cardiac target under study is shown over each bar chart. Y-axes show the detected luciferase signal, normalized to the control experimental condition (non-targeting miRNA). Error bars show SEM and statistical analysis by Mann-Whitney test.

Because the bioinformatics analysis in the GTEx population could be affected by donor and/or sample covariates (i.e., cause of death, RIN, postmortem interval, premortem conditions), gene expression was primarily analyzed in a small group of LV samples from living donors, ideally devoid of this possible source of variability. As compared to GTEx donors, the trend of change of the relative expression median values was conserved for most of the analyzed genes with increasing BA (**Figure 21**, **Tables 12-13**, available in the online publication as Tables S14-S15).

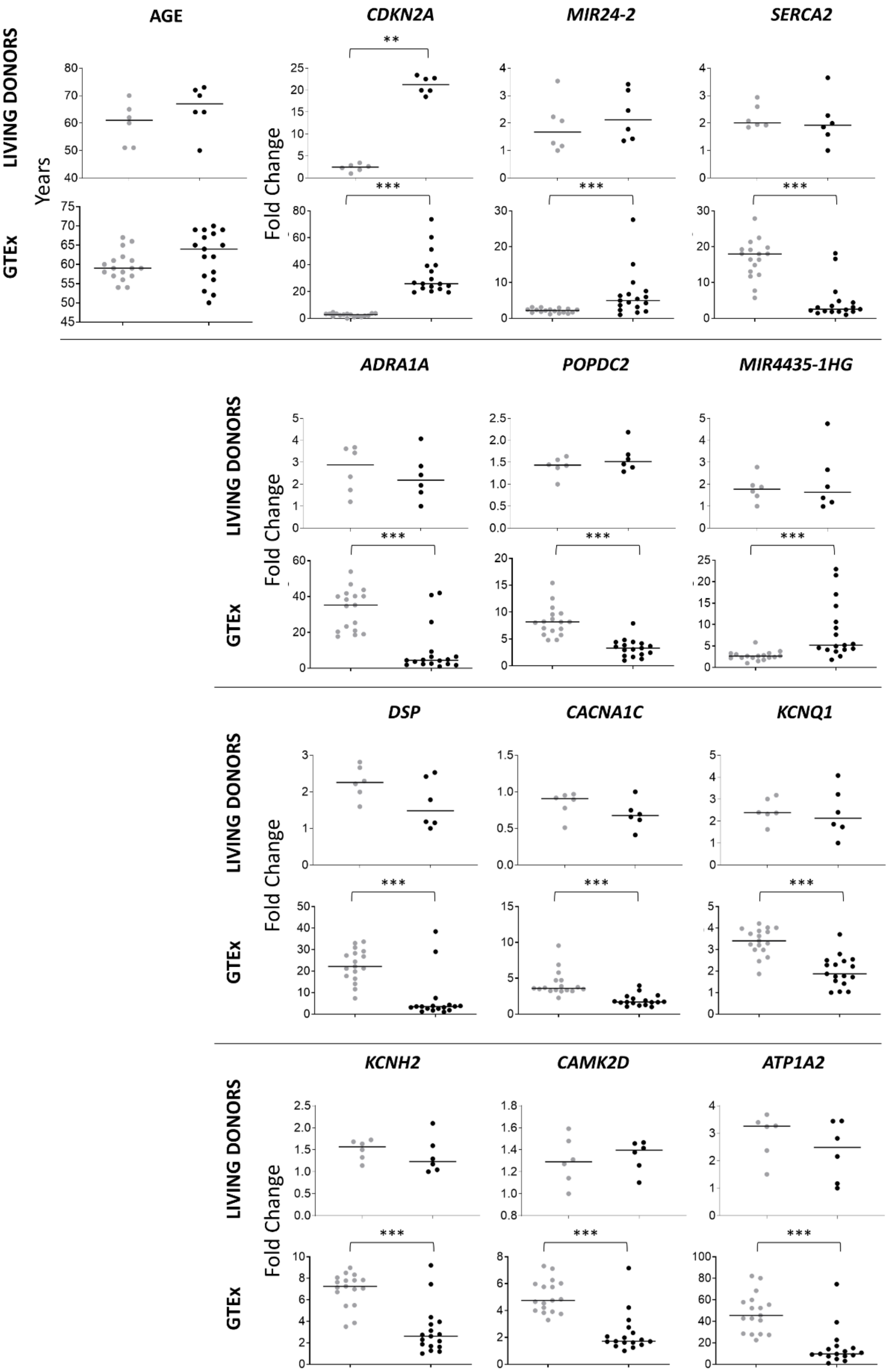

Figure 21. Gene expression of BIO-AGEmiRNA and mirror targets in LV of living donors. Relative gene expression (fold change, $2^{-\Delta\Delta Ct}$) in LV samples from living (top row) and GTEx (bottom row) donors with low (grey dots) and high (black dots) *CDKN2A* expression. The chronological age (age) of the selected individuals is also represented (Mann-Whitney test **, p<0.01; ***, p<0.001).

In summary, miRNAs upregulated and downregulated with BA and their putative regulated targets were identified. According to this analysis, BA-related miRNAs might play a pivotal role regulating genes involved in human LV function. This study establishes the first bioinformatic BIO-AGEmiRNA gene regulation network of LV dysfunction associated with age in humans.

2.3.6 Identification of LV-enriched biomarkers of aging

The final objective was to find age-related LV-enriched miRNAs that could eventually be used to assess cardiac BA in peripheral body fluids. BIO-AGEmiRNAs expression levels were assessed in different human tissues of the GTEx database that had a minimum number of samples. Among the upregulated BIO-AGEmiRNAs, *MIR4461* was the most LV-enriched in BA-old individuals as compared to young, with an associated SPM of 0.39 (**Table 14**, available in the online publication as Table S16). The expression values of MIR4461 were significantly different in the LV as compared to other 23 tissues, except for the atrial appendage **(Figure 22A)**. Among the downregulated BIO-AGEmiRNAs, hsa-mir-490 was the most LV-enriched in BA-young individuals as compared to elder, having an SPM of 0.33 **(Table 14**, available in the online publication as Table S16). Significant differences were found when comparing its expression values with 23 other tissues except for atrial appendage and testis (**Figure 22B**).

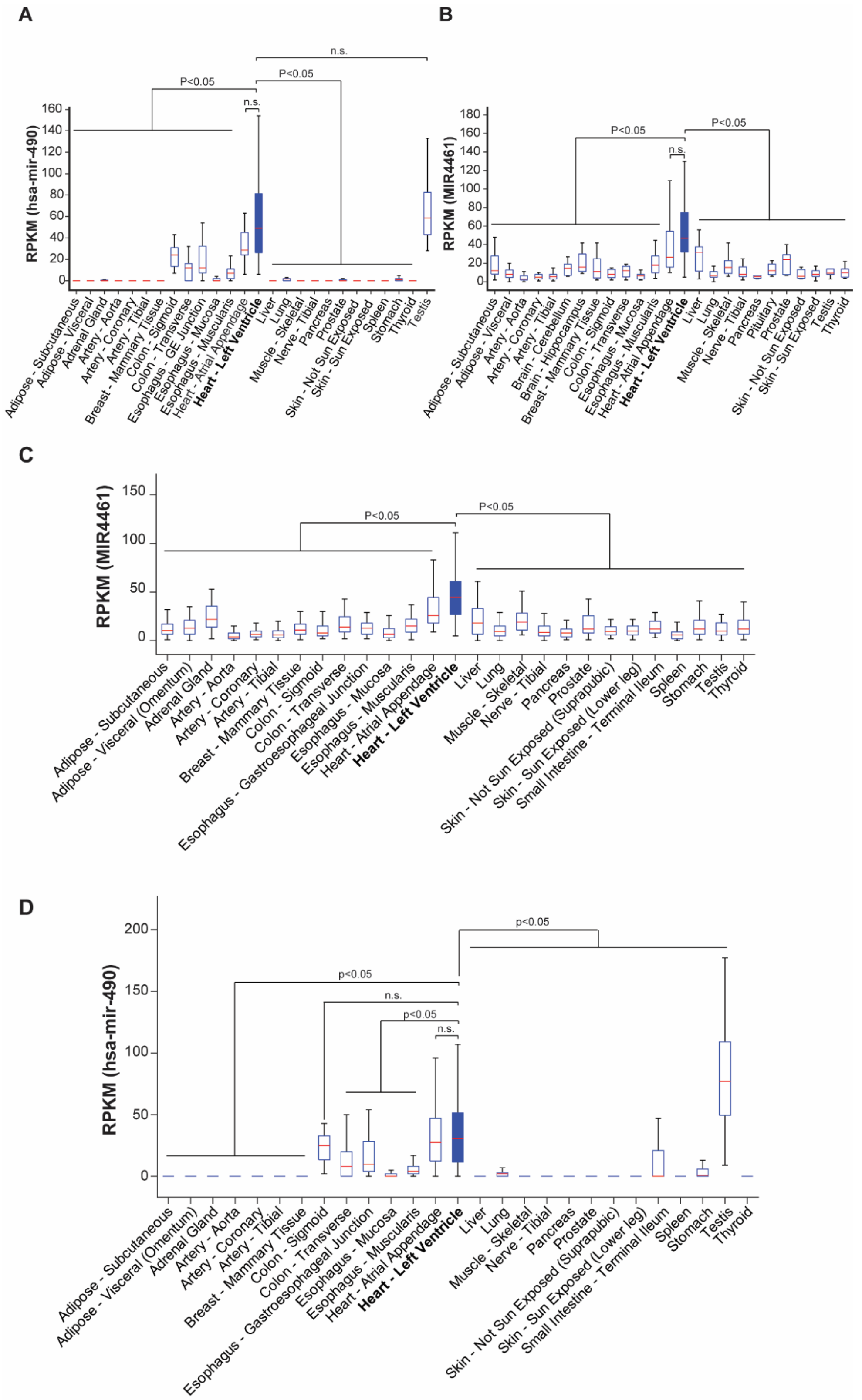

Figure 22. Assessment of BIO-AGEmiRNA tissue specificity. Box plots showing the expression levels (RPKM) of the two BIO-AGEmiRNAs with the highest LV specificity: MIR4461 **(A)** and has-mir-490 **(B)**. Median RPKM values are shown in red lines and p-values from Mann-Whitney tests comparing LV with each of the other tissues are indicated. MIR4461 **(C)** and hsa-mir-490 **(D)** in all NCD individuals. Median RPKM values are shown in red lines, p-values from Mann-Whitney tests comparing LV with each of the other tissues are indicated.

LV enrichment of *MIR4461* and hsa-mir-490 was similar across tissues over the whole range of ages (**Figure 22 C-D**). In the LV samples from living donors, the expression of the cardiac-enriched BIO-AGEmiRNAs followed the trend of change with increasing BA observed in GTEx **(Figure 23A).** In addition, the preliminary correlation analysis between the levels in LV and plasma are near significance for hsa-miR-4461 (Spearman R=0.48, p-value=0.17) (**Figure 23B**). Therefore, this tissue enrichment analysis identifies two cardiac-enriched BIO-AGEmiRNAs in the human LV, *MIR4461* and hsa-mir-490, which are both present in plasma and miR-4461 shows a tendency to reflect the levels in LV.

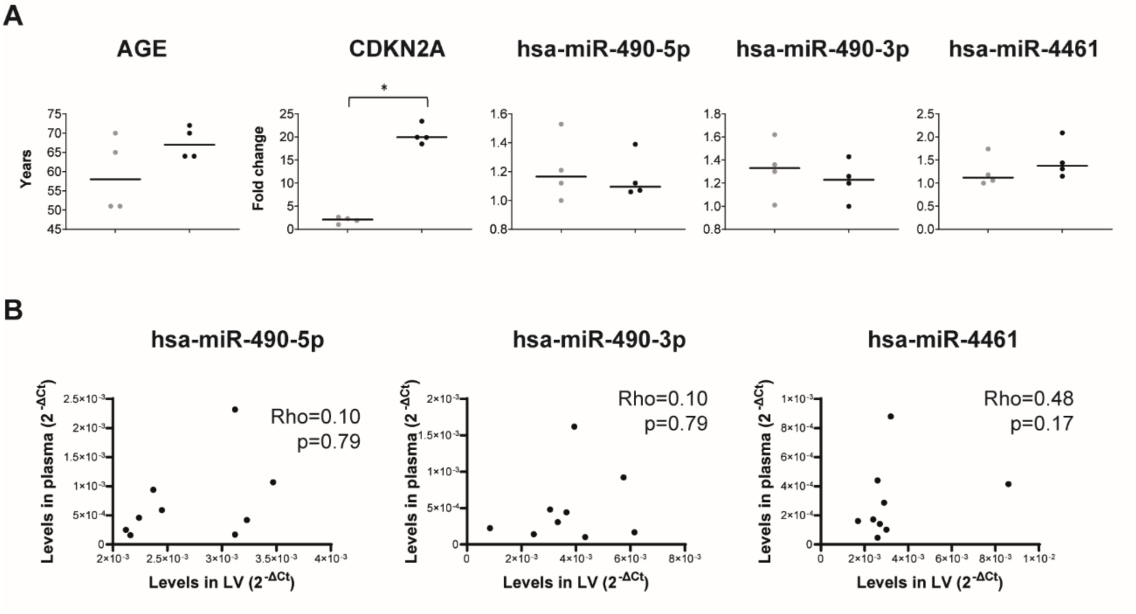

Figure 23. BIO-AGEmiRNA relative gene expression in the human LV. A) Relative gene expression (fold change, $2^{-\Delta\Delta Ct}$) in LV samples from living donors with low (grey dots) and high (black dots) *CDKN2A* expression. The chronological age (age) of the selected individuals is also represented (Mann-Whitney test *, p<0.05). **B)** Spearman correlation analysis of the levels ($2^{-\Delta Ct}$) of mature miR-490-5p, miR-490-3p and miR-4461 in plasma and LV paired samples.

2.4 Discussion

In this work, the transcriptional landscape of human LV aging is investigated at the whole tissue level from a BA and CA point of view with interest in describing the contribution of miRNAs as key transcriptional regulators of genes involved in age-induced cardiac dysfunction and as potential biomarkers of LV BA.

2.4.1 AppAge and *CDKN2A* are TA markers to assess BA in human LV

Here, transcriptional changes along aging comparing CA with simple (*CDKN2A* expression) and complex (AppAge) TA markers are evaluated. The aim is to understand whether accounting for inter-individual aging rate variability can uncover relevant age-related mechanisms in human LV otherwise unseen by CA. TA markers better represent the LV transcriptome along aging and are more sensitive than CA to detect DEGs and heart-related enriched/depleted functions. TA markers are thus more effective in unveiling organ-specific alterations with aging. Importantly, most information uncovered by CA-based analysis is also captured by *CDKN2A* expression or AppAge and the outcome of the single TA marker *CKDN2A* is unbiased towards its gene-specific functions. Altogether, these findings support this working hypothesis that accounting for inter-individual aging rate variability by TA markers improves the detection of relevant age-related processes.

Besides its reduced sensitivity compared to AppAge, *CDKN2A* expression is set here as the BA marker because a single gene, present in LV and in many aged tissues [266], renders data susceptible of verification across studies. Whether *CDKN2A* expression comes from a specific cell type or it is dispersed among cell types is non-relevant for the conclusions reached in this work since the study is carried out at the whole tissue level. On this basis, this research relevantly contributes to the establishment of a simple and cohort-independent TA marker, namely *CDKN2A* expression, for the study of the molecular basis of biological aging in the human LV.

2.4.2 TA markers are biologically validated for cardiac aging

It is well established that cardiac aging entails an increase in the degree of LV fibrosis that leads to ventricular dysfunction [291]. Here, biological validation of the relation of this CA-associated aging trait with the TA markers is provided. At the histological level, the age-related content of fibrosis in human LV has been analyzed only in two studies [73], [292]. In both, comparable higher amounts of collagen deposition were observed in elder (67-87 y.o.) as compared to young persons (20-28 y.o.). The CA results agree with these observations, but differ in the total amount of observed fibrosis, which seems slightly higher in this case. This is likely due to the method used for quantification. Hematoxylin-eosin staining does not specifically detect collagen fibers as Masson trichrome staining, the gold-standard technique used to study fibrosis. Instead, it stains the whole extracellular matrix in light pink color contrasting with the dark staining of myocytes, the main cell type contributing to the tissue structure (**Figure 13**). The computational quantification approach used here, although is pretty faithful, could account for the observed difference since all matrix fibers are detected, not just collagen. At the single gene level, the expression profiles of members of the *TGF-β* pathway and components of the ECM confirm the trend observed at the histological level. The association of TA markers with cardiac fibrosis again highlight their increased sensitivity to account for the individual aging rate and the relevance of conducting aging studies from the biological perspective. The relation of TA markers with a main cardiac aging phenotype is hereby empirically demonstrated.

2.4.3 Depleted and enriched functions in biologically and chronologically old individuals

In GSEA, the top 20 enriched GO groups by the three age markers have been mainly related to immunity, inflammation and chemotaxis. This study confirms previous observations such as the inflammatory response during aging [5]. Other enriched groups in the CA and *CDKN2A*-based analysis are related to angiogenesis. Although there is extensive literature on impaired angiogenesis in the elderly [293], these findings would agree with pathological angiogenesis related to the senescence-associated secretory phenotype [294].

Commonly depleted functional processes for the three aging markers are mainly involved in mitochondrial and energy metabolism, which coincides with previous observations [5]. Functions related to protein synthesis are also depleted in all of them, this being in line with the well-described alterations in the translation process during aging. Reduction in protein synthesis has been shown to range from 20 to 75% in many tissues and organisms and translation has been reported to become selective with age, promoting the synthesis of proteins involved in repairing mechanisms and stress response [295].

Interestingly, this study unveils relevant cardiac-related processes as depleted in individuals with high *CDKN2A* expression and/or high AppAge, but not in CA-old individuals. These cardiac processes constitute up to 25% or 40% (*CDKN2A* and AppAge, respectively) of the top 20 GOs. Aside of the cardiac-specific GOs, other CA-undetected functions include depletion of cytoskeleton-related processes. The appearance of cytoskeleton GOs ("Regulation of actin filament-based movement", "Myofibril assembly" or "Actin-mediated cell contraction") agrees with the mechanism of myofibril disorganization that alters cardiac contractility and shortens lifespan in Drosophila [296]. For bone and cartilage-related functions enriched in AppAge, previous studies have reported that genes involved in cartilage development participate also in vascular calcification in the heart [297], [298]. Moreover, proteins involved in bone morphogenesis are necessary during heart development [299] and it is known that expression of fetal genes is re-activated during aging [300]. Therefore, both vascular calcification and emergence of fetal genes could be indicative of aging phenotypes.

In agreement with the results on fibrosis and aging, *CDKN2A*- and AppAge-focused enrichment analysis yielded functional groups related to extracellular matrix organization, which is associated with fibrotic remodeling in human aged hearts [301]. SMAD protein-related processes in CA could agree as well with age-induced cardiac fibrosis [302]. The similarities between *CKDN2A*- and AppAge-based analysis, as well as the great number of cardiac-specific functions differentially depleted by *CDKN2A* and/or AppAge, further support the importance of not only considering CA but also BA in aging investigations.

Single cell RNA-seq could help to determine genes and functional groups relevant for biological aging at the individual cell level. Still, whole tissue transcriptomics is highly informative as it has been demonstrated for decades. In particular for human aging research, the high inter-individual variability across lifespan demands using a sufficiently high number of subjects to obtain relevant results, as demonstrated in this work. Carrying out a study of the magnitude of this one by single cell RNA-seq would be technically challenging. These results could however contribute to guide insightful aging research at the single cell level using the recently described human heart atlas [303].

In summary, these results confirm well-known aging landmarks in human LV at the same time that BA-based analysis demonstrates a remarkable potential to unveil novel cardiac-specific and age-related functional and structural impairments.

2.4.4 Identification of biological age-related miRNAs

The important role of miRNAs in the regulation of human LV aging is shown in this study. Twenty BIO-AGEmiRNAs are identified by *CDKN2A*-based analysis, a 3.3% of the LV miRNome. Similar studies in other tissues reported 8% and 16.8% age-related miRNAs [304], [305]. The more stringent criteria used in this study could explain this difference. A criterion including all miRNAs with *CDKN2A*-based differential expression would have retrieved 51 BIO-AGEmiRNAs (8.4%), but additional conditions to also account for life-long correlation with age in adulthood were imposed.

In the literature, a variety of miRNAs have been related to age-induced alterations. BIO-AGEmiRNA *MIR22HG*, downregulated with BA in the human LV data, has been previously found to be upregulated with CA in mouse heart, neonatal rat cardiomyocytes and human atria [107], [274]. miR-22 inhibits autophagy [274] and is essential for stress-induced cardiac hypertrophy in mice [306], both processes involved in cardiac aging [293]. In the case of the downregulated miRNAs from the MIR17HG family (miR-17, -18a, -19a, -19b1, -20a and -92a), some of them have been found to be downregulated in several cellular aging models [307]. Consistent with these findings, miR-17 has been reported to inhibit senescence in mouse cardiac fibroblasts [308] and miR-19a and -19b to indirectly inhibit autophagy and apoptosis in human cardiac fibroblasts. MIR155-HG was found to be upregulated. Interestingly, upregulation of miR-155 was related to hypertrophy [309], which is tightly related to aging. Other miRNAs have been shown to play a role in the aging process in previous studies. In particular, miR-34a has been described to be essential in promoting heart aging in mice and its expression to correlate with CA in human atria [108]. However, this miRNA did not emerge in this human LV study.

This study describes the involvement of miRNAs in the aging process and partially agree with previous reports. Most of the cited studies are based on *in vitro* or *in vivo* research in other species. Animal models, especially the small ones, have remarkable physiological differences, reduced lifespan and lower exposure to the environment as compared to humans. All this could account for the observed discrepancies. Also, differences in the tissue of origin could play a role, like for the human atrium age-associated mir-34a [108]. Chamber-specific miRNA expression and response to stimuli are reported in mice [310], [311].

This work remarks the significance of conducting aging studies from human LV samples, particularly by BA-based analysis, and stresses the need to further investigate the role of the herein described miRNAs in human systems, like iPSC-derived cardiac cells.

2.4.5 miRNA-based regulation network of genes involved in human LV biological aging

In this study, predicted miRNA-target gene regulatory networks specific of human LV biological aging are built. The network of upregulated BIO-AGEmiRNAs contributes to the regulation of genes involved in cardiac function to a higher extent than the downregulated network (72 vs 34 cardiac-related genes). This agrees with the functional group enrichment results where heart-related processes appear only as depleted during BA (**Figure 17B**).

Some of the mirror targets of the upregulated BIO-AGEmiRNA network are related to cell-cell communication, a depleted functional group in the *CDKN2A*-based GSEA (**Table 16**, GO:0086065, available at the online publication as Table S12). Desmosomes provide mechanical continuity in the myocardium by linking the intermediate filaments of the cytoskeleton between two adjacent myocytes and are associated with arrhythmogenic cardiomyopathies [312]. *JUP*, *DSC2* and *DSP*, which encode proteins of the desmosome, are mirror targets of MIR3916, indicating that *miR-3916* may be responsible for desmosome destabilization during aging. Also, MIR4435-1HG could participate in this process by downregulating *DSP*, tightly involved in conduction [313], an interaction that is proved *in vitro* in this work. But lack of MIR4435-1HG increase with BA in this pilot validation data (**Figure 21**) questions this regulation axis and asks for further investigation. Also linked to cell-cell communication and specifically related to conduction, connexin 43 (encoded by *GJA1*), the main ventricular connexin in the intercalated discs of human LV forming GAP junctions, is a mirror target of hsa-mir-6080. *POPDC2* has been postulated to have a role in cell-cell communication [314] and this experimental validation shows its downregulation by hsa-miR-24-2, even if in the LV tissue from living donors its expression does not significantly change with *CDKN2A* expression.

Regarding cardiac action potential, two groups are identified as downregulated in BA-old individuals ("Cardiac muscle cell action potential" and "Regulation of cardiac muscle cell action potential"), which rely on ion channels. Indeed, from the 72 identified cardiac-related mirror targets, 12 of them encode for ion channels and *KCNQ1*, *KCNH2* and *ATP1A2* tend to decrease with age in living donors. Although ion channel malfunction can produce ventricular arrhythmias [315], their expression has been scarcely studied in relation to aging. Only *HCN2* has been reported to be downregulated at the protein level in the senescent rat sinoatrial node [316] and *KCNJ11* to be mildly downregulated with aging in guinea pig hearts [317]. Here, in agreement with the bioinformatics analysis, preliminary evidence of *KCNQ1*, *KCNH2* and *ATP1A2* downregulation with BA in human LV is provided.

Calcium handling, reported to be impaired in old individuals (Chiao & Rabinovitch 2015), involves many genes including *ATP2A2* (*SERCA2)* and *CASQ2*, which are mirror targets of *MIR24-2* and *MIR3916* (and *CASQ2* of hsa-mir-6080). In fact, downregulation of *SERCA2* by hsa-mir-24-2 has been validated *in vitro* in this study and analyzed in samples from living donors, together with *CACNA1C*, where the later tends to decline with BA. The expression of *SERCA2* is known to reduce with age in murine cardiomyocytes and human atrium [102], [301] but seems to remain constant in the data from living patients. Further research is needed to fully portray *SERCA2* expression changes in the aging human LV. Yet, these results suggest that these BIO-AGEmiRNAs, could have a role in the altered intracellular calcium management in aged individuals.

Sarcomeric and cytoskeleton proteins, responsible for the physical contraction of cardiomyocytes, appear in this regulatory network as downregulated. Although many studies have connected altered sarcomeric function with age [318], no studies have so far associated it with specific genes nor specific regulatory mechanisms. *TNNC1*, *TNNT2*, *ACTN2*, *ACTC1*, *TPM1* are all mirror targets of hsa-mir-6080 and *MIR3916*. *TNNI1* and *MYBPC3* (a regulatory subunit of myosin) are regulated by *MIR4435-1HG*, while *MIR24-2* regulates *TTN*, *TMOD1* and *ACTN2*.

These last two interactions have been proved *in vitro* in this work, suggesting that *miR-24-2* could be impairing the contraction process due to their participation in cytoskeleton-related functions [319], [320]. These results are novel in postulating that, at the transcriptional level, the expression of sarcomeric or cytoskeletal proteins, and thus cardiac contraction, could be modulated by BIO-AGEmiRNAs.

The autonomic nervous system has a well-known role in the modulation of heart function [321] and specifically, α1-adrenergic receptors (encoded by *ADRA1A*) have a protective role in cardiomyocytes [322], [323]. Here, *ADRA1A* expression is demonstrated to be downregulated by hsa-mir-24-2 and that its tendency is to decrease with age in living donors, suggesting that this BIO-AGEmiRNA could take part in the age-related cardiomyocyte damage. In the downregulated BIO-AGEmiRNA network (**Figure 19B**), there is a remarkably lower number of mirror targets than in the upregulated BIO-AGEmiRNA network, coinciding with the observation that heart-related functions are mainly downregulated in biologically old individuals (**Figure 17**).

In summary, an LV-specific gene regulation network controlled by BIO-AGEmiRNAs that could contribute to explain age-induced LV impairments is stablished. This study is in line with previously reported electromechanical alterations in old hearts, but it settles the need to validate every interaction of the computationally generated network and their effect *in vitro* or in human systems. This network offers an overview of miRNA-gene regulation in the aged human LV and sets the basis for future studies aimed at designing cardiac-specific therapies based on BIO-AGEmiRNAs.

2.4.6 BIO-AGEmiRNAs with potential as biomarkers of LV aging

The association of circulating blood miRNAs with age has been investigated in different studies aiming to determine age biomarkers in a non-invasive way [109]. However, most of the studies compare the healthy/diseased or young/old status and its association with certain miRNAs present in body fluids disregarding the miRNA tissue source [324]. This study identifies two age-related miRNAs, *MIR4461* and hsa-mir-490 as highly enriched in the human LV myocardium compared to more than 20 other human tissues across aging. Both miRNAs are present in plasma and the plasma levels of *miR-4461* correlate not significantly with the ones in LV. Despite a greater number of individuals would be required to properly assess this association, this result suggest that cardiac-enriched miRNAs could inform in a minimally invasive manner about the

BA of the heart in body fluids. Specifically, given the sensitivity and specificity of RNA detection by PCR or other cutting-edge diagnostic tools, like SHERLOCK [325], cardiac-enriched miRNAs would inform about accelerated heart aging in individuals whose plasma levels are over average values of a population chronologically contemporary, even before presenting clinical sings of heart function decline. This could allow to anticipate specific treatments to prevent any deleterious effects and improve the wellbeing of many individuals whose genetics and/or environment hasten their heart aging process. As a conclusion, two cardiac-enriched miRNAs that could have a significant impact for age-related cardiac risk prediction as biomarkers are proposed.

2.5 Conclusion

The adequacy for transcriptional analysis of human LV aging based on BA is shown and the potential of *CDKN2A* as a BA marker is demonstrated in comparison to another complex index measuring apparent age based on thousands of genes. Aiming at finding regulatory molecules of LV aging with potential therapeutic value, this research proposes 20 BIO-AGEmiRNAs and their associated mirror targets. These results point to a relevant role of miRNAs in contributing to the regulation of genes involved in human ventricular structural and functional changes during aging. The description of LV-enriched age-related miRNAs present in plasma constitutes a major advance in the proposal of non-invasive biomarkers of accelerated cardiac aging. This work sets the ground for future studies addressing the development of LV-specific miRNA-based anti-aging therapies and the assessment of cardiac biomarkers to stratify the risk for BA-related heart diseases.

Chapter 3

Natural and Induced Human Cardiac Aging: *Lamin A Δ50* does not accumulate naturally, but accelerates aging *in vitro*

This chapter has been partially adapted from the submitted manuscript entitled "Natural and Induced Human Cardiac Aging: *Lamin A Δ50* does not accumulate naturally, but accelerates aging *in vitro*" by García-Mendívil✉ and colleagues [326].

3.1 Introduction

Age-related changes are observed in the heart at different levels: functionally (e.g., deterioration of diastolic function, prolonged QT interval or lower cardiac reserve), structurally (e.g., left ventricular hypertrophy or vascular stiffening), histologically (e.g., extracellular matrix remodeling), cellularly (e.g., reduced cardiomyocyte number or cardiomyocyte hypertrophy) and subcellularly (oxidative stress, altered mitochondrial function, increased intracellular complexity and granularity, nuclear dysmorphia or genomic instability and damage) [29], [293], [327]–[331] . Changes at the gene (Chapter 1) and protein expression levels also occur. Examples are the decrease in SERCA2 expression [332], increased expression of cell senescence marker P16 [267] or changes in the expression of sarcomeric proteins (e.g., TITIN, TNNI3, MYH6/MHY7 balance) [100], [332]. The effects of age in the human heart at structural and functional levels are well known at the clinical levels. However, the knowledge of the molecular and cellular mechanisms responsible for age-related cardiac changes comes fundamentally from animal models, having thus unknown translational value. In humans, ethical and practical reasons make longitudinal and mechanistic studies at cellular and molecular levels unfeasible. Thus, human research at these levels is scant and mostly cross-sectional, which hampers medical advances towards healthy cardiac aging.

Animal models of induced aging, like D-galactose-induced aging, have shown similarities with natural aging [193], proving their suitability and time efficiency for aging research. In humans, Hutchinson-Gilford progeria syndrome (HGPS) is an extremely rare disease caused by mutations in the *LMNA* gene, typically *LMNA*$^{+/G608G}$, that is characterized by accelerated aging. This mutation exposes a cryptic splice site in exon 11 that leads to the expression of *LMNA* Δ50 variant, which codes for a dominant toxic truncated version of lamin A, progerin [333], which accumulates abnormally in the nuclear envelope causing nuclear morphological alterations and abnormalities that lead to changes in heterochromatin structure, gene transcription, mitosis, DNA replication and DNA repair [258]. HGPS patients manifest many aging-like pathologies observed in natural aging, including cardiovascular abnormalities like atherosclerosis, ventricular hypertrophy, cardiac fibrosis or endothelial dysfunction [259].

Small and large animal models of HGPS have been created [184], [185], [334], which recapitulate cardiovascular damage seen in HGPS patients. They have been even compared to naturally aged ones. Progeroid mice developed heart failure with similar cardiac electrical abnormalities as naturally aged mice [184]. Other studies have shown causal evidence of progerin to induce premature aging, either by inhibiting progerin in progeroid models or by activating it on healthy animals. For example, Lee and colleagues [335] showed that a reduction in progerin interaction with lamin A in progeroid mice led to a decrease in age-related markers, such as the cell senescence marker P16. In two other studies, specific inducible expression of progerin in the endothelium or cardiomyocytes of mice provoked cardiovascular pathology and altered heart function with age-related features (low heart rate, high QT interval and Ca^{2+} alterations), respectively [336], [337]. Thus, forced expression of progerin in an otherwise healthy background also led to age-related features *in vivo*. Adding to this evidence, Ashapkin and colleagues [258] reviewed common aging molecular mechanisms shared between cells affected by the progeria disease and of natural aging and reported relevant parallelisms. Also, the expression of progerin at the RNA or protein levels has been reported in non-diseased human tissues [329], [338]–[340], including ventricular tissue of healthy young/middle-age individuals [341], and it is considered to be implicated in physiological aging [329]. Whether progerin accumulates in myocardium beyond midlife with natural cardiac aging, potentially triggering age-related mechanisms, is unknown.

hiPSCs have been used for the molecular and cellular study of the mechanisms controlling physiology and disease, including the cardiac lineage [204]. As such, they have been used to study age-related features. Attempts to induce aging to hiPSC-derived cardiomyocytes (iCMs) have been reported by keeping cells in culture for a long time [251], changing the extracellular matrix [342] or exposing the cells to genotoxic agents like doxorubicin [252], [253]. Progerin has been used to induce aging in neurons to study late onset traits of Parkinson's disease [256]. But to date, no progerin-based model of accelerated aging has been established in iCMs to facilitate carrying out longitudinal and mechanistic investigations of human cardiac cellular aging.

In this chapter, the expression levels of *LMNA* and *LMNA Δ50* in human myocardium from midlife onwards are determined. Also, this work develops and characterizes a *LMNA Δ50* inducible-expression hiPSC line under the hypothesis that progerin-induced premature aging can recapitulate fundamental molecular and cellular aspects of natural cardiac aging.

3.2 Methods

3.2.1 Collection of left ventricular tissues and RNA extraction

Human transmural LV tissue specimens were collected at Hospital Universitario Miguel Servet (Zaragoza, Spain) and Hospital Universitario Virgen de la Victoria (Málaga, Spain) as described in Chapter 2. Also, the clinical characteristics of the patients were the same as in Chapter 2. A total of 21 LV samples covering age ranges from 51 to 83 y.o. (**Table 19**) were used. The samples were processed for RNA extraction and retrotranscription as described in Chapter 2.

Table 19. Left ventricle tissue donors.

Donor code	Hospital	Gender	Age
R406	Zaragoza	M	71
R408	Zaragoza	M	78
R409	Zaragoza	M	65
R412	Zaragoza	F	57
R413	Zaragoza	F	74
R414	Malaga	F	68
R415	Malaga	M	72
R417	Malaga	F	65
R419	Malaga	M	59
R423	Zaragoza	M	68
R424	Zaragoza	M	73
R436	Malaga	M	51
R437	Malaga	M	75
R438	Malaga	M	78
R440	Malaga	M	70
R444	Zaragoza	M	67
R446	Zaragoza	F	76
R448	Zaragoza	M	70
R449	Zaragoza	M	83
R491	Zaragoza	M	62
R492	Zaragoza	M	64

3.2.2 Generation of hiPSC with inducible progerin expression

The hiPSC-MCL#3 master cell line derived from Bj1 fibroblasts that contained flippase recognition target (FRT) sequences in the *AAVS1* locus [343] was used to create a *LMNA Δ50* doxycycline-inducible cell line by flippase recombinase mediated cassette exchange. The *LMNA Δ50* donor vector was created using standard molecular cloning by replacing the tandem dimer Tomato reporter from the *pZ:F3-P (cHS4)X4 TetOn 3f-tdT-F* vector [343], [344] by the coding sequence of progerin form pLPC-Progerin vector, a kind gift from Gerardo Ferbeyre (Addgene plasmid #69061) [345]) (**Figure 24**).

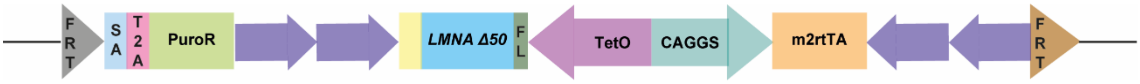

Figure 24. Doxycycline-inducible progerin expression cassette for recombinase mediated cassette exchange to generate the hiPSC-LMNA Δ50 line. Heterotypic FRT sequences (triangles) flank the construct formed by a T2A-led promoterless (SA, splicing acceptor) puromycin selection unit (5' side) and a doubly insulated unit (purple arrows) that contains the tetracycline inducible expression system that express the 3FLAG (FL)-progerin (coded by *LMNA Δ50*).

3.2.3 Culture of hiPSCs and differentiation to cardiomyocytes

hiPSCs were cultured on hESC qualified matrigel (45354277, CULTEK, Spain)-coated plates in E8 medium (05990, Stem Cells Technologies, Canada). At approximately 90% confluency, hiPSCs were collected using EDTA 0.5 mM (15575020, Thermo Fisher, USA) and seeded at a cell density of 84000 cells/cm^2 on hESC qualified matrigel coated plates with 5 µM Rock Inhibitor (72304, Stem Cells Technologies, Canada). hiPSCs were differentiated into iCMs following the GiWi protocol by Lian and colleagues [346] using 9 µM CHIR (SML1046, MERK Life Sciences, Germany) to inhibit Gsk3 and 48 hours incubation with 5 µM IWP2 (3533/10, Biotechne R&D System, USA). In some experiments, cardiomyocytes were expanded using the protocol developed by Buikema [347], [348].

After differentiation into iCM (day 16 after differentiation onset), induction with doxycycline at 0.5 µg/mL was carried out for 6 or 16 days. The cells were subsequently collected for downstream characterization analysis.

3.2.4 Immunofluorescence in cell cultures

For immunostaining, iCMs were detached using TrypLE Select (10X) without phenol red (A1217701, Thermo Fisher, USA) and seeded on cover slips at 1.5x10^4 cells/cm^2. Cells were fixed with 4% PFA (sc-281692, Biogen Cientifica, Spain) for 20 minutes at 4ºC after removing the medium and washing once with PBS. Then, undiluted protein block (X0909, Agilent, USA) was added for 25 minutes followed by 3 washes with PBS and 15 minutes permeabilization of 0.1% Triton X-100 (142314.1611, LANAU, Spain). The primary antibodies γ-H2AX 1:200 (Ab22551, Abcam, UK), FLAG (1:100, F1804, Sigma Aldrich, USA) or TNNT2 (1:50, Abcam, UK) diluted in 0.1% Triton-PBS were incubated overnight at 4ºC. The following day, secondary antibody Alexa Fluor 555 goat anti-mouse (A21424, Thermo Fisher, USA) or Alexa Fluor 488 goat anti-rabbit (A11034, Thermo Fisher, USA) in 1:1000 dilution in 0.1% Triton-PBS was added for 30 minutes in darkness followed by 20 minutes incubation in darkness with DAPI 3 µM (ab228549, Abcam, UK) diluted in PBS. After staining with primary and secondary antibodies and DAPI, 3 washes of 5 minutes with PBS were applied. Finally, samples were mounted on slides (AAAA000080, Thermo Fisher, USA) with fluorescent mounting medium Fluoromont-G (00-4958-02, Thermo Fisher, USA).

After staining, images were acquired using Carl Zeiss LSM 880 confocal microscope (Carl Zeiss, Germany). The image acquisition parameters were kept constant for each analyzed marker among samples.

3.2.5 Image processing and analysis

Image processing was performed to quantify the amount of nuclear γ-H2AX signal. Original CZI 16-bit images were handled with ZEN Blue software (Carl Zeiss, Germany). The orthogonal projection was applied and the raw (unadjusted) 16-bit grayscale images were exported as TIFF files. To obtain contrasted 16-bit depth DAPI images, the exported TIFF file was adjusted in ImageJ 2.5.0 using the "best fit" values retrieved from ZEN Blue software. Next, a binary mask for DAPI signal was obtained by thresholding using the open software MARTA [349]. Regarding γ-H2AX, the original 16-bit images exported from Zen were used. A script in MATLAB was developed to analyze all the images at once to obtain the amount of nuclear DNA damage, determined as amount of γ-H2AX signal ($\gamma\text{-H2AX}_a$). That is, the pixel intensity (PI) for each image was calculated as the sum of the intensity of the pixels in the original 16-bit γ-H2AX image that colocalized with the DAPI binary mask ($IP_{\gamma\text{-H2AX}}$) divided by the total number of pixels in the DAPI binary mask (NP_{DAPI}):

$$\gamma\text{-H2AX}_a = IP_{\gamma\text{-H2AX}} / NP_{DAPI}$$

Every doxycycline-induced condition was normalized with its untreated control (corresponding to the same differentiation experiment).

3.2.6 Cellular and nuclear morphology analysis

Cellular size and internal complexity were qualitatively evaluated by flow cytometry using forward scatter (FS), which informs about cell size, and side scatter (SS), a well-established indicator of cell granularity related to cell senescence [350]–[352]. The FS height (FS-H) versus SS height (SS-H) contour plot was used to compare each progerin-induced iCM population with its untreated iCM control population by observing the displacement of the density lines. Qualitatively, using a quad gate placed in the right high corner of the inner density line of the contour plots of each untreated control, size (sum of events in quadrants Q2+Q3) and granularity (events in Q1+Q2) shifts relative to their untreated controls were determined.

Nuclear abnormalities, calculated as the percentage of aberrant nuclei, were assessed in the iCM DAPI images of progerin-induced and its untreated controls. Three different observers performed this quantification as a blind test in which images were randomized.

3.2.7 Analysis of mitochondrial dynamics and intracellular ROS by superoxide indicator staining

iCMs were dissociated with TrypLE Select (10X) (A1217701, Thermo Fisher, USA) and incubated for 30 minutes at 37ºC with either 50 nM of Mito Tracker Green FM (M7514, Thermo Fisher, USA) or 12.5 nM of the superoxide indicator dihydroethidium (hydroethidine) (D1168, Thermo Fisher, USA). Afterwards, cells were centrifuged, resuspended in PBS and fluorescence was immediately measured using a Gallios 10 Flow Cytometer (Beckman Coulter, USA). The Median Intensity Fluorescence (MIF) was calculated for each sample and relative to their untreated control.

3.2.8 Gene expression analysis: transcriptomic data and quantification by qPCR

Transcriptomic data obtained from the GTEx database and differential gene expression analysis described in Chapter 2 were used to obtain the fold change expression between old and young individuals, based on both CA and AppAge, of a number of selected genes.

qPCR was made in a Viia 7 Real-Time PCR System (Applied Biosystems, USA) using Power SYBR Green PCR Master Mix (4309155, Thermo Fisher, USA) or iQ Multiplex Powermix (1725848, BioRad, Spain) and oligonucleotides and a probe described in **Table 20**. Transcript variant-specific oligonucleotides were designed to discriminate between *LMNA* and the *LMNA Δ50* (**Figure 25**). Technical triplicates were performed for each sample and *POLR2A* expression was used for normalization [353]. *LMNA* and *LMNA Δ50* expression levels were calculated as $2^{-\Delta Ct}$ while relative gene expression between induced and non-induced conditions was determined by $2^{-\Delta\Delta Ct}$ or fold change expression for all other genes.

3.2.9 Statistical analysis

As described in Chapter 2, Spearman correlation analysis was used to test the strength and direction of association between two variables. Mann-Whitney test was used to assess differences between two independent groups. In this chapter, the significance threshold was maintained at 0.05 for the analysis of human donor data, but it was established at 0.1 for the analysis of *in vitro* experiments due to reduced number of samples from independent experiments, and so, statistical power. Unless otherwise indicated, data are presented as mean ± SEM.

Table 20. Oligonucleotides used for qPCR.

Gene	**Forward primer sequence**	**Reverse primer sequence**	**Probe**
ACTN2	CATCAGAATCAGCTCAAGCAAC	ACGAGTTGCTTCACCTTGTC	
DSP	GATGCTTACCAGAAAAGGCTTC	GGACACTGATGGCTTTATAAAGG	
KCNH2	ATCCCCTTCGACCTGCTC	CAGCCCGATCAGCTCCTC	
KCNN2	GGTCTGATCATCGTGTACCA	GCTATTCTCCAGTCATCTGCTC	
LMNA	CCTACCTCCTGGGCAACTC	AGGTCCCAGATTACATGATGC	
LMNA Δ50	GCTGAGTACAACCTGCGCT	TTCTGGGGGCTCTGGG**C**T	
MYH6	CGTGTCTCAGGGAGAGGTG	GCACGTCAAAGGCACTATCG	
POLR2A (cells)	CTCCCTCATCATACCTGGTCA	CATTCTCCACCACCACCTTG	
SCN5A	AGTCAGCGTCCTCACCAG	GCGAGACTCCTCTAACTCTTCC	
SERCA2	GGTGCTGAAAATCTCCTTGCC	CGGTTACTCCAGTATTGCAGGT	
POLR2A (tissue)	GGTCACATCAATTGTATCCGTACC	CATTCTCCACCACCACCTTG	CAGCACCCATCCCGATGATGAAGA
CDKN2A (tissue)	GGAAGGTCCCTCAGACATC	GCAGTTGTGGCCCTGTAG	AGGCTCTGAGAAACCTCGGGAAACT

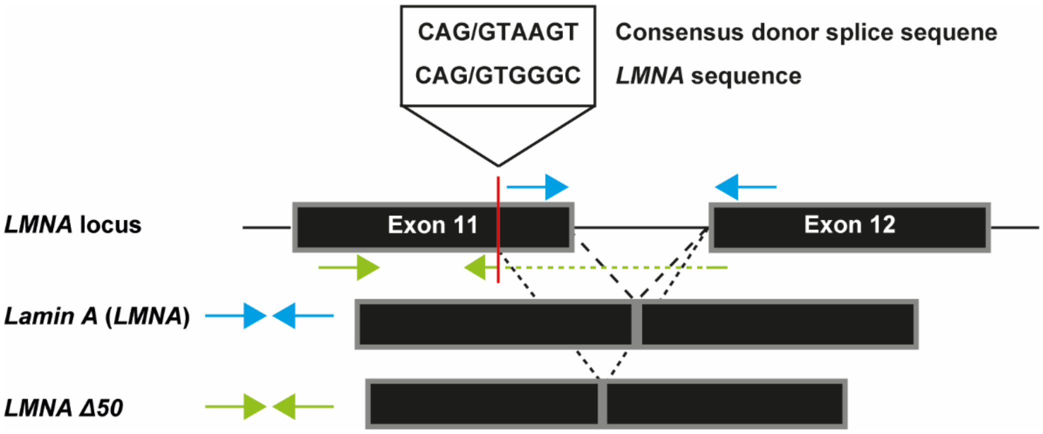

Figure 25. Primers design for *LMNA* and *LMNA Δ50* gene expression assays in the human left ventricle. Diagram depicting the qPCR strategy used to quantify *LMNA* and *LMNA Δ50*.

3.3 Results

3.3.1 *LMNA Δ50* is barely expressed in the human left ventricle and has weak correlation with age

To assess whether progerin expression is altered in natural aging in the human heart, particularly from midlife onwards where the effects of age become physiologically more evident, the expression of *LMNA Δ50* in human healthy LV tissues of 21 donors with age ranging from 51 to 83 years was quantified **(Figure 26)**. *LMNA Δ50* showed a non-significant tendency to increase with age in relation to CA (Rho coefficient of 0.24) (**Figure 26A**). A similar tendency was observed for the transcriptomic BA marker of human LV *CDKN2A*, described in Chapter 2 (**Figure 26B**). Similarly, *LMNA* expression levels tended to increase with CA (Rho coefficient 0.26), although non-significantly (**Figure 26C**). *LMNA* expression level had a stronger correlation with the transcriptomic BA marker *CDKN2A* that neared significance (**Figure 26D**). *LMNA Δ50* was nearly

1000-fold less expressed than *LMNA,* but a strong significant correlation between the two splice variants was found (Rho coefficient of 0.74) (**Figure 26E-F**). The correlation persisted even after removing the data point with an extremely large value of *LMNA* expression (**Figure 26G**).

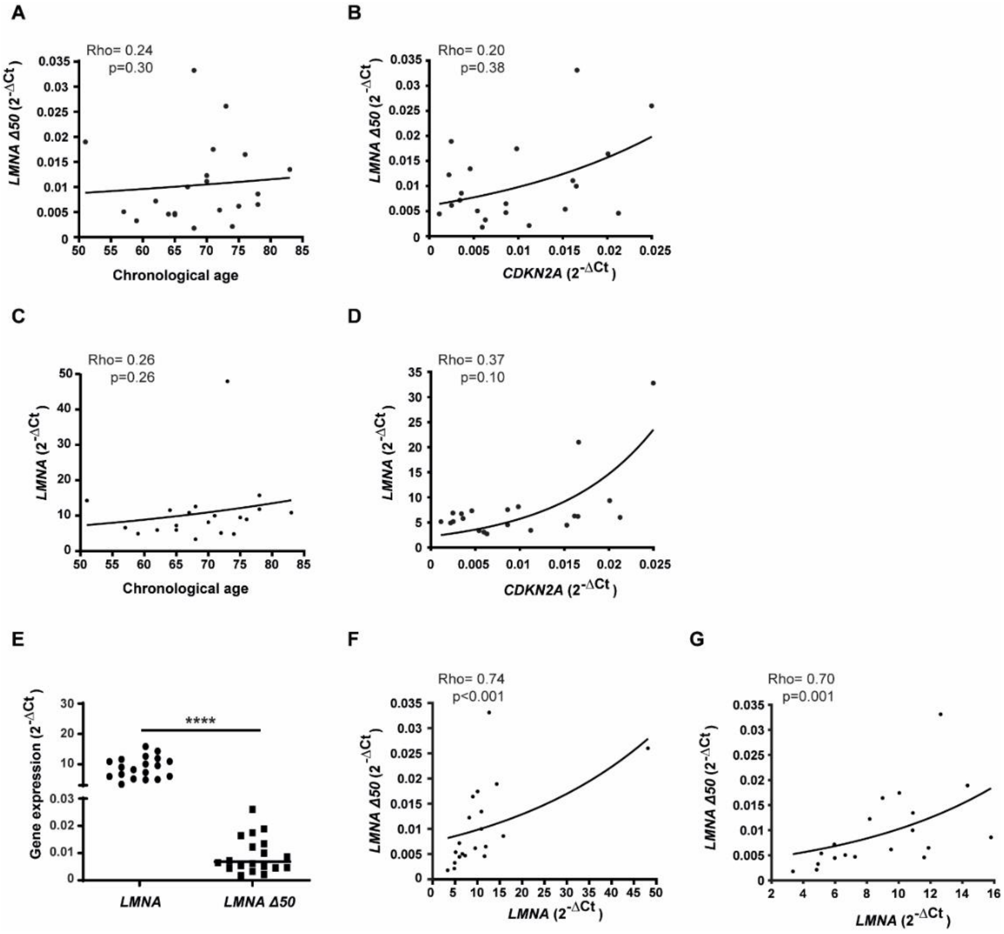

Figure 26. Quantification of *LMNA* and *LMNA Δ50* in the human left ventricle. A) Correlation between *LMNA Δ50* expression levels ($2^{-\Delta Ct}$) and chronological age and **B)** *CDKN2A* expression levels ($2^{-\Delta Ct}$). Correlation between *LMNA* expression levels ($2^{-\Delta Ct}$) and chronological age **(C)** and *CDKN2A* expression levels ($2^{-\Delta Ct}$) **(D)**. **E)** Gene expression levels of *LMNA* and *LMNA Δ50* ($2^{-\Delta Ct}$). **F)** Correlation between *LMNA* and *LMNA Δ50* expression levels ($2^{-\Delta Ct}$). **G)** Correlation between *LMNA* and *LMNA Δ50* disregarding an outlying donor. Spearman correlation coefficients (Rho) and p-values (p) are shown. *p-value < 0.1, ** p-value < 0.05, *** p-value < 0.01 and **** p-value < 0.001.

3.3.2 Generation of a hiPSC cell line for inducible expression of progerin

Using the hiPSC-MCL#3 cell line with FRT docking sites, recombinase mediated cassette exchange [343] was used to create the hiPSC-*LMNA Δ50* line. Specifically, a copy of a *3FLAG*-tagged *LMNA Δ50* was introduced into the *AAVS1* locus under the control of a tetracycline responsible promoter (**Figure 24**). Induction with 0.5 µg/mL of doxycycline in iCM for 6 days led to fairly homogeneous progerin expression (monitored by 3FLAG immunostaining) (**Figure 27A**).

TNNT2 expression was used to monitor the homogeneity of the differentiation towards the cardiac lineage. Only differentiations with populations in which at least 85% of the iCMs expressed TNNT2 were used in this study (**Figure 27B**).

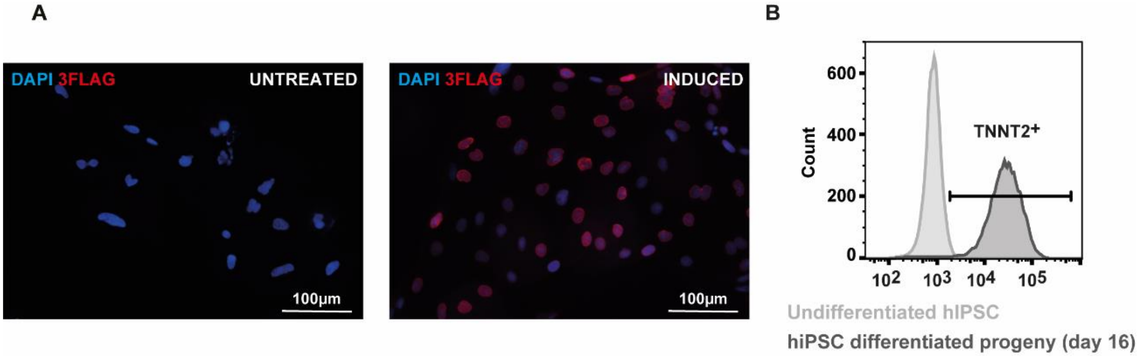

Figure 27. Generation of hiPSC with inducible expression of progerin and differentiation to cardiomyocytes. A) Representative image of progerin expression immunostaining monitored by 3FLAG staining in hiPSC-*LMNA Δ50*-derived cardiomyocytes in doxycycline treated (right) and untreated (left). **B)** Representative flow cytometry data of TNNT2 expression in undifferentiated hiPSC-*LMNA Δ50* and in hiPSC-*LMNA Δ50*-derived cardiomyocytes after 15 days of differentiation.

3.3.3 Progerin expression leads to the detection of aging landmarks in iCMs

Next, the effects of the inducible expression of progerin in committed iCMs from the hiPSC-*LMNA Δ50* line on well-established markers of natural aging were investigated. Two timepoints of induction, 6 and 16 days, were selected based on previous studies [256]. DNA damage in response to progerin expression was evaluated by determining the amount of γ-H2AX signal. After 6 days of induction, a small but significant increase in DNA damage was observed compared to the uninduced control. However, this effect was much greater after 16 days induction of progerin, when a significant increase in γ-H2AX-related DNA damage of 78% was observed (**Figure 28A**). At the level of cellular and nuclear morphology, 27% more nuclear structural abnormalities after 6 days of progerin induction with respect to the untreated ones were observed (**Figure 28B**). Morphologically, the complexity of iCMs increased by 20% after 16 days of induction as compared to the non-induced controls. Qualitatively, a shift of the population density lines towards higher complexity than in the non-induced cells was evident (**Figure 28C**). Finally, a functional characterization of mitochondrial activity and ROS production was performed. Progerin expression did not lead to decreased mitochondrial mass after 16 days with doxycycline doses of 0.5 µg/mL. However higher non-toxic dosages showed a significant reduction (**Figure 28D**). In agreement with the decreasing mitochondrial mass, ROS production diminished with a similar trend, being significantly lower at dose 2.5 µg/mL (**Figure 28E**).

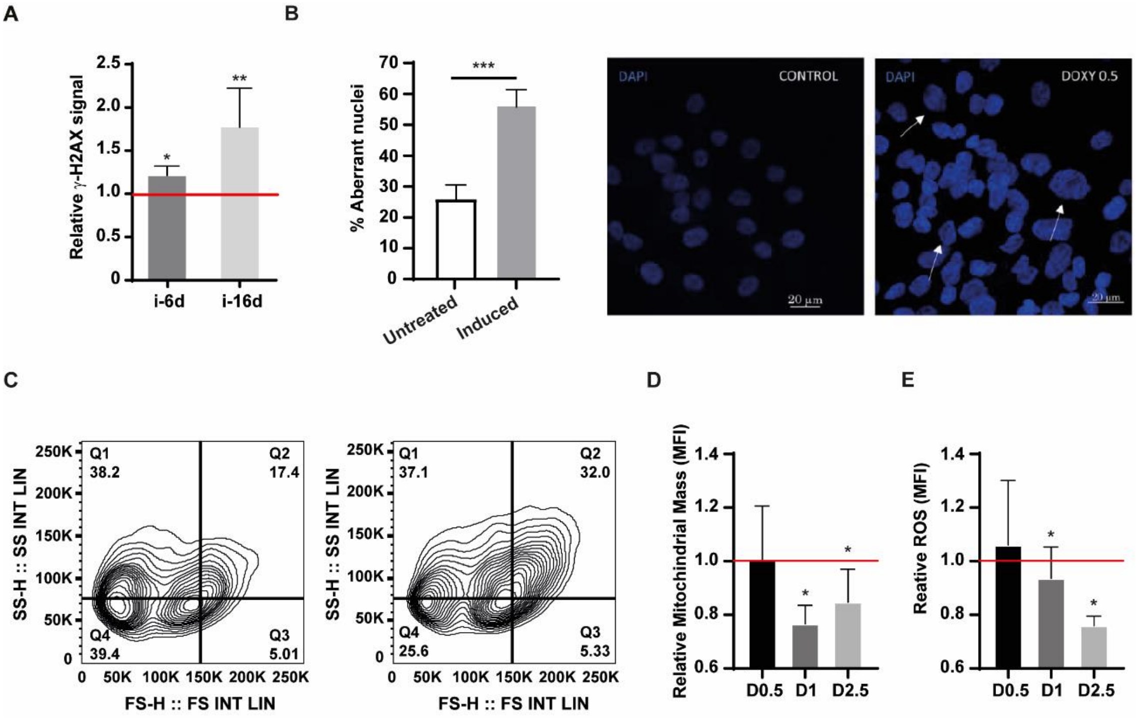

Figure 28. Characterization of aging hallmarks in hiPSC-*LMNA Δ50*-derived cardiomyocytes. A) Left: Quantification of γ-H2AX-related DNA damage after 6 (i-6d) and 16 (i-16d) days of progerin induction with 0.5 µg/mL of doxycycline relative to untreated cells. Red line represents the untreated condition. **B)** Left: Quantification of the percentage of aberrant nuclei in untreated and progerin-induced iCM cultures. Right: Representative images of untreated and progerin induced iCM cultures for 16 days. Arrows indicate examples of dysmorphic nuclei. **C)** Representative images of morphological complexity analysis of untreated hiPSC-*LMNA Δ50*-derived iCM and progerin-induced for 16 days. **D)** Quantification of mitochondrial mass (Median Fluorescence Intensity, MFI) relative to untreated cells in 16 days induced cultures. **E)** Quantification of ROS production (Median Fluorescence Intensity, MFI) relative to untreated cells in 16 days induced cultures. n≥3 for A and C and n≥2 for E, F and G. Non-parametric Mann-Whitney test was used to compare the untreated condition versus progerin induced ones. *p-value < 0.1, ** p-value < 0.05 and *** p-value < 0.01.

3.3.4 Progerin induces gene expression changes in iCM that mimic age-related changes in human LV

Next, this work investigated whether progerin can induce cardiac-specific gene expression changes that recapitulate observations from human tissue. Cardiac-related genes whose expression changed with both CA and AppAge (in this case all significantly with AppAge) were selected based on the transcriptional dynamics of human LV (with a focus on genes involved in cardiac function) described in Chapter 2. The selected genes were *ACTN2, MYH6, SERCA2, DSP, KCNN2, KCNH2* and *SCN5A*. *ACTN2* (alpha actinin 2) anchors myofibrillar actin thin filaments and titin to Z-discs of the sarcomere, key for cardiac contraction. *MYH6* is the alpha heavy chain subunit of cardiac myosin, and it is involved in cardiac contraction too. *SERCA2* transports Ca^{2+}

ions from the cytosol back to the SR following muscle contraction and it is crucial for Ca^{2+} handling and contraction. *DSP* is the desmoplakin, the fundamental desmosomal protein involved in cardiac force transmission. *KCNN2*, *KCNH2* and *SCN5A* are ion channels involved in the cardiac action potential. All these genes decreased significantly with AppAge in the LV of old individuals as compared to young ones and all, significantly or not, with CA (**Figure 29**). Gene expression analysis in iCM overexpressing progerin for 6 or 16 days mainly replicated the *in vivo* age-related changes. *DSP* augment was observed after 6 days induction, but its expression was reduced after 16 days. *ACTN2*, *SERCA2*, *KCNN2*, *KCNH2* and *SCN5A* showed reduced expression for both timepoints, being at least one of them significantly reduced as compared to untreated controls. *MYH6* decreases at both timepoints, but non-significantly in any case (**Figure 29**).

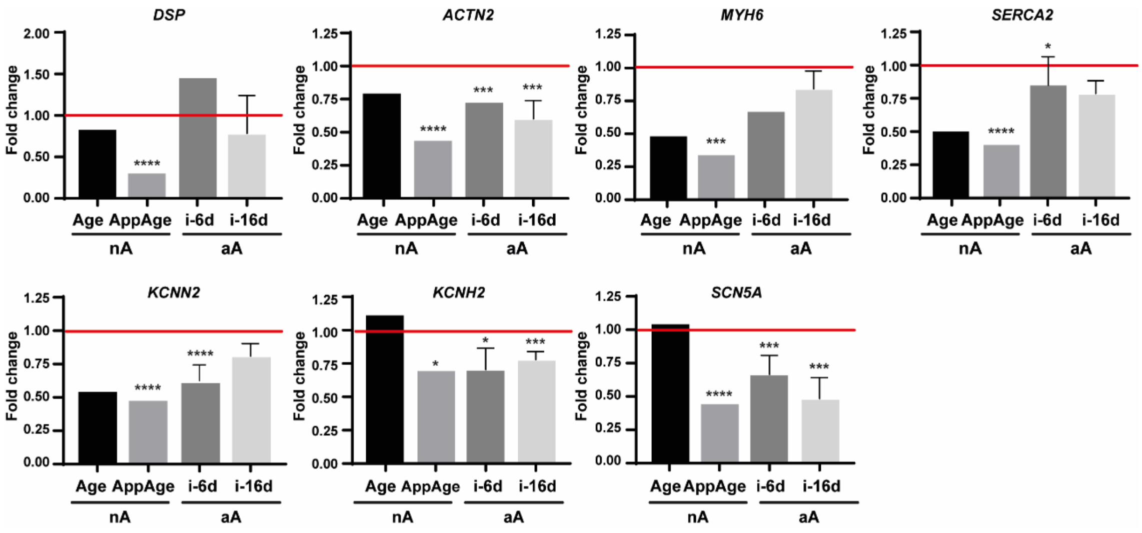

Figure 29. Quantification of the gene expression levels of cardiac genes on hiPSC-*LMNA Δ50* **iCM after progerin expression.** Natural aging (Na) refers to the analysis of RNAseq transcriptomic data in which gene expression from old versus young individuals by chronological age (Age) and biological age (AppAge) are reported. Fold change is calculated as $2^{log2Ratio}$ comparing old versus young individuals. Accelerated aging (Aa) refers to relative gene expression calculated as fold change ($2^{-\Delta\Delta Ct}$) in iCM after 6 (6d) or 16 (16d) days of progerin induction with 0.5 µg/mL doxycycline referred to the non-induced condition. Red line represents the untreated condition (n≥3). *p-value < 0.1, ** p-value < 0.05, *** p-value < 0.01 and **** p-value < 0.001.

3.4 Discussion

3.4.1 Presence of *LMNA Δ50* in the human LV

In this work, the spontaneous presence of *LMNA Δ50* in the human heart is confirmed, which is in agreement with previous studies [341]. *LMNA Δ50* is expressed almost 1000 times less than the native *LMNA* in the human LV. These large differences between expression levels have also been reported for other human tissues [338], [339]. The data shows a slight tendency of *LMNA Δ50* and *LMNA* to increase with CA and *CDKN2A* BA indicator, with this relation being only nearly significant for *LMNA* and BA, possibly in relation to the better capacity of BA to describe age-related transcriptomic changes, as reported in Chapter 2. The high correlation between both splice variants indicates that the rate of alternative processing of *LMNA Δ50* from *LMNA* keeps constant with age from midlife to elder age in human myocardium. Thus, a shift towards the production of the *LMNA Δ50* does not seem to occur with age, contrary to what is reported in HGPS patients where *LMNA Δ50* also increases with age [354], [355]. This is likely due to the weakness of the cryptic splice donor site in healthy individuals and the absence of age-related changes in splicing in this locus. Thus, this data suggests that the *LMNA Δ50* variant is unlikely to be a key effector of natural aging in the human heart in old age.

3.4.2 Progerin inducible expression model of iCM aging

Based on the existing evidence that progerin induces premature aging and shares molecular mechanisms [258], [333], [356] and cardiovascular changes with natural aging [259], a progerin-inducible expression hiPSC line to promote accelerated aging in iCMs was developed. Until now, studies on accelerated aging in iCMs have used hiPSCs from HGPS patients [357], [358]. In contrast, this model relies on progerin activation after iCMs commitment, thus separating the effects of progerin-mediated induction from those intrinsic to HGPS disease in terms of constitutive progerin expression. This model is expected to allow thorough analysis of the molecular mechanisms triggered by progerin and its accumulation in the nuclear envelope in non-diseased cells already committed to a specific cell lineage. This will lead to novel insights into the molecular dynamics of laminopathies at a cell lineage dependent-level, here cardiomyocytes, but also into the study of age-related mechanisms, given the well-established causality of progerin in premature aging [335]–[337].

Several approaches to create aged iCMs have been reported, like doxorubicin treatment [252], [253] or prolonged cell culture time [251]. Doxorubicin is a highly genotoxic chemotherapeutic whose main side effect in oncologic patients is a dose-dependent life-threatening cardiotoxicity [254]. Doxorubicin's molecular target is topoisomerase II, a key regulator of genomic stability, but doxorubicin also contributes to cardiac energy starvation, cell death and increased ROS production, which leads to cardiac muscle dysfunction and heart failure [255]. Lazzarini´s model [252], based on doxorubicin treatment of iCM, recapitulated aging landmarks as well as some age-related cardiac features. Whether the doxorubicin-triggered mechanisms follow the pathways of physiological aging or represent cardiotoxic-specific damage, in contrast to progerin-induced mechanisms, remains to be elucidated. On the other hand, four months in culture of iCM led to the recapitulation of some aging landmarks and age-related cardiac mechanisms [251]. However, the time required to obtain representative aging effects *in vitro* in cardiomyocytes without external pressure might make this approach impractical. Basically, *in vivo* cardiomyocytes do not proliferate and thus accumulate age-related damage over a lifetime. As an alternative to these approaches, progerin induction actively initiates processes that *in vivo* lead to premature aging phenotypes in multiple organs and at the organismal level.

The iCM progerin-inducible model was associated with aging hallmarks. Enhanced DNA damage, nuclear abnormalities and increased cellular complexity, were present after progerin induction for 6 and/or 16 days as compared to non-induced cells. At the doxycycline tested dose, mitochondrial abnormalities and, thus, concomitant alterations in ROS production, were not observed after 16 days induction. However higher doses led to the appearance of such age-related marks after 16 days, indicating that either longer treatments or higher induction levels might better recapitulate aging signatures. Still, results of this study allowed to confirm that progerin induction in iCMs reproduced fundamental aspects of aging, suggesting that this approach leads to the generation of prematurely aged human CMs *in vitro*.

Subsequently, cardiac-specific features found to change with natural aging in human LV at the transcriptomic level were characterized. The observed decrease in *SERCA2* found in the human LV data and aged iCMs agrees with previous studies in which a reduction in SERCA2 expression with age was reported in the human myocardium [102] as well as in animal models [359], which can lead to age-associated diastolic dysfunction [102], [360]. Mutations in *DSP*, *ACTN2*, *MYH6*, *KCNN2*, *KCNH2* and *SCN5A* have been associated with different cardiac diseases including hypertrophic cardiomyopathy, long QT syndrome type or Brugada syndrome and other cardiac conditions associated with high risk for ventricular arrhythmias or fibrosis [361]–[366], supporting the significance of these genes in cardiac function. The *in vitro* data mimics observations in human tissue with CA and, more importantly, BA, thus reinforcing the validity of this accelerated aging model. These results also support the hypothesis that data based on BA can be more faithfully translated into *in vitro* accelerated aging systems and *vice versa*. This is relevant to the establishment of predictive longitudinal human aging models to perform translational mechanistic investigations that are otherwise not feasible in humans and that provide novel molecular insights. Indeed, this model system supports further functional studies on age-related changes in sarcomere function, cellular connectivity and electrophysiology.

3.5 Conclusions

This study rules out an imbalance in *LMNA Δ50* processing relative to *LMNA* leading to its accumulation beyond midlife in human myocardium. This implies that, most likely, progerin is not pivotal in triggering physiological cardiac aging. On the other hand, *in vitro* progerin induces both general and cardiac-specific age-related features in iCMs that mimic changes observed in human ventricular aged myocardium. Thus, although progerin might not be key in natural cardiac aging, its pathological effects seem to replicate pathways of cardiac natural aging *in vitro*, in agreement with common knowledge derived from HGPS research [258]. In the future, this model can be used as a basis to perform longitudinal studies of human cardiac aging that overcome the limits of transversal studies in humans to identify possible anti-aging targets. Furthermore, the *LMNA Δ50* hiPSC cell line generated here could be applied to any cell lineage to obtain aged models of neurons or hepatocytes, among others.

Chapter 4

Analysis of age-related left ventricular collagen remodeling in living donors: implications in arrhythmogenesis

This chapter has been partially adapted from the publication "Analysis of age-related left ventricular collagen remodeling in living donors: implications in arrhythmogenesis" by García-Mendívil✉ and colleagues [367].

4.1 Introduction

As described in Chapter 1, age-induced accumulation of myocardial interstitial fibrosis leads to cardiac mechanical and electrical dysfunction and is commonly associated with CVDs, the foremost cause of death worldwide [67], [368]. The extracellular matrix is a key component of the myocardium that contributes to its biomechanical behavior. Within the protein network, collagen fibrils are principal constituents that provide support to the contractile machinery. From animals studies, it is known that while collagen helps to maintain myocardial structure in healthy young hearts, the increased collagen content in aged hearts, together with additional age-related cardiac remodeling, reduces cell-to-cell coupling and impedes normal electrical propagation, facilitating arrhythmias [81], [369]. Not only the amount of collagen, but also its spatial distribution and architecture, play a role in impulse conduction and arrhythmogenesis [77], [80], [81], [370].

In human hearts, macroscopic fibrosis is evaluated *in vivo* mainly by non-invasive cardiac magnetic resonance imaging (CMRI) [369]. Strong dependence of magnetic resonance fibrosis markers on age [371] and correlation with ventricular arrhythmias and sudden cardiac death [372] have been reported. However, CMRI and other non-invasive methods do not possess cellular or subcellular resolution [373]. The lack of microscopic definition hinders structural investigations at the histological level that could provide insight into fibrosis-related arrhythmogenic mechanisms. Histological evaluation of collagen is commonly performed by immune detection or histochemical procedures, like Masson's trichrome or Picrosirius red staining, but these techniques can disrupt the collagen fibrils and thus hamper structural analysis. Also, the automatic quantitative analysis can be affected by the variability that the staining procedures can introduce on the color balance of the staining due to technical issues such as changes in the chemical formulations of the stains or the protocol used for sample fixation and storage.

Fibrillar collagen is non-centrosymmetric and has a remarkable non-linear potential, thus being capable of generating very bright second harmonics. Second-harmonic generation (SHG) microscopy exploits this property to specifically investigate the collagen matrix in different tissues. SHG microscopy has a label-free nature [374] that, besides providing highly specific signal, it is an interesting feature when tissue samples are scarce, as those from human LV biopsies from living donors, as it does not consume sample. Also, it has submicron resolution [375], which enables structural analysis of collagen organization, rather than just amount quantification. Assessment of collagen deposition in the human heart by SHG microscopy has been mostly evaluated from atrial tissues [376], [377], while information from the human LV is scant [378], [379]. In addition to the described SHG characteristics, its specificity and resolution enable the development of precise methods for (semi-)automatic quantification [380], [381]. Currently employed methods for fibrosis characterization from SHG images study mainly collagen fiber alignment and the degree of isotropy [377], [381], [382]. A few works in the literature also characterize its spatial distribution [383], [384], but as far as I know none of them in relation to myocardial fibrosis.

To the best of my knowledge, the amount of age-related collagen deposition in the human LV has been analyzed in very few studies using standard histochemical techniques [72], [73]. Comparisons were carried out between young (twenties) and elder (from sixties to eighties) individuals, thus leaving unresolved the age ranges of clinical relevance related to increased arrhythmic risk [385]. In addition, such studies disregard collagen organization. In agreement with the results of these studies, in Chapter 2 the age-related increase in total LV fibrosis in comparable age-ranges is reported. These results suggested that accounting for the aging rate by transcriptomic BA better explained the increased fibrosis as compared to CA. Thus, histological BA could also yield a more precise understanding of the dynamics of collagen deposition in the aging human LV. This is of special interest from midlife onwards, where changes in fibrosis could be expected to be more variable and clinically relevant than in youth, given the cumulative action of genetics and/or environment over time. Detection of increased fibrosis during middle-age could be critical for early application of anti-fibrotic therapies, even at stages of subclinical evidence, as a strategy to prevent fibrosis-related ventricular arrhythmias and sudden cardiac deaths. Further studies on collagen deposition from middle-age onwards are needed. Also, characterization of age-related LV myocardial fibrosis as an arrhythmogenic substrate has been mostly studied in animal models [386] or using numerical methods to simulate general fibrosis characteristics [370], but not using patient-specific models representative of cardiac tissue images.

In this chapter, transmural LV tissue sections from young, adult and old pigs as well as middle-age to elder humans are analyzed by SHG microscopy. An automated method is developed to quantify the amount, aggregation and spatial distribution of collagen, the two latter ones based on a new variable to measure collagen assembly. To account for the fact that the aging rate highly varies among individuals, these three features are evaluated not only as a function of CA but also in relation to the amount of the aging pigment lipofuscin [49]. Subsequently, the results from the experimental collagen characterization are introduced into two-dimensional computational models of human LV electrophysiology and the impact of collagen characteristics in electrical propagation and pro-arrhythmicity is assessed, obtaining improved assessment of the effect of fibrosis as a substrate for cardiac arrhythmia generation.

4.2 Methods

4.2.1 Collection and processing of left ventricular tissues

Pig transmural LV tissue specimens were collected from young female pigs (12-16 weeks old, 35 kg, n=7) at the Experimental Surgery Service of the Biomedical Research Center of Aragón (CIBA, Zaragoza, Spain), adult male and female pigs (6 months, 110 kg, n=8) at Mercazaragoza slaughterhouse (Zaragoza, Spain) and boars (4-5 years old, 300 kg, n=11) at The Pink Pig slaughterhouse (Zuera, Spain). The samples were obtained 10-15 minutes after the sacrifice using a disposable 14 G tru-cut biopsy needle (Bard Mission 1410MS, Bard). All animal experiments complied with the regulations of the local animal welfare committee for the care and use of experimental animals and were approved by local ethics authorities (Ethics Committee on Animal Experimentation, CEAEA, of the University of Zaragoza). All animal procedures conformed to the guidelines from Directive 2010/63/EU of the European Parliament on the protection of animals used for scientific purposes.

Human transmural LV tissue specimens were collected at Hospital Universitario Miguel Servet (Zaragoza, Spain) following the procedure described in Chapter 2. Also, the clinical characteristics of the patients (n=26) were the same as in Chapter 2. The specimens were transferred to 4% paraformaldehyde fixative solution for 1h at 4°C and stored in 0.01% sodium-azide in PBS at 4°C until embedded in paraffin blocks. Tissue sections of 5 µm were mounted on microscope slides for SHG analysis. For comparison purposes, two age groups were established: middle-age (54.8±4.97, n=5) and elder (75.92±3.0, n=12). For correlation analysis, samples from all the individuals were used.

4.2.2 Non-linear optical microscopy

SHG microscopy was used to quantitatively assess collagen deposition in LV tissue samples combined with two-photon excitation fluorescence microscopy to detect cellular and lipofuscin autofluorescence. A Zeiss LSM 880 (Carl Zeiss, AG, Jena, Germany) mounted on the rear port of an Axio Observer.Z1 stand was employed. Excitation was provided by a femtosecond pulsed laser (Mai Tai DeepSee, Spectra-Physics, CA, USA) tuned to a central wavelength of 810 nm, passed through an acousto-optic modulator and coupled into the LSM880 scanhead. The laser light was directed to the sample using a 760 nm shortpass dichroic mirror (MBS 760+) and ~80 mW average power was focused on the sample through a plan-apochromat 20x objective (NA 0.8, Carl Zeiss, AG, Jena, Germany). Throughout the experiments, images were acquired with a bit depth of 16 bits, used a constant pixel dwell time of 4.48 µs, unidirectional scanning and a zoom factor of 1.3 that resulted in a constant square pixel size of 170 nm x 170 nm when imaging with a resolution of 1872 by 1872 pixels to fulfill Nyquist criterion. For samples larger than a single field of view, a tile scan was performed to cover the complete sample with 10% overlap between the tiles to enable a seamless stitching of these tiles.

To facilitate fast acquisitions of large samples, three channels were simultaneously recorded with a fully opened pinhole, using the 34 channel QUASAR spectral detector unit (2 PMTs (Ch1 and Ch2) + 32 channel GaAsP array (ChS1)). SHG signal was detected in Ch1 (PMT, wavelength range 380-420 nm, detector gain 750, digital offset 256). Cellular autofluorescence was detected using ChS1 (32 channel GaAsP array, wavelength range 500-552 nm, detector gain 680, digital offset 64). Lipofuscin autofluorescence was detected in Ch2 (PMT, wavelength range 650-735 nm, detector gain 750, digital offset 256).

4.2.3 Masson's trichrome staining

Masson's trichrome staining was performed after SHG. Briefly, 5-µm-thick deparaffinized sections were stained with hematoxylin for 5 minutes. The slides were subsequently washed and, following 5 minutes of ponceau/fucsine solution and washing, phosphomolybdic acid 1% was applied for 5 minutes. Collagen was stained with Aniline Blue Solution for 8 minutes, following which phosphomolybdic acid 1% was applied again for 5 minutes. Finally, the sections were rinsed in acetic acid 1% for 1 minute, before dehydrating and mounting in DPX mounting medium. Slides were left to dry overnight and were evaluated using a Leica DM5000B microscope (Leica Microsystems, Germany).

4.2.4 Image processing for evaluation of collagen amount, aggregation and spatial distribution

Original images (czi format) were exported as 16-bit TIFF images using Zen blue software (Carl Zeiss, Jena, Germany), with each detection channel in a different channel. Images were processed for automatic brightness scaling using ImageJ [387] and to remove isolated image segments, e.g. fluorescence artifacts or areas of clear perivascular fibrosis, before the quantitative analysis.

An in-house MATLAB v2020b user interface was developed to characterize the amount and distribution of collagen in the collected SHG microscopy data. From the 16-bit TIFF image, myocardial tissue (blue channel) and SHG signal (green channel) were extracted and converted into gray-level images. A binarization filter was applied to each of these gray-level images to generate binary masks for both myocardial tissue and SHG signal. Empty spaces in the myocardial tissue mask with less than 20 pixels were filled, and tissue segments with less than 15 pixels were associated with artifacts and discarded. For the SHG binary mask, isolated regions with less than 15 pixels were identified as correspondent with noise artifacts and were removed. SHG signal contained both myosin and collagen signals, being collagen the SHG signal that does not colocalize with the myocardial tissue. This lack of colocalization was used to obtain the collagen mask from the SHG mask. The image processing procedure developed renders tissue masks that faithfully represent the outcome obtained by standard Masson trichrome staining (**Figure 30**).

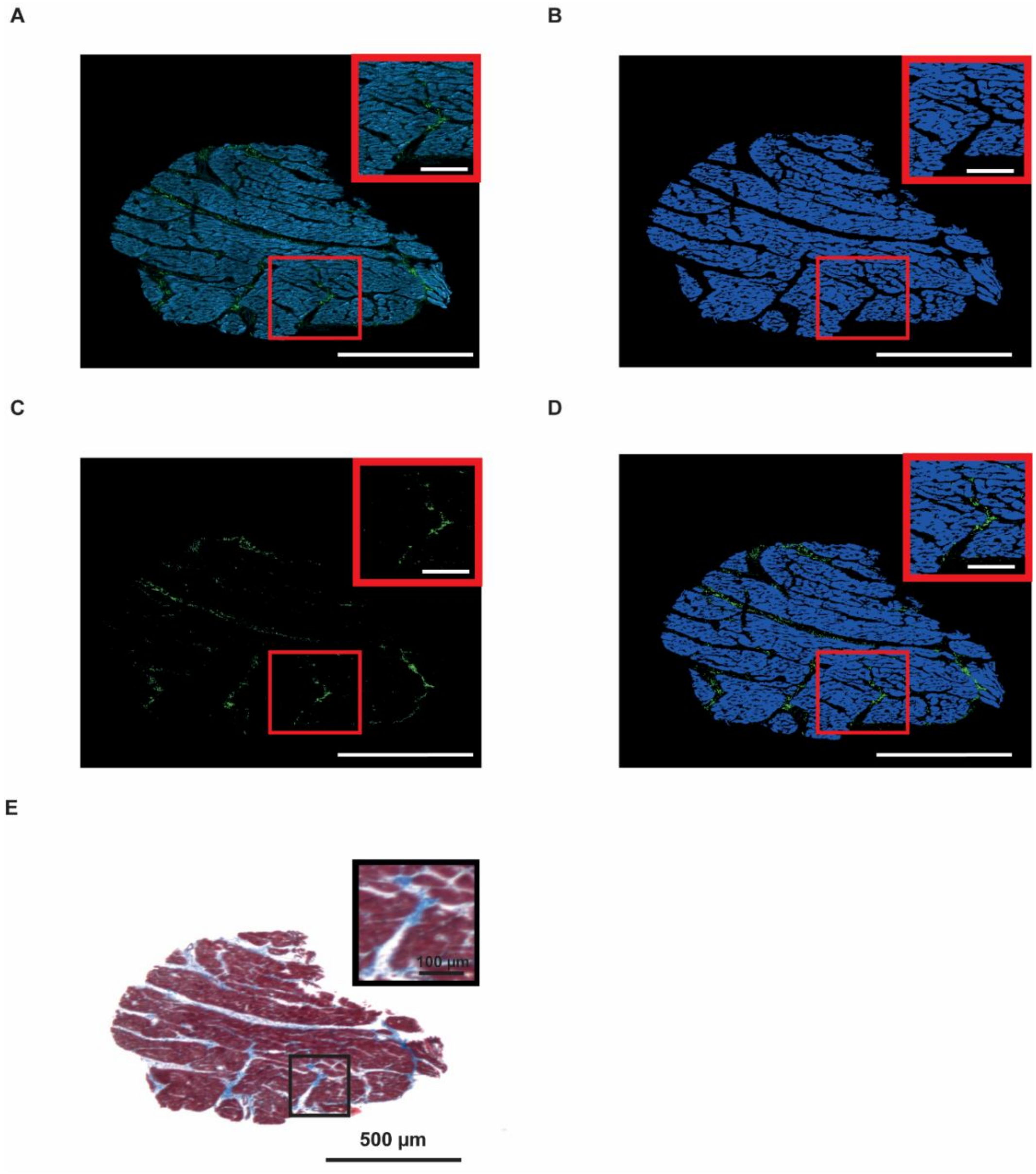

Figure 30. Collagen evaluation in SHG images using an automatic method. A) Unprocessed SHG image (green) and autofluorescence (blue) levels of an LV tissue specimen. **B)** Extracted tissue mask obtained from the tissue autofluorescence signal. **C)** Collagen mask obtained by subtraction of autofluorescence to SHG signal. **D)** Merge of collagen (green) and tissue (blue) masks. **E)** Masson trichrome staining of a serial section of the sample shown in A.

From the myocardial tissue and collagen masks, the percentage of collagen, P_c, was estimated as the number of activated pixels in the collagen mask (N_c) divided by the sum of activated pixels in the myocardial tissue (N_m) and the collagen masks:

$$P_c = \frac{Nc}{Nc + Nm}\ 100$$

From the collagen mask, the global clustering degree was calculated as the number of collagen pixels surrounded by collagen pixels in a circle of 2-pixel radius divided by the total number of collagen pixels. Additionally, a relative clustering measure was estimated as the product of percentages of collagen and clustering degree and it was expressed as per ten thousand (‱).

Furthermore, the spatial distribution of collagen clusters was obtained by windowing the collagen mask into 500x500 pixel subimages and calculating the collagen clustering in each of these subimages. An additional filter was applied to set a minimum number of pixels in any given subimage for it to be included in the analysis, and the threshold was set to 200 pixels. For the histogram of clustering degrees in all subimages of an image, the clustering distribution median was calculated as the median of the distribution, and the clustering distribution dispersion was estimated as the interquartile range of the distribution.

The pixel radius for global clustering, the window size for the spatial distribution of collagen clustering and the threshold for subimage acceptance were determined empirically. A 2-pixel radius, a window of 500x500 pixels and a threshold of 200 pixels were found to be adequate for evaluation of global collagen aggregation and its spatial distribution.

The reason for choosing a radius of 2 pixels was that clustering analysis using a smaller radius (radius of 1 pixel) led to almost every pixel of collagen being recognized as a cluster itself; with higher radius values (radius of 3-4-5 pixels), many collagen aggregates were not detected. The 2-pixel radius was the one more faithfully detecting grouped collagen pixels versus finely scattered one without losing small collagen aggregates. For spatial distribution analysis, 500x500 pixels was chosen as the area of subimages since it was observed to best fit the rationale of retrieving a sufficient amount of frames in all kind of tissue sections (big and small) that are large enough to avoid leaving tissue areas unconsidered due to low pixel count or, on the contrary, to reduce the analysis to just a few frames that won't capture distribution differences. The threshold for a minimum pixel amount in a subimage to be included in the distribution analysis was set to 200 pixels to avoid including isolated pixels in the quantification.

4.2.5 Image processing for lipofuscin quantification

The percentage of lipofuscin (P_l) was calculated as the amount of activated pixels in the lipofuscin mask (N_l) divided by the activated pixels in the myocardial tissue mask (N_m). The image processing method to determine the percentage of lipofuscin is shown in **Figure 31**.

$$P_l = \frac{\mathrm{Nl}}{\mathrm{Nm}}\ 100$$

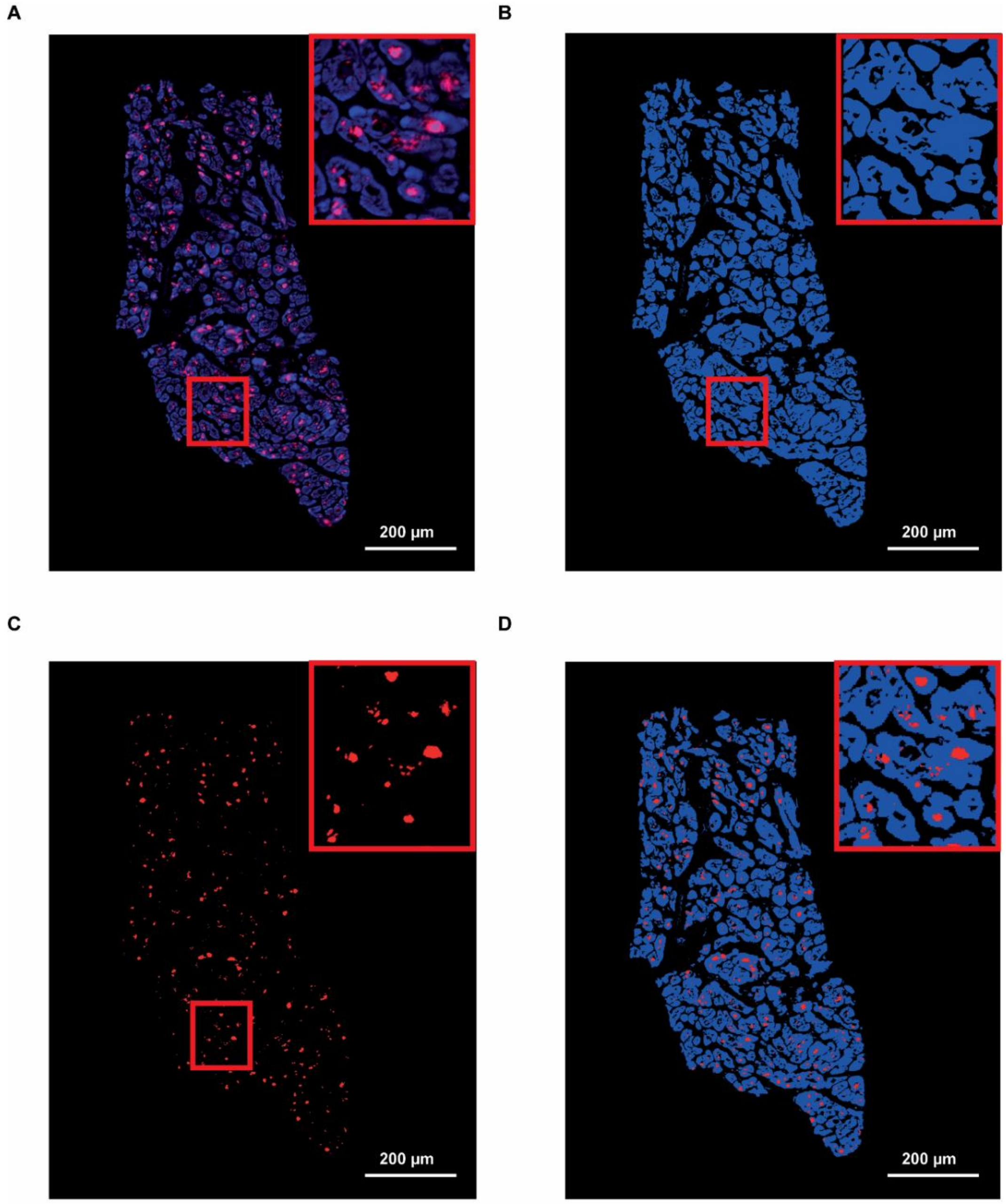

Figure 31. Quantification of lipofuscin accumulation by an automatic method. A) Unprocessed confocal microscopy image of a human LV tissue section with lipofuscin (red) and tissue autofluorescence (blue) channels. **B)** Computed myocardial tissue mask. **C)** Computed lipofuscin mask. **D)** Merge of lipofuscin and myocardial tissue masks.

4.2.6 Inter-observer agreement

All image processing analysis was performed by two independent observers. To compare the results obtained by the two observers, Bland-Altman plots were obtained. For all quantifications, the level of agreement between the two observers, both in pig (**Figure 32**) and in human samples (**Figure 33**), was reported.

A % Collagen

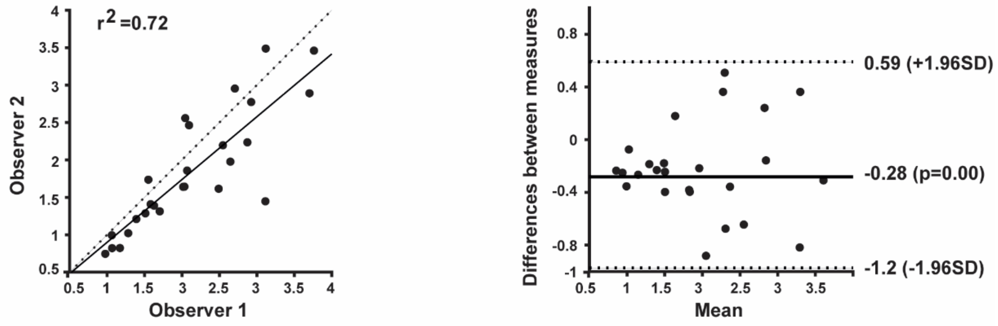

B % Clustering degree

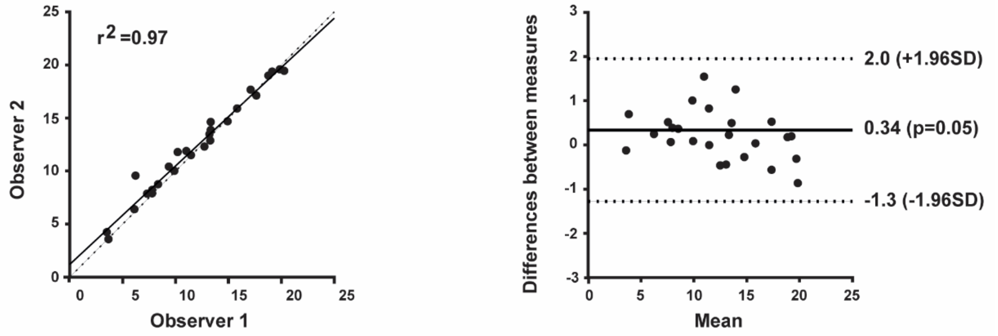

C Relative clustering

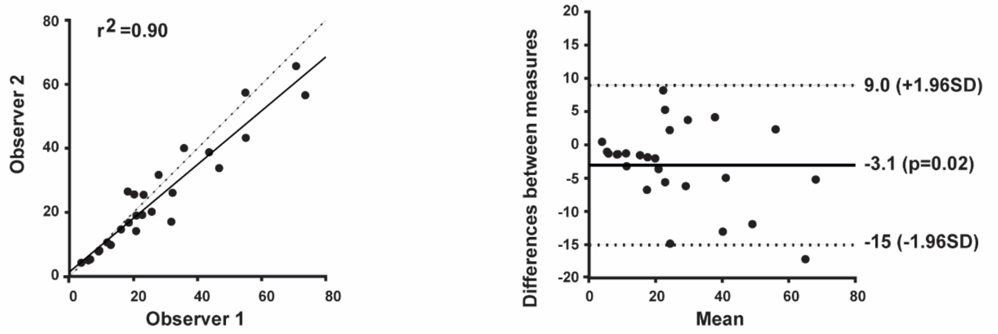

Figure 32. Comparison of the analysis by the two observers for the pig samples using Bland-Altman test. Test´s results for **A)** collagen, **B)** clustering degree, and **C)** relative clustering. On the left graphs the correlation of the measures by the two observers for every sample and the R^2 coefficient are shown. On the right graphs, the black line represents the mean difference, and the dashed lines are 1.96 positive and negative standard deviation.

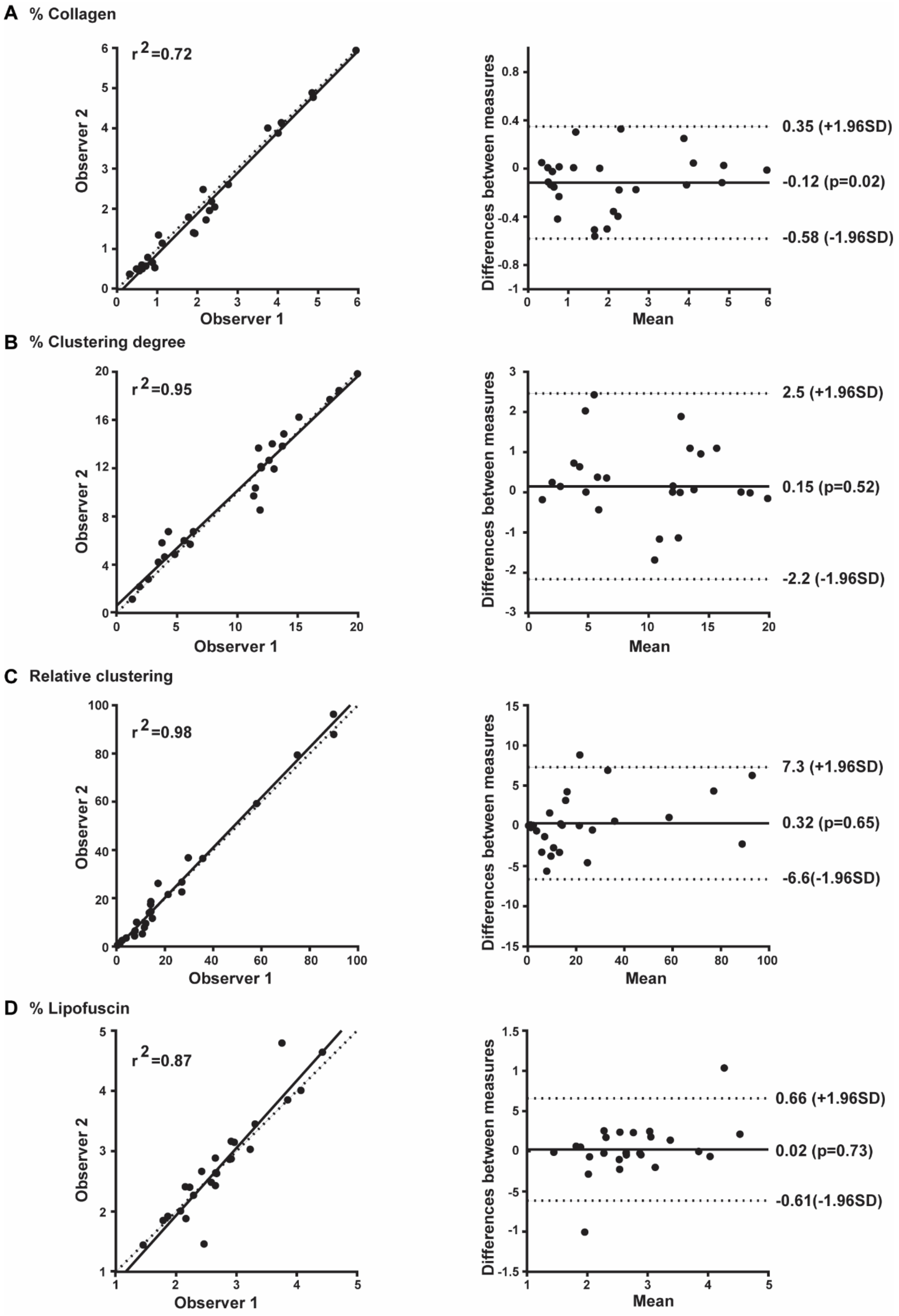

Figure 33. Comparison of the analysis by the two observers for the human samples using Bland-Altman test. Test´s results for **A)** collagen, **B)** clustering degree, and **C)** relative clustering. On the left graphs the correlation of the measures by the two observers for every sample and the R^2 coefficient are shown. On the right graphs, the black line represents the mean difference, and the dashed lines are 1.96 positive and negative standard deviation.

4.2.7 Simulation of ventricular electrical activity as a function of collagen characteristics

To assess the impact of the amount and distribution of collagen in cardiac AP propagation, two-dimensional computational tissue models of human ventricular electrophysiology representative of a set of the analyzed tissues were built. Specifically, eight LV tissue sections from patients with ages ranging from 58 to 81 y.o. were taken and the myocardial and collagen masks generated as described above were merged. From this merged image, a square was taken in each case to avoid possible effects on arrhythmia vulnerability associated with tissue geometry. These square images were resized to reduce the number of pixels and, thus, alleviate the computational cost of the simulations. The obtained images were subsequently converted into quadrilateral meshes by assigning a quadrilateral element to each pixel of the image. For each mesh, the pixel size was rescaled to obtain 5x5 cm^2 simulated tissues.

The vertices of the mesh elements corresponding to collagen pixels were assigned the label "fibrotic" and their electrophysiology was represented by the MacCannell model of mammalian ventricular fibroblasts described in Chapter 1 [9]. The rest of vertices were assigned the label "myocardial" and their electrophysiology was described by the O'Hara-Rudy model of human ventricular cardiomyocytes described in Chapter 1 [8]. The longitudinal conductivity in the myocardial region was set to 0.13 mS/cm, while the transverse-to-longitudinal conductivity ratio was set to 0.25. In the fibrotic region, the conductivity values were three times lower than in the myocardial region.

The effect of fibrosis on spiral wave generation was investigated by applying an S1-S2 cross stimulation protocol [388], with a sequence of periodic S1 stimuli followed by an extra stimulus S2 to assess pro-arrhythmicity due to the interaction of the S2 stimulus wave front with the S1 stimulus wave tail. In a first set of simulations, the S1 stimuli were applied at the left side of the tissue at t_{S1} = 50 ms, with duration t_d = 2 ms, period t_T = 1 s and amplitude A equal to twice the diastolic threshold. The S2 stimulus was applied on a patch region at the top left corner of the tissue with the same values of t_d and A as for the S1 stimulus. In a second set of simulations, the S1 stimuli were applied on the right side of the tissue and the S2 stimulus was applied at the top right corner. The stimulus time was varied to compute the vulnerability window (VW), defined as the time interval during which the S1-S2 interaction leads to the generation of a sustained spiral wave. The length of the VW was calculated, individually for each tissue, as the average of the VW lengths computed from the first and the second set of simulations.

To assess the effect of collagen amount on VW, simulations were conducted for each of the eight selected tissues under both control conditions (i.e., no collagen in the tissue) and fibrotic conditions (i.e., with the distribution of collagen as derived from processing the tissue images). When simulating control conditions, the O'Hara-Rudy action potential model was assigned to all vertices of the tissue mesh. To assess vulnerability to reentry, continuous tissues were simulated by filling any holes in them. To keep the percentages of collagen similar to the ones before filling the holes, i.e., as quantified in the original patients´ images, collagen was added to the filled regions according to a uniform random distribution to guarantee that those regions had the same collagen percentage as the original image.

To assess the effect of collagen distribution on VW, simulations were run for a patchy fibrosis configuration (with the image-derived collagen distribution as described in the previous paragraph) and for a diffuse fibrosis configuration (with collagen assumed to be uniformly randomly distributed across the tissue). For each tissue, the patchy and diffuse configurations contained the same percentage of collagen, measured as the ratio of mesh elements labeled as fibrotic divided by the total number of mesh elements.

Simulations were performed using ELECTRA which is an in-house cardiac electrophysiology solver implementing the Finite Element Method and Meshless methods [388], [389] for the solution of the cardiac monodomain model [389], [390]. In this work, the dual-adaptive explicit integration algorithm [390] was used to efficiently solve the monodomain model.

4.2.8 Statistical analysis

As described in Chapters 2 and 3, Mann-Whitney test was used to assess differences between two independent groups and Spearman correlation analysis was used to test the strength and direction of association between two variables. The significance threshold was established at p-value=0.05 for both Mann-Whitney and Spearman correlation. Unless otherwise indicated, data are presented as median [interquartile range (IQR)]. All statistical analysis were performed with MATLAB v2020b.

4.3 Results

4.3.1 Age alters the amount, aggregation and spatial distribution of collagen in pig LV tissue

Evaluation of collagen characteristics by SHG in young, adult and old pigs revealed age differences in the amount of collagen (**Figure 34A**). These results were consistent between observers (**Figure 32**). In the whole set of analyzed samples, borderline significant differences in the collagen content were found between young (median [IQR]: 1.49% [1.28%-2.02%], n=7) and old pigs (median [IQR]: 2.07% [1.79%-2.8%], n=11), but not between adult (median [IQR]: 2.07% [1.53%-2.68%], n=8) and old pigs. Of note, a higher degree of inter-individual variability could be observed in the old pigs, reflecting large heterogeneity in the age modulation of LV structural characteristics. These data indicated that age increases the percentage of collagen fibrils in pig LV tissue, and this is accompanied by a subtle increase in inter-individual variability (**Figure 34B**).

To evaluate collagen aggregation, its clustering degree was measured by quantifying the number of pixels in the collagen mask that were surrounded by a circle of collagen with a 2-pixel radius (**Figure 34C**). Adult pigs (median [IQR]: 13.33% [10.7%-16.3%] had significantly higher collagen clustering degree than young ones (median [IQR]: 6.95% [6.25-11.08%], whereas differences between old (median [IQR]: 13.35% [8.63%-18.38%]) and young pigs were borderline significant (p-value=0.056), and there were no differences between adult and old ones (p=0.952). In relation to the percentage of collagen, the relative clustering was also increased (median [IQR]: 25.75‱ [17.36‱-52.26‱]) in old and adult pigs (median [IQR]: 25.57‱ [19.45‱-41.33‱] compared to young ones (median [IQR]: 13.58‱ [9.06‱-20.51‱]). The amount of collagen significantly correlated with the clustering degree (Rho=0.59, p-value=0.002) (**Figure 34C**).

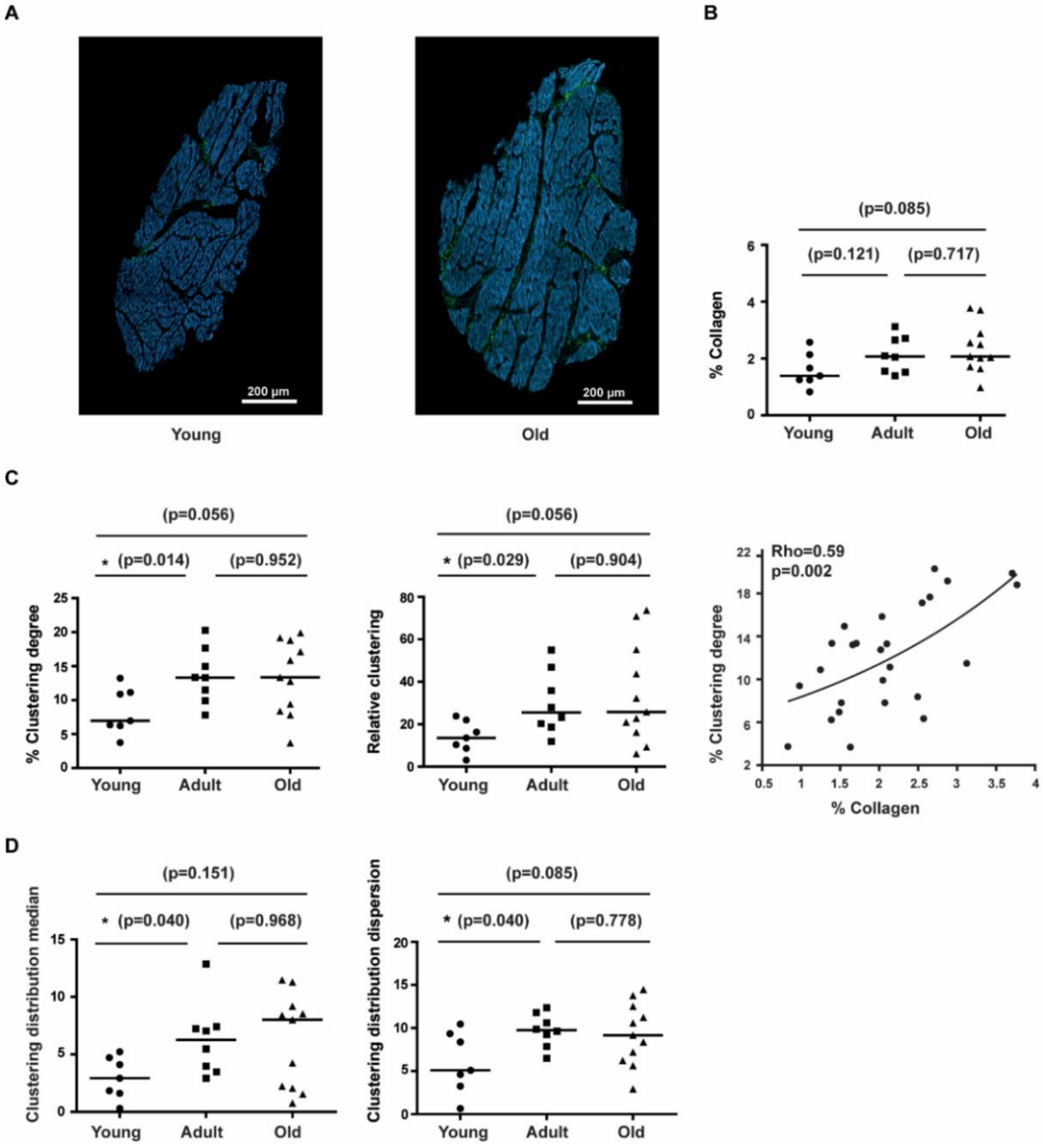

Figure 34. Quantification of collagen amount, aggregation and spatial distribution in pig LV sections. A) Representative SHG images of LV sections from young (left) and old (right) pigs with low and high collagen content. **B)** Quantification of collagen content in young to old pigs. **C)** Quantification of clustering degree (left) and relative clustering (middle) in young, middle-age and old pigs. Correlation between collagen and clustering degree (right). **D)** Quantification of clustering distribution median (left) and clustering distribution dispersion (right) of collagen aggregations in young to old pigs. In comparison between groups black lines represent the median. Non-parametric Mann-Whitney test is used and p-values (p) are shown. For correlation Spearman non-parametric test is used and correlation coefficients (Rho) and p-values (p) are shown.

To go further in the clustering evaluation, its spatial distribution was quantified by dividing every image in windows of 500x500 pixels and measuring the median and the dispersion of the clustering degree of all subimages (**Figure 34D**). Young pigs (median [IQR]: 2.93% [1.68%-4.57%] presented significantly and nearly significantly lower clustering dispersion median of collagen aggregation than adult (median [IQR]: 6.27% [3.73%-7.33%]) and old pigs (median [IQR]: 8.02% [2.10%-9.03%]), respectively. A similar tendency was observed for the clustering distribution dispersion between young (median [IQR]: 5.10% (3.60%-9.10%) and adult (median [IQR]: 9.74% (8.55%-11.19%) or old pigs (median [IQR]: 9.16% (6.46%-12.18%). This indicates that young animals have less clustered collagen and a more homogeneous distribution of collagen clusters than the two older groups. No difference was observed between adults and old animals. Thus, the observed increase in clustering degree in the elder groups as compared to young animals is accompanied by a change in its spatial distribution that is not different between adult and old.

4.3.2 Age alters the amount, aggregation and spatial distribution of collagen in human LV tissue

Alterations induced by age in the collagen characteristics of human LV tissue showed similar trends as those reported for pigs (**Figure 35**). Also in this case, results were comparable between observers (**Figure 33**). Elder individuals had moderately higher percentages of collagen (median [IQR]: 1.72% [0.63%-3.26%], n=12) than middle-age individuals (median [IQR]: 1.04% [0.85%-1.88%], n=5), although differences were not statistically significant. In the elder, there was a notably higher degree of data variability than in middle-age, indicating that collagen deposition can be largely individual-dependent in this group (**Figure 35A-B**).

The analysis of collagen aggregation showed that the percentage of clustered collagen did not vary between middle-age (median [IQR]: 12.01% [9.19%-13.78%]) and elder (median [IQR]: 11.64% [4.57%-12.31%]) individuals. A similar tendency was observed for the relative clustering between middle-age (median [IQR]: 14.28% [8.45%-23.52%]) and elder individuals (median [IQR]: 15.78% [3.21%-31.47%]). Similarly, to the absolute amount of collagen, high inter-individual variability in elder was observed for both parameters (**Figure 35C**). Like in pigs, the increase in the percentage of collagen was accompanied by enhanced clustering degree with correlation near significance (Rho=0.38 and p-value=0.059) (**Figure 35C**).

As per the distribution of clustered collagen, the median clustering over subimages did not change significantly between middle-age (median [IQR]: 4.4% [2.99%-6.74%]) and elder groups (median [IQR]: 2.89% [1.69%-5.65%]) for the median, and a similar trend was observed for the dispersion of clustering over subimages between middle-age (median [IQR]: 8.68% [6.4%-9.96%]) and elder individuals (median [IQR]: 8.72% [3.42%-10.7%]) (**Figure 35D**). Thus, age did not induce evident changes in the spatial distribution of clustered collagen in the human left ventricle from midlife onwards.

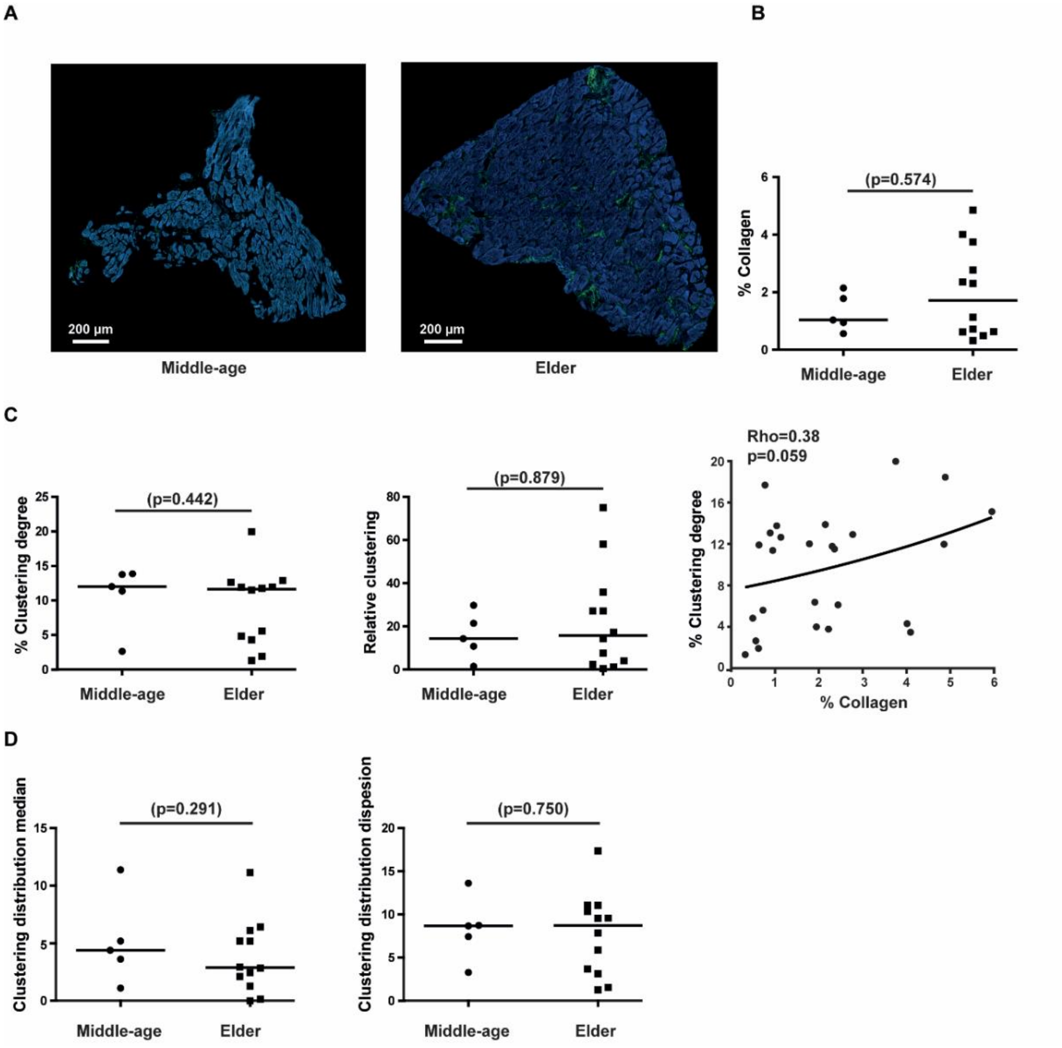

Figure 35. Quantification of collagen amount, aggregation and spatial distribution in human LV sections. A) Representative SHG images of LV sections from middle-age (left) and elder (right) donors with low and high collagen content. **B)** Quantification of collagen content in middle-age to elder individuals. **C)** Quantification of clustering degree (left) and relative clustering (middle) in middle-age and elder individuals. Correlation between collagen and clustering degree (right). **D)** Quantification of clustering distribution median (left) and clustering distribution dispersion (right) of collagen aggregations in middle-age to elder individuals. In comparison between groups black lines represent the median. Non-parametric Mann-Whitney test is used and p-values (p) are shown. For correlation Spearman non-parametric test is used and correlation coefficients (Rho) and p-values (p) are shown.

4.3.3 Age-induced collagen alterations correlate better with lipofuscin accumulation than with chronological age in human LV tissue

Since CA does not necessarily reflect the structural and/or functional state of an organ, it was assessed whether such degree of variability could be explained by differences in BA, which gathers genetic and environmental factors in addition to the temporal influence of CA. For that purpose, the content of the autofluorescent aging pigment lipofuscin was determined (**Figure 36A-B** and **Figure 31**), obtaining similar results between observers (**Figure 33**). Despite the well-established relation of lipofuscin with CA [49], [50], the lipofuscin content in these age groups did not differ, likely representing the high inter-individual variability in the CA groups, clearly observed for the collagen amount (**Figure 35B**). Thus, based on the expected better resolution of BA markers to explain age-related traits and the lack of relation of collagen parameters with CA in humans, the collagen features in the groups of individuals of low versus high lipofuscin content was analyzed. Individuals with high lipofuscin content have significantly higher values for collagen amount (median [IQR]: 2.77% [2.09%-4.23%]), clustering degree (median [IQR]: 12.91% [5.85%-15.01%]) and relative clustering (median [IQR]: 29.79% [15.98%-49.37%]) than the individuals with low lipofuscin content: median [IQR]: 0.72% [0.55%-1.20%] for collagen amount, median [IQR]: 3.99% [1.76%-7.04%] for the clustering degree, and median [IQR]: 4.06% [1.00%-8.51%] for the relative clustering (**Figure 36C**).

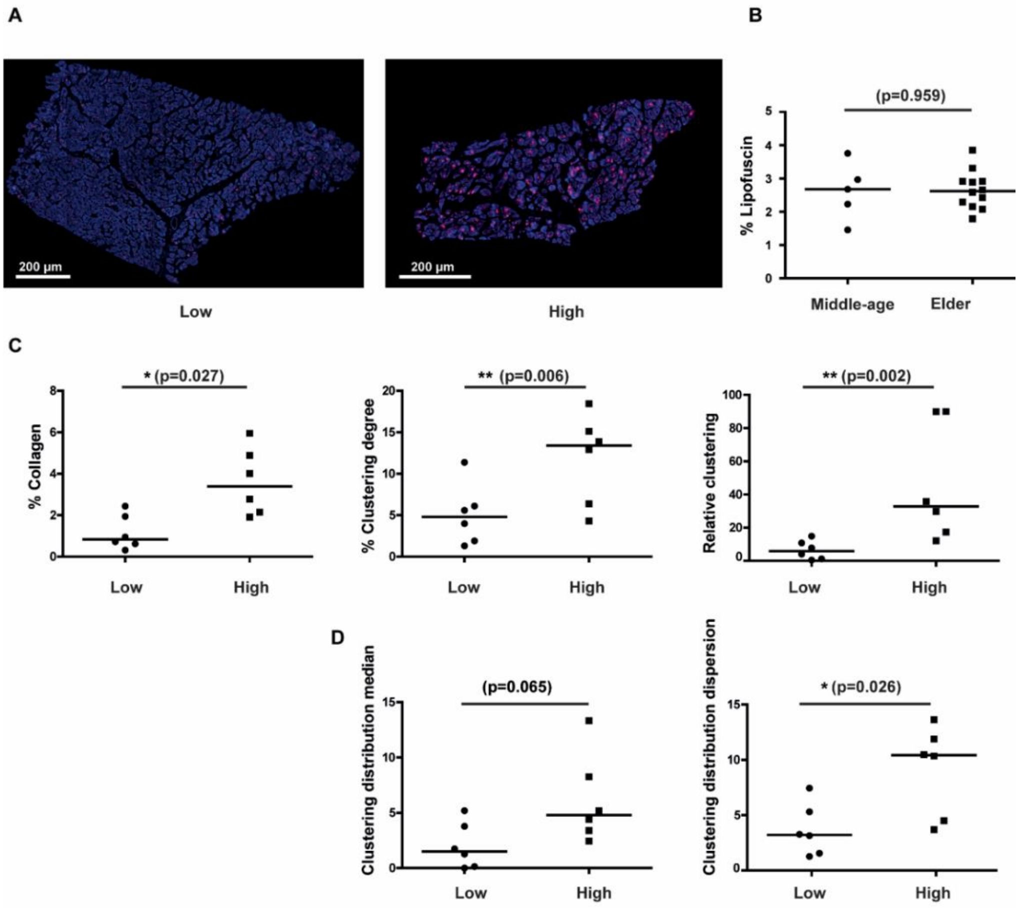

Figure 36. Quantification of lipofuscin amount in human LV sections. A) Representative images of human LV tissue sections from individuals with low (left) and high (right) lipofuscin content. **B)** Lipofuscin content in middle-age versus elder humans. **C)** Comparison of collagen amount (left), clustering degree (middle) and relative clustering (right) between individuals with low and high lipofuscin content. **D)** Quantification of clustering distribution median (left) and clustering distribution dispersion (right) of collagen aggregations in middle-age to elder individuals. In comparison between groups black lines represent the median. Non-parametric Mann-Whitney test is used, and p-values (p) are shown.

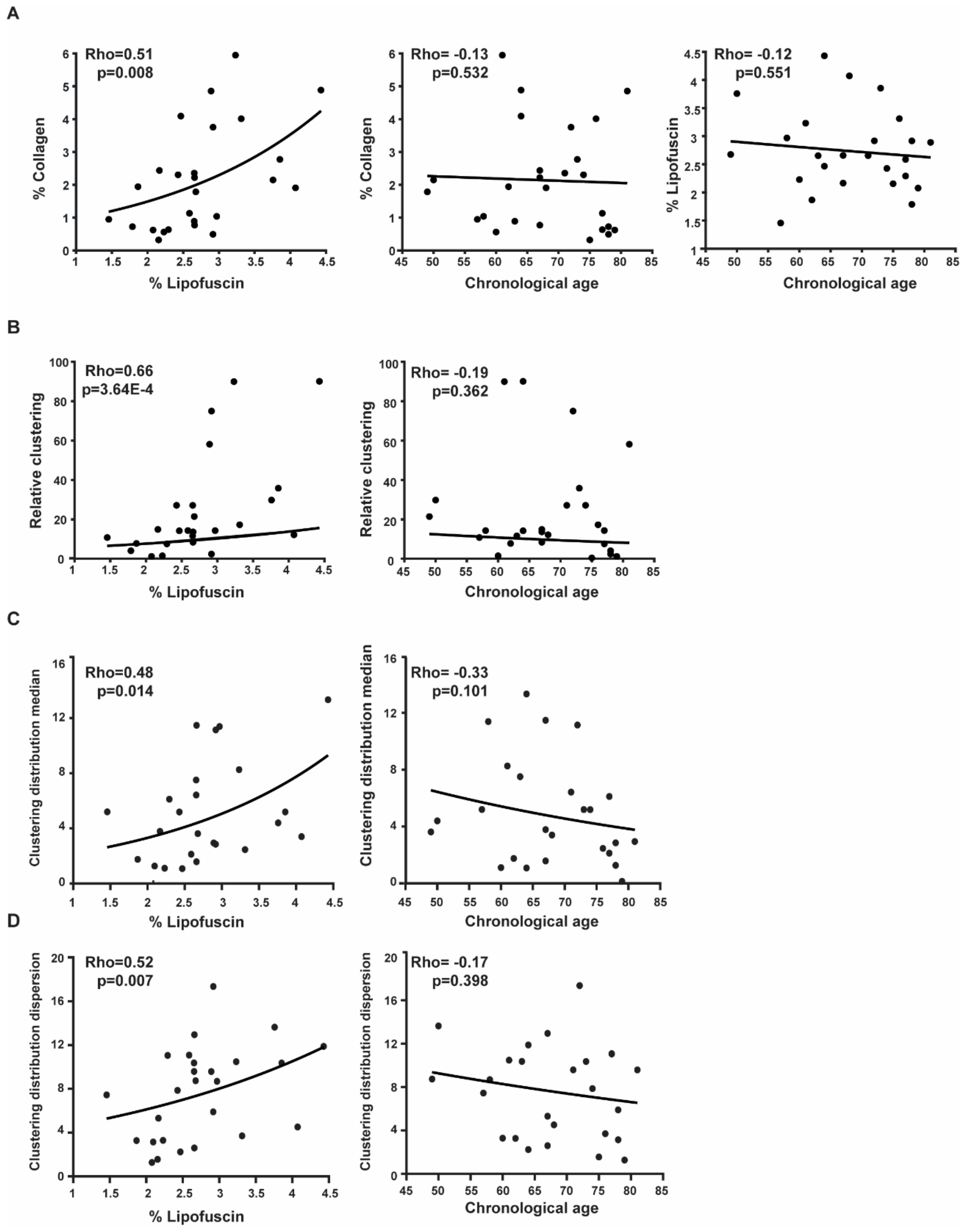

Figure 37. Correlation of collagen amount, aggregation and spatial distribution versus both age markers. A) Correlation between collagen and lipofuscin (left), between collagen and chronological age (middle), and between chronological age and lipofuscin (right). **B)** Correlation between relative clustering and each of the two age markers, lipofuscin (left) and chronological age (right). **C)** Correlation between clustering distribution median and lipofuscin (left) or chronological age (right). **D)** Correlation between clustering distribution dispersion and lipofuscin (left) or chronological age (right). For correlations Spearman non-parametric test is used and correlation coefficients (Rho) and corresponding p-values (p) are shown.

As per the spatial distribution of collagen aggregation, individuals with high-lipofuscin content had nearly significantly higher values for the clustering distribution median (median [IQR]: 4.40% [3.16%-7.23%]) in comparison to individuals with low-lipofuscin content (median [IQR]: 1.26% [0.10%-2.61%]), and significantly higher clustering distribution dispersion (median [IQR]: 10.35% [4.31%-12.31%] in comparison to individuals with low-lipofuscin content (median [IQR]: 3.14% [1.48%-4.31%]) (**Figure 36D**). Thus, with increased BA a higher degree of collagen aggregation and spatial dispersion of aggregation was found.

To further investigate the relationship between collagen features and both age markers, CA and lipofuscin, Spearman correlation analysis with the full set of human samples was performed (**Figure 37**). The percentages of collagen and lipofuscin were significantly correlated, while the correlation of each of them with CA was not significant in this cohort (**Figure 37A**). Although there is extensive literature evidence that collagen accumulates with age, the data for mid to late life age range indicated that collagen content correlated better with the age-pigment lipofuscin than with CA in humans (**Figure 37A**). The same is true for the relative clustering of collagen and its spatial distribution (**Figure 37B-D**).

4.3.4 Collagen alterations associated with age play a major role in ventricular electrical propagation and pro-arrhythmicity

The following step was to understand how the amount, aggregation and distribution of age-related collagen could influence the propagation of the electrical impulse in LV myocardium through *in silico* simulations. Therefore, we used the collagen and tissue masks obtained from the analysis of the SHG images from donors to build two-dimensional computational tissue models in which each node of the corresponding tissue mesh was assigned collagen or myocardial properties based on these two masks (**Figure 38A**).

Images from patients with five different degrees of collagen (1%, 2.5%, 4%, 5% and 6%) were used. Two-dimensional computational models were built, and the vulnerability window (VW) was quantified compared to the control condition (without fibrosis) and after varying the spatial distribution from patchy fibrosis, as observed in the patient, to diffuse fibrosis, simulating random scattering, but keeping constant the collagen percentage between both distributions (**Figure 38B**). The VW is defined as the time interval where, if a premature stimulus is delivered, it can lead to a reentrant arrhythmia. For simulated tissues with diffuse fibrosis, a low VW length for 1% fibrosis was observed, which was increased for collagen percentages ranging from 2.5% to 6% (**Table 21**). For simulated tissues with patchy fibrosis, high variability in the VW length was observed, with no consistent pattern of VW length increase or decrease with larger collagen percentage (**Table 22**). These results highlight not only the effect of collagen amount, but also of its distribution on arrhythmia vulnerability. VW difference quantifies the VW length in a diffuse or patchy fibrosis scenario with respect to the control scenario.

Table 21. VW characteristics for the diffuse scenario (uniformly randomly distributed).

Diffuse	% Fibrosis	VW length (ms)
Tissue 1	1%	7
Tissue 4	2.5%	16
Tissue 6	4%	14
Tissue 7	5%	15
Tissue 8	6%	18

Table 22. VW characteristics for the patchy scenario (image-based) based on patient-specific **images.**

Patchy	% Fibrosis	VW length (ms)
Tissue 1	1%	0
Tissue 2	1%	1
Tissue 3	2.5%	8.5
Tissue 4	2.5%	14
Tissue 5	4%	3.5
Tissue 6	4%	16.5
Tissue 7	5%	9
Tissue 8	6%	16.5

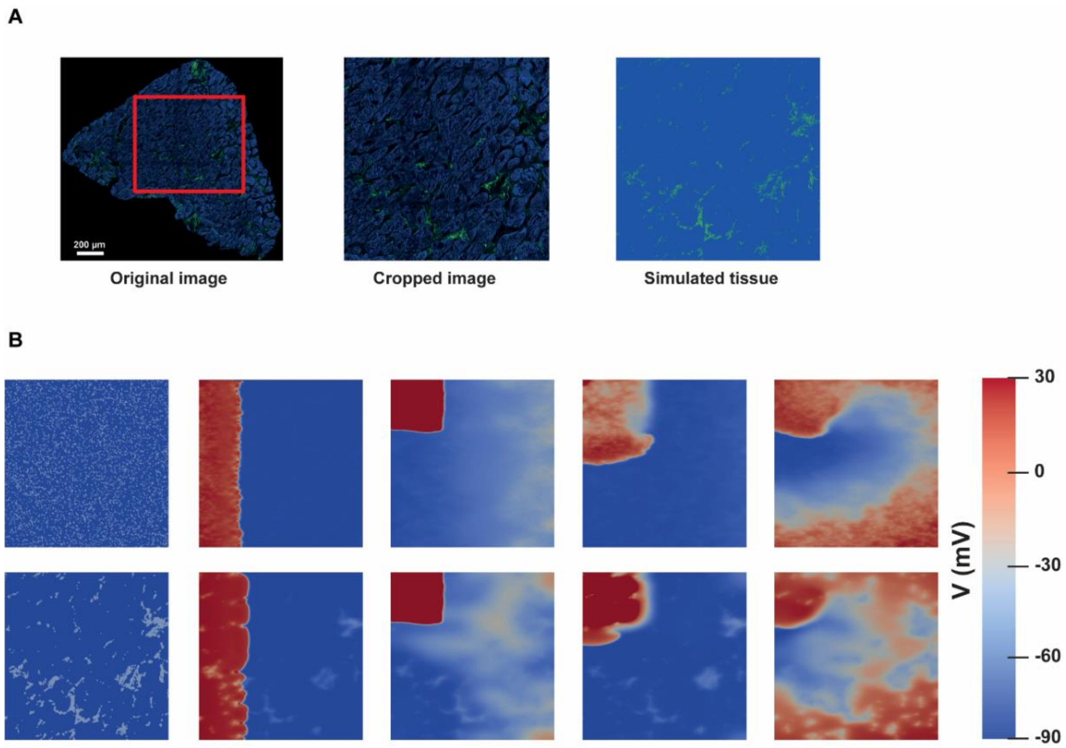

Figure 38. Assessment of changes in VW length in relation to age-related fibrosis in human LV samples. A) Original image from a patient (left), cropped imaged selected for the simulation (middle), and merge image of collagen and tissue masks used in the simulation (right). **B)** Spiral wave generation with S1-S2 cross-stimulation protocol for cases of diffuse collagen distribution (top row) and patchy collagen distribution (bottom row).

4.4 Discussion

4.4.1 Collagen remodeling from midlife onwards correlated with BA

In this work, SHG images of pig and human LV samples from living donors were collected and processed. An increasing tendency in LV myocardial collagen deposition with age in the two species was reported. The degree of collagen clustering and its spatial dispersion increases from young age to adulthood, but not from adulthood to old age in pigs and not from middle-age to old age in humans. All the studied collagen features correlate with BA better than with CA. Using computational modeling and simulation of two-dimensional human ventricular tissues based on patient-specific SHG images, it was shown how age-induced changes in collagen content and organization can contribute to pro-arrhythmicity.

The tendency to higher LV collagen content in old versus young pigs agrees with the established association of increased collagen deposition with age in animal models [391]. Specifically in pigs, these results agree with reported larger degrees of interstitial fibrosis in the LV and septum in mini-pigs with Hutchinson-Gilford progeria syndrome as compared to controls [334]. In the human LV, a moderate trend towards higher collagen content in elder (median: 1.72%) versus middle-age (median: 1.04%) individuals was found. Despite extensive research in animal models, there is a paucity of studies in the literature quantifying changes in collagen percentage in the human LV with aging. One study using Picrosirius staining and polarized filters on autopsy samples from the esternocostal region of the LV showed increased collagen content in elder (67-87 y.o., n=6, mean: 5.92%) versus young (20-25, n=6, mean: 3.86%) individuals with no previous pathology [72]. Similar results with comparable age ranges were described in another study using Picrosirius red staining too [73]. These results, obtained with a more sensitive technique and automated quantification, are in line with these findings even if the collagen amounts reported in this work are smaller, likely due to the higher specificity of SHG for collagen detection over histological techniques. Also, collagen III is likely to not be detected properly with this image acquisition setup due to its low intensity SHG signal, but this would be systematic in these data. However, in the human age ranges analyzed here, such differences are not statistically significant, similarly to the comparison of adult and old pigs. Only when comparing to young animals, the age-related differences become borderline significant. Altogether, this study supports increased collagen deposition with advanced CA in both human and pig LV, which is accompanied by higher inter-individual variability in the elder.

Distinct forms of fibrosis exist that act through different mechanisms: replacement fibrosis, which repairs damaged areas found e.g., after myocardial infarction, or reactive fibrosis, a fine fibrosis that is generally present perivascularly or in the interstitium. Reactive interstitial fibrosis has a diffuse aspect while replacement and perivascular fibrosis are patchier. These types of fibrosis can coexist and classification of the predominant type of fibrosis is capital to develop potential curative treatments or to predict fibrosis-related arrhythmia risk [392]. The global increase in collagen deposition in pigs is chiefly accounted by non-clustered one (**Figure 34D**), thus diffuse interstitial fibrosis, but it is accompanied by raised patchy fibrosis that increases its spatial dispersion as the level of clustered collagen elevates. This collagen dynamics agree with what would be expected for a chronic fibrotic process like aging and with what is known from animal models [67]. In the human LV, similarly to the porcine LV, most of the collagen is not clustered both for middle-age and elder groups and the relation between increased spatial dispersion and raising clustering is also verified. These results are novel in quantifying the degree of LV fibrosis being clustered and non-clustered with age in humans and in a clinically relevant large animal model like the pig. The parallelism observed between humans and healthy farm pigs (particularly, middle-age and elder humans, and adult and old pigs) for all evaluated collagen features could experimentally support the use of pig to investigate the effects of LV fibrotic remodeling with natural aging.

In humans, high inter-individual variability in the collagen content in the analyzed age groups is observed, but even higher in the elder group. Since all the biopsies were collected from the same LV region and transmural depth, regional differences are not expected to contribute to the observed variability. In addition, previous studies have shown similar collagen content among LV regions and from the inner to the outer layers of the LV wall in normal human hearts [393]. Thus, this work postulated that inter-individual differences in the aging rates could help to better explain the observed variability in the relationship between fibrosis and CA. All the collagen parameters were more remarkably correlated with the lipofuscin percentage than with CA. Thus, the histological BA better represents structural remodeling in the human LV as compared to CA. Unfortunately, this relationship in pigs could not be investigated since lipofuscin was not detectable by either autofluorescence or hematoxylin-eosin staining. Even if hematoxylin-eosin staining is not specific for lipofuscin detection, clear brown perinuclear aggregates could be observed in human samples but not in pig ones. Lipofuscin aggregates have been found in swine brain [394], but, to the best of my knowledge, there are no reports indicating its presence in porcine LV myocardium. Thus, in humans, the use of lipofuscin as a biological indicator of age in middle-age to elder individuals is suggested as an improved descriptor of LV fibrotic remodeling as compared to CA.

4.4.2 Role of fibrosis content and distribution on arrhythmogenicity

Next, the role of age-induced accumulation of collagen in the LV in promoting cardiac arrhythmias was investigated, whose incidence is well known to increase in aged hearts, particularly from the sixth decade of life [385], [395], [396]. The association between increased fibrosis and arrhythmias, including ventricular tachycardia and ventricular fibrillation, has been well established in diseased hearts [397]–[400]. This promotion occurs both by altering cardiac conduction and thus facilitating reentry as well as by modulating the formation of early afterdepolarizations leading to triggered activity [76]. In aged hearts, fibrosis has been shown to act as a substrate that, together with a mild form of stress, can cause arrhythmias, which would not otherwise occur in non-fibrotic hearts subjected to the same stress [76], [401]. It should be noted, however, that most of these studies on age-induced fibrosis and arrhythmias have been conducted in small animals, possibly due to the difficulty in obtaining human LV samples from non-diseased myocardium. This work used the results of the experimental characterization to feed computational models of ventricular electrophysiology by translating the tissue geometry and collagen amount and organization from the human LV samples into the 2D meshes used in the simulations. Although other studies have evaluated the effect of fibrosis amount and spatial scattering on ventricular electrophysiology by using different fibrosis distributions [402], this work built tissue models representative of a set of tissue geometries, collagen amounts and distributions corresponding to these analyzed SHG images obtained from living donors rather than assigning generic collagen distributions not specific of individual patients. This work reported that in the human LV, not only the total amount of fibrosis, but also its spatial distribution are fundamental factors in determining arrhythmia vulnerability, in accordance with previous investigations [77], [370], [386]. In fact, when fibrosis was simulated in diffuse form and in the form of patches as in the SHG images, it was observed that the effects on VW were different for these two forms even if the total amount of fibrosis was kept constant. These findings are in agreement with studies reporting an impact of intermediate, but not of very mild (below 4%) or severe (above 40%) fibrosis in arrhythmia propensity [403]–[405], even if this work reported a substantial increase in VW length for fibrosis percentages above 2.5%.

In the realistic patchy fibrosis simulations, high variability between tissues was observed highlighting not only the effect of collagen amount, but also of its distribution on arrhythmia vulnerability. The differences between diffuse and patchy distribution, even if the collagen percentage was kept constant, underline the value of performing patient-specific simulations based on real distributions and not using generic collagen distributions that, although useful, can lead to partially different conclusions. Taken together, this work adds to previous evidence on the potential of LV myocardial fibrosis as an indicator of adverse pro-arrhythmic outcomes [76], [81], [399] with particular emphasis in this study on age-associated effects in the human heart. Fibrosis characterization at microscopic levels, which remains so far very limited for the human LV, and the potential of the performed patient-specific computational simulations are major contributions from this work.

4.5 Conclusions

This work validated that collagen content, clustering and spatial distribution can be analyzed using SHG microscopy and automatic processing methods that avoid discrepancies between observers and yield higher specificity and resolution than cardiac imaging techniques used routinely. Even though SHG cannot be used in the clinical context as an *in vivo* imaging tool, it has the potential to render new insights at the molecular and histological levels that could advance the medical practice. For example, as reported here, it is technically feasible to obtain transmural tissue biopsies from living donors where SHG in combination with lipofuscin content could aid in establishing basic features of age-related cardiac remodeling that, even if quantified by other methods, could eventually be used in patient management strategies. Although age-related collagen dynamics has limited relation with CA in mid to late life, this work have shown that it is more closely related to lipofuscin, which highlights the use of BA markers in age-associated cardiac fibrosis research, particularly in clinically relevant age ranges. By integrating the results of processing SHG images into *in silico* two-dimensional electrophysiological models, tissue simulations show the value of collagen amount and distribution as risk indicators for cardiac arrhythmias. Additionally, to the study on human LV tissues, this study highlights the pig as a suitable model of age-related LV structural remodeling over natural chronological aging.

Chapter 5

Inter-individual age-independent differences in human CX43 impact ventricular arrhythmic risk

This chapter has been partially adapted from the submitted manuscript entitled "Inter-individual age-independent differences in human CX43 impact ventricular arrhythmic risk" by García-Mendívil✉ and colleagues [406].

5.1 Introduction

Gap junctions, formed predominantly by CX43 in the ventricular myocardium, are intercellular communication structures that, in the heart, are primarily located at the intercalated disks connecting longitudinally adjacent cardiomyocytes. With lower density, gap junctions can also be found in the lateral borders of cardiomyocytes. They mediate the electrical cell coupling needed for the transmission of the electrical excitation, which normally propagates with higher CV in the direction of the longitudinal axis of cardiomyocytes than in the transverse one [407].

Altered Cx43 expression and/or distribution can affect ventricular electrical coupling and can lead to impulse conduction abnormalities and arrhythmias, particularly when combined with additional structural and functional changes associated with pathological remodeling or aging. In humans, altered CX43 patterns have been reported in atrial fibrillation, heart failure, dilated cardiomyopathy or left ventricular hypertrophy [88], [90], [408]. Animal models with reduced Cx43 expression have been used to assess the effect of Cx43 on CV. Some studies have shown unaltered CV [409], [410], whereas others have reported significantly lower CV [411], [412] with diminished Cx43 expression. Studies in mouse models with conditional cardiac knock-out of Cx43 or heterogeneous expression of CX43 have reported an association between decreased Cx43 and arrhythmia generation [413], [414]. These and other *in vivo* studies have suggested that not only the amount of Cx43 content but also its spatial distribution in the tissue is important for arrhythmia generation [413], [415], [416]. In fact, the spatial distribution of CX43 has been correlated with the presence of ventricular arrhythmia in patients with chronic heart failure [415]. Also, the CX43 distribution within cardiomyocytes has been related to arrhythmic risk. Seidel and colleagues [89] have reported a significant increase in the lateral CX43 accompanied by a significant augment in the transversal CV in human atrial fibrillation, suggesting that CX43 lateralization could also have a proarrhythmic effect.

Age-related alterations in Cx43 characteristics have been investigated using animal models, with divergent results depending on the animal species and the compared age groups. A decrease in Cx43 content, expressed as percentage of Cx43, has been reported in aged or adult mice [92], [93] and rats [97] compared to young. Besides, an age-related reduction in Cx43 expression levels has been described in mice [92] and rats [96]. Regarding Cx43 lateralization, only Dhein and colleagues [94] reported an increase in aged versus young rabbits. In humans, however, studies of CX43 changes with age, in terms of percentage, expression, location within cardiomyocytes and spatial distribution in tissue, and of their effects on cardiac function are lacking.

Cardiomyocytes in the LV are embedded in the extracellular matrix which provides tissue strength, cell support and allows cell-to-cell contact [82]. Age has been associated with increased extracellular matrix deposition, both in animal and human LV [73], [292] as it has also been reported in Chapters 2 and 4. This increased deposition modifies the electromechanical function of the heart and increases the vulnerability to arrhythmia [67], as also reported in Chapter 4. The observations that cardiac aging is associated with decreased Cx43 and increased fibrotic content have led to postulate a relationship between the two [417], [418]. Using aged mice with 100% or 50% Cx43 expression, more pronounced fibrosis levels in the 50% Cx43 expression aged mice were observed [419]. There is no description of this interaction with age in humans, however. Alterations in Cx43 expression or fibrosis formation can increase arrhythmia predisposition [407], [420], as cardiac impulse propagation requires a fine interplay between electrical coupling, cardiomyocyte excitability and tissue architecture. Increased fibrosis, which alters impulse propagation due to the distinct properties of the replacement tissue compared to the normal myocardium [77], [421], has been associated with enhanced arrhythmic risk in human hearts both in the presence of disease [397], [400] and in relation to aging as reported in Chapter 4. Although mouse models have suggested a possible interplay between decreased Cx43 and fibrosis accumulation in arrhythmogenesis, proposing that both factors are required for the generation of arrhythmias [422], [423], the implications that this may have in humans is yet unclear.

In this chapter, a thorough characterization of CX43 dynamics with age in the human LV is presented and the relationship with fibrosis accumulation in a population of middle-aged to old individuals is evaluated. This research is performed in relation to CA, but also in relation to lipofuscin, as a measure of BA that better resolves the effects of aging [49]. The better resolution of lipofuscin than CA has also been reported in Chapter 4. Next, the experimental results are feed to computational models of human LV electrophysiology, and the effects of alterations in CX43 and fibrosis characteristics on arrhythmia vulnerability are assessed. .

5.2 Methods

5.2.1 Collection and processing of left ventricular tissues

A total of 44 human transmural LV tissue specimens were collected at Hospital Universitario Miguel Servet (Zaragoza, Spain) as described in Chapter 2 and processed for histological analysis as described in Chapter 4. Also, the clinical characteristics of the patients were the same as in Chapter 2. For comparison purposes, two age groups were established: the youngest individuals formed the middle-aged group (50-59 y.o., n=8) and the oldest individuals, the elder group (77-84 y.o., n=8). Samples from all individuals were used for correlation analysis.

5.2.2 Fluorescent immunohistochemistry staining

Tissue sections were stained following standard immunohistochemistry protocols. Briefly, samples were deparaffinated by two washes with xylol and four steps with ethanol 100%-100%-96%-70%. Samples were rehydrated first with tap water followed by distilled water before antigen retrieval with citrate buffer for 30 minutes. Then, samples were blocked for 1h with Protein Block Serum-Free (X090930-2, Agilent, USA). Primary antibodies incubation was performed at 4°C overnight and, after three washes with 0.5% BSA-PBS, secondary antibodies incubation was performed for 1h at room temperature in darkness. Primary antibodies were mouse monoclonal anti-SERCA2 (1:1000, ab2817, Abcam, UK) and rabbit polyclonal anti-CX43 (1:1000, ab11370, Abcam, UK). Secondary antibodies were Alexa Fluor 488 goat anti-mouse (1:1000, A11029, Thermo Fisher, USA) and Alexa Fluor 633 goat anti-rabbit (1:1000, A21071, Thermo Fisher, USA). The extracellular matrix was stained with Alexa Fluor 555 wheat germ agglutinin (WGA) (1:500, W32464, Thermo Fisher, USA). To reduce variability, a single mix for primary and secondary antibodies and washing buffer was prepared and all sections were stained simultaneously.

Images were acquired with a confocal microscope Zeiss LSM 880 (Carl Zeiss, Germany) and the parameter settings for the imaging were kept constant for all the samples.

5.2.3 Label-free imaging of lipofuscin and tissue autofluorescence

For each individual, a serial section of the one used for the multiple fluorescent immunohistochemistry was used for the label-free imaging of tissue autofluorescence and lipofuscin. The acquisitions were performed with a confocal microscope Zeiss LSM 880 (Carl Zeiss, Germany) and all the parameter settings were kept constant between samples. The wavelength used for excitation and detection of the tissue autofluorescence was 488 and 499-533 nm, respectively. For lipofuscin, excitation was at 633 nm and emission at 650-735 nm.

5.2.4 Image analysis

The procedure followed for the analysis of CX43, fibrosis and lipofuscin characteristics was the following. Two independent observers performed all image processing and quantification analysis. Each observer established the thresholds for the generation of binary masks, from which computations were performed automatically to compute CX43, SERCA2, WGA, tissue autofluorescence and lipofuscin characteristics. All the results reported along the manuscript correspond to the average results from the two observers.

<u>Quantification of the total amount of CX43 and the percentage of lateralized CX43</u>

Original CZI images were handled with ZEN Blue 2.5 software (Carl Zeiss, Germany). The maximum intensity projections were generated using all planes of the SERCA2, WGA and CX43 z-stacks. The resulting images were exported as 8-bit raw-TIFF individual images. These were processed for automatic brightness scaling using ImageJ [387] and for removal of isolated image segments (fluorescence artifacts or areas of clear perivascular fibrosis, among others). Next, images were analyzed with the semiautomated open software MARTA [349] to quantify the amount and degree of lateralization of CX43. Briefly, the software MARTA used the separate channels of SERCA2, CX43 and WGA of each individual as TIFF images. Binary masks for CX43 were generated by applying erosion and dilation operations and by establishing a threshold in the CX43 histogram to separate the CX43 signal from the background [349]. Analogously, binary masks for SERCA2 and WGA were generated from the automatically adjusted, gray-level SERCA2 and WGA images by applying a binarization filter.

The amount of CX43 was estimated using two different approaches. In the first approach, the percentage of CX43 is quantified with respect to the area of the cardiomyocytes, according to the SERCA2 mask as:

$\%CX43_{CM}$ = number of positive CX43 pixels x 100 / number of positive SERCA2 pixels

In the second approach, the percentage of CX43 is quantified with respect to the entire left ventricular tissue, which was determined from the SERCA2 and WGA masks, with pixels being positive in both masks counted only once. The percentage of CX43 was calculated as:

$\%CX43_{T}$ = number of positive CX43 pixels x 100 / (number of positive SERCA2 and WGA pixels*)

* Pixels being positive in both masks counted only once

For quantification of CX43 lateralization, the software MARTA delimited the cardiomyocytes using the SERCA2 and WGA signals [349]. Next, each identified cardiomyocyte was divided into four rectangles and MARTA quantified the amount of CX43 in the two middle areas of the cardiomyocyte (i.e., the lateral sides) with respect to the total amount of CX43 in the cardiomyocyte (**Figure 39A**). MARTA performed this analysis automatically for every cardiomyocyte detected in the tissue section. For each individual, a percentage of CX43 lateralization ($\%CX43_{LAT}$) was computed as the average value of the measures in all detected cardiomyocytes. Based on previous studies [88], [90], [94], $\%CX43_{LAT}$ was estimated only in tissue samples with primary longitudinally oriented cardiomyocytes (31 out of 44). In addition, an inclusion criterion was applied for $\%CX43_{LAT}$ calculation in each tissue sample: only cardiomyocytes confirmed by the observer to be longitudinally oriented were accepted. The set of 31 samples was divided in fifths for the comparison of age groups, with 6 donors in each of the CA-based groups, middle-age (54-60 y.o.) and elder (76-84 y.o.), and in each of the BA-based groups (lowest and highest lipofuscin content).

Quantification of CX43 expression levels

CX43 expression level was quantified in the 16-bit raw-TIFF CX43 images exported from Zen Blue 2.5 using in-house MATLAB code but only in the positive pixels of the CX43 binary masks generated by the software MARTA obtained in the previous section. As above, two approaches were used to measure CX43 expression level: relative to the cardiomyocyte area and to the total tissue area (including interstitial tissue). In the first approach, the CX43 expression level was calculated as:

$CX43_{E\text{-}CM}$ = sum of intensities of positive CX43 pixels / number of positive SERCA2 pixels

In the second approach, the CX43 expression level was made relative to the sum of positive SERCA2 and WGA pixels to account for the whole LV tissue:

$CX43_{E\text{-}T}$ = sum of intensities of positive CX43 pixels / (number of positive SERCA2 and WGA pixels*)
* Pixels being positive in both masks counted only once

Quantification of CX43 heterogeneity

CX43 heterogeneity ($CX43_H$) was quantified using in-house MATLAB code implementing the method proposed by Boulaksil [415]. The method departed from the CX43 binary mask generated by the software MARTA and calculated, for each positive CX43 pixel, the shortest distance to the next positive CX43 pixel in a virtual circle around that pixel. The standard deviation of all shortest distances of all pixels was used as a measure of $CX43_H$.

Quantification of fibrosis percentage

Fibrosis quantification was performed using WGA staining [424], as in previous studies evaluating cardiac fibrosis [425]. Image analysis was based on the approximation for collagen quantification using non-linear optical microscopy described in Chapter 4. Briefly, taking the above described SERCA2 and WGA binary masks as an input, an in-house MATLAB code was used to compute the number of positive WGA pixels not positive in the SERCA2 mask. Then the following formula was applied to calculate the percentage of fibrosis:

%Fibrosis = number of pixels only positive to WGA x 100 / (number of positive SERCA2 and WGA pixels*)
* Pixels being positive in both masks counted only once

Quantification of lipofuscin content

For lipofuscin quantification, original CZI images from all donors were handled with ZEN Blue 2.5 software. Both lipofuscin and tissue autofluorescence signals were exported as raw 16-bit TIFF images and were processed with ImageJ. For tissue autofluorescence, images were adjusted to remove the 0.2% of the highest and lowest values of the histogram. Image adjustment for lipofuscin quantification was determined empirically after revising all the samples of the study, and finally only the range 0-3500 of the histogram was used for image analysis. From the obtained gray-scale images, a threshold was established, and binary masks were generated. Lipofuscin content was calculated using in-house MATLAB software as:

%Lipofuscin = number of positive lipofuscin pixels / number of positive tissue autofluorescence pixels

5.2.5 *In silico* modeling and simulation of ventricular electrical activity for varying CX43 characteristics and fibrosis percentage

To assess the impact of CX43 features and the amount of fibrosis on cardiac electrical activity, two-dimensional computational tissue models of human ventricular electrophysiology were feed with the experimental characterizations. A 3x3cm^2 mesh in which all the mesh nodes were assigned with the electrophysiological properties of epicardial cells except for three islands composed of nodes with the electrophysiological properties of midmyocardial cells was built. As in Chapter 4, the O'Hara-Rudy model was used to describe the human ventricular AP for the two types of cells [8]. A control scenario was defined in which the longitudinal diffusion coefficient was set to 0.0013 cm^2/ms [403] and the transverse-to-longitudinal conductivity ratio was set to 0.19, with this ratio corresponding to the median value of CX43 lateralization in the population.

To model variations in the content of CX43 (%CX43$_{CM}$), the longitudinal diffusion coefficient was varied. The value 0.0013 cm^2/ms was assigned to the median of the middle-aged group and simulations with a 10%, 20%, 30% and 40% reduction in the longitudinal conductivity of the tissue based on the experimental data were performed. This was based on the fact that the elder had, in median, 10% lower %CX43$_{CM}$ compared to the median of the middle-aged group, the high lipofuscin individuals had, in median, a 20% reduction in %CX43$_{CM}$ in comparison with the low lipofuscin individuals, high lipofuscin individuals had 30% lower %CX43$_{CM}$ than the middle-age and the case of 40% decrease corresponded to the lowest %CX43$_{CM}$ in the population compared to the median of the middle-aged group. To model variations in the degree of CX43 lateralization (%CX43$_{LAT}$), the transverse-to-longitudinal conductivity ratio were varied. The median of %CX43$_{LAT}$ in the population, 19%, was set as the control value. Simulations with ratios of 0.23, 0.27, 0.31 and 0.35 were performed, as these values cover the range from the median to the highest value of the population. To model variations in the percentages of fibrosis, some of the tissue elements were assigned with electrophysiological properties of fibroblasts using a uniform random distribution. The AP of the fibroblasts was represented by the MacCannell model of mammalian ventricular fibroblasts described in Chapter 1 [9]. 7%, 11%, 15% and 19% fibrosis based on the experimental data were simulated. 7% corresponds to the median of the low lipofuscin individuals and 11% to the median of the high lipofuscin ones. 15% is an intermediate value and 19% is the maximum fibrosis percentage in the population. The longitudinal conductivity between fibroblasts or between myocytes and fibroblasts was set to be three times lower than the conductivity between cardiomyocytes.

To evaluate the impact of variations in CX43 characteristics and fibrosis deposition on CV and APD, a train of stimuli in a region at the left side of the tissue and the middle of the mesh with a size of 120x20 nodes were applied. The stimuli had an amplitude of twice the diastolic threshold, a duration of 2 ms duration and were delivered at a cycle length of 1000 ms. For each of the simulated scenarios, the CV magnitude and the APD were evaluated. CV was determined using a previously reported method [426]. The APD was calculated by measuring the elapsed time between the activation, defined as the time occurrence of the maximum derivative of the action potential upstroke, and the time for 90% repolarization.

5.2.6 *In silico* assessment of arrhythmic risk for varying CX43 characteristics and fibrosis percentage

Next, the role that different CX43 characteristics and fibrosis percentages play on arrhythmic risk was assessed. For that purpose, the repolarization gradient and the VW for the highest changes in diffusion (DIF 40%), lateralization (LAT 0.35) and fibrosis (FIB 19%) and the combinations of two or three of these factors were evaluated. From the simulations described in the previous section, the repolarization gradient was estimated, for each pixel, using methods previously described in the literature in which a radius of one pixel was used in the computations [427]–[429]. For each simulated scenario, the percentage of tissue with a repolarization gradient higher than an empirically established threshold of 9 ms/mm, named as areas of High Repolarization Gradient (HRG), was calculated. It should be noted that this measure is considered to be a metric of dispersion of repolarization and a surrogate for arrhythmic risk [427].

Additionally, the length of the VW as a measure of the likelihood for induction of reentrant arrhythmias was evaluated. 5x5cm^2 meshes were generated by rescaling the 3x3cm^2 meshes described above and the generation of spiral waves after application of an S1-S2 cross stimulation protocol was evaluated [388]. The stimulation protocol used in these simulations was the same reported in Chapter 4 with the only exception that in this study stimuli were only applied on the left side of the tissue, and not at the left and right side as reported in Chapter 4.

Further arrhythmic risk assessment was performed after including CX43 heterogeneity in the models. Two meshes with CX43 heterogeneity were obtained as follows. The tissue sample of an individual whose measure of CX43$_H$ was similar to the median of the middle-aged group was selected and, similarly, the tissue sample of an individual from the old group was taken. Based on the CX43 intensities of the sample, a histogram was constructed, and divided it into 20 bins. The intermediate bin was associated with the median of the histogram and was assigned the longitudinal diffusion coefficient set in control (0.0013 cm^2/ms). The 20 different values of longitudinal diffusion were assigned randomly to the nodes of the mesh according to the distribution given by the histogram. The sum of the longitudinal diffusion coefficients of all nodes was kept constant between the three meshes: the one without heterogeneity in which the longitudinal diffusion coefficient was constant, and the two with heterogeneity representative of the middle-aged and old groups. Regarding VW, its length and the increment in VW length after including CX43 heterogeneity with respect to the corresponding scenario without heterogeneity were calculated. Specifically, the increment was calculated by dividing the VW length of the scenario with heterogeneity by the same scenario without heterogeneity.

As described in Chapter 4, simulations were performed using ELECTRA, implementing the Finite Element Method and meshless methods [388], [389] for the solution of the cardiac monodomain model [389], [390] and the dual-adaptive explicit integration algorithm [390] was used to efficiently solve the monodomain model.

5.2.7 Statistical analysis

As described in previous chapters, Mann-Whitney test was used to assess differences between two independent groups and Spearman correlation analysis was used to test the strength and direction of association between two variables. The significance threshold was established by setting a p-value=0.05 for both Spearman correlation and Mann-Whitney test. Unless otherwise indicated, data are presented as median [interquartile range (IQR)].

5.3 Results

5.3.1 CX43 amount, expression level, lateralization and spatial heterogeneity present high inter-individual variability

To investigate CX43 dynamics with age in human myocardium, CX43-related features in transmural LV biopsies of 44 patients aged 50 to 84 years were quantified and their distribution in the population was characterized (**Figure 39B**). The amount of CX43 in relation to cardiomyocyte area (%$CX43_{CM}$) varied from 0.44% to 5.34% in the study population, with a median of 2.73% and high dispersion, as can be observed in the histogram. The CX43 expression level in cardiomyocytes ($CX43_{E\text{-}CM}$) ranged from 52.29 normalized fluorescence units (n.f.u.) to 1095.87 n.f.u., being 319.59 n.f.u. the median of the population. CX43 heterogeneity ($CX43_H$), measuring the non-uniformity of CX43 spatial distribution, spanned from 19.61 µm to 276.41 µm in the population, with a median of 19.2 µm. In a reduced set of donors (31 out of 44) whose LV tissue samples were oriented longitudinally, CX43 distribution within the cardiomyocyte was additionally evaluated. An index of lateralization that quantifies the average percentage of CX43 in the lateral (non-polar) sides of the cardiomyocytes in each individual was measured (%$CX43_{LAT}$) (**Figure 39B**) and renders information on the contribution to transverse conduction. %$CX43_{LAT}$ varied from 6.42% to 35.78%, with 18.78% being the median in the population (**Figure 39B**).

The amount of CX43 per cardiomyocyte area, %$CX43_{CM}$, significantly correlated with its expression level $CX43_{E\text{-}CM}$ (Rho=0.88, p-value<0.001), indicating that it is uniformly expressed across different tissue areas. $CX43_H$ did not correlate with either %$CX43_{CM}$ or $CX43_{E\text{-}CM}$ (**Figure 39C**). %$CX43_{LAT}$ did not correlate with any of the other CX43 features (**Figure 39D**).

5.3.2 CX43 characteristics are poorly related with chronological and biological age beyond midlife, with increased CX43 heterogeneity being the more distinctive feature in old age

Next, the relationship between CX43 traits (%$CX43_{CM}$, $CX43_{E\text{-}CM}$, $CX43_H$ and %$CX43_{LAT}$) and CA in the human LV tissue was investigated. There was no correlation between age and any of the four CX43 characteristics (**Figure 40A**). The lower and upper ends of the age range were compared, which corresponded to middle-aged and elder individuals in the population.

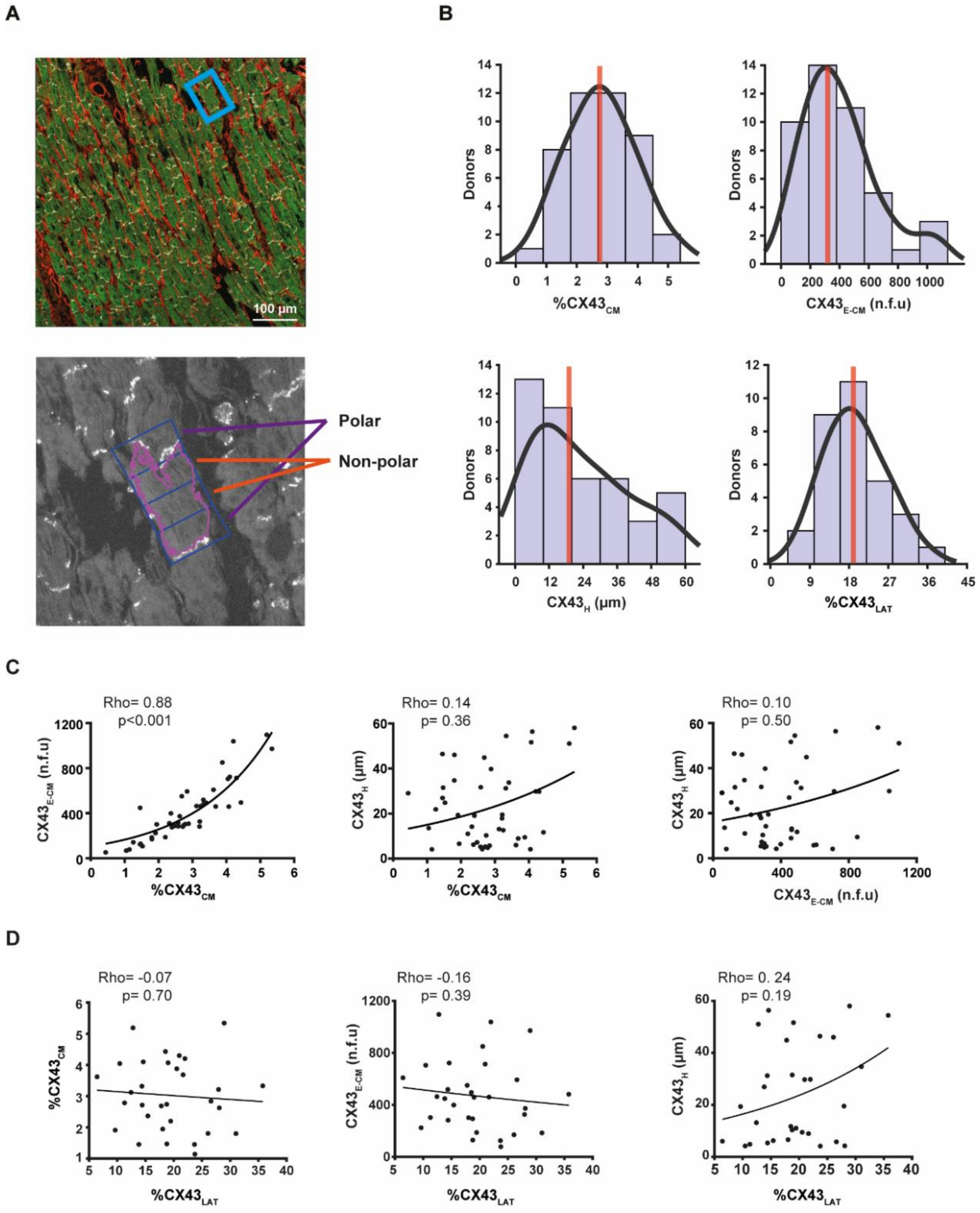

Figure 39. Quantification of CX43 features with respect to the cardiomyocyte area. A) Distribution of CX43 amount (%CX43$_{\mathrm{CM}}$), CX43 expression level (CX43$_{\mathrm{E\text{-}CM}}$), CX43 heterogeneity (CX43$_{\mathrm{H}}$) and CX43 lateralization (%CX43$_{\mathrm{LAT}}$) in the population. **B)** Fluorescence immunohistochemistry staining of CX43, SERCA2 and WGA in a LV tissue section (up) and a representative image of a cardiomyocyte identified and delimited in polar and non-polar zones by MARTA software (down). MARTA displays individual images for each detected cardiomyocyte. **C)** Correlation between CX43 amount and heterogeneity (left), CX43 amount and expression level (middle) and CX43 expression level and heterogeneity (right). **D)** Correlation between CX43 lateralization and CX43 amount (left), CX43 expression level (middle) and CX43 heterogeneity (right). Spearman correlation coefficients (Rho) and p-values (p) are shown.

A slight non-significant decrease in the %CX43$_{CM}$ was observed in the elder (median [IQR]: 2.7% [2.45%-3.13%], n=8) as compared to the middle-aged individuals (median [IQR]: 2.91% [2.43%-3.95%], n=8). Similarly, CX43$_{E\text{-}CM}$ did not change in elder (median [IQR]: 400.92 [282.55-571.68 n.f.u.], n=8) versus middle-aged individuals (median [IQR]: 386.44 [280.93-479.03 n.f.u.], n=8). CX43$_{H}$ median value increased by 45%, when comparing elder (median [IQR]: 21.96 [9.66-32.71 µm]) versus middle-aged individuals (median [IQR]: 12.16 [8.09-21.93 µm]), even if this difference did not reach statistical significance. No significant differences were either observed in %CX43$_{LAT}$ (median [IQR] in elder: 17.43% [14.41%-20.97%], n=6) versus middle-age (median [IQR]: 18.65% [14.37-21.66%], n=6) (**Figure 40B**).

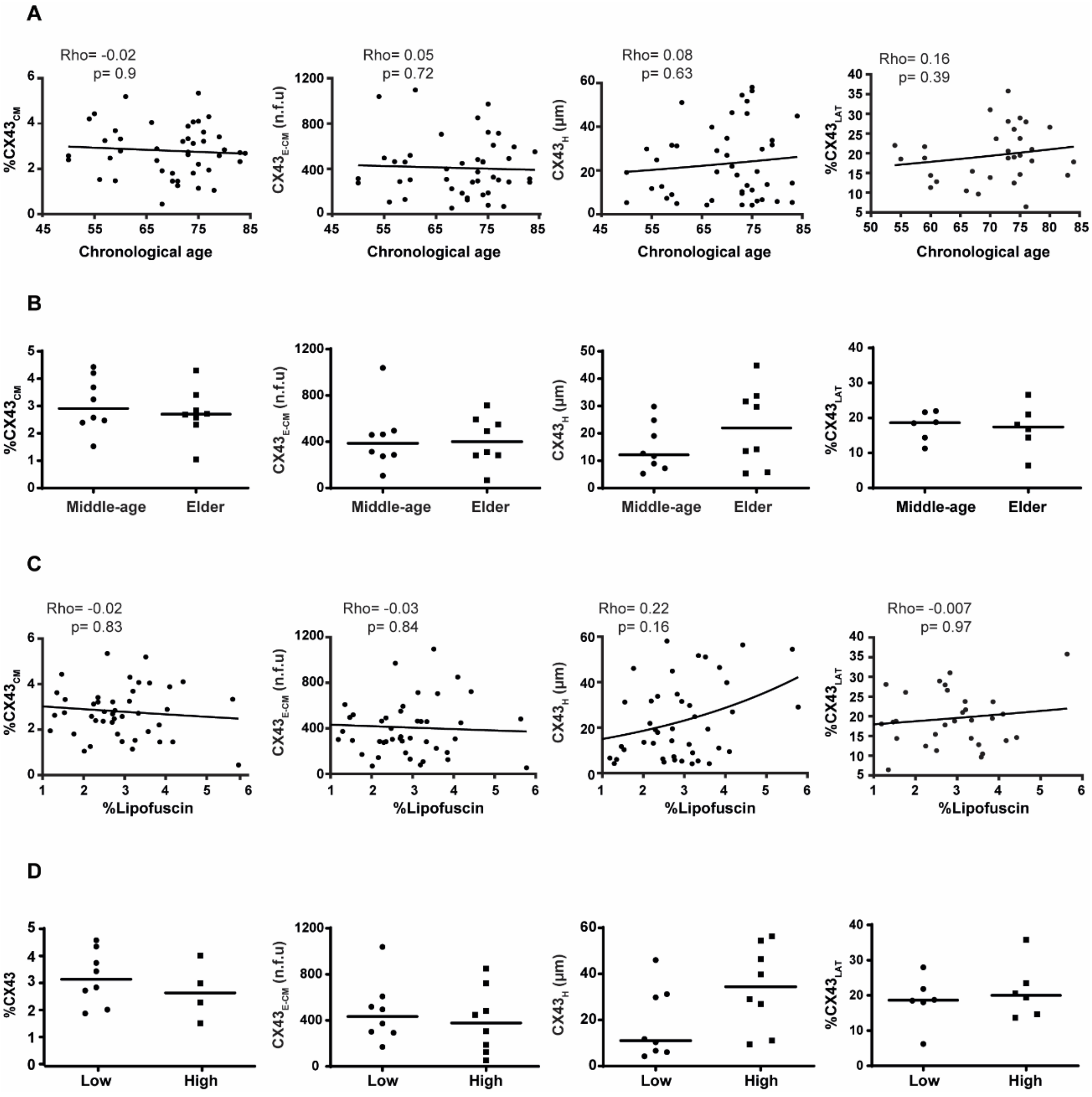

Figure 40. Characterization of CX43 dynamics with chronological and biological age. A) From left to right: correlation between age and CX43 amount (%CX43$_{CM}$), CX43 expression levels (CX43$_{E\text{-}CM}$), CX43 heterogeneity (CX43$_{H}$) and CX43 lateralization (%CX43$_{LAT}$). **B)** From left to right: comparison of %CX43, CX43$_{E\text{-}CM}$, CX43$_{H}$ and %CX43$_{LAT}$ in middle-aged versus elder humans. **C)** From left to right: correlation between lipofuscin and %CX43, CX43$_{E\text{-}CM}$, CX43$_{H}$ and %CX43$_{LAT}$. **D)** From left to right: comparison of %CX43$_{CM}$, CX43$_{E\text{-}CM}$, CX43$_{H}$ and %CX43$_{LAT}$ in low versus high

lipofuscin content individuals. In panels A and C Spearman correlation coefficients (Rho) and p-values (p) are shown. In panels B and D black lines represent the median.

To account for age-related effects beyond the mere temporal factor of CA, namely accounting for the effect of genetics and environment, CX43 characteristics as a function of the aging pigment lipofuscin were assessed. No correlation was either observed, with only $CX43_H$ being modestly but not significantly correlated with lipofuscin content (correlation coefficient of 0.22) (**Figure 40C**). When comparing groups representing the individuals with the lowest and highest amounts of lipofuscin, a non-significant 16% decrease in the median $\%CX43_{CM}$ in the high lipofuscin group (median [IQR]: 2.54% [1.45%-3.61%], n=8) versus the low lipofuscin group (median [IQR]: 3.03% [2.29%-3.91%], n=8) was observed, which was accompanied by a similar non-significant decrease of 13% in $CX43_{E\text{-}CM}$ in high lipofuscin individuals (median [IQR]: 377.52 [155.69-601.93 n.f.u.], n=8) in relation to individuals with low lipofuscin (media [IQR]: 433.75 [296.99-563.37 n.f.u.], n=8). The largest differences with BA were found for $CX43_H$, which presented a non-significant 68% increase in the high lipofuscin group (median [IQR]: 34.41 [18.97-50.43 µm], n=8) versus low lipofuscin group (media [IQR]: 11.01 [6.30-30.51 µm], n=8). Finally, a slight non-significant increase in $\%CX43_{LAT}$ in high lipofuscin group (median [IQR]: 20% [14.66%-23.53%], n=6) versus low lipofuscin group (media [IQR]: 18.64% [18.04%-21.86%], n=6) was observed (**Figure 40D**).

5.3.3 CX43 characteristics are not related to fibrosis accumulation beyond midlife

The percentage of fibrosis beyond midlife did not correlate with CA (correlation coefficient of 0.13), while it had a modest, non-significant relationship with cardiac BA (correlation coefficient of 0.2) (**Figure 41A**), in line with the results reported in Chapters 2 and 4. Furthermore, the relationship between CX43 characteristics and fibrosis deposition was investigated, since previous evidence suggests their interplay with age [419], [430]. No significant correlation between fibrosis content and any of the CX43-related traits, $\%CX43_{CM}$, $CX43_{E\text{-}CM}$, $CX43_H$ or $\%CX43_{LAT}$, was observed (**Figure 41B**).

In line with previous research evaluating CX43 quantity relative to the myocardial tissue area rather than to cardiomyocyte area, the relationship of CX43 with age in the whole tissue ($CX43_{E\text{-}T}$) was further characterized. Minor changes, with only slight, non-significant variations in $\%CX43_T$ and $CX43_{E\text{-}T}$ in elder versus middle-aged individuals were observed (**Figure 42A**). For the analysis based on BA, similar results were observed for $\%CX43_T$ and $CX43_{E\text{-}T}$, with somewhat more marked decreases in their median values in biologically old versus young individuals (**Figure 42B**). The relation of fibrosis with CX43 amount or expression level was also similar when CX43 quantity was measured by $CX43_{E\text{-}T}$ (**Figure 42C**).

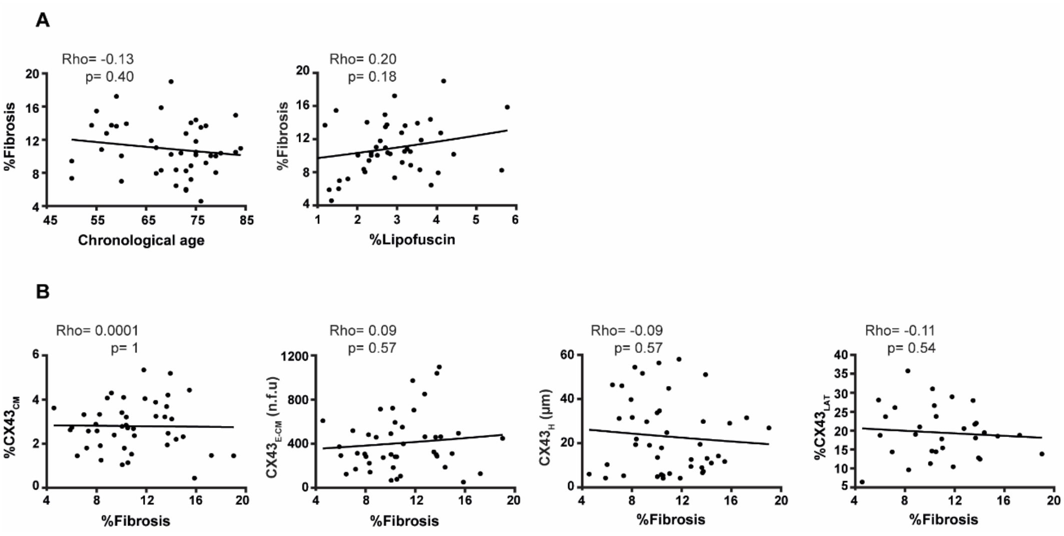

Figure 41. Characterization of CX43 remodeling in relation with fibrosis content. A) Correlation between fibrosis content and chronological age (left) and lipofuscin amount (right). **B)** Correlation between fibrosis and CX43 features: from left to right CX43 amount (%$CX43_{CM}$), CX43 expression levels ($CX43_{E\text{-}CM}$), CX43 heterogeneity ($CX43_H$) and CX43 lateralization (%$CX43_{LAT}$). Spearman correlation coefficients (Rho) and p-values (p) are shown.

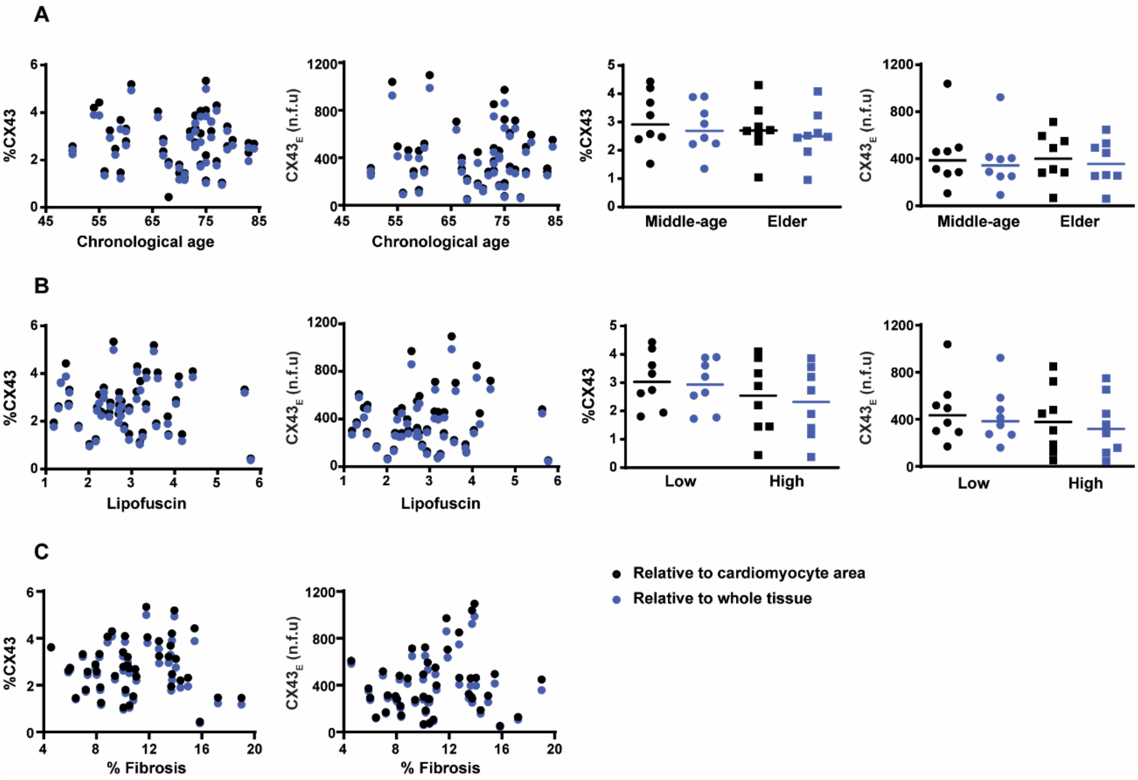

Figure 42. Comparison of the analysis of CX43 remodeling with respect to the cardiomyocyte area or the whole LV tissue. A) Correlation of CX43 amount (%CX43) and expression level ($CX43_E$) versus chronological age (the two leftmost panels) and quantification of %CX43 and

$CX43_E$ in middle-aged versus elder individuals (the two rightmost panels). **B)** Correlation of %CX43 and $CX43_E$ versus lipofuscin content (the two leftmost panels) and quantification of %CX43 and $CX43_E$ in low versus high lipofuscin individuals (the two rightmost panels). **C)** Correlation between fibrosis accumulation and CX43 amount (left) and expression level (right). Spearman correlation coefficients (Rho) and p-values (p) are shown. Black dots and squares correspond with the method with respect to the cardiomyocyte area, and blue dots and squares with the method with respect to the LV tissue.

5.3.4 CX43 characteristics and fibrosis deposition have marked effects on human ventricular electrical activity

In spite of the lack of evident age-related remodeling of CX43 in the middle-aged to old population, high inter-individual variability in the analyzed CX43 characteristics was observed. Thus, the effect of such inter-individual variability on cardiac electrophysiology was assessed. Computational models of human LV electrophysiology were built and simulations to assess how the amount (defined as $\%CX43_{CM}$), lateralization and heterogeneity of CX43 individually and/or in combination with the deposition of collagen could influence CV, action potential duration (APD) and arrhythmogenesis in the LV were run. Variations in CX43 expression levels were not simulated run, as $CX43_{E\text{-}CM}$ was highly correlated to $\%CX43_{CM}$, indicating uniform expression levels of CX43 across different tissue areas (**Figure 39C**).

Specifically, these experimental results were used to feed two-dimensional computational models of human LV electrophysiology composed of epicardial and midmyocardial regions. A control scenario with longitudinal diffusion coefficient set to 0.0013 cm^2/ms, transverse-to-longitudinal conductivity ratio set to 0.19 and absence of fibrosis was defined. This control scenario was associated with a CV magnitude of 59.71 cm/s, in agreement with experimentally reported values [431]. Next, a 10-40% decrease in longitudinal conductivity, mimicking the range of variation of $\%CX43_{CM}$ observed in the population, was modeled. Such a reduction caused a 6.31%-26.85% decrease in the median CV. The range of lateralization observed in the population was modeled by setting the transverse-to-longitudinal conductivity ratio to 0.23, 0.27, 0.31 and 0.35, without changing the global conductivity (represented by the sum of the longitudinal and transverse conductivities). Increased lateralization led to a 6%-13.95% increment in CV. When including fibrosis in the models by randomly assigning some parts of the tissue with fibroblast electrophysiological properties, an inverse correlation was observed between the degree of fibrosis and CV. The lowest fibrosis percentage (7%) in the population data caused a 6.16% reduction in CV and the highest fibrosis percentage (19%) led to a 17.79% reduction. The effects of combining these three factors (reduced longitudinal conductivity, increased transverse-to-longitudinal conductivity ratio and increased fibrosis) were also assessed in four different extents. The four cases led to reduced CV (**Figure 43**).

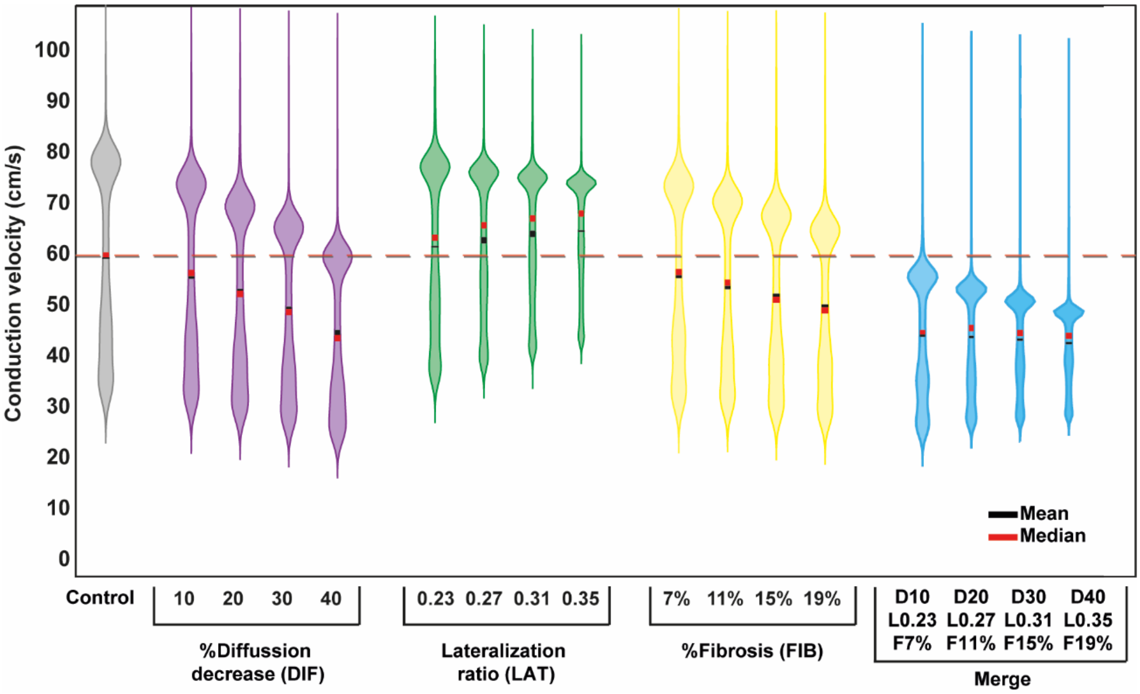

Figure 43. Evaluation of conduction velocity for all simulated scenarios involving reduction in the longitudinal diffusion coefficient, increase in transverse-to-longitudinal diffusion ration, increase in the content of fibrosis and the combination of these three factors. '%Diffusion decrease (DIF)' stands for an increase in the longitudinal diffusion coefficient of 10%, 20%, 30% and 40%, respectively, associated to changing amounts of CX43 (%CX43). 'Lateralization ratio (LAT)' stands for an increase in the transverse-to-longitudinal diffusion ratio to 0.23, 0.27, 0.31 and 0.35, respectively, related to variations in de degree of CX43 lateralization (%$CX43_{LAT}$). '%Fibrosis (FIB)' stands for addition of fibrosis by 9%, 11%, 15% and 19%, respectively. 'D10/L0.23/F7%' stands for 10% decrease in DIF, LAT of 0.23 and 7% of FIB, and analogously for the other combinations.

For subsequent analysis only the extreme cases were simulated, that is: the highest reduction in the longitudinal conductivity (40%, from now on, DIF 40%), the highest lateralization (0.35, from now on, LAT 0.35) and the greatest fibrosis percentage (19%, from now on, FIB 19%) individually or combining two or three of them. DIF 40%, FIB 19% and particularly the combination of the two of them were all associated with a decrease in CV. Because LAT 0.35 was associated with a higher CV than in control, combining LAT 0.35 with DIF 40%, FIB 19% or both yielded a higher CV than when LAT 0.35 was not simulated (**Figure 44A**).

Regarding APD, no changes were observed except for the simulations with fibrosis, which had the shortest APD. This reduction in the mean APD of the tissue, justified by the coupling of cardiomyocytes and fibroblasts and the shorter APD of the fibroblasts, ranged from 33% to 57% for the cases with the lowest and highest percentages of fibrosis, respectively. Similar APD shortening was observed when fibrosis was combined with DIF 40% and/or LAT 0.35 (data not shown).

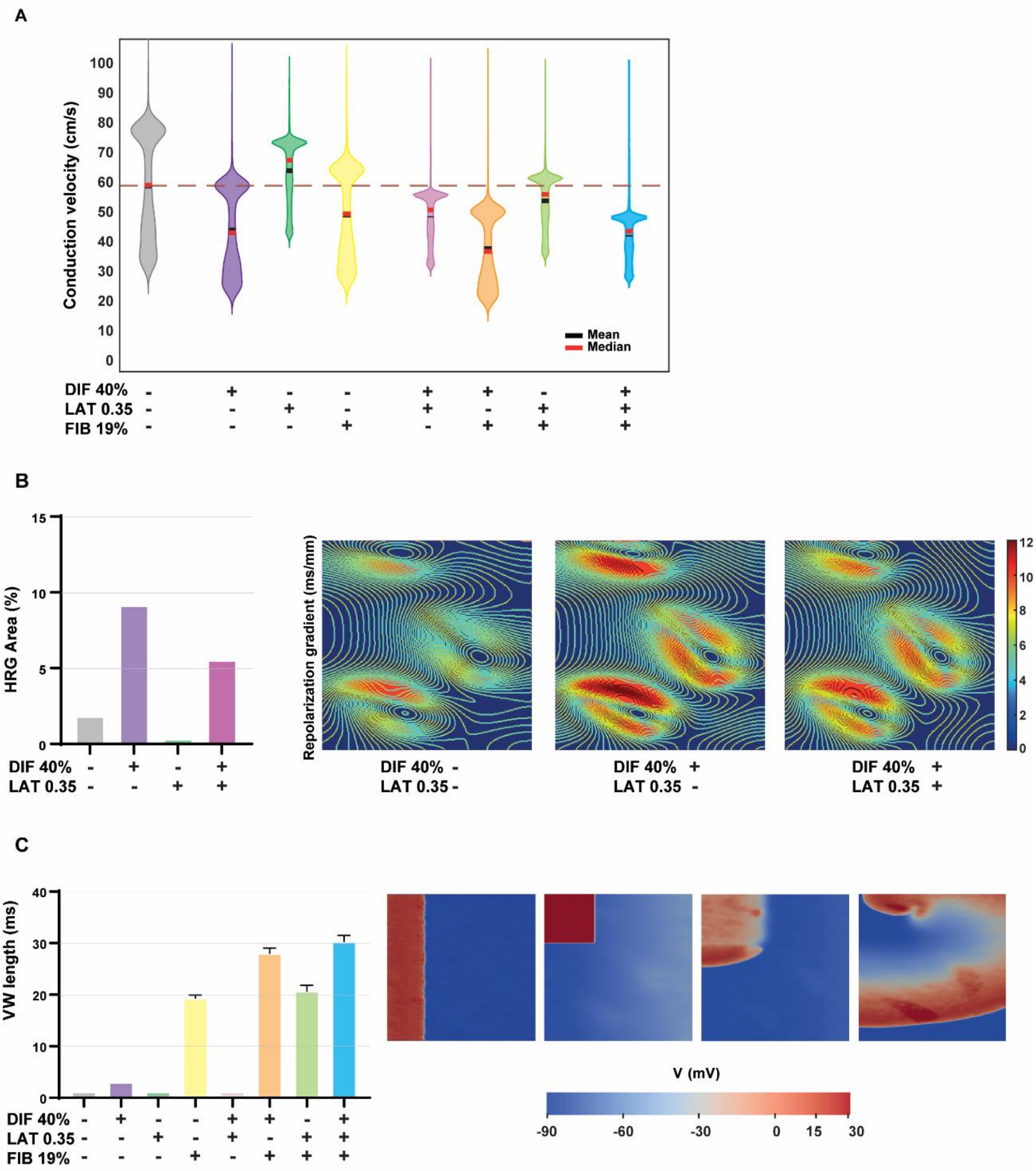

Figure 44. Evaluation of the effect of CX43 remodeling and fibrosis deposition on ventricular electrophysiology and arrhythmic risk. A) Violin plot of the conduction velocity for the control scenario and for scenarios involving variations in CX43 features (diffusion 40% -DIF 40%- and lateralization 0.35 -LAT 0.25-), fibrosis 19% (FIB 19%) and their combination. **B)** Effect of CX43 quantity, lateralization and the combination of the two on the HRG area. **C)** Effect of CX43 quantity and lateralization, fibrosis and their combination on the vulnerability window (VW) length. Representative images of the spiral waves generated for one of the simulated scenarios coded for voltage (V) values. Bar graphs represent mean ± standard deviation.

5.3.5 Reduced CX43 quantity, increased CX43 heterogeneity and larger fibrosis deposition enhance arrhythmic risk

Next, the role of the inter-individual variability in CX43 and fibrosis deposition in arrhythmogenesis was evaluated by calculating the repolarization gradient and the VW length. For each simulated scenario, the percentage of tissue with HRG was calculated. When FIB 19% was simulated, a decrease in the HRG area in comparison to control was observed due to the different properties between epicardial and midmyocardial nodes. The addition of fibrosis in the same proportion and distribution in a tissue with uniform cell properties would be, however, associated with an increase in the HRG area (**Figure 45A** for an epicardial tissue). When DIF 40% and LAT 0.35 were simulated, an increase and a decrease were observed, respectively, in the HRG area with respect to control while the combination of both led to an intermediate situation (**Figure 44B**). Evaluation of VW length led to the observation that DIF 40%, LAT 0.35 and the combination of the two had either little or no effect on VW. FIB 19% was associated with higher VW. The combination of FIB 19% with LAT 0.35 and/or DIF 40% further increased VW (**Figure 44C**).

Finally, another set of simulations were performed to represent spatial distribution of CX43 in the tissue as in the experimental results. The tissue samples of two individuals whose $CX43_H$ were representative of the middle-aged and old groups were taken, and corresponding tissue meshes for electrophysiological simulations were created. This work found that the spatial CX43 heterogeneity in the middle-age and even further in the old age was associated with a larger HRG area than in control (with no heterogeneity). When any of the two heterogeneity distributions were combined with DIF 40%, the HRG area increased remarkably (**Figure 45B**). In terms of VW, $CX43_H$ combined with FIB 19%, DIF 40% and/or LAT 0.35 led to enhanced pro-arrhythmicity compared with the cases without heterogeneity. This increase was slightly more marked in the heterogeneity associated with the old group than the middle-aged one (**Figure 45C).** The combination of any of the two $CX43_H$ with FIB 19% or the three factors, i.e., DIF 40%, FIB 19% and LAT 0.35, led to the greatest effect on VW (**Figure 45D**). Spiral waves for one of the simulated cases are shown in **Figure 44C**.

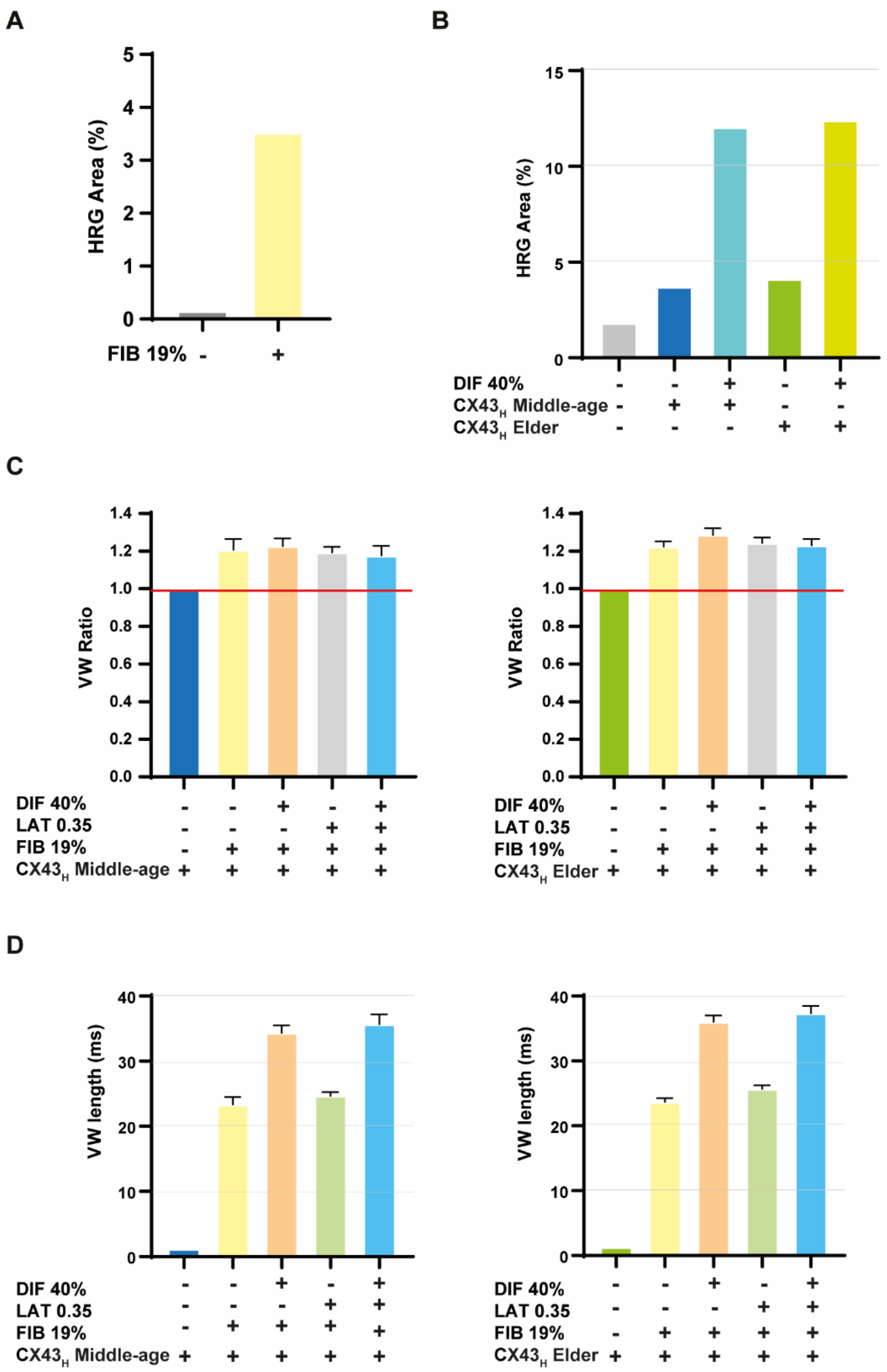

Figure 45. Analysis of the effect of CX43 spatial heterogeneity combined with fibrosis and CX43 quantity and lateralization on repolarization gradient and reentrant arrhythmias. A) HRG area in a mesh with only epicardial nodes without (left column) or with (right column) 19% fibrosis. **B)** Effect of CX43 heterogeneity ($CX43_H$), quantity (diffusion -DIF 40%-) and lateralization (LAT 0.35) on HRG area. **C)** Effect of $CX43_H$ in middle-aged (left) and elder (right) individuals together with %CX43 (diffusion -DIF 40%-) and $\%CX43_{LAT}$ (LAT 0.35) and fibrosis (FIB 19%) on VW length relative to the same scenarios without heterogeneity. The red line represents the same scenario without heterogeneity. **D)** Effect of $CX43_H$ in middle-aged (left) and elder (right) individuals together with %CX43 (diffusion -DIF 40%-) and $\%CX43_{LAT}$ (LAT 0.35) and fibrosis (FIB 19%), on VW length. Bar graphs represent mean ± standard deviation.

5.4 Discussion

5.4.1 Absence of CX43 remodeling beyond midlife

Methods to quantify CX43 characteristics in a population of middle-aged to old individuals were developed. The role of variations in such characteristics on cardiac electrical activity was investigated. The obtained results showed only slight CX43 remodeling associated with CA and BA in the human LV beyond midlife, with high inter-individual variability in all age segments. The observed variability is unlikely to arise from regional LV differences, as all tissue samples corresponded to the same LV region and transmural depth and might be better explained by the large heterogeneity in genetic background and environmental conditions of the donors.

As far as I know there are no studies characterizing CX43 remodeling with age in the human LV and only limited research is available from animal models. Some animal studies have reported a decrease in Cx43 amount with age [92], [93], [97]. Regarding other Cx43 characteristics, a comparison of these results with previous research proves difficult, as most available studies evaluating Cx43 expression levels only perform qualitative assessments [92], [96], studies assessing Cx43 heterogeneity changes with age are scarce [414] and there are no studies on age-related Cx43 lateralization in humans and just a few in animal models, all of them reporting an increase of Cx43 in the lateral membrane of the cardiomyocytes with age [94], [432]. Besides, previous research on animal models has compared young animals with either adult or old ones, but there is a paucity of studies comparing adult and old animals despite the age range from midlife onwards being precisely the one expected to be most clinically relevant in terms of cardiac risk.

Next, the relationship between CX43 characteristics and fibrosis was investigated. Although age is widely reported to enhance cardiac fibrosis [67], in this study population only a non-significant increase in fibrosis with BA and no relationship with CA was observed, in agreement with the previous results reported in Chapter 4, where collagen-related fibrosis increased from midlife onwards only with BA. Nevertheless, it should be noted that this works used WGA, a broader staining agent than the collagen-specific Second-Harmonic-Generation microscopy used in the study reported in Chapter 4 that captures slightly different fibrosis-related information. Contrary to other studies in animal models [418], no correlation between CX43 remodeling and fibrosis content in the age range of this population was observed. This finding would imply that, in healthy human ventricular myocardium, no regulatory interplay between the extracellular matrix and CX43 exists from midlife onwards. Whether disease alters this relation in humans and could, thus, be a potential pharmacological target remains to be elucidated. Given the species differences, further studies that investigate this would require the use of human models like e. g. cardiac cells derived from human induced-pluripotent stem cells.

Even though BA, estimated as lipofuscin content, seems to represent CX43 remodeling better than CA, particularly for $CX43_H$ and the fibrosis content, significant changes are still not observed. Yet, these results would support the relevance of using BA markers as better indicators of the actual structural state of the heart [433] as it was also reported in Chapters 2 and 4.

Finally, CX43 quantity in relation to the area of the LV tissue on top of the area of the cardiomyocytes was also characterized. No large differences were observed between the two methods, suggesting that the outcomes from previous studies with similar content of fibrosis (up to 20%), would not have changed excessively if Cx43 would have been analyzed in relation to the area of the cardiomyocytes.

Altogether, novel and relevant insights into age-related CX43 and fibrosis dynamics and their interplay in the human LV are provided. This constitutes a major progress over investigations carried out so far, with most studies being conducted in animal models and based on CA.

5.4.2 Role of CX43 characteristics and fibrosis in arrhythmogenesis

Based on the results of the experimental characterizations, a range of values for CX43 characteristics and fibrosis deposition was simulated using mathematical modeling of human LV tissue electrophysiology. The reduction in CV observed in response to a reduction in CX43 quantity is in line with previous *in vivo* animal models [411], [412] and *in silico* studies [403]. The effects of larger CX43 lateralization on increased CV agree with studies using animal models [90], [434] and *in silico* models [89]. The reduced CV associated with increased fibrosis is in agreement with previous studies, which, however, reported greater effects [403], possibly due to the assignment of fibrotic properties to the elements of the simulated tissue.

The simulations did not lead to an association between CX43 remodeling changes in APD. Increased fibrosis, however, notably reduced APD, in accordance with other *in silico* studies [435], [436].Thus, the physiological range of variation of human CX43 features has an effect on ventricular electrical conduction but not on repolarization duration, as could be expected.

For arrhythmic risk assessment, the repolarization gradient was evaluated and the percentage of LV tissue with HRG using a threshold of 9 ms/mm was quantified. Previous studies have used thresholds ranging from 3 ms/mm [428] to 12.4±3.5 ms/mm in heart failure [429] or 25 ms/mms at the edge of the border zone [437]. Also, the length of the VW to assess the probability of a premature ventricular stimulus to induce reentrant arrhythmias was evaluated.

In these simulations, %$CX43_{LAT}$ increased VW length, but it reduced the HRG area. A disparity of evidence can be found in the literature regarding the effects of %$Cx43_{LAT}$. Some authors have reported an increase in CV associated with higher lateralization [89], [90], [434], whereas others have reported a decrease in CV [438], [439]. In this study, $CX43_{H}$ is the CX43 feature whose values change to a larger extent with age. When spatial heterogeneity in CX43 was simulated, it was found that it contributed to the proarrhythmicity induced by larger fibrosis and reduced CX43 quantity. Overall, the simulated data indicates that physiological values of CX43 features and fibrosis can synergistically increment the risk of ventricular arrhythmias in humans.

5.5 Conclusions

This work characterized CX43 remodeling with age by assessing its content, expression level, heterogeneity and lateralization. Although BA was more strongly correlated with some CX43 characteristics than CA beyond midlife, in general non-significant CX43 remodeling with age was observed, thus ruling out a population-level role of CX43 as a potential arrhythmic modulator in relation to age. Nevertheless, larger inter-individual variability in CX43 characteristics at all age segments was observed. The experimental CX43 characterizations were integrated, individually and in combination with the observations on fibrosis deposition, into two-dimensional human LV electrophysiological models. Simulation results showed that a physiological reduction in the amount of CX43, an increase in its heterogeneity and a larger fibrosis deposition can lead to enhanced arrhythmic risk.

Chapter 6

6. Conclusions and Future Work

6.1 Conclusions

6.1.1 General conclusions

This thesis investigates aging hallmarks in the human LV by combining molecular and histological analysis of LV samples from living donors and *in vitro* and *in silico* methodologies. The studied age-related cardiac mechanisms are gene expression, with a focus on miRNAs (key pleiotropic post-transcriptional regulators), fibrosis deposition and CX43 remodeling. Additionally, *in vitro* and *in silico* tools are created to further investigate the effects of human cardiac aging. This thesis proves the potential of *CDKN2A* and AppAge as LV transcriptomic age descriptors and shows they perform better than CA to unveil age-related changes in a cross-sectional study. Based on *CKDN2A*-related results, supported by findings using the AppAge approach, a bioinformatics LV-specific gene regulation network controlled by BIO-AGEmiRNAs provides new insights into the potential mechanisms regulated by miRNAs in age-induced LV impairments. Also, two LV-enriched age-related BIO-AGEmiRNAs present in plasma are proposed as non-invasive secreted biomarkers of the aging myocardium status. In conclusion, we report novel and high-resolution data on the miRNA and gene expression changes that govern natural human LV biological aging.

Next, the obtained transcriptomic data on natural aging is integrated into the investigations on accelerated aging to validate an *in vitro* model of aged cardiomyocytes. The hiPSC model based on *LMNA Δ50* inducible expression recapitulates the hallmarks of aging as well as the CA and BA age-related gene expression changes of physiological aging. This work proves the translation from human cross-sectional data to an *in vitro* longitudinal modeling system that will enable future translational mechanistic and functional research. In addition, this thesis rules out *LMNA Δ50* as a major contributor to natural cardiac aging. In conclusion, natural aging seems to be independent of *LMNA Δ50* expression but can be recapitulated *in vitro* by mimicking *LMNA Δ50*-induced pathological accelerated aging.

Regarding collagen deposition, this work validates the use of SHG microscopy and automatic image processing and analysis to quantify collagen content, clustering and spatial distribution with high specificity and resolution in human and pig LV tissue. Consistency between pig and human results, supporting the pig as a relevant and translational model to study age-related remodeling, was observed. From midlife onwards, changes in collagen characteristics show a poor relationship with CA but are more closely related to the values of the age pigment lipofuscin. This again confirms the superior resolution of BA markers in explaining known aging phenotypes in cross-sectional studies. Subsequently, patient-specific electrophysiological models of LV tissues that integrate experimental results are built. *In silico* simulations show that the amount and organization of fibrosis modulate arrhythmia vulnerability and highlight that collagen spatial distribution should be considered for arrhythmia risk assessment. Overall, this thesis concludes that collagen remodeling associated with BA increases arrhythmic risk from midlife onwards in humans.

With respect to CX43, its structural dynamics are characterized by assessing its content, expression level, heterogeneity and lateralization. Non-significant CX43 remodeling beyond midlife either by CA or BA is found. Also, the lack of correlation between CX43 characteristics and fibrosis deposition in humans, in contrast to observations in animal species, highlights the importance of developing human-based models both *in silico* and *in vitro* for insightful aging research. Tissue simulations representing the obtained experimental results on CX43 remodeling prove that a reduction in the amount of CX43 and/or an increment in CX43 spatial heterogeneity combined with higher levels of fibrosis enhanced arrhythmogenesis. In conclusion, CX43 remodeling is ruled out as an age-related arrhythmic modulator from midlife onwards at a population level, but certain CX43-related factors remain arrhythmogenic at an individual level.

Overall, the research in this thesis provides: a thorough experimental characterization of human cardiac aging hallmarks, both from the point of view of CA and BA; the implications in terms of arrhythmic risk of some of these hallmarks based on realistic *in silico* investigations; and the creation and characterization of an *in vitro* model of cardiac cell aging. This thesis demonstrates the importance of using integrative interdisciplinary research, with the different methodologies being able to complement and synergize with each other to advance in the characterization of human cardiac aging and progress towards novel future solutions for healthy cardiac aging.

6.1.2 BIO-AGEmiRNAs as therapeutic targets and cardiac risk indicators

In Chapter 2, a LV-specific gene regulation network regulated by BIO-AGEmiRNAs is built. As miRNA therapeutics is an emerging field, this network paves the way for future studies aimed at developing cardiac-specific anti-aging therapies based on miRNAs. Besides, two of the miRNAs, *MIR4461* and *hsa-mir-490*, are highly enriched in the human LV as compared to other human tissues and are also present in plasma. These results propose that cardiac-specific BIO-AGEmiRNAs could be used as indicators of the BA of the heart in liquid biopsies, thus reflecting its functional state and therefore being useful as risk predictors of cardiac malfunctioning with a minimally invasive approach. BIO-AGEmiRNA biomarkers could be potentially detected in an easier and more sensitive way (based on the highly sensitive PCR technique) than other biomarkers currently used to assess cardiac damage or cardiovascular risk, such as cardiac proteins in serum or ECG indicators, which might require a high degree of organic damage to be informative.

6.1.3 Biological age as descriptor of human cardiac aging

The age-related cardiac mechanisms studied in all the chapters are evaluated based on both CA and BA. In all the cases, BA demonstrated to be a better age descriptor than CA. Chapter 2 reports *CDKN2A* expression, a cell senescence marker, and AppAge, a highly complex transcriptional index, to better describe the age-related LV transcriptomic changes than CA and to uncover depleted cardiac-specific processes, among other relevant functions, undetected by CA. In Chapter 3, higher correlation of *LMNA* expression with *CDKN2A* than with CA is observed and gene expression changes by AppAge in natural aging (non-significant by CA) can be faithfully translated into *in vitro* accelerated aging models. In Chapter 4, all collagen characteristics show no relation with CA, but are correlated with the age-pigment lipofuscin. In Chapter 5, the non-significant changes in CX43 remodeling are slightly better described by the lipofuscin content. Overall, even if BA does not have a well-established indicator, these data highlight the value of BA markers, whether transcriptomic or histologic, to overcome the masking effects of inter-individual variability and provide results of higher resolution and power in cross-sectional aging studies.

Of note, in this thesis, transcriptomic changes detect activation of pro-fibrotic pathways and related genes with advancing BA from adulthood to the elderly range (Chapter 2). This is also observed at the histological level by BA in the middle-aged to elders range, which is associated to an increase in the arrhythmic risk (Chapter 4). Thus, this thesis links BA-related remodeling from gene expression to tissue structure and electrophysiological function. In this manner, it shows the value of integrative approaches at multiple levels to explain human physiology and disease from its molecular basis all the way up to function.

6.1.4 Age-related cardiac remodeling from midlife onwards

The characterization of collagen deposition and CX43 remodeling described in Chapters 4 and 5, respectively, are performed in middle-age to elder individuals. Both studies show that from midlife onwards there are no changes in these features in relation to CA while most collagen-related ones significantly change in relation to BA and CX43 shows slight variation with BA. However, in the literature, these cardiac features are reported to highly vary when comparing young and old, particularly in animal studies. Here again, the results obtained in this thesis highlight the importance of conducting studies in human donors to surmount differences between species. Also, it remarks the importance of studying age-related cardiac mechanisms in middle to old age, which is a more clinically relevant age range in which arrhythmic risk is expected to be more pronounced.

6.1.5 Transferring the experimental characterization into computational models

The translation from the experimental characterization into *in silico* models is described in Chapters 4 and 5. The amount and distribution of collagen in Chapter 3 and CX43 amount, lateralization and heterogeneity and fibrosis content in Chapter 4 are used to feed two-dimensional computational models of human ventricular electrophysiology. Certain levels or patterns of collagen spatial distribution and CX43 properties are shown to be arrhythmogenic, so these factors should gain relevance in future computational models. More specifically, the integrative approach used in this thesis underlines the importance of considering spatial factors when developing novel *in silico* models so as to increase the reliability of future computational research and thus improve health management. Particularly in this case, the improvement can be obtained by better assessing arrhythmic risk associated with cardiac aging mechanisms.

6.1.6 Cardiac aging at molecular and cellular level

The knowledge of the molecular and cellular mechanisms responsible for age-related cardiac changes comes fundamentally from animal models, as ethical and practical reasons make human longitudinal and mechanistic studies at cellular and molecular levels unfeasible. The generated hiPSC line described in Chapter 3 represents a pioneering tool to perform longitudinal molecular, mechanistic and functional research on human cardiac cell aging. It theoretically allows to overcome the limitations associated with human cross-sectional studies that hinder medical progress towards healthy cardiac aging. Findings from human tissues and *in silico* studies in Chapters 4 and 5 could be validated in the *in vitro* model, and *vice versa*, the *in vitro* model could be used to study the mechanisms that regulate fibrosis and CX43 with age to enrich the *in silico* models and thus establish a positive feedback loop between *in vitro* and *in silico* research.

6.2 Study limitations and Future work

- Cardiac-enriched BIO-AGEmiRNAs detected in blood from Chapter 2 are potential indicators of cardiac BA and, thus, of cardiac disease risk. Future work could be directed to investigate the relation of these BIO-AGEmiRNAs in liquid biopsies with established biochemical or ECG-related markers of cardiac disease risk and to determine their potency to risk stratify patients.

- The developed iCM model of accelerated aging recapitulates aging hallmarks as well as altered mechanisms reported in human cardiac aging. Although there are not large differences between induction times employed in this study, some aging mechanisms in iCMs seem to require 16 days of progerin induction or even further for mitochondrial function and ROS production. Future work could characterize these and other aging features more exhaustively and test other times and/or induction doses.

- The research of this thesis shows the translation from natural human cardiac aging to accelerated aging *in vitro*, with iCMs reproducing gene expression changes of aged individuals based on a transcriptomic analysis of 132 human donors. Since iCMs are immature cells, future work could extend the present one to implement progerin induction in matured iCMs, which could be obtained by applying the latest advances in the field (reviewed in Chapter 1) and enhance the predictive value of the hereby generated model.

- The research of this thesis presents the utility of LV biopsies from living donors to characterize two aging hallmarks: alterations in the extracellular matrix remodeling and in intercellular communication. In both cases, the number of samples used is significantly higher than in other human studies. Nevertheless, future studies could extend the present work by increasing the size and/or age range of the study population, with the later allowing to fully characterize the age-related changes from adulthood. In particular, the analysis of samples from young individuals could allow to confirm whether there is an evident remodeling when comparing young and adult or elder individuals, as occurs in animal species. Specifically, regarding the characterization of CX43 dynamics, the absence of age-related remodeling could be attributed to the fact that such changes do not occur from midlife onwards indeed or to this remodeling being hidden by the high inter-individual variability and the reduced size of our population. Taking into account the expected better resolution of BA markers (as reported in Chapters 2 and 4), it is likely that there is not CX43 remodeling beyond midlife. However, changes in CX43 with age could be more subtle than other features and a more extensive study would be required to uncover them. Therefore, the suggested future studies including a larger number of individuals and a wider age range, with additional inclusion of analysis in LV samples from pigs as a translational model of age-related cardiac remodeling, could help to clarify this point.

- The changes in CX43 heterogeneity observed from the analysis of human LV samples are introduced in mathematical models of cardiac electrophysiology by spatially varying the longitudinal diffusion coefficient and, correspondingly, the transverse diffusion coefficient. This is performed by taking the spatial distributions of CX43 from some of the individuals in the study population. Future studies could extend this work by developing personalized electrophysiological tissue models that represent the CX43 spatial heterogeneity on a one-to-one basis. This would allow to more accurately decipher its potential arrhythmogenic effect.

Publications

JCR Publications Derived from the Thesis

- E. Ramos-Marquès **& L. García-Mendívil**✉, M. Pérez-Zabalza, H. Santander-Badules, S. Srinivasan, J.C. Oliveros, R. Torres-Pérez, A. Cebollada, J.M. Vallejo-Gil, P.C. Fresneda-Roldán, J. Fañanás-Mastral, M. Vázquez-Sancho, M. Matamala-Adell, F. Sorribas-Berjón, J.A. Bellido-Morales, F.J. Mancebón-Sierra, A.S. Vaca-Núñez, C. Ballester-Cuenca, M. Jiménez-Navarro, J.M. Villaescusa, E. Garrido-Huéscar, M. Segovia-Roldán, A. Oliván-Viguera, C. Gómez-González, G. Muñiz, E. Diez, L. Ordovás, E. Pueyo. "Chronological and biological aging of the human left ventricular myocardium: Analysis of microRNAs contribution". *Aging Cell* 2021. 2021 Jul,20(7):e13383. **Corresponding Author**

- **L. García-Mendívil**✉, M. Pérez-Zabalza, K. Mountris, S. Duwé, N. Smisdom, M. Pérez, L. Luján, E. Wolfs, R.B. Driesen, J.M. Vallejo-Gil, P.C. Fresneda-Roldán, J. Fañanás-Mastral, M. Vázquez-Sancho, M. Matamala-Adell, J.F. Sorribas-Berjón, J.A. Bellido-Morales, F.J. Mancebón-Sierra, A.S. Vaca-Núñez, C. Ballester-Cuenca, A. Oliván-Viguera, E. Diez, L. Ordovás, E. Pueyo. Analysis of age-related left ventricular collagen remodeling in living donors: implications in arrhythmogenesis, iSCIENCE (2022). **Corresponding Author**

- **L. García-Mendívil**✉, M. Pérez-Zabalza, J.M. Vallejo-Gil, J. Fañanás-Mastral, M. Vázquez-Sancho, J.A. Bellido-Morales, A.S. Vaca-Núñez, C. Ballester-Cuenca, E. Diez, L. Ordovás, E. Pueyo. "Inter-individual age-independent differences in human CX43 impact ventricular arrhythmic risk". **Corresponding Author**

- **L. García-Mendívil**✉, N. Hernández-Bellido, M. Sánchez-Barat, M. Pérez-Zabalza, E. Garrido-Huéscar, J.M. Vallejo-Gil, M. Matamala-Adell, J.F. Sorribas-Berjón, J.A. Bellido-Morales, A.S. Vaca-Núñez, C.M. Verfaillie, C. Ballester-Cuenca, E. Pueyo, L. Ordovás. "Natural and Induced Human Cardiac Aging: *Lamin A Δ50* does not accumulate naturally but accelerates aging *in vitro*". **Corresponding Author**

Other JCR Publications

- A. Oliver-Gelabert, **L. García-Mendívil**, J.M. Vallejo-Gil, P.C. Fresneda-Roldán, J. Fañanás-Mastral, M. Vázquez-Sancho, M. Matamala-Adell, F. Sorribas-Berjón, C. Ballester-Cuenca, L. Ordovás, E.R. Diez, E. Pueyo. “Automatic Quantification of Cardiomyocyte Dimensions and Connexin 43 Lateralization in Fluorescence Images”. *Biomolecules*. 2020 Sep 17, 10(9):1334

- A. Oliván-Viguera, M. Pérez-Zabalza, **L. García-Mendívil**, K.A. Mountris, S. Orós-Rodrigo, E. Ramos-Marquès, J.M. Vallejo-Gil, P.C. Fresneda-Roldán, J. Fañanás-Mastral, M. Vázquez-Sancho, M. Matamala-Adell, F. Sorribas-Berjón, J.A. Bellido-Morales, F.J. Mancebón-Sierra, A.S. Vaca-Núñez, C. Ballester-Cuenca, M.A. Marigil, C. Pastor, L. Ordovás, R. Köhler, E. Diez, E. Pueyo. “Minimally invasive system to reliably characterize ventricular electrophysiology from living donors”. *Sci Rep*. 2020 Nov 17, 10(1):19941

- F.J. Sánchez, V.A. Gonzalez, M. Farrando, A.O. Baigorria-Jayat, M. Segovia-Roldan, **L. García-Mendívil**, L. Ordovás, N.J. Prado, E. Pueyo, E.R. Diez. “Atrial Dyssynchrony Measured by Strain Echocardiography as a Marker of Proarrhythmic Remodeling and Oxidative Stress in Cardiac Surgery Patients”. *Oxid Med Cell Longev*. 2020 Dec 30, 2020:8895078

- **L. García-Mendívil,** D.R. Mediano, A. Hernaiz, D. Sanz-Rubio, F.J. Vázquez, B. Marín, O. López-Pérez, A. Otero, J.J. Badiola, P. Zaragoza, L. Ordovás, R. Bolea, I. Martín-Burriel. “Effect of Scrapie Prion Infection in Ovine Bone Marrow-Derived Mesenchymal Stem Cells and Ovine Mesenchymal Stem Cell-Derived Neurons”. Animals (Basel). 2021 Apr 15,11(4):1137

Conference Proceedings

- M. Pérez-Zabalza, **L. García-Mendívil**, K. Mountris, A. Oliván-Viguera, J.M. Vallejo-Gil, P.C. Fresneda-Roldán, J. Fañanás-Mastral, M. Vázquez-Sancho, M. Matamala-Adell, F. Sorribas-Berjón, J.A. Bellido-Morales, F.J. Mancebón-Sierra, A.S. Vaca-Núñez, C. Ballester-Cuenca, L. Ordovás, E. Pueyo. “Age-Associated Changes in Myocardial Fibrosis Amount and Distribution Quantified from Nonlinear Optical Microscopy Images”. Computing in Cardiology CinC 2021.

Bachelor and Master Thesis Supervision

- Co-Supervisor of Molecular and Cellular Biology Master´s thesis entitled “Development of human cardiac cell aging models”. University of Zaragoza (Spain).

- Co-Supervisor of Biotechnology Bachelor´s thesis entitled “Characterization of *in vitro* models of human cardiac aging”. University of Zaragoza (Spain)

Bibliography

[1] European Heart Network, “European Cardiovascular Disease Statistics 2017 edition,” 2017, Accessed: Nov. 09, 2022. [Online]. Available: www.ehnheart.org.

[2] D. S. Desai and S. Hajouli, “Arrhythmias,” *StatPearls*, 2022. https://www.ncbi.nlm.nih.gov/books/NBK558923/.

[3] J. Kaplan, A. Kanwal, and V. Lala, “Reentrant Arrhythmias,” *StatPearls*, 2022. https://www.ncbi.nlm.nih.gov/books/NBK557775/.

[4] World Health Organisation, “Cardiovascular diseases,” 2021. https://www.who.int/.

[5] C. López-Otín, M. A. Blasco, L. Partridge, M. Serrano, and G. Kroemer, “The hallmarks of aging.,” *Cell*, vol. 153, no. 6, pp. 1194–1217, Jun. 2013, doi: 10.1016/j.cell.2013.05.039.

[6] Y. A. Chiao and P. S. Rabinovitch, “The Aging Heart,” *Cold Spring Harb. Perspect. Med.*, vol. 5, no. 9, p. a025148, Sep. 2015, doi: 10.1101/cshperspect.a025148.

[7] C. López-Otín, M. A. Blasco, L. Partridge, M. Serrano, and G. Kroemer, “Hallmarks of aging: An expanding universe,” *Cell*, vol. 186, no. 2, pp. 243–278, Jan. 2023, doi: 10.1016/J.CELL.2022.11.001.

[8] T. O’Hara, L. Virág, A. Varró, and Y. Rudy, “Simulation of the undiseased human cardiac ventricular action potential: Model formulation and experimental validation,” *PLoS Comput. Biol.*, vol. 7, no. 5, p. e1002061, 2011, doi: 10.1371/journal.pcbi.1002061.

[9] K. A. MacCannell, H. Bazzazi, L. Chilton, Y. Shibukawa, R. B. Clark, and W. R. Giles, “A mathematical model of electrotonic interactions between ventricular myocytes and fibroblasts,” *Biophys. J.*, vol. 92, no. 11, pp. 4121–4132, 2007, doi: 10.1529/biophysj.106.101410.

[10] Y. Wang, Y. Li, C. He, B. Gou, and M. Song, “Mitochondrial regulation of cardiac aging,” *Biochim. Biophys. acta. Mol. basis Dis.*, vol. 1865, no. 7, pp. 1853–1864, Jul. 2019, doi: 10.1016/J.BBADIS.2018.12.008.

[11] K. R. Chaudhary, H. El-Sikhry, J. M. Seubert, K. R. Chaudhary, H. El-Sikhry, and J. M. Seubert, “Mitochondria and the aging heart,” *J. Geriatr. Cardiol. 2011, Vol. 8, Issue 3, Pages 159-167*, vol. 8, no. 3, pp. 159–167, 2011, doi: 10.3724/SP.J.1263.2011.00159.

[12] D. L. Schmucker and H. G. Sachs, “Age-dependent alterations in rat ventricular myocardium: a quantitative analysis,” *Mech. Ageing Dev.*, vol. 31, no. 1, pp. 89–101, 1985, doi: 10.1016/0047-6374(85)90028-4.

[13] G. Corsetti *et al.*, “Morphometric changes induced by amino acid supplementation in skeletal and cardiac muscles of old mice,” *Am. J. Cardiol.*, vol. 101, no. 11A, Jun. 2008, doi: 10.1016/J.AMJCARD.2008.02.078.

[14] E. L. Tate and G. H. Herbener, “A morphometric study of the density of mitochondrial cristae in heart and liver of aging mice,” *J. Gerontol.*, vol. 31, no. 2, pp. 129–134, 1976, doi: 10.1093/GERONJ/31.2.129.

[15] K. Boengler, M. Kosiol, M. Mayr, R. Schulz, and S. Rohrbach, “Mitochondria and ageing: role in heart, skeletal muscle and adipose tissue,” *J. Cachexia. Sarcopenia Muscle*, vol. 8, no. 3, pp. 349–369, Jun. 2017, doi: 10.1002/JCSM.12178.

[16] C. Franceschi *et al.*, “Inflamm-aging. An evolutionary perspective on immunosenescence,” *Ann. N. Y. Acad. Sci.*, vol. 908, pp. 244–254, 2000, doi: 10.1111/J.1749-6632.2000.TB06651.X.

[17] Hae Young Chung, Hyon Jeen Kim, Jung Won Kim, and Byung Pal Yu, “The Inflammation Hypothesis of Aging,” *Ann. N. Y. Acad. Sci.*, vol. 928, no. 1, pp. 327–335, Apr. 2001, doi: 10.1111/J.1749-6632.2001.TB05662.X.

[18] D. Harman, “The Free Radical Theory of Aging,” *https://home.liebertpub.com/ars*, vol. 5, no. 5, pp. 557–561, Jul. 2004, doi: 10.1089/152308603770310202.

[19] E. S. Chocron, E. Munkácsy, and A. M. Pickering, “Cause or casualty: The role of

mitochondrial DNA in aging and age-associated disease," *Biochim. Biophys. Acta - Mol. Basis Dis.*, vol. 1865, no. 2, pp. 285–297, Feb. 2019, doi: 10.1016/J.BBADIS.2018.09.035.

[20] A. W. Linnane, T. Ozawa, S. Marzuki, and M. Tanaka, "Mitochondrial DNA mutations as an important contributor to ageing and degenerative diseases," *Lancet*, vol. 333, no. 8639, pp. 642–645, Mar. 1989, doi: 10.1016/S0140-6736(89)92145-4.

[21] L. Emelyanova *et al.*, "Selective downregulation of mitochondrial electron transport chain activity and increased oxidative stress in human atrial fibrillation," *Am. J. Physiol. - Hear. Circ. Physiol.*, vol. 311, no. 1, pp. H54–H63, Jul. 2016, doi: 10.1152/AJPHEART.00699.2015/ASSET/IMAGES/LARGE/ZH40111619670007.JPEG.

[22] S. Kuka, Z. Tatarkova, P. Racay, J. Lehotsky, D. Dobrota, and P. Kaplan, "Effect of aging on formation of reactive oxygen species by mitochondria of rat heart," *Gen. Physiol. Biophys.*, vol. 32, no. 3, pp. 415–420, 2013, doi: 10.4149/GPB_2013049.

[23] F. Rizvi *et al.*, "Effects of Aging on Cardiac Oxidative Stress and Transcriptional Changes in Pathways of Reactive Oxygen Species Generation and Clearance," *J. Am. Heart Assoc.*, vol. 10, no. 16, Aug. 2021, doi: 10.1161/JAHA.120.019948.

[24] V. Obas and R. S. Vasan, "The aging heart," no. February, pp. 1367–1382, 2018.

[25] N. B. Fakouri *et al.*, "Toward understanding genomic instability, mitochondrial dysfunction and aging," *FEBS J.*, vol. 286, no. 6, pp. 1058–1073, Mar. 2019, doi: 10.1111/FEBS.14663.

[26] L. J. Mah, A. El-Osta, and T. C. Karagiannis, "γH2AX as a molecular marker of aging and disease," *http://dx.doi.org/10.4161/epi.5.2.11080*, vol. 5, no. 2, pp. 129–136, 2010, doi: 10.4161/EPI.5.2.11080.

[27] M. S. Siddiqui, M. François, M. F. Fenech, and W. R. Leifert, "Persistent γH2AX: A promising molecular marker of DNA damage and aging," *Mutat. Res. Mutat. Res.*, vol. 766, pp. 1–19, Oct. 2015, doi: 10.1016/J.MRREV.2015.07.001.

[28] M. B. Stope, "Phosphorylation of histone H2A.X as a DNA-associated biomarker (Review)," *World Acad. Sci. J.*, vol. 3, no. 3, pp. 1–5, May 2021, doi: 10.3892/WASJ.2021.102/HTML.

[29] R. Anderson *et al.*, "Length-independent telomere damage drives post-mitotic cardiomyocyte senescence," *EMBO J.*, vol. 38, no. 5, Mar. 2019, doi: 10.15252/EMBJ.2018100492.

[30] E. H. Blackburn, "Switching and Signaling at the Telomere," *Cell*, vol. 106, no. 6, pp. 661–673, Sep. 2001, doi: 10.1016/S0092-8674(01)00492-5.

[31] V. Calvanese, E. Lara, A. Kahn, and M. F. Fraga, "The role of epigenetics in aging and age-related diseases," *Ageing Res. Rev.*, vol. 8, no. 4, pp. 268–276, Oct. 2009, doi: 10.1016/J.ARR.2009.03.004.

[32] B. Richardson, "Impact of aging on DNA methylation," *Ageing Res. Rev.*, vol. 2, no. 3, pp. 245–261, Jul. 2003, doi: 10.1016/S1568-1637(03)00010-2.

[33] Z. Jin and Y. Liu, "DNA methylation in human diseases," *Genes Dis.*, vol. 5, no. 1, p. 1, Mar. 2018, doi: 10.1016/J.GENDIS.2018.01.002.

[34] M. Esteller, "Epigenetics in cancer," *N. Engl. J. Med.*, vol. 358, no. 11, pp. 1148–1159, Mar. 2008, doi: 10.1056/NEJMRA072067.

[35] T. Kouzarides, "Chromatin Modifications and Their Function," *Cell*, vol. 128, no. 4, pp. 693–705, Feb. 2007, doi: 10.1016/J.CELL.2007.02.005.

[36] H. Tamaru, "Confining euchromatin/heterochromatin territory: jumonji crosses the line," *Genes Dev.*, vol. 24, no. 14, p. 1465, Jul. 2010, doi: 10.1101/GAD.1941010.

[37] S. Han and A. Brunet, "Histone methylation makes its mark on longevity," *Trends Cell Biol.*, vol. 22, no. 1, pp. 42–49, Jan. 2012, doi: 10.1016/J.TCB.2011.11.001.

[38] M. F. Fraga and M. Esteller, "Epigenetics and aging: the targets and the marks," *Trends Genet.*, vol. 23, no. 8, pp. 413–418, Aug. 2007, doi: 10.1016/J.TIG.2007.05.008.

[39] W. Zhang, M. Song, J. Qu, and G. H. Liu, "Epigenetic Modifications in Cardiovascular Aging and Diseases," *Circ. Res.*, vol. 123, no. 7, pp. 773–786, Sep. 2018, doi:

10.1161/CIRCRESAHA.118.312497.

[40] R. Gilsbach *et al.*, “Dynamic DNA methylation orchestrates cardiomyocyte development, maturation and disease,” *Nat. Commun.*, vol. 5, Oct. 2014, doi: 10.1038/NCOMMS6288.

[41] A. Moreno-García, A. Kun, O. Calero, M. Medina, and M. Calero, “An Overview of the Role of Lipofuscin in Age-Related Neurodegeneration.,” *Front. Neurosci.*, vol. 12, p. 464, 2018, doi: 10.3389/fnins.2018.00464.

[42] D. Vilchez, I. Saez, and A. Dillin, “The role of protein clearance mechanisms in organismal ageing and age-related diseases,” *Nat. Commun.*, vol. 5, 2014, doi: 10.1038/NCOMMS6659.

[43] D. A. Bosco, M. J. LaVoie, G. A. Petsko, and D. Ringe, “Proteostasis and movement disorders: Parkinson’s disease and amyotrophic lateral sclerosis.,” *Cold Spring Harb. Perspect. Biol.*, vol. 3, no. 10, p. a007500, Oct. 2011, doi: 10.1101/cshperspect.a007500.

[44] S. Finkbeiner, “Huntington’s Disease.,” *Cold Spring Harb. Perspect. Biol.*, vol. 3, no. 6, Jun. 2011, doi: 10.1101/cshperspect.a007476.

[45] D. J. Selkoe, “Alzheimer’s disease.,” *Cold Spring Harb. Perspect. Biol.*, vol. 3, no. 7, Jul. 2011, doi: 10.1101/cshperspect.a004457.

[46] J. F. Munnell and R. Getty, “Rate of accumulation of cardiac lipofuscin in the aging canine.,” *J. Gerontol.*, vol. 23, no. 2, pp. 154–158, Apr. 1968, doi: 10.1093/geronj/23.2.154.

[47] M. Nakano and S. Gotoh, “Accumulation of cardiac lipofuscin depends on metabolic rate of mammals.,” *J. Gerontol.*, vol. 47, no. 4, pp. B126-9, Jul. 1992, doi: 10.1093/geronj/47.4.b126.

[48] B. L. Strehler, D. D. Mark, and A. S. Mildvan, “GEE MV: Rate and magnitude of age pigment accumulation in the human myocardium.,” *J. Gerontol.*, vol. 14, pp. 430–439, Oct. 1959, doi: 10.1093/geronj/14.4.430.

[49] Y. Kakimoto *et al.*, “Myocardial lipofuscin accumulation in ageing and sudden cardiac death,” *Sci. Rep.*, vol. 9, no. 1, pp. 1–8, 2019, doi: 10.1038/s41598-019-40250-0.

[50] U. T. Brunk and A. Terman, “Lipofuscin: mechanisms of age-related accumulation and influence on cell function,” *Free Radic. Biol. Med.*, vol. 33, no. 5, pp. 611–619, 2002, doi: https://doi.org/10.1016/S0891-5849(02)00959-0.

[51] X. Tang, P.-H. Li, and H.-Z. Chen, “Cardiomyocyte Senescence and Cellular Communications Within Myocardial Microenvironments.,” *Front. Endocrinol. (Lausanne).*, vol. 11, p. 280, 2020, doi: 10.3389/fendo.2020.00280.

[52] N. A. Gude, K. M. Broughton, F. Firouzi, and M. A. Sussman, “Cardiac ageing: extrinsic and intrinsic factors in cellular renewal and senescence.,” *Nat. Rev. Cardiol.*, vol. 15, no. 9, pp. 523–542, Sep. 2018, doi: 10.1038/s41569-018-0061-5.

[53] M. Matjusaitis, G. Chin, E. A. Sarnoski, and A. Stolzing, “Biomarkers to identify and isolate senescent cells,” *Ageing Res. Rev.*, vol. 29, pp. 1–12, Aug. 2016, doi: 10.1016/J.ARR.2016.05.003.

[54] J. C. Acosta *et al.*, “Chemokine signaling via the CXCR2 receptor reinforces senescence,” *Cell*, vol. 133, no. 6, pp. 1006–1018, Jun. 2008, doi: 10.1016/J.CELL.2008.03.038.

[55] J. C. Acosta *et al.*, “A complex secretory program orchestrated by the inflammasome controls paracrine senescence,” *Nat. Cell Biol. 2013 158*, vol. 15, no. 8, pp. 978–990, Jun. 2013, doi: 10.1038/ncb2784.

[56] N. Ohtani, “The roles and mechanisms of senescence-associated secretory phenotype (SASP): can it be controlled by senolysis?,” *Inflamm. Regen.*, vol. 42, no. 1, pp. 1–8, Dec. 2022, doi: https://doi.org/10.1186/s41232-022-00197-8.

[57] M. Demaria *et al.*, “An essential role for senescent cells in optimal wound healing through secretion of PDGF-AA,” *Dev. Cell*, vol. 31, no. 6, pp. 722–733, Dec. 2014, doi: 10.1016/j.devcel.2014.11.012.

[58] S. Corda, J. L. Samuel, and L. Rappaport, “Extracellular Matrix and Growth Factors During Heart Growth,” *Hear. Fail. Rev. 2000 52*, vol. 5, no. 2, pp. 119–130, 2000, doi:

10.1023/A:1009806403194.

[59] H.-B. Kwak, “Aging, exercise, and extracellular matrix in the heart,” *J. Exerc. Rehabil.*, vol. 9, no. 3, pp. 338–347, 2013, doi: 10.12965/jer.130049.

[60] M. Rienks, A.-P. Papageorgiou, N. G. Frangogiannis, and S. Heymans, “Myocardial extracellular matrix: an ever-changing and diverse entity.,” *Circ. Res.*, vol. 114, no. 5, pp. 872–888, Feb. 2014, doi: 10.1161/CIRCRESAHA.114.302533.

[61] J. Glaser and K. Stienecker, “Pancreas and aging: a study using ultrasonography,” *Gerontology*, vol. 46, no. 2, pp. 93–96, 2000, doi: 10.1159/000022141.

[62] N. Gagliano *et al.*, “Age-dependent expression of fibrosis-related genes and collagen deposition in rat kidney cortex,” *J. Gerontol. A. Biol. Sci. Med. Sci.*, vol. 55, no. 8, 2000, doi: 10.1093/GERONA/55.8.B365.

[63] C. K. Abrass, M. J. Adcox, and G. J. Raugi, “Aging-Associated Changes in Renal Extracellular Matrix,” *Am. J. Patbology*, vol. 146, no. 3, 1995.

[64] C. Calabresi *et al.*, “Natural aging, expression of fibrosis-related genes and collagen deposition in rat lung,” *Exp. Gerontol.*, vol. 42, no. 10, pp. 1003–1011, Oct. 2007, doi: 10.1016/J.EXGER.2007.06.016.

[65] D. E. Hinton and W. L. Williams, “Hepatic Fibrosis Associated with Aging in Four Stocks of Mice,” *J. Gerontol.*, vol. 23, no. 2, pp. 205–211, Apr. 1968, doi: 10.1093/GERONJ/23.2.205.

[66] N. Gagliano, F. Grizzi, and G. Annoni, “Mechanisms of aging and liver functions,” *Dig. Dis.*, vol. 25, no. 2, pp. 118–123, Apr. 2007, doi: 10.1159/000099475.

[67] A. Biernacka and N. G. Frangogiannis, “Aging and Cardiac Fibrosis,” *Aging Dis.*, vol. 2, no. 2, pp. 158–173, 2011, doi: 10.1016/j.bbi.2008.05.010.

[68] M. Eghbali, M. Eghbali, T. F. Robinson, S. Seifter, and O. O. Blumenfeld, “Collagen accumulation in heart ventricles as a function of growth and aging,” *Cardiovasc. Res.*, vol. 23, no. 8, pp. 723–729, Aug. 1989, doi: 10.1093/CVR/23.8.723.

[69] J. M. Capasso, T. Palackal, G. Olivetti, and P. Anversa, “Severe myocardial dysfunction induced by ventricular remodeling in aging rat hearts,” *Am. J. Physiol.*, vol. 259, no. 4 Pt 2, 1990, doi: 10.1152/AJPHEART.1990.259.4.H1086.

[70] J. Lin *et al.*, “Age-related cardiac muscle sarcopenia: Combining experimental and mathematical modeling to identify mechanisms,” *Exp. Gerontol.*, vol. 43, no. 4, pp. 296–306, Apr. 2008, doi: 10.1016/J.EXGER.2007.12.005.

[71] B. I. Jugdutt *et al.*, “Aging-related early changes in markers of ventricular and matrix remodeling after reperfused st-segment elevation myocardial infarction in the canine model: Effect of early therapy with an angiotensin II type 1 receptor blocker,” *Circulation*, vol. 122, no. 4, pp. 341–351, Jul. 2010, doi: 10.1161/CIRCULATIONAHA.110.948190.

[72] C. R. Gazoti Debessa, L. B. Mesiano Maifrino, and R. Rodrigues de Souza, “Age related changes of the collagen network of the human heart,” *Mech. Ageing Dev.*, vol. 122, no. 10, pp. 1049–1058, 2001, doi: 10.1016/S0047-6374(01)00238-X.

[73] A. B. L. Mendes, M. Ferro, B. Rodrigues, M. R. de Souza, R. C. Araujo, and R. R. de Souza, “Quantification of left ventricular myocardial collagen system in children, young adults, and the elderly.,” *Medicina (B. Aires).*, vol. 72, no. 3, pp. 216–20, 2012, [Online]. Available: http://www.ncbi.nlm.nih.gov/pubmed/22763158.

[74] A. Burkauskiene, Z. Mackiewicz, I. Virtanen, and Y. T. Konttinen, “Age-related changes in myocardial nerve and collagen networks of the auricle of the right atrium,” *Acta Cardiol.*, vol. 61, no. 5, pp. 513–518, Oct. 2006, doi: 10.2143/AC.61.5.2017765.

[75] F. Gramley *et al.*, “Age-related atrial fibrosis,” *Age (Omaha).*, vol. 31, no. 1, pp. 27–38, Mar. 2009, doi: https://doi.org/10.1007%2Fs11357-008-9077-9.

[76] H. S. Karagueuzian, “Targeting cardiac fibrosis : a new frontier in antiarrhythmic therapy?,” *Am. J. Cardiovasc. Dis.*, vol. 1, no. 2, pp. 101–109, 2011.

[77] T. Kawara *et al.*, “Activation Delay After Premature Stimulation in Chronically Diseased Human Myocardium Relates to the Architecture of Interstitial Fibrosis,” *Circulation*, vol.

104, no. 25, pp. 3069–3075, 2001, doi: https://doi.org/10.1161/hc5001.100833.
[78] B. Swynghedauw, “Molecular mechanisms of myocardial remodeling,” *Physiol. Rev.*, vol. 79, no. 1, pp. 215–262, 1999, doi: 10.1152/PHYSREV.1999.79.1.215.
[79] J. M. De Bakker *et al.*, “Reentry as a cause of ventricular tachycardia in patients with chronic ischemic heart disease: electrophysiologic and anatomic correlation,” *Circulation*, vol. 77, no. 3, pp. 589–606, 1988, doi: 10.1161/01.CIR.77.3.589.
[80] J. M. de Bakker *et al.*, “Slow conduction in the infarcted human heart. ‘Zigzag’ course of activation.,” *Circulation*, vol. 88, no. 3, pp. 915–926, Sep. 1993, doi: 10.1161/01.cir.88.3.915.
[81] S. de Jong, T. A. B. van Veen, H. V. M. van Rijen, and J. M. T. de Bakker, “Fibrosis and Cardiac Arrhythmias,” *J. Cardiovasc. Pahrmacology*, vol. 57, no. 6, pp. 630–638, 2011, doi: 10.1097/FJC.0b013e318207a35f.
[82] E. L. Kessler, M. Boulaksil, H. V. M. van Rijen, M. A. Vos, and T. A. B. van Veen, “Passive ventricular remodeling in cardiac disease: focus on heterogeneity.,” *Front. Physiol.*, vol. 5, p. 482, 2014, doi: 10.3389/fphys.2014.00482.
[83] S. Dhein, “Gap junction channels in the cardiovascular system: pharmacological and physiological modulation.,” *Trends Pharmacol. Sci.*, vol. 19, no. 6, pp. 229–241, Jun. 1998, doi: 10.1016/s0165-6147(98)01192-4.
[84] N. S. Peters, C. R. Green, P. A. Poole-Wilson, and N. J. Severs, “Reduced content of connexin43 gap junctions in ventricular myocardium from hypertrophied and ischemic human hearts.,” *Circulation*, vol. 88, no. 3, pp. 864–875, Sep. 1993, doi: 10.1161/01.cir.88.3.864.
[85] A. F. Bruce, S. Rothery, E. Dupont, and N. J. Severs, “Gap junction remodelling in human heart failure is associated with increased interaction of connexin43 with ZO-1.,” *Cardiovasc. Res.*, vol. 77, no. 4, pp. 757–765, Mar. 2008, doi: 10.1093/cvr/cvm083.
[86] E. Dupont *et al.*, “Altered connexin expression in human congestive heart failure,” *J. Mol. Cell. Cardiol.*, vol. 33, no. 2, pp. 359–371, 2001, doi: 10.1006/JMCC.2000.1308.
[87] S. R. Kaplan *et al.*, “Remodeling of myocyte gap junctions in arrhythmogenic right ventricular cardiomyopathy due to a deletion in plakoglobin (Naxos disease),” *Hear. Rhythm*, vol. 1, no. 1, pp. 3–11, May 2004, doi: 10.1016/J.HRTHM.2004.01.001.
[88] A. Salameh *et al.*, “The signal transduction cascade regulating the expression of the gap junction protein connexin43 by beta-adrenoceptors.,” *Br. J. Pharmacol.*, vol. 158, no. 1, pp. 198–208, Sep. 2009, doi: 10.1111/j.1476-5381.2009.00344.x.
[89] T. Seidel, A. Salameh, and S. Dhein, “A simulation study of cellular hypertrophy and connexin lateralization in cardiac tissue.,” *Biophys. J.*, vol. 99, no. 9, pp. 2821–2830, Nov. 2010, doi: 10.1016/j.bpj.2010.09.010.
[90] L. Polontchouk *et al.*, “Effects of chronic atrial fibrillation on gap junction distribution in human and rat atria.,” *J. Am. Coll. Cardiol.*, vol. 38, no. 3, pp. 883–891, Sep. 2001, doi: 10.1016/s0735-1097(01)01443-7.
[91] S. Kostin, G. Klein, Z. Szalay, S. Hein, E. P. Bauer, and J. Schaper, “Structural correlate of atrial fibrillation in human patients.,” *Cardiovasc. Res.*, vol. 54, no. 2, pp. 361–379, May 2002, doi: 10.1016/s0008-6363(02)00273-0.
[92] T. A. Bonda *et al.*, “Remodeling of the intercalated disc related to aging in the mouse heart.,” *J. Cardiol.*, vol. 68, no. 3, pp. 261–268, Sep. 2016, doi: 10.1016/j.jjcc.2015.10.001.
[93] K. Boengler *et al.*, “Loss of ischemic preconditioning’s cardioprotection in aged mouse hearts is associated with reduced gap junctional and mitochondrial levels of connexin 43.,” *Am. J. Physiol. Heart Circ. Physiol.*, vol. 292, no. 4, pp. H1764-9, Apr. 2007, doi: 10.1152/ajpheart.01071.2006.
[94] S. Dhein and S. B. Hammerath, “Aspects of the intercellular communication in aged hearts: effects of the gap junction uncoupler palmitoleic acid.,” *Naunyn. Schmiedebergs. Arch. Pharmacol.*, vol. 364, no. 5, pp. 397–408, Nov. 2001, doi: 10.1007/s002100100462.
[95] M. Chen and D. L. Jones, “Age- and myopathy-dependent changes in connexins of normal

and cardiomyopathic Syrian hamster ventricular myocardium.," *Can. J. Physiol. Pharmacol.*, vol. 78, no. 8, pp. 669–678, Aug. 2000.

[96] M. Watanabe, S. Ichinose, and M. Sunamori, "Age-related changes in gap junctional protein of the rat heart.," *Exp. Clin. Cardiol.*, vol. 9, no. 2, pp. 130–132, 2004.

[97] S. Moscato *et al.*, "Heart and liver connexin expression related to the first stage of aging: A study on naturally aged animals.," *Acta Histochem.*, vol. 122, no. 8, p. 151651, Dec. 2020, doi: 10.1016/j.acthis.2020.151651.

[98] D. W. Laird, P. D. Lampe, and R. G. Johnson, "Dinámica y función de las uniones intercelulares," *Investig. y ciencia, ISSN 0210-136X, Nº 466, 2015, págs. 66-73*, no. 466, pp. 66–73, 2015, Accessed: Feb. 13, 2023. [Online]. Available: https://dialnet.unirioja.es/servlet/articulo?codigo=5155220.

[99] L. Carrier *et al.*, "Expression of the sarcomeric actin isogenes in the rat heart with development and senescence.," *Circ. Res.*, vol. 70, no. 5, pp. 999–1005, 1992, doi: 10.1161/01.RES.70.5.999.

[100] N. Bodyak *et al.*, "Gene expression profiling of the aging mouse cardiac myocytes.," *Nucleic Acids Res.*, vol. 30, no. 17, pp. 3788–3794, Sep. 2002, doi: 10.1093/nar/gkf497.

[101] M. U. Koban, A. F. Moorman, J. Holtz, M. H. Yacoub, and K. R. Boheler, "Expressional analysis of the cardiac Na-Ca exchanger in rat development and senescence.," *Cardiovasc. Res.*, vol. 37, no. 2, pp. 405–423, Feb. 1998, doi: 10.1016/s0008-6363(97)00276-9.

[102] B. S. Cain *et al.*, "Human SERCA2a levels correlate inversely with age in senescent human myocardium," *J. Am. Coll. Cardiol.*, vol. 32, no. 2, pp. 458–467, Aug. 1998, doi: 10.1016/S0735-1097(98)00233-2.

[103] C. De Lucia *et al.*, "MicroRNA in cardiovascular aging and age-related cardiovascular diseases," *Front. Med.*, vol. 4, p. 74, Jun. 2017, doi: 10.3389/FMED.2017.00074/BIBTEX.

[104] S. Dimmeler and P. Nicotera, "MicroRNAs in age-related diseases," *EMBO Mol. Med.*, vol. 5, no. 2, pp. 180–190, Feb. 2013, doi: 10.1002/EMMM.201201986.

[105] S. Lin and R. I. Gregory, "MicroRNA biogenesis pathways in cancer," *Nat. Rev. Cancer 2015 156*, vol. 15, no. 6, pp. 321–333, May 2015, doi: 10.1038/nrc3932.

[106] G. C. van Almen *et al.*, "MicroRNA-18 and microRNA-19 regulate CTGF and TSP-1 expression in age-related heart failure," *Aging Cell*, vol. 10, no. 5, pp. 769–779, 2011, doi: 10.1111/j.1474-9726.2011.00714.x.

[107] V. Jazbutyte *et al.*, "MicroRNA-22 increases senescence and activates cardiac fibroblasts in the aging heart.," *Age (Dordr).*, vol. 35, no. 3, pp. 747–762, Jun. 2013, doi: 10.1007/s11357-012-9407-9.

[108] R. A. Boon *et al.*, "MicroRNA-34a regulates cardiac ageing and function," *Nature*, vol. 495, p. 107, Feb. 2013, [Online]. Available: http://dx.doi.org/10.1038/nature11919.

[109] I. Rusanova *et al.*, "Analysis of Plasma MicroRNAs as Predictors and Biomarkers of Aging and Frailty in Humans.," *Oxid. Med. Cell. Longev.*, vol. 2018, p. 7671850, 2018, doi: 10.1155/2018/7671850.

[110] J. Yang *et al.*, "Synchronized age-related gene expression changes across multiple tissues in human and the link to complex diseases," *Sci. Rep.*, vol. 5, no. October, p. 15145, 2015, doi: 10.1038/srep15145.

[111] J. Jylhävä, N. L. Pedersen, and S. Hägg, "Biological Age Predictors," *EBioMedicine*, vol. 21, pp. 29–36, Jul. 2017, doi: 10.1016/J.EBIOM.2017.03.046.

[112] S. Studenski *et al.*, "Gait speed and survival in older adults," *JAMA*, vol. 305, no. 1, pp. 50–58, Jan. 2011, doi: 10.1001/JAMA.2010.1923.

[113] R. J. J. Gobbens, M. A. L. M. van Assen, and M. J. D. Schalk, "The prediction of disability by self-reported physical frailty components of the Tilburg Frailty Indicator (TFI)," *Arch. Gerontol. Geriatr.*, vol. 59, no. 2, pp. 280–287, Sep. 2014, doi: 10.1016/J.ARCHGER.2014.06.008.

[114] R. Cooper, D. Kuh, and R. Hardy, "Objectively measured physical capability levels and

mortality: systematic review and meta-analysis," *BMJ*, vol. 341, no. 7774, p. 639, Sep. 2010, doi: 10.1136/BMJ.C4467.

[115] E. L. de Hollander *et al.*, "The association between waist circumference and risk of mortality considering body mass index in 65- to 74-year-olds: a meta-analysis of 29 cohorts involving more than 58 000 elderly persons," *Int. J. Epidemiol.*, vol. 41, no. 3, pp. 805–817, Jun. 2012, doi: 10.1093/IJE/DYS008.

[116] I. Janssen, S. B. Heymsfield, and R. Ross, "Low relative skeletal muscle mass (sarcopenia) in older persons is associated with functional impairment and physical disability," *J. Am. Geriatr. Soc.*, vol. 50, no. 5, pp. 889–896, 2002, doi: 10.1046/J.1532-5415.2002.50216.X.

[117] S. MacMahon *et al.*, "Body-mass index and cause-specific mortality in 900 000 adults: collaborative analyses of 57 prospective studies," *Lancet (London, England)*, vol. 373, no. 9669, pp. 1083–1096, Mar. 2009, doi: 10.1016/S0140-6736(09)60318-4.

[118] K. H. Wagner, D. Cameron-Smith, B. Wessner, and B. Franzke, "Biomarkers of Aging: From Function to Molecular Biology," *Nutrients*, vol. 8, no. 6, Jun. 2016, doi: 10.3390/NU8060338.

[119] N. Sarwar *et al.*, "Triglycerides and the risk of coronary heart disease: 10,158 incident cases among 262,525 participants in 29 Western prospective studies," *Circulation*, vol. 115, no. 4, pp. 450–458, Jan. 2007, doi: 10.1161/CIRCULATIONAHA.106.637793.

[120] S. MacMahon *et al.*, "Blood cholesterol and vascular mortality by age, sex, and blood pressure: a meta-analysis of individual data from 61 prospective studies with 55,000 vascular deaths," *Lancet (London, England)*, vol. 370, no. 9602, pp. 1829–1839, Dec. 2007, doi: 10.1016/S0140-6736(07)61778-4.

[121] C. Franceschi *et al.*, "Inflamm-aging: An Evolutionary Perspective on Immunosenescence," *Ann. N. Y. Acad. Sci.*, vol. 908, no. 1, pp. 244–254, Jun. 2000, doi: 10.1111/J.1749-6632.2000.TB06651.X.

[122] S. Giovannini *et al.*, "Interleukin-6, C-reactive protein, and tumor necrosis factor-alpha as predictors of mortality in frail, community-living elderly individuals," *J. Am. Geriatr. Soc.*, vol. 59, no. 9, pp. 1679–1685, Sep. 2011, doi: 10.1111/J.1532-5415.2011.03570.X.

[123] Y. Arai *et al.*, "Inflammation, But Not Telomere Length, Predicts Successful Ageing at Extreme Old Age: A Longitudinal Study of Semi-supercentenarians," *EBioMedicine*, vol. 2, no. 10, pp. 1549–1558, Oct. 2015, doi: 10.1016/J.EBIOM.2015.07.029.

[124] S. Horvath, "DNA methylation age of human tissues and cell types," *Genome Biol.*, vol. 14, no. 10, pp. 1–20, Oct. 2013, doi: 10.1186/gb-2013-14-10-r115.

[125] G. Hannum *et al.*, "Genome-wide methylation profiles reveal quantitative views of human aging rates," *Mol. Cell*, vol. 49, no. 2, pp. 359–367, Jan. 2013, doi: 10.1016/J.MOLCEL.2012.10.016.

[126] A. E. Field, N. A. Robertson, T. Wang, A. Havas, T. Ideker, and P. D. Adams, "DNA Methylation Clocks in Aging: Categories, Causes, and Consequences," *Mol. Cell*, vol. 71, no. 6, p. 882, Sep. 2018, doi: 10.1016/J.MOLCEL.2018.08.008.

[127] M. J. Peters *et al.*, "The transcriptional landscape of age in human peripheral blood," *Nat. Commun.*, vol. 6, Oct. 2015, doi: 10.1038/NCOMMS9570.

[128] H. Rhinn and A. Abeliovich, "Differential Aging Analysis in Human Cerebral Cortex Identifies Variants in TMEM106B and GRN that Regulate Aging Phenotypes," *Cell Syst.*, vol. 4, no. 4, pp. 404-415.e5, Apr. 2017, doi: 10.1016/j.cels.2017.02.009.

[129] J. Rutledge, H. Oh, and T. Wyss-Coray, "Measuring biological age using omics data," *Nat. Rev. Genet. 2022 2312*, vol. 23, no. 12, pp. 715–727, Jun. 2022, doi: 10.1038/s41576-022-00511-7.

[130] X. Xia, W. Chen, J. McDermott, and J.-D. J. Han, "Molecular and phenotypic biomarkers of aging.," *F1000Research*, vol. 6, p. 860, 2017, doi: 10.12688/f1000research.10692.1.

[131] J. Krishnamurthy *et al.*, "Ink4a/Arf expression is a biomarker of aging," *J. Clin. Invest.*, vol. 114, no. 9, pp. 1299–1307, Nov. 2004, doi: 10.1172/JCI22475.

[132] M. E. C. Waaijer *et al.*, "The number of p16INK4a positive cells in human skin reflects

biological age," *Aging Cell*, vol. 11, no. 4, pp. 722–725, Aug. 2012, doi: 10.1111/J.1474-9726.2012.00837.X.

[133] Y. Liu *et al.*, "Expression of p16INK4a in peripheral blood T-cells is a biomarker of human aging," *Aging Cell*, vol. 8, no. 4, pp. 439–448, Aug. 2009, doi: 10.1111/J.1474-9726.2009.00489.X.

[134] K. S. Kudryashova, K. Burka, A. Y. Kulaga, N. S. Vorobyeva, and B. K. Kennedy, "Aging Biomarkers: From Functional Tests to Multi-Omics Approaches," *Proteomics*, vol. 20, no. 5–6, p. 1900408, Mar. 2020, doi: 10.1002/PMIC.201900408.

[135] C. Soriano-Tárraga *et al.*, "Biological Age is a predictor of mortality in Ischemic Stroke," *Sci. Reports 2018 81*, vol. 8, no. 1, pp. 1–8, Mar. 2018, doi: 10.1038/s41598-018-22579-0.

[136] L. Lind, E. Ingelsson, J. Sundström, A. Siegbahn, and E. Lampa, "Methylation-based estimated biological age and cardiovascular disease," *Eur. J. Clin. Invest.*, vol. 48, no. 2, p. e12872, Feb. 2018, doi: 10.1111/ECI.12872.

[137] A. C. Guyton and J. E. Hall, *Textbook of Medical Physiology*, 12th ed. Elsevier, 2011.

[138] A. O. Grant, "Cardiac Ion Channels," *Circ. Arrhythmia Electrophysiol.*, vol. 2, no. 2, pp. 185–194, Apr. 2009, doi: 10.1161/CIRCEP.108.789081.

[139] E. N. Marieb and K. Hoehn, *Human Anatomy & Physiology*. 2013.

[140] F. H. Martini and J. L. Nath, *Fundamentals of anatomy & Physiology*. Pearson, 2015.

[141] Z. Song, C. Y. Ko, M. Nivala, J. N. Weiss, and Z. Qu, "Calcium-Voltage Coupling in the Genesis of Early and Delayed Afterdepolarizations in Cardiac Myocytes," *Biophys. J.*, vol. 108, no. 8, p. 1908, Apr. 2015, doi: 10.1016/J.BPJ.2015.03.011.

[142] M. Hoekstra, C. L. Mummery, A. A. M. Wilde, C. R. Bezzina, and A. O. Verkerk, "Induced pluripotent stem cell derived cardiomyocytes as models for cardiac arrhythmias," *Front. Physiol.*, vol. 3, 2012, doi: 10.3389/FPHYS.2012.00346.

[143] M. K. Stokke, F. Rivelsrud, I. Sjaastad, O. M. Sejersted, and F. Swift, "From global to local: a new understanding of cardiac electromechanical coupling.," *Tidsskr. Nor. Laegeforen.*, vol. 132, no. 12–13, pp. 1457–1460, Jun. 2012, doi: 10.4045/tidsskr.11.1353.

[144] S. A. Niederer, P. J. Hunter, and N. P. Smith, "A Quantitative Analysis of Cardiac Myocyte Relaxation: A Simulation Study," *Biophys. J.*, vol. 90, no. 5, pp. 1697–1722, Mar. 2006, doi: 10.1529/BIOPHYSJ.105.069534.

[145] P. Kohl, C. Bollensdorff, and A. Garny, "Effects of mechanosensitive ion channels on ventricular electrophysiology: experimental and theoretical models," *Exp. Physiol.*, vol. 91, no. 2, pp. 307–321, Mar. 2006, doi: 10.1113/EXPPHYSIOL.2005.031062.

[146] P. Taggart and M. Lab, "Cardiac mechano-electric feedback and electrical restitution in humans," *Prog. Biophys. Mol. Biol.*, vol. 97, no. 2–3, pp. 452–460, Jun. 2008, doi: 10.1016/J.PBIOMOLBIO.2008.02.021.

[147] D. A. Jaye, Y.-F. Xiao, and D. C. Sigg, "Basic Cardiac Electrophysiology: Excitable Membranes," *Card. Electrophysiol. Methods Model.*, pp. 41–51, 2010, doi: 10.1007/978-1-4419-6658-2_2.

[148] P. R. E. Harris, "The Normal Electrocardiogram: Resting 12-Lead and Electrocardiogram Monitoring in the Hospital.," *Crit. Care Nurs. Clin. North Am.*, vol. 28, no. 3, pp. 281–296, Sep. 2016, doi: 10.1016/j.cnc.2016.04.002.

[149] R. B. Colquitt, D. A. Colquhoun, and R. H. Thiele, "In silico modelling of physiologic systems," *Best Pract. Res. Clin. Anaesthesiol.*, vol. 25, no. 4, pp. 499–510, 2011, doi: 10.1016/J.BPA.2011.08.006.

[150] A. L. Hodgkin and A. F. Huxley, "A quantitative description of membrane current and its application to conduction and excitation in nerve," *J. Physiol.*, vol. 117, no. 4, p. 500, Aug. 1952, doi: 10.1113/JPHYSIOL.1952.SP004764.

[151] R. Appali, U. van Rienen, and T. Heimburg, "Chapter Nine - A Comparison of the Hodgkin–Huxley Model and the Soliton Theory for the Action Potential in Nerves," vol. 16, A. Iglič, Ed. Academic Press, 2012, pp. 275–299.

[152] D. Noble, “A modification of the Hodgkin--Huxley equations applicable to Purkinje fibre action and pace-maker potentials.,” *J. Physiol.*, vol. 160, no. 2, pp. 317–352, Feb. 1962, doi: 10.1113/jphysiol.1962.sp006849.

[153] H. Krause, H. Antoni, and A. Fleckenstein, “[An electronic model for the formation of local and transmitted stimuli on the myocardium fibers based upon variable current-voltage characteristics for potassium and sodium ions].,” *Pflugers Arch. Gesamte Physiol. Menschen Tiere*, vol. 289, no. 1, pp. 12–36, 1966.

[154] D. Noble, A. Garny, and P. J. Noble, “How the Hodgkin-Huxley equations inspired the Cardiac Physiome Project,” *J. Physiol.*, vol. 590, no. 11, pp. 2613–2628, Jun. 2012, doi: 10.1113/JPHYSIOL.2011.224238.

[155] A. P. Benson, H. J. Stevenson-Cocks, D. G. Whittaker, E. White, and M. A. Colman, “Multi-scale approaches for the simulation of cardiac electrophysiology: II – Tissue-level structure and function,” *Methods*, vol. 185, pp. 60–81, Jan. 2021, doi: 10.1016/J.YMETH.2020.01.010.

[156] K. H. W. J. Ten Tusscher and A. V. Panfilov, “Alternans and spiral breakup in a human ventricular tissue model,” *Am. J. Physiol. Heart Circ. Physiol.*, vol. 291, no. 3, 2006, doi: 10.1152/AJPHEART.00109.2006.

[157] E. Grandi, F. S. Pasqualini, and D. M. Bers, “A novel computational model of the human ventricular action potential and Ca transient,” *J. Mol. Cell. Cardiol.*, vol. 48, no. 1, pp. 112–121, Jan. 2010, doi: 10.1016/J.YJMCC.2009.09.019.

[158] B. Carbonell-Pascual, E. Godoy, A. Ferrer, L. Romero, and J. M. Ferrero, “Comparison between Hodgkin–Huxley and Markov formulations of cardiac ion channels,” *J. Theor. Biol.*, vol. 399, pp. 92–102, Jun. 2016, doi: 10.1016/J.JTBI.2016.03.039.

[159] Z. Qu *et al.*, “Early afterdepolarizations in cardiac myocytes: beyond reduced repolarization reserve,” *Cardiovasc. Res.*, vol. 99, no. 1, pp. 6–15, Jul. 2013, doi: 10.1093/CVR/CVT104.

[160] P. Pathmanathan *et al.*, “A numerical guide to the solution of the bi-domain equations of cardiac electrophysiology.,” *Prog. Biophys. Mol. Biol.*, vol. 102, no. 2–3, pp. 136–155, 2010, doi: 10.1016/j.pbiomolbio.2010.05.006.

[161] E. Vigmond and G. Plank, “Cardiac Modeling,” *Encycl. Biomed. Eng.*, vol. 1–3, pp. 1–20, Jan. 2019, doi: 10.1016/B978-0-12-801238-3.99985-9.

[162] E. Cevenini *et al.*, “Human models of aging and longevity,” *Expert Opin. Biol. Ther.*, vol. 8, no. 9, pp. 1393–1405, Sep. 2008, doi: 10.1517/14712598.8.9.1393.

[163] P. Gueresi *et al.*, “The MALVA (MAntova LongeVA) study: An investigation on people 98 years of age and over in a province of Northern Italy,” *Exp. Gerontol.*, vol. 38, no. 10, pp. 1189–1197, 2003, doi: 10.1016/j.exger.2003.08.006.

[164] L. Deiana *et al.*, “AKEntAnnos. The Sardinia study of extreme longevity,” *Aging Clin. Exp. Res.*, vol. 11, no. 3, pp. 142–149, Jun. 1999, doi: 10.1007/BF03399655/METRICS.

[165] P. Sansoni *et al.*, “The immune system in extreme longevity,” *Exp. Gerontol.*, vol. 43, no. 2, pp. 61–65, Feb. 2008, doi: 10.1016/J.EXGER.2007.06.008.

[166] J. Deelen *et al.*, “A meta-analysis of genome-wide association studies identifies multiple longevity genes,” *Nat. Commun. 2019 101*, vol. 10, no. 1, pp. 1–14, Aug. 2019, doi: 10.1038/s41467-019-11558-2.

[167] D. C. Willcox, B. J. Willcox, W. C. Hsueh, and M. Suzuki, “Genetic determinants of exceptional human longevity: insights from the Okinawa Centenarian Study,” *Age (Omaha).*, vol. 28, no. 4, p. 313, Dec. 2006, doi: 10.1007/S11357-006-9020-X.

[168] T. T. Perls *et al.*, “Life-long sustained mortality advantage of siblings of centenarians,” *Proc. Natl. Acad. Sci. U. S. A.*, vol. 99, no. 12, pp. 8442–8447, Jun. 2002, doi: 10.1073/PNAS.122587599.

[169] G. Atzmon, C. Schechter, W. Greiner, D. Davidson, G. Rennert, and N. Barzilai, “Clinical phenotype of families with longevity,” *J. Am. Geriatr. Soc.*, vol. 52, no. 2, pp. 274–277, Feb. 2004, doi: 10.1111/J.1532-5415.2004.52068.X.

[170] H. Nybo, D. Gaist, B. Jeune, M. McGue, J. W. Vaupel, and K. Christensen, “Functional status and self-rated health in 2,262 nonagenarians: the Danish 1905 Cohort Survey,” *J. Am. Geriatr. Soc.*, vol. 49, no. 5, pp. 601–609, 2001, doi: 10.1046/J.1532-5415.2001.49121.X.

[171] A. Bootsma-van der Wiel *et al.*, “A high response is not essential to prevent selection bias: Results from the Leiden 85-plus study,” *J. Clin. Epidemiol.*, vol. 55, no. 11, pp. 1119–1125, Nov. 2002, doi: 10.1016/S0895-4356(02)00505-X.

[172] L. Ferrucci *et al.*, “Subsystems contributing to the decline in ability to walk: bridging the gap between epidemiology and geriatric practice in the InCHIANTI study,” *J. Am. Geriatr. Soc.*, vol. 48, no. 12, pp. 1618–1625, 2000, doi: 10.1111/J.1532-5415.2000.TB03873.X.

[173] A. Brunet, “Old and new models for the study of human ageing,” *Nat. Rev. Mol. Cell Biol.*, vol. 21, no. 9, pp. 491–493, Sep. 2020, doi: 10.1038/S41580-020-0266-4.

[174] M. D. W. Piper and L. Partridge, “Drosophila as a model for ageing,” *Biochim. Biophys. Acta - Mol. Basis Dis.*, vol. 1864, no. 9, pp. 2707–2717, Sep. 2018, doi: 10.1016/J.BBADIS.2017.09.016.

[175] A. Denoth Lippuner, T. Julou, and Y. Barral, “Budding yeast as a model organism to study the effects of age,” *FEMS Microbiol. Rev.*, vol. 38, no. 2, pp. 300–325, Mar. 2014, doi: 10.1111/1574-6976.12060.

[176] A. Olsen, M. C. Vantipalli, and G. J. Lithgow, “Using Caenorhabditis elegans as a model for aging and age-related diseases,” *Ann. N. Y. Acad. Sci.*, vol. 1067, no. 1, pp. 120–128, 2006, doi: 10.1196/ANNALS.1354.015.

[177] S. J. Mitchell, M. Scheibye-Knudsen, D. L. Longo, and R. De Cabo, “Animal models of aging research: implications for human aging and age-related diseases,” *Annu. Rev. Anim. Biosci.*, vol. 3, pp. 283–303, Feb. 2015, doi: 10.1146/ANNUREV-ANIMAL-022114-110829.

[178] M. J. H. Gilbert, T. C. Zerulla, and K. B. Tierney, “Zebrafish (Danio rerio) as a model for the study of aging and exercise: physical ability and trainability decrease with age,” *Exp. Gerontol.*, vol. 50, no. 1, pp. 106–113, Dec. 2014, doi: 10.1016/J.EXGER.2013.11.013.

[179] G. S. Roth, J. A. Mattison, M. A. Ottinger, M. E. Chachich, M. A. Lane, and D. K. Ingram, “Aging in rhesus monkeys: relevance to human health interventions,” *Science*, vol. 305, no. 5689, pp. 1423–1426, Sep. 2004, doi: 10.1126/SCIENCE.1102541.

[180] H. F. Huber, P. W. Nathanielsz, and G. D. Clarke, “Summary and Assessment of Studies on Cardiac Aging in Nonhuman Primates,” *Comp. Med.*, vol. 71, no. 6, p. 1, Dec. 2021, doi: 10.30802/AALAS-CM-21-000038.

[181] M. Kaeberlein, K. E. Creevy, and D. E. L. Promislow, “The dog aging project: translational geroscience in companion animals,” *Mamm. Genome*, vol. 27, no. 7–8, pp. 279–288, Aug. 2016, doi: 10.1007/S00335-016-9638-7.

[182] J. M. Hoffman, K. E. Creevy, A. Franks, D. G. O’Neill, and D. E. L. Promislow, “The companion dog as a model for human aging and mortality,” *Aging Cell*, vol. 17, no. 3, Jun. 2018, doi: 10.1111/ACEL.12737.

[183] B. Dorado *et al.*, “Generation and characterization of a novel knockin minipig model of Hutchinson-Gilford progeria syndrome,” *Cell Discov. 2019 51*, vol. 5, no. 1, pp. 1–15, Mar. 2019, doi: 10.1038/s41421-019-0084-z.

[184] V. Fanjul *et al.*, “Identification of common cardiometabolic alterations and deregulated pathways in mouse and pig models of aging,” *Aging Cell*, vol. 19, no. 9, p. e13203, Sep. 2020, doi: 10.1111/ACEL.13203.

[185] F. Wang *et al.*, “Generation of a Hutchinson–Gilford progeria syndrome monkey model by base editing,” *Protein Cell*, vol. 11, no. 11, pp. 809–824, Nov. 2020, doi: https://doi.org/10.1007/s13238-020-00740-8.

[186] N. Cai, Y. Wu, and Y. Huang, “Induction of Accelerated Aging in a Mouse Model,” *Cells*, vol. 11, no. 9, May 2022, doi: 10.3390/CELLS11091418.

[187] E. Fielder *et al.*, “Sublethal whole-body irradiation causes progressive premature frailty in mice,” *Mech. Ageing Dev.*, vol. 180, pp. 63–69, Jun. 2019, doi:

10.1016/J.MAD.2019.03.006.

[188] L. Käsmann *et al.*, “Radiation-induced lung toxicity - Cellular and molecular mechanisms of pathogenesis, management, and literature review,” *Radiat. Oncol.*, vol. 15, no. 1, pp. 1–16, Sep. 2020, doi: 10.1186/s13014-020-01654-9.

[189] A. Trifunovic *et al.*, “Premature ageing in mice expressing defective mitochondrial DNA polymerase,” *Nat. 2004 4296990*, vol. 429, no. 6990, pp. 417–423, May 2004, doi: 10.1038/nature02517.

[190] D. Carrero, C. Soria-Valles, and C. López-Otín, “Hallmarks of progeroid syndromes: lessons from mice and reprogrammed cells,” *Dis. Model. Mech.*, vol. 9, no. 7, p. 719, Jul. 2016, doi: 10.1242/DMM.024711.

[191] K. F. Azman and R. Zakaria, “d-Galactose-induced accelerated aging model: an overview,” *Biogerontology 2019 206*, vol. 20, no. 6, pp. 763–782, Sep. 2019, doi: 10.1007/S10522-019-09837-Y.

[192] T. Cebe *et al.*, “A comprehensive study of myocardial redox homeostasis in naturally and mimetically aged rats,” *Age (Dordr).*, vol. 36, no. 6, Nov. 2014, doi: 10.1007/S11357-014-9728-Y.

[193] M. Ji *et al.*, “Comparison of naturally aging and D-galactose induced aging model in beagle dogs,” *Exp. Ther. Med.*, vol. 14, no. 6, pp. 5881–5888, Dec. 2017, doi: 10.3892/ETM.2017.5327/HTML.

[194] D. Games *et al.*, “Alzheimer-type neuropathology in transgenic mice overexpressing V717F β-amyloid precursor protein,” *Nat. 1995 3736514*, vol. 373, no. 6514, pp. 523–527, Feb. 1995, doi: 10.1038/373523a0.

[195] A. M. Hall and E. D. Roberson, “Mouse models of Alzheimer’s disease,” *Brain Res. Bull.*, vol. 88, no. 1, pp. 3–12, May 2012, doi: 10.1016/J.BRAINRESBULL.2011.11.017.

[196] S. Oddo *et al.*, “Triple-transgenic model of Alzheimer’s Disease with plaques and tangles: Intracellular Aβ and synaptic dysfunction,” *Neuron*, vol. 39, no. 3, pp. 409–421, Jul. 2003, doi: 10.1016/S0896-6273(03)00434-3.

[197] D. Capitanio *et al.*, “Collagen VI null mice as a model for early onset muscle decline in aging,” *Front. Mol. Neurosci.*, vol. 10, p. 337, Oct. 2017, doi: 10.3389/FNMOL.2017.00337/BIBTEX.

[198] S. Q. Gregg *et al.*, “A mouse model of accelerated liver aging due to a defect in DNA repair,” *Hepatology*, vol. 55, no. 2, p. 609, Feb. 2012, doi: 10.1002/HEP.24713.

[199] N. A. Noll, H. Lal, and W. D. Merryman, “Mouse Models of Heart Failure with Preserved or Reduced Ejection Fraction,” *Am. J. Pathol.*, vol. 190, no. 8, pp. 1596–1608, Aug. 2020, doi: 10.1016/J.AJPATH.2020.04.006.

[200] C. Withaar *et al.*, “The effects of liraglutide and dapagliflozin on cardiac function and structure in a multi-hit mouse model of heart failure with preserved ejection fraction,” *Cardiovasc. Res.*, vol. 117, no. 9, pp. 2108–2124, Jul. 2021, doi: 10.1093/CVR/CVAA256.

[201] K. Takahashi and S. Yamanaka, “Induction of Pluripotent Stem Cells from Mouse Embryonic and Adult Fibroblast Cultures by Defined Factors,” *Cell*, vol. 126, no. 4, pp. 663–676, 2006, doi: 10.1016/j.cell.2006.07.024.

[202] K. Takahashi *et al.*, “Induction of Pluripotent Stem Cells from Adult Human Fibroblasts by Defined Factors,” *Cell*, vol. 131, no. 5, pp. 861–872, 2007, doi: 10.1016/j.cell.2007.11.019.

[203] E. A. Chang, S. W. Jin, M. H. Nam, and S. D. Kim, “Human Induced Pluripotent Stem Cells : Clinical Significance and Applications in Neurologic Diseases,” *J. Korean Neurosurg. Soc.*, vol. 62, no. 5, pp. 493–501, Sep. 2019, doi: 10.3340/JKNS.2018.0222.

[204] E. Giacomelli, C. L. Mummery, and M. Bellin, “Human heart disease: lessons from human pluripotent stem cell-derived cardiomyocytes,” *Cell. Mol. Life Sci.*, vol. 74, no. 20, pp. 3711–3739, Oct. 2017, doi: 10.1007/S00018-017-2546-5.

[205] T. Egashira *et al.*, “Disease characterization using LQTS-specific induced pluripotent stem cells,” *Cardiovasc. Res.*, vol. 95, no. 4, pp. 419–429, Sep. 2012, doi: 10.1093/CVR/CVS206.

[206] P. W. Burridge *et al.*, “Chemically defined generation of human cardiomyocytes,” *Nat.*

Methods 2014 118, vol. 11, no. 8, pp. 855–860, Jun. 2014, doi: 10.1038/nmeth.2999.

[207] D. A. Elliott *et al.*, “NKX2-5eGFP/w hESCs for isolation of human cardiac progenitors and cardiomyocytes,” *Nat. Methods 2011 812*, vol. 8, no. 12, pp. 1037–1040, Oct. 2011, doi: 10.1038/nmeth.1740.

[208] N. C. Dubois *et al.*, “SIRPA is a specific cell-surface marker for isolating cardiomyocytes derived from human pluripotent stem cells,” *Nat. Biotechnol.*, vol. 29, no. 11, pp. 1011–1018, Nov. 2011, doi: 10.1038/NBT.2005.

[209] C. C. Veerman, G. Kosmidis, C. L. Mummery, S. Casini, A. O. Verkerk, and M. Bellin, “Immaturity of human stem-cell-derived cardiomyocytes in culture: fatal flaw or soluble problem?,” *Stem Cells Dev.*, vol. 24, no. 9, pp. 1035–52, 2015, doi: 10.1089/scd.2014.0533.

[210] E. Matsa, J. H. Ahrens, and J. C. Wu, “Human induced pluripotent stem cells as a platform for personalized and precision cardiovascular medicine,” *Physiol. Rev.*, vol. 96, no. 3, pp. 1093–1126, Jul. 2016, doi: 10.1152/PHYSREV.00036.2015/ASSET/IMAGES/LARGE/Z9J0031627670005.JPEG.

[211] A. Moretti *et al.*, “Patient-Specific Induced Pluripotent Stem-Cell Models for Long-QT Syndrome,” *N. Engl. J. Med.*, vol. 363, no. 15, pp. 1397–1409, Oct. 2010, doi: 10.1056/NEJMOA0908679/SUPPL_FILE/NEJMOA0908679_DISCLOSURES.PDF.

[212] D. Ma *et al.*, “Characterization of a novel KCNQ1 mutation for type 1 long QT syndrome and assessment of the therapeutic potential of a novel IKs activator using patient-specific induced pluripotent stem cell-derived cardiomyocytes,” *Stem Cell Res. Ther.*, vol. 6, no. 1, pp. 1–13, Mar. 2015, doi: https://doi.org/10.1186/s13287-015-0027-z.

[213] Y. Wang *et al.*, “Genome Editing of Isogenic Human Induced Pluripotent Stem Cells Recapitulates Long QT Phenotype for Drug Testing,” *J. Am. Coll. Cardiol.*, vol. 64, no. 5, pp. 451–459, Aug. 2014, doi: 10.1016/J.JACC.2014.04.057.

[214] E. Matsa *et al.*, “Drug evaluation in cardiomyocytes derived from human induced pluripotent stem cells carrying a long QT syndrome type 2 mutation,” *Eur. Heart J.*, vol. 32, no. 8, pp. 952–962, Apr. 2011, doi: 10.1093/EURHEARTJ/EHR073.

[215] S. R. Braam *et al.*, “Repolarization reserve determines drug responses in human pluripotent stem cell derived cardiomyocytes,” *Stem Cell Res.*, vol. 10, no. 1, pp. 48–56, Jan. 2013, doi: 10.1016/J.SCR.2012.08.007.

[216] I. Itzhaki *et al.*, “Modelling the long QT syndrome with induced pluripotent stem cells,” *Nat. 2010 4717337*, vol. 471, no. 7337, pp. 225–229, Jan. 2011, doi: 10.1038/nature09747.

[217] A. L. Lahti *et al.*, “Model for long QT syndrome type 2 using human iPS cells demonstrates arrhythmogenic characteristics in cell culture,” *Dis. Model. Mech.*, vol. 5, no. 2, pp. 220–230, Mar. 2012, doi: 10.1242/DMM.008409.

[218] M. Bellin *et al.*, “Isogenic human pluripotent stem cell pairs reveal the role of a KCNH2 mutation in long-QT syndrome,” *EMBO J.*, vol. 32, no. 24, pp. 3161–3175, Dec. 2013, doi: 10.1038/EMBOJ.2013.240.

[219] A. Mehta *et al.*, “Re-trafficking of hERG reverses long QT syndrome 2 phenotype in human iPS-derived cardiomyocytes,” *Cardiovasc. Res.*, vol. 102, no. 3, pp. 497–506, Jun. 2014, doi: 10.1093/CVR/CVU060.

[220] H. P. Huang *et al.*, “Human Pompe disease-induced pluripotent stem cells for pathogenesis modeling, drug testing and disease marker identification,” *Hum. Mol. Genet.*, vol. 20, no. 24, pp. 4851–4864, Dec. 2011, doi: 10.1093/HMG/DDR424.

[221] K. K. Raval *et al.*, “Pompe disease results in a Golgi-based glycosylation deficit in human induced pluripotent stem cell-derived cardiomyocytes,” *J. Biol. Chem.*, vol. 290, no. 5, pp. 3121–3136, Jan. 2015, doi: 10.1074/jbc.M114.628628.

[222] Y. Sato *et al.*, “Disease modeling and lentiviral gene transfer in patient-specific induced pluripotent stem cells from late-onset Pompe disease patient,” *Mol. Ther. - Methods Clin. Dev.*, vol. 2, p. 15023, Apr. 2015, doi: 10.1038/mtm.2015.23.

[223] T. Higuchi *et al.*, “The generation of induced pluripotent stem cells (iPSCs) from patients with infantile and late-onset types of Pompe disease and the effects of treatment with acid-α-glucosidase in Pompe’s iPSCs,” *Mol. Genet. Metab.*, vol. 112, no. 1, pp. 44–48, May 2014, doi: 10.1016/J.YMGME.2014.02.012.

[224] S. J. Chou *et al.*, “Energy utilization of induced pluripotent stem cell-derived cardiomyocyte in Fabry disease,” *Int. J. Cardiol.*, vol. 232, pp. 255–263, Apr. 2017, doi: 10.1016/j.ijcard.2017.01.009.

[225] J. M. Itier *et al.*, “Effective clearance of GL-3 in a human iPSC-derived cardiomyocyte model of Fabry disease,” *J. Inherit. Metab. Dis.*, vol. 37, no. 6, pp. 1013–1022, Nov. 2014, doi: 10.1007/S10545-014-9724-5.

[226] S. Kawagoe *et al.*, “Morphological features of iPS cells generated from Fabry disease skin fibroblasts using Sendai virus vector (SeVdp),” *Mol. Genet. Metab.*, vol. 109, no. 4, pp. 386–389, Aug. 2013, doi: 10.1016/J.YMGME.2013.06.003.

[227] Y. Chien *et al.*, “Interleukin-18 deteriorates Fabry cardiomyopathy and contributes to the development of left ventricular hypertrophy in Fabry patients with GLA IVS4+919 G>A mutation,” *Oncotarget*, vol. 7, no. 52, pp. 87161–87179, 2016, doi: 10.18632/ONCOTARGET.13552.

[228] S. I. Hashem *et al.*, “Brief Report: Oxidative Stress Mediates Cardiomyocyte Apoptosis in a Human Model of Danon Disease and Heart Failure,” *Stem Cells*, vol. 33, no. 7, pp. 2343–2350, Jul. 2015, doi: 10.1002/STEM.2015.

[229] F. Lan *et al.*, “Abnormal calcium handling properties underlie familial hypertrophic cardiomyopathy pathology in patient-specific induced pluripotent stem cells,” *Cell Stem Cell*, vol. 12, no. 1, pp. 101–113, Jan. 2013, doi: 10.1016/j.stem.2012.10.010.

[230] A. Fatima *et al.*, “In vitro Modeling of Ryanodine Receptor 2 Dysfunction Using Human Induced Pluripotent Stem Cells,” *Cell. Physiol. Biochem.*, vol. 28, no. 4, pp. 579–592, 2011, doi: 10.1159/000335753.

[231] E. Di Pasquale *et al.*, “CaMKII inhibition rectifies arrhythmic phenotype in a patient-specific model of catecholaminergic polymorphic ventricular tachycardia,” *Cell Death Dis. 2013 410*, vol. 4, no. 10, pp. e843–e843, Oct. 2013, doi: 10.1038/cddis.2013.369.

[232] C. B. Jung *et al.*, “Dantrolene rescues arrhythmogenic RYR2 defect in a patient-specific stem cell model of catecholaminergic polymorphic ventricular tachycardia,” *EMBO Mol. Med.*, vol. 4, no. 3, pp. 180–191, Mar. 2012, doi: 10.1002/EMMM.201100194.

[233] I. Itzhaki *et al.*, “Modeling of Catecholaminergic Polymorphic Ventricular Tachycardia With Patient-Specific Human-Induced Pluripotent Stem Cells,” *J. Am. Coll. Cardiol.*, vol. 60, no. 11, pp. 990–1000, Sep. 2012, doi: 10.1016/J.JACC.2012.02.066.

[234] K. Kujala *et al.*, “Cell Model of Catecholaminergic Polymorphic Ventricular Tachycardia Reveals Early and Delayed Afterdepolarizations,” *PLoS One*, vol. 7, no. 9, p. e44660, Sep. 2012, doi: 10.1371/JOURNAL.PONE.0044660.

[235] X. H. Zhang *et al.*, “Ca2+ signaling in human induced pluripotent stem cell-derived cardiomyocytes (iPS-CM) from normal and catecholaminergic polymorphic ventricular tachycardia (CPVT)-afflicted subjects,” *Cell Calcium*, vol. 54, no. 2, pp. 57–70, Aug. 2013, doi: 10.1016/J.CECA.2013.04.004.

[236] J. T. Hinson *et al.*, “Titin mutations in iPS cells define sarcomere insufficiency as a cause of dilated cardiomyopathy,” *Science (80-.).*, vol. 349, no. 6251, pp. 982–986, Aug. 2015, doi: 10.1126/SCIENCE.AAA5458/SUPPL_FILE/HINSON.SM.PDF.

[237] N. Sun *et al.*, “Patient-specific induced pluripotent stem cells as a model for familial dilated cardiomyopathy,” *Sci. Transl. Med.*, vol. 4, no. 130, Apr. 2012, doi: https://doi.org/10.1126/scitranslmed.3003552.

[238] H. Wu *et al.*, “Epigenetic Regulation of Phosphodiesterases 2A and 3A Underlies Compromised β-Adrenergic Signaling in an iPSC Model of Dilated Cardiomyopathy,” *Cell Stem Cell*, vol. 17, no. 1, pp. 89–100, Jul. 2015, doi: 10.1016/j.stem.2015.04.020.

[239] R. E. Ahmed, T. Anzai, N. Chanthra, and H. Uosaki, “A Brief Review of Current Maturation

Methods for Human Induced Pluripotent Stem Cells-Derived Cardiomyocytes," *Front. Cell Dev. Biol.*, vol. 8, p. 178, Mar. 2020, doi: 10.3389/FCELL.2020.00178/BIBTEX.

[240] X. Yang *et al.*, "Tri-iodo-l-thyronine promotes the maturation of human cardiomyocytes-derived from induced pluripotent stem cells," *J. Mol. Cell. Cardiol.*, vol. 72, pp. 296–304, 2014, doi: 10.1016/J.YJMCC.2014.04.005.

[241] M. J. Birket *et al.*, "Contractile Defect Caused by Mutation in MYBPC3 Revealed under Conditions Optimized for Human PSC-Cardiomyocyte Function," *Cell Rep.*, vol. 13, no. 4, pp. 733–745, Oct. 2015, doi: 10.1016/j.celrep.2015.09.025.

[242] C. Correia *et al.*, "Distinct carbon sources affect structural and functional maturation of cardiomyocytes derived from human pluripotent stem cells," *Sci. Rep.*, vol. 7, no. 1, Dec. 2017, doi: 10.1038/S41598-017-08713-4.

[243] T. K. Feaster *et al.*, "A method for the generation of single contracting human-induced pluripotent stem cell-derived cardiomyocytes," *Circ. Res.*, vol. 117, no. 12, pp. 995–1000, Oct. 2015, doi: 10.1161/CIRCRESAHA.115.307580/-/DC1.

[244] L. B. Hazeltine *et al.*, "Effects of substrate mechanics on contractility of cardiomyocytes generated from human pluripotent stem cells," *Int. J. Cell Biol.*, vol. 2012, 2012, doi: 10.1155/2012/508294.

[245] M. Biermann *et al.*, "Epigenetic Priming of Human Pluripotent Stem Cell-Derived Cardiac Progenitor Cells Accelerates Cardiomyocyte Maturation," *Stem Cells*, vol. 37, no. 7, pp. 910–923, Jul. 2019, doi: 10.1002/STEM.3021.

[246] K. Kroll, M. Chabria, K. Wang, F. Häusermann, F. Schuler, and L. Polonchuk, "Electro-mechanical conditioning of human iPSC-derived cardiomyocytes for translational research," *Prog. Biophys. Mol. Biol.*, vol. 130, no. Pt B, pp. 212–222, Nov. 2017, doi: 10.1016/J.PBIOMOLBIO.2017.07.003.

[247] Y. C. Chan *et al.*, "Electrical stimulation promotes maturation of cardiomyocytes derived from human embryonic stem cells," *J. Cardiovasc. Transl. Res.*, vol. 6, no. 6, pp. 989–999, Dec. 2013, doi: 10.1007/S12265-013-9510-Z.

[248] K. Ronaldson-Bouchard *et al.*, "Advanced maturation of human cardiac tissue grown from pluripotent stem cells," *Nat. 2018 5567700*, vol. 556, no. 7700, pp. 239–243, Apr. 2018, doi: 10.1038/s41586-018-0016-3.

[249] C. Mummery *et al.*, "Differentiation of human embryonic stem cells to cardiomyocytes: role of coculture with visceral endoderm-like cells," *Circulation*, vol. 107, no. 21, pp. 2733–2740, Jun. 2003, doi: 10.1161/01.CIR.0000068356.38592.68.

[250] C. Liu, X. Feng, G. Li, P. Gokulnath, and J. Xiao, "Generating 3D human cardiac constructs from pluripotent stem cells," *eBioMedicine*, vol. 76, Feb. 2022, doi: 10.1016/J.EBIOM.2022.103813.

[251] A. Acun, T. D. Nguyen, and P. Zorlutuna, "In vitro aged, hiPSC-origin engineered heart tissue models with age-dependent functional deterioration to study myocardial infarction," *Acta Biomater.*, vol. 94, pp. 372–391, Aug. 2019, doi: 10.1016/J.ACTBIO.2019.05.064.

[252] E. Lazzarini *et al.*, "Stress-induced premature senescence is associated with a prolonged QT interval and recapitulates features of cardiac aging," *Theranostics*, vol. 12, no. 11, pp. 5237–5257, 2022, doi: 10.7150/THNO.70884.

[253] S. Morris *et al.*, "Inner mitochondrial membrane structure and fusion dynamics are altered in senescent human iPSC-derived and primary rat cardiomyocytes," *Biochim. Biophys. acta. Bioenerg.*, vol. 1864, no. 2, Apr. 2022, doi: 10.1016/J.BBABIO.2022.148949.

[254] P. S. Rawat, A. Jaiswal, A. Khurana, J. S. Bhatti, and U. Navik, "Doxorubicin-induced cardiotoxicity: An update on the molecular mechanism and novel therapeutic strategies for effective management," *Biomed. Pharmacother.*, vol. 139, p. 111708, Jul. 2021, doi: 10.1016/J.BIOPHA.2021.111708.

[255] N. Osataphan, A. Phrommintikul, S. C. Chattipakorn, and N. Chattipakorn, "Effects of

doxorubicin-induced cardiotoxicity on cardiac mitochondrial dynamics and mitochondrial function: Insights for future interventions," *J. Cell. Mol. Med.*, vol. 24, no. 12, pp. 6534–6557, Jun. 2020, doi: 10.1111/JCMM.15305.

[256] J. D. Miller *et al.*, "Human iPSC-based modeling of late-onset disease via progerin-induced aging," *Cell Stem Cell*, vol. 13, no. 6, pp. 691–705, Dec. 2013, doi: 10.1016/J.STEM.2013.11.006.

[257] N. J. Ullrich and L. B. Gordon, "Hutchinson-Gilford progeria syndrome," *Handb. Clin. Neurol.*, vol. 132, pp. 249–264, 2015, doi: 10.1016/B978-0-444-62702-5.00018-4.

[258] V. V. Ashapkin, L. I. Kutueva, S. Y. Kurchashova, and I. I. Kireev, "Are there common mechanisms between the Hutchinson-Gilford progeria syndrome and natural aging?," *Front. Genet.*, vol. 10, no. MAY, p. 455, May 2019, doi: 10.3389/FGENE.2019.00455/BIBTEX.

[259] M. R. Hamczyk, L. Del Campo, and V. Andrés, "Aging in the Cardiovascular System: Lessons from Hutchinson-Gilford Progeria Syndrome," *Annu. Rev. Physiol.*, vol. 80, pp. 27–48, Feb. 2018, doi: 10.1146/ANNUREV-PHYSIOL-021317-121454.

[260] T. Nesterova, D. Shmarko, K. Ushenin, and O. Solovyova, "In-silico analysis of aging mechanisms of action potential remodeling in human atrial cardiomyocites," *BIO Web Conf.*, vol. 22, p. 1025, 2020, doi: 10.1051/bioconf/20202201025.

[261] M. Courtemanche, R. J. Ramirez, and S. Nattel, "Ionic mechanisms underlying human atrial action potential properties: insights from a mathematical model.," *Am. J. Physiol.*, vol. 275, no. 1, pp. H301-21, Jul. 1998, doi: 10.1152/ajpheart.1998.275.1.H301.

[262] A. Dokuchaev, S. Khamzin, and O. Solovyova, "In-silico study of age-related ionic remodeling in human ventricular cardiomyocytes," *BIO Web Conf.*, vol. 22, p. 1024, 2020, doi: 10.1051/bioconf/20202201024.

[263] N. A. Balakina-Vikulova, A. Panfilov, O. Solovyova, and L. B. Katsnelson, "Mechano-calcium and mechano-electric feedbacks in the human cardiomyocyte analyzed in a mathematical model.," *J. Physiol. Sci.*, vol. 70, no. 1, p. 12, Feb. 2020, doi: 10.1186/s12576-020-00741-6.

[264] T. Sulman, L. B. Katsnelson, O. Solovyova, and V. S. Markhasin, "Mathematical Modeling of Mechanically Modulated Rhythm Disturbances in Homogeneous and Heterogeneous Myocardium with Attenuated Activity of Na+–K+ Pump," *Bull. Math. Biol.*, vol. 70, no. 3, pp. 910–949, 2008, doi: 10.1007/s11538-007-9285-y.

[265] E. Ramos-Marquès *et al.*, "Chronological and biological aging of the human left ventricular myocardium: analysis of microRNAs contribution," *Aging Cell*, 2021, doi: 10.1111/acel.13383.

[266] M. L. Idda *et al.*, "Survey of senescent cell markers with age in human tissues," *Aging (Albany. NY).*, vol. 12, no. 5, pp. 4052–4066, Mar. 2020, doi: 10.18632/AGING.102903.

[267] C. Chimenti *et al.*, "Senescence and Death of Primitive Cells and Myocytes Lead to Premature Cardiac Aging and Heart Failure," *Circ. Res.*, vol. 93, no. 7, pp. 604–613, Oct. 2003, doi: 10.1161/01.RES.0000093985.76901.AF.

[268] L. Grosse *et al.*, "Defined p16High Senescent Cell Types Are Indispensable for Mouse Healthspan," *Cell Metab.*, vol. 32, no. 1, pp. 87-99.e6, Jul. 2020, doi: 10.1016/J.CMET.2020.05.002.

[269] D. Torella *et al.*, "Cardiac Stem Cell and Myocyte Aging, Heart Failure, and Insulin-Like Growth Factor-1 Overexpression," *Circ. Res.*, vol. 94, no. 4, pp. 514–524, Mar. 2004, doi: 10.1161/01.RES.0000117306.10142.50.

[270] I. Shimizu and T. Minamino, "Cellular senescence in cardiac diseases," *J. Cardiol.*, vol. 74, no. 4, pp. 313–319, Oct. 2019, doi: 10.1016/j.jjcc.2019.05.002.

[271] A. Walaszczyk *et al.*, "Pharmacological clearance of senescent cells improves survival and recovery in aged mice following acute myocardial infarction," *Aging Cell*, vol. 18, no. 3, p. e12945, Jun. 2019, doi: 10.1111/ACEL.12945.

[272] Y. Zhu *et al.*, "The Achilles' heel of senescent cells: from transcriptome to senolytic

drugs,” *Aging Cell*, vol. 14, no. 4, pp. 644–658, Aug. 2015, doi: 10.1111/ACEL.12344.

[273] H. Rhinn and A. Abeliovich, “Differential Aging Analysis in Human Cerebral Cortex Identifies Variants in TMEM106B and GRN that Regulate Aging Phenotypes,” *Cell Syst.*, vol. 4, no. 4, pp. 404-415.e5, 2017, doi: 10.1016/j.cels.2017.02.009.

[274] S. K. Gupta *et al.*, “Preclinical Development of a MicroRNA-Based Therapy for Elderly Patients With Myocardial Infarction,” *J. Am. Coll. Cardiol.*, vol. 68, no. 14, pp. 1557–1571, Oct. 2016, doi: 10.1016/J.JACC.2016.07.739.

[275] J. Yang *et al.*, “Synchronized age-related gene expression changes across multiple tissues in human and the link to complex diseases,” *Sci. Reports 2015 51*, vol. 5, no. 1, pp. 1–16, Oct. 2015, doi: 10.1038/srep15145.

[276] L. J. Carithers *et al.*, “A Novel Approach to High-Quality Postmortem Tissue Procurement: The GTEx Project,” *Biopreserv. Biobank.*, vol. 13, no. 5, pp. 311–319, Oct. 2015, doi: 10.1089/bio.2015.0032.

[277] K. R. Boheler *et al.*, “Sex- and age-dependent human transcriptome variability: implications for chronic heart failure.,” *Proc. Natl. Acad. Sci. U. S. A.*, vol. 100, no. 5, pp. 2754–9, Mar. 2003, doi: 10.1073/pnas.0436564100.

[278] P. G. Ferreira *et al.*, “The effects of death and post-mortem cold ischemia on human tissue transcriptomes,” *Nat. Commun.*, vol. 9, no. 1, 2018, doi: 10.1038/s41467-017-02772-x.

[279] M. I. Love, W. Huber, and S. Anders, “Moderated estimation of fold change and dispersion for RNA-seq data with DESeq2,” *Genome Biol.*, vol. 15, no. 12, p. 550, Dec. 2014, doi: 10.1186/s13059-014-0550-8.

[280] E. Howe, K. Holton, S. Nair, D. Schlauch, R. Sinha, and J. Quackenbush, “MeV: MultiExperiment viewer,” in *Biomedical Informatics for Cancer Research*, Springer US, 2010, pp. 267–277.

[281] B. Subramanian, S. Gao, M. J. Lercher, S. Hu, and W. H. Chen, “Evolview v3: A webserver for visualization, annotation, and management of phylogenetic trees,” *Nucleic Acids Res.*, vol. 47, no. W1, pp. W270–W275, Jul. 2019, doi: 10.1093/nar/gkz357.

[282] a. Subramanian *et al.*, “Gene set enrichment analysis: A knowledge-based approach for interpreting genome-wide expression profiles,” *Proc. Natl. Acad. Sci.*, vol. 102, no. 43, pp. 15545–15550, 2005, doi: 10.1073/pnas.0506580102.

[283] V. K. Mootha *et al.*, “PGC-1alpha-responsive genes involved in oxidative phosphorylation are coordinately downregulated in human diabetes.,” *Nat. Genet.*, vol. 34, no. 3, pp. 267–273, 2003, doi: 10.1038/ng1180.

[284] J. C. Oliveros, “Venny. An interactive tool for comparing lists with Venn’s diagrams.,” 2007. .

[285] M. E. Ritchie *et al.*, “Limma powers differential expression analyses for RNA-sequencing and microarray studies,” *Nucleic Acids Res.*, vol. 43, no. 7, p. e47, Jan. 2015, doi: 10.1093/nar/gkv007.

[286] C. Sticht, C. De La Torre, A. Parveen, and N. Gretz, “miRWalk: An online resource for prediction of microRNA binding sites,” *PLoS One*, vol. 13, no. 10, p. e0206239, Oct. 2018, doi: 10.1371/JOURNAL.PONE.0206239.

[287] A. Oliván-Viguera *et al.*, “Minimally invasive system to reliably characterize ventricular electrophysiology from living donors.,” *Sci. Rep.*, vol. 10, no. 1, p. 19941, Nov. 2020, doi: 10.1038/s41598-020-77076-0.

[288] C. E. Molina *et al.*, “Identification of optimal reference genes for transcriptomic analyses in normal and diseased human heart,” *Cardiovasc. Res.*, vol. 114, no. 2, pp. 247–258, Feb. 2018, doi: 10.1093/CVR/CVX182.

[289] J.-B. Pan *et al.*, “PaGenBase: A Pattern Gene Database for the Global and Dynamic Understanding of Gene Function,” *PLoS One*, vol. 8, no. 12, p. e80747, Dec. 2013, doi: 10.1371/journal.pone.0080747.

[290] A. Piek, R. A. de Boer, and H. H. W. Silljé, “The fibrosis-cell death axis in heart failure,”

Hear. Fail. Rev. 2016 212, vol. 21, no. 2, pp. 199–211, Feb. 2016, doi: 10.1007/S10741-016-9536-9.

[291] A. González, E. B. Schelbert, J. Díez, and J. Butler, "Myocardial Interstitial Fibrosis in Heart Failure: Biological and Translational Perspectives," *J. Am. Coll. Cardiol.*, vol. 71, no. 15, pp. 1696–1706, Apr. 2018, doi: 10.1016/J.JACC.2018.02.021.

[292] C. R. Gazoti Debessa, L. B. Mesiano Maifrino, and R. Rodrigues de Souza, "Age related changes of the collagen network of the human heart," *Mech. Ageing Dev.*, vol. 122, no. 10, pp. 1049–1058, Jul. 2001, doi: 10.1016/S0047-6374(01)00238-X.

[293] V. Obas and R. S. Vasan, "The aging heart," *Clin. Sci.*, vol. 132, no. 13, pp. 1367–1382, Jul. 2018, doi: 10.1042/CS20171156.

[294] M. Oubaha *et al.*, "Senescence-associated secretory phenotype contributes to pathological angiogenesis in retinopathy," *Sci. Transl. Med.*, vol. 8, no. 362, Oct. 2016, doi: 10.1126/SCITRANSLMED.AAF9440/SUPPL_FILE/8-362RA144_SM.PDF.

[295] Y. Gonskikh and N. Polacek, "Alterations of the translation apparatus during aging and stress response," *Mech. Ageing Dev.*, vol. 168, pp. 30–36, Dec. 2017, doi: 10.1016/J.MAD.2017.04.003.

[296] G. C. Melkani *et al.*, "TRiC/CCT chaperonins are essential for maintaining myofibril organization, cardiac physiological rhythm, and lifespan," *FEBS Lett.*, vol. 591, no. 21, pp. 3447–3458, Nov. 2017, doi: 10.1002/1873-3468.12860.

[297] L. A. Fitzpatrick, R. T. Turner, and E. R. Ritman, "Endochondral Bone Formation in the Heart: A Possible Mechanism of Coronary Calcification," *Endocrinology*, vol. 144, no. 6, pp. 2214–2219, Jun. 2003, doi: 10.1210/EN.2002-0170.

[298] A. Trion and A. Van Der Laarse, "Vascular smooth muscle cells and calcification in atherosclerosis," *Am. Heart J.*, vol. 147, no. 5, pp. 808–814, May 2004, doi: 10.1016/J.AHJ.2003.10.047.

[299] B. van Wijk, A. F. M. Moorman, and M. J. B. van den Hoff, "Role of bone morphogenetic proteins in cardiac differentiation," *Cardiovasc. Res.*, vol. 74, no. 2, pp. 244–255, May 2007, doi: 10.1016/J.CARDIORES.2006.11.022/2/74-2-244-FIG5.GIF.

[300] E. Dirkx, P. A. da Costa Martins, and L. J. De Windt, "Regulation of fetal gene expression in heart failure," *Biochim. Biophys. Acta*, vol. 1832, no. 12, pp. 2414–2424, Dec. 2013, doi: 10.1016/J.BBADIS.2013.07.023.

[301] Y. A. Chiao and P. S. Rabinovitch, "The Aging Heart.," *Cold Spring Harb. Perspect. Med.*, vol. 5, no. 9, p. a025148, Sep. 2015, doi: 10.1101/cshperspect.a025148.

[302] Y. A. Chiao *et al.*, "Matrix metalloproteinase-9 deletion attenuates myocardial fibrosis and diastolic dysfunction in ageing mice," *Cardiovasc. Res.*, vol. 96, no. 3, pp. 444–455, Dec. 2012, doi: 10.1093/CVR/CVS275.

[303] M. Litviňuková *et al.*, "Cells of the adult human heart," *Nat. 2020 5887838*, vol. 588, no. 7838, pp. 466–472, Sep. 2020, doi: 10.1038/s41586-020-2797-4.

[304] T. Huan *et al.*, "Age-associated microRNA expression in human peripheral blood is associated with all-cause mortality and age-related traits," *Aging Cell*, vol. 17, no. 1, p. e12687, Feb. 2018, doi: 10.1111/ACEL.12687.

[305] L. M. Simon *et al.*, "Human platelet microRNA-mRNA networks associated with age and gender revealed by integrated plateletomics," *Blood*, vol. 123, no. 16, pp. e37–e45, Apr. 2014, doi: 10.1182/BLOOD-2013-12-544692.

[306] Z. P. Huang *et al.*, "MicroRNA-22 regulates cardiac hypertrophy and remodeling in response to stress," *Circ. Res.*, vol. 112, no. 9, pp. 1234–1243, Apr. 2013, doi: 10.1161/CIRCRESAHA.112.300682/-/DC1.

[307] M. Hackl *et al.*, "miR-17, miR-19b, miR-20a, and miR-106a are down-regulated in human aging," *Aging Cell*, vol. 9, no. 2, pp. 291–296, Apr. 2010, doi: 10.1111/J.1474-9726.2010.00549.X.

[308] W. W. Du *et al.*, "The microRNA miR-17-3p inhibits mouse cardiac fibroblast senescence by targeting Par4," *J. Cell Sci.*, vol. 128, no. 2, pp. 293–304, Jan. 2015, doi:

10.1242/JCS.158360/259103/AM/EXPRESSION-OF-MICRORNA-MIR-17-3P-INHIBITS-MOUSE.

[309] H. Y. Seok *et al.*, “Loss of MicroRNA-155 protects the heart from pathological cardiac hypertrophy,” *Circ. Res.*, vol. 114, no. 10, pp. 1585–1595, 2014, doi: 10.1161/CIRCRESAHA.114.303784/-/DC1.

[310] Y. Kakimoto, M. Tanaka, H. Kamiguchi, H. Hayashi, E. Ochiai, and M. Osawa, “MicroRNA deep sequencing reveals chamber-specific miR-208 family expression patterns in the human heart,” *Int. J. Cardiol.*, vol. 211, pp. 43–48, May 2016, doi: 10.1016/J.IJCARD.2016.02.145.

[311] S. Gioffré *et al.*, “Plasmatic and chamber-specific modulation of cardiac microRNAs in an acute model of DOX-induced cardiotoxicity,” *Biomed. Pharmacother.*, vol. 110, pp. 1–8, Feb. 2019, doi: 10.1016/J.BIOPHA.2018.11.042.

[312] M. Delmar and W. J. McKenna, “The Cardiac Desmosome and Arrhythmogenic Cardiomyopathies,” *Circ. Res.*, vol. 107, no. 6, pp. 700–714, Sep. 2010, doi: 10.1161/CIRCRESAHA.110.223412.

[313] S. R. Kaplan, J. J. Gard, L. Carvajal-Huerta, J. C. Ruiz-Cabezas, G. Thiene, and J. E. Saffitz, “Structural and molecular pathology of the heart in Carvajal syndrome,” *Cardiovasc. Pathol.*, vol. 13, no. 1, pp. 26–32, Jan. 2004, doi: 10.1016/S1054-8807(03)00107-8.

[314] S. Soni *et al.*, “A Proteomics Approach to Identify New Putative Cardiac Intercalated Disk Proteins,” *PLoS One*, vol. 11, no. 5, p. e0152231, May 2016, doi: 10.1371/JOURNAL.PONE.0152231.

[315] C. E. Clancy and R. S. Kass, “Inherited and acquired vulnerability to ventricular arrhythmias: Cardiac Na+ and K+ channels,” *Physiol. Rev.*, vol. 85, no. 1, pp. 33–47, Jan. 2005, doi: 10.1152/PHYSREV.00005.2004/ASSET/IMAGES/LARGE/Z9J0010503432007.JPEG.

[316] X. Huang, P. Yang, Z. Yang, H. Zhang, and A. Ma, “Age-associated expression of HCN channel isoforms in rat sinoatrial node,” *Exp. Biol. Med.*, vol. 241, no. 3, pp. 331–339, Feb. 2016, doi: 10.1177/1535370215603515.

[317] H. J. Ranki, R. M. Crawford, G. R. Budas, and A. Jovanovic, “Ageing is associated with a decrease in the number of sarcolemmal ATP-sensitive K+ channels in a gender-dependent manner,” *Mech. Ageing Dev.*, vol. 123, no. 6, pp. 695–705, Mar. 2002, doi: 10.1016/S0047-6374(01)00415-8.

[318] A. O. Sessions and A. J. Engler, “Mechanical Regulation of Cardiac Aging in Model Systems,” *Circ. Res.*, vol. 118, no. 10, pp. 1553–1562, May 2016, doi: 10.1161/CIRCRESAHA.116.307472.

[319] K. Y. Kong and L. Kedes, “Leucine 135 of Tropomodulin-1 Regulates Its Association with Tropomyosin, Its Cellular Localization, and the Integrity of Sarcomeres,” *J. Biol. Chem.*, vol. 281, no. 14, pp. 9589–9599, Apr. 2006, doi: 10.1074/JBC.M512064200.

[320] G. Cooper, “Cytoskeletal networks and the regulation of cardiac contractility: Microtubules, hypertrophy, and cardiac dysfunction,” *Am. J. Physiol. - Hear. Circ. Physiol.*, vol. 291, no. 3, pp. 1003–1014, 2006, doi: 10.1152/AJPHEART.00132.2006/ASSET/IMAGES/LARGE/ZH40080667830015.JPEG.

[321] A. Lymperopoulos, G. Rengo, and W. J. Koch, “Adrenergic Nervous System in Heart Failure,” *Circ. Res.*, vol. 113, no. 6, pp. 739–753, 2013, doi: 10.1161/CIRCRESAHA.113.300308.

[322] Y. Huang *et al.*, “An α1A-Adrenergic–Extracellular Signal-Regulated Kinase Survival Signaling Pathway in Cardiac Myocytes,” *Circulation*, vol. 115, no. 6, pp. 763–772, Feb. 2007, doi: 10.1161/CIRCULATIONAHA.106.664862.

[323] S. C. Wu, E. F. Dahl, C. D. Wright, A. L. Cypher, C. L. Healy, and T. D. O’Connell, “Nuclear localization of a1A-adrenergic receptors is required for signaling in cardiac myocytes: an ‘ inside-out’ a1-AR signaling pathway.,” *J. Am. Heart Assoc.*, vol. 3, no. 2, Apr. 2014, doi: 10.1161/JAHA.113.000145.

[324] S. Kumar, M. Vijayan, J. S. Bhatti, and P. H. Reddy, "MicroRNAs as Peripheral Biomarkers in Aging and Age-Related Diseases," *Prog. Mol. Biol. Transl. Sci.*, vol. 146, pp. 47–94, Jan. 2017, doi: 10.1016/BS.PMBTS.2016.12.013.

[325] J. S. Gootenberg *et al.*, "Nucleic acid detection with CRISPR-Cas13a/C2c2," *Science (80-.).*, vol. 356, no. 6336, pp. 438–442, Apr. 2017, doi: 10.1126/science.aam9321.

[326] L. García-Mendívil *et al.*, "Natural and Induced Human Cardiac Aging: Lamin A Δ50 does not accumulate naturally, but accelerates aging in vitro," 2023.

[327] J. B. Strait and E. G. Lakatta, "Aging-associated cardiovascular changes and their relationship to heart failure," *Heart Fail. Clin.*, vol. 8, no. 1, pp. 143–164, Jan. 2012, doi: 10.1016/J.HFC.2011.08.011.

[328] S. M. Kwon, S. M. Hong, Y. K. Lee, S. Min, and G. Yoon, "Metabolic features and regulation in cell senescence," *BMB Rep.*, vol. 52, no. 1, p. 5, Jan. 2019, doi: 10.5483/BMBREP.2019.52.1.291.

[329] P. Scaffidi and T. Misteli, "Lamin A-dependent nuclear defects in human aging," *Science (80-.).*, vol. 312, no. 5776, pp. 1059–1063, May 2006, doi: 10.1126/SCIENCE.1127168/SUPPL_FILE/SCAFFIDI.SOM.PDF.

[330] L. J. Mah, A. El-Osta, and T. C. Karagiannis, "GammaH2AX as a molecular marker of aging and disease," *Epigenetics*, vol. 5, no. 2, pp. 129–136, 2010, doi: 10.4161/EPI.5.2.11080.

[331] R. U. Pathak, M. Soujanya, and R. K. Mishra, "Deterioration of nuclear morphology and architecture: A hallmark of senescence and aging," *Ageing Res. Rev.*, vol. 67, May 2021, doi: 10.1016/J.ARR.2021.101264.

[332] F. S. Loffredo, A. P. Nikolova, J. R. Pancoast, and R. T. Lee, "Heart Failure With Preserved Ejection Fraction," *Circ. Res.*, vol. 115, no. 1, pp. 97–107, Jun. 2014, doi: 10.1161/CIRCRESAHA.115.302929.

[333] M. A. Merideth *et al.*, "Phenotype and Course of Hutchinson–Gilford Progeria Syndrome," *https://doi.org/10.1056/NEJMoa0706898*, vol. 358, no. 6, pp. 592–604, Feb. 2008, doi: 10.1056/NEJMOA0706898.

[334] B. Dorado *et al.*, "Generation and characterization of a novel knockin minipig model of Hutchinson-Gilford progeria syndrome," *Cell Discov.*, vol. 5, no. 1, p. 16, 2019, doi: 10.1038/s41421-019-0084-z.

[335] S. J. Lee *et al.*, "Interruption of progerin–lamin A/C binding ameliorates Hutchinson-Gilford progeria syndrome phenotype," *J. Clin. Invest.*, vol. 126, no. 10, pp. 3879–3893, Oct. 2016, doi: 10.1172/JCI84164.

[336] W. P. Wang *et al.*, "Progerin in muscle leads to thermogenic and metabolic defects via impaired calcium homeostasis," *Aging Cell*, vol. 19, no. 2, p. e13090, Feb. 2020, doi: 10.1111/ACEL.13090.

[337] S. Osmanagic-Myers *et al.*, "Endothelial progerin expression causes cardiovascular pathology through an impaired mechanoresponse," *J. Clin. Invest.*, vol. 129, no. 2, pp. 531–545, Feb. 2019, doi: 10.1172/JCI121297.

[338] D. McClintock *et al.*, "The Mutant Form of Lamin A that Causes Hutchinson-Gilford Progeria Is a Biomarker of Cellular Aging in Human Skin," *PLoS One*, vol. 2, no. 12, p. e1269, Dec. 2007, doi: 10.1371/JOURNAL.PONE.0001269.

[339] S. Rodriguez, F. Coppedè, H. Sagelius, and M. Eriksson, "Increased expression of the Hutchinson–Gilford progeria syndrome truncated lamin A transcript during cell aging," *Eur. J. Hum. Genet. 2009 177*, vol. 17, no. 7, pp. 928–937, Jan. 2009, doi: 10.1038/ejhg.2008.270.

[340] F. Cao *et al.*, "Transcriptional and Functional Profiling of Human Embryonic Stem Cell-Derived Cardiomyocytes," *PLoS One*, vol. 3, no. 10, p. e3474, 2008, doi: 10.1371/journal.pone.0003474.

[341] M. Messner *et al.*, "Upregulation of the aging related LMNA splice variant progerin in dilated cardiomyopathy," *PLoS One*, vol. 13, no. 4, p. e0196739, Apr. 2018, doi: 10.1371/JOURNAL.PONE.0196739.

[342] S. G. Ozcebe, G. Bahcecioglu, X. S. Yue, and P. Zorlutuna, “Effect of cellular and ECM aging on human iPSC-derived cardiomyocyte performance, maturity and senescence,” *Biomaterials*, vol. 268, p. 120554, Jan. 2021, doi: 10.1016/J.BIOMATERIALS.2020.120554.

[343] L. Ordovás *et al.*, “Efficient recombinase-mediated cassette exchange in hPSCs to study the hepatocyte lineage reveals AAVS1 locus-mediated transgene inhibition,” *Stem Cell Reports*, vol. 5, no. 5, pp. 918–931, Nov. 2015, doi: 10.1016/j.stemcr.2015.09.004.

[344] S. Suttiprapa, G. Rinaldi, and P. J. Brindley, “Prototypic chromatin insulator cHS4 protects retroviral transgene from silencing in Schistosoma mansoni,” *Transgenic Res.*, vol. 21, no. 3, pp. 555–566, Jun. 2012, doi: 10.1007/S11248-011-9556-0.

[345] O. Moiseeva, F. Lessard, M. Acevedo-Aquino, M. Vernier, Y. S. Tsantrizos, and G. Ferbeyre, “Mutant lamin A links prophase to a p53 independent senescence program,” *Cell Cycle*, vol. 14, no. 15, p. 2408, Aug. 2015, doi: 10.1080/15384101.2015.1053671.

[346] X. Lian *et al.*, “Directed cardiomyocyte differentiation from human pluripotent stem cells by modulating Wnt/β-catenin signaling under fully defined conditions,” *Nat. Protoc.*, vol. 8, no. 1, pp. 162–175, Jan. 2013, doi: 10.1038/NPROT.2012.150.

[347] R. G. C. Maas *et al.*, “Massive expansion and cryopreservation of functional human induced pluripotent stem cell-derived cardiomyocytes,” *STAR Protoc.*, vol. 2, no. 1, p. 100334, Mar. 2021, doi: 10.1016/J.XPRO.2021.100334.

[348] J. W. Buikema *et al.*, “Wnt Activation and Reduced Cell-Cell Contact Synergistically Induce Massive Expansion of Functional Human iPSC-Derived Cardiomyocytes,” *Cell Stem Cell*, vol. 27, no. 1, pp. 50-63.e5, Jul. 2020, doi: 10.1016/J.STEM.2020.06.001.

[349] A. Oliver-Gelabert *et al.*, “Automatic Quantification of Cardiomyocyte Dimensions and Connexin 43 Lateralization in Fluorescence Images.,” *Biomolecules*, vol. 10, no. 9, Sep. 2020, doi: 10.3390/biom10091334.

[350] Y. S. Yoon, J. H. Lee, S. C. Hwang, K. S. Choi, and G. Yoon, “TGF β1 induces prolonged mitochondrial ROS generation through decreased complex IV activity with senescent arrest in Mv1Lu cells,” *Oncogene 2005 2411*, vol. 24, no. 11, pp. 1895–1903, Jan. 2005, doi: 10.1038/sj.onc.1208262.

[351] Y. H. Seo *et al.*, “Enhanced glycogenesis is involved in cellular senescence via GSK3/GS modulation,” *Aging Cell*, vol. 7, no. 6, pp. 894–907, Dec. 2008, doi: 10.1111/J.1474-9726.2008.00436.X.

[352] Y. M. Kim *et al.*, “Implications of time-series gene expression profiles of replicative senescence,” *Aging Cell*, vol. 12, no. 4, pp. 622–634, 2013, doi: 10.1111/ACEL.12087.

[353] C. E. Molina *et al.*, “Identification of optimal reference genes for transcriptomic analyses in normal and diseased human heart,” *Cardiovasc. Res.*, vol. 114, no. 2, pp. 247–258, Feb. 2018, doi: 10.1093/cvr/cvx182.

[354] R. D. Goldman *et al.*, “Accumulation of mutant lamin A causes progressive changes in nuclear architecture in Hutchinson-Gilford progeria syndrome,” *Proc. Natl. Acad. Sci. U. S. A.*, vol. 101, no. 24, pp. 8963–8968, Jun. 2004, doi: 10.1073/PNAS.0402943101.

[355] D. McClintock, L. B. Gordon, and K. Djabali, “Hutchinson-Gilford progeria mutant lamin A primarily targets human vascular cells as detected by an anti-Lamin A G608G antibody,” *Proc. Natl. Acad. Sci. U. S. A.*, vol. 103, no. 7, pp. 2154–2159, Feb. 2006, doi: 10.1073/PNAS.0511133103.

[356] R. L. Pollex and R. A. Hegele, “Hutchinson–Gilford progeria syndrome,” *Clin. Genet.*, vol. 66, no. 5, pp. 375–381, Nov. 2004, doi: 10.1111/J.1399-0004.2004.00315.X.

[357] G. Monnerat *et al.*, “Modelling premature cardiac aging with induced pluripotent stem cells from a hutchinson-gilford Progeria Syndrome patient,” *Front. Physiol.*, vol. 13, p. 2440, Nov. 2022, doi: 10.3389/FPHYS.2022.1007418/BIBTEX.

[358] K. Asensi, T. Kasai-Brunswick, A. De Figueiredo, and A. Campos-de-Carvalho, “Cardiac Differentiation of induced pluripotent stem cell derived from patients with Hutchinson-Gilford Progeria Syndrome,” *Cytotherapy*, vol. 23, no. 4, p. 6, Apr. 2021, doi: 10.1016/J.JCYT.2021.02.022.

[359] A. M. Janczewski, H. A. Spurgeon, and E. G. Lakatta, "Action potential prolongation in cardiac myocytes of old rats is an adaptation to sustain youthful intracellular Ca2+ regulation.," *J. Mol. Cell. Cardiol.*, vol. 34, no. 6, pp. 641–648, Jun. 2002, doi: 10.1006/jmcc.2002.2004.

[360] S. Dupont *et al.*, "The onset of left ventricular diastolic dysfunction in SHR rats is not related to hypertrophy or hypertension," *Am. J. Physiol. Heart Circ. Physiol.*, vol. 302, no. 7, Apr. 2012, doi: 10.1152/AJPHEART.00955.2010.

[361] K. Zhong *et al.*, "SK Channels and Heart Disease," Apr. 2022, doi: 10.5772/INTECHOPEN.104115.

[362] D. I. Keller *et al.*, "Characterization of novel KCNH2 mutations in type 2 long QT syndrome manifesting as seizures," *Can. J. Cardiol.*, vol. 25, no. 8, pp. 455–462, 2009, doi: 10.1016/S0828-282X(09)70117-5.

[363] W. Li, L. Yin, C. Shen, K. Hu, J. Ge, and A. Sun, "SCN5A variants: Association with cardiac disorders," *Front. Physiol.*, vol. 9, no. OCT, p. 1372, Oct. 2018, doi: 10.3389/FPHYS.2018.01372/BIBTEX.

[364] E. D. Smith *et al.*, "Desmoplakin Cardiomyopathy, a Fibrotic and Inflammatory Form of Cardiomyopathy Distinct From Typical Dilated or Arrhythmogenic Right Ventricular Cardiomyopathy," *Circulation*, vol. 141, no. 23, pp. 1872–1884, Jun. 2020, doi: 10.1161/CIRCULATIONAHA.119.044934.

[365] C. Chiu *et al.*, "Mutations in alpha-actinin-2 cause hypertrophic cardiomyopathy: a genome-wide analysis," *J. Am. Coll. Cardiol.*, vol. 55, no. 11, pp. 1127–1135, Mar. 2010, doi: 10.1016/J.JACC.2009.11.016.

[366] J. T. Granados-Riveron *et al.*, "Alpha-cardiac myosin heavy chain (MYH6) mutations affecting myofibril formation are associated with congenital heart defects," *Hum. Mol. Genet.*, vol. 19, no. 20, pp. 4007–4016, Jul. 2010, doi: 10.1093/HMG/DDQ315.

[367] L. García-Mendívil *et al.*, "Analysis of age-related left ventricular collagen remodeling in living donors: Implications in arrhythmogenesis.," *iScience*, vol. 25, no. 2, p. 103822, Feb. 2022, doi: 10.1016/j.isci.2022.103822.

[368] B. S. Burlew and K. T. Weber, "Cardiac fibrosis as a cause of diastolic dysfunction.," *Herz*, vol. 27, no. 2, pp. 92–98, Mar. 2002, doi: 10.1007/s00059-002-2354-y.

[369] T. Suk, C. Edwards, H. Hart, and J. P. Christiansen, "Myocardial Scar Detected by Contrast-Enhanced Cardiac Magnetic Resonance Imaging is Associated with Ventricular Tachycardia in Hypertrophic Cardiomyopathy Patients," *Hear. Lung Circ.*, vol. 17, no. 5, pp. 370–374, 2008, doi: 10.1016/j.hlc.2008.03.080.

[370] I. V. Kazbanov, K. H. W. J. ten Tusscher, and A. V. Panfilov, "Effects of Heterogeneous Diffuse Fibrosis on Arrhythmia Dynamics and Mechanism," *Sci. Rep.*, vol. 6, no. 20835, pp. 1–14, 2016, doi: 10.1038/srep20835.

[371] C.-Y. Liu *et al.*, "Evaluation of age-related interstitial myocardial fibrosis with cardiac magnetic resonance contrast-enhanced T1 mapping Multi-Ethnic Study of Atherosclerosis (MESA)," *J. Am. Coll. Cardiol.*, vol. 62, no. 14, pp. 1280–1287, Oct. 2013, doi: 10.1016/j.jacc.2013.05.078.

[372] M. Disertori, M. Masè, and F. Ravelli, "Myocardial fibrosis predicts ventricular tachyarrhythmias," *Trends Cardiovasc. Med.*, vol. 27, no. 5, pp. 363–372, 2017, doi: https://doi.org/10.1016/j.tcm.2017.01.011.

[373] S. Hassan, C. J. Barrett, and D. J. Crossman, "Imaging tools for assessment of myocardial fibrosis in humans: the need for greater detail," *Biophys. Rev.*, vol. 12, no. 4, pp. 969–987, Aug. 2020, doi: 10.1007/s12551-020-00738-w.

[374] L. Mostaço-Guidolin, N. L. Rosin, and T.-L. Hackett, "Imaging Collagen in Scar Tissue: Developments in Second Harmonic Generation Microscopy for Biomedical Applications," *Int. J. Mol. Sci.*, vol. 18, no. 8, p. 1772, Aug. 2017, doi: 10.3390/ijms18081772.

[375] R. M. Williams, W. R. Zipfel, and W. W. Webb, "Interpreting Second-Harmonic Generation Images of Collagen I Fibrils," *Biophys. J.*, vol. 88, no. 2, pp. 1377–1386, 2005, doi:

https://doi.org/10.1529/biophysj.104.047308.

[376] P. Büttner, R. Galli, D. Husser, and A. Bollmann, “Label-free imaging of myocardial remodeling in atrial fibrillation using nonlinear optical microscopy: A Feasibility Study,” *J. Atr. Fibrillation*, vol. 10, no. 5, pp. 3–7, 2018, doi: https://dx.doi.org/10.4022%2Fjafib.1644.

[377] M.-R. Tsai, Y.-W. Chiu, M. T. Lo, and C.-K. Sun, “Second-harmonic generation imaging of collagen fibers in myocardium for atrial fibrillation diagnosis.,” *J. Biomed. Opt.*, vol. 15, no. 2, p. 26002, 2010, doi: 10.1117/1.3365943.

[378] F. Perbellini, A. K. L. Liu, S. A. Watson, I. Bardi, S. M. Rothery, and C. M. Terracciano, “Free-of-Acrylamide SDS-based Tissue Clearing (FASTClear) for three dimensional visualization of myocardial tissue,” *Sci. Rep.*, vol. 7, no. 5188, 2017, doi: 10.1038/s41598-017-05406-w.

[379] F. Perbellini *et al.*, “Investigation of cardiac fibroblasts using myocardial slices.,” *Cardiovasc. Res.*, vol. 114, no. 1, pp. 77–89, Jan. 2018, doi: 10.1093/cvr/cvx152.

[380] Y.-W. Chiu *et al.*, “Applying Harmonic Optical Microscopy for Spatial Alignment of Atrial Collagen Fibers,” *PLoS One*, vol. 5, no. 11, pp. 1–9, 2010, doi: 10.1371/journal.pone.0013917.

[381] Y. Liu, A. Keikhosravi, G. S. Mehta, C. R. Drifka, and K. W. Eliceiri, “Methods for Quantifying Fibrillar Collagen Alignment.,” *Methods Mol. Biol.*, vol. 1627, pp. 429–451, 2017, doi: 10.1007/978-1-4939-7113-8_28.

[382] F. J. Ávila and J. M. Bueno, “Analysis and quantification of collagen organization with the structure tensor in second harmonic microscopy images of ocular tissues,” *Appl. Opt.*, vol. 54, no. 33, pp. 9848–9854, Nov. 2015, doi: 10.1364/AO.54.009848.

[383] M. Strupler *et al.*, “Second harmonic imaging and scoring of collagen in fibrotic tissues,” *Opt. Express*, vol. 15, no. 7, pp. 4054–65, 2007, doi: 10.1364/OE.15.004054.

[384] K. Tilbury, J. Hocker, B. L. Wen, N. Sandbo, V. Singh, and P. J. Campagnola, “Second harmonic generation microscopy analysis of extracellular matrix changes in human idiopathic pulmonary fibrosis.,” *J. Biomed. Opt.*, vol. 19, no. 8, p. 86014, Aug. 2014, doi: 10.1117/1.JBO.19.8.086014.

[385] M. Segovia-Roldan, E. R. Diez, and E. Pueyo, “Melatonin to Rescue the Aged Heart: Antiarrhythmic and Antioxidant Benefits.,” *Oxid. Med. Cell. Longev.*, vol. 2021, p. 8876792, 2021, doi: 10.1155/2021/8876792.

[386] P. Comtois and S. Nattel, “Interactions between cardiac fibrosis spatial pattern and ionic remodeling on electrical wave propagation.,” *Annu. Int. Conf. IEEE Eng. Med. Biol. Soc. IEEE Eng. Med. Biol. Soc. Annu. Int. Conf.*, vol. 2011, pp. 4669–4672, 2011, doi: 10.1109/IEMBS.2011.6091156.

[387] C. A. Schneider, W. S. Rasband, and K. W. Eliceiri, “NIH Image to ImageJ: 25 years of image analysis.,” *Nat. Methods*, vol. 9, no. 7, pp. 671–675, Jul. 2012, doi: 10.1038/nmeth.2089.

[388] K. A. Mountris and E. Pueyo, “Cardiac Electrophysiology Meshfree Modeling through the Mixed Collocation Method,” *arXiv e-prints*, p. arXiv:2110.06671, 2021.

[389] K. A. Mountris and E. Pueyo, “The radial point interpolation mixed collocation method for the solution of transient diffusion problems,” *Eng. Anal. Bound. Elem.*, vol. 121, pp. 207–216, 2020, doi: https://doi.org/10.1016/j.enganabound.2020.10.005.

[390] K. A. Mountris and E. Pueyo, “A dual adaptive explicit time integration algorithm for efficiently solving the cardiac monodomain equation.,” *Int. j. numer. method. biomed. eng.*, p. e3461, Mar. 2021, doi: 10.1002/cnm.3461.

[391] M. A. Horn and A. W. Trafford, “Aging and the cardiac collagen matrix: Novel mediators of fibrotic remodelling,” *J. Mol. Cell. Cardiol.*, vol. 93, pp. 175–185, 2016, doi: 10.1016/j.yjmcc.2015.11.005.

[392] R. A. de Boer *et al.*, “Towards better definition, quantification and treatment of fibrosis in heart failure. A scientific roadmap by the Committee of Translational Research of the Heart Failure Association (HFA) of the European Society of Cardiology.,” *Eur. J. Heart Fail.*,

vol. 21, no. 3, pp. 272–285, Mar. 2019, doi: 10.1002/ejhf.1406.

[393] M. Tanaka, H. Fujiwara, T. Onodera, D. J. Wu, Y. Hamashima, and C. Kawai, "Quantitative analysis of myocardial fibrosis in normals, hypertensive hearts, and hypertrophic cardiomyopathy.," *Br. Heart J.*, vol. 55, no. 6, pp. 575–581, Jun. 1986, doi: 10.1136/hrt.55.6.575.

[394] B. S. Nanda and R. Getty, "Lipofuscin pigment in the nervous system of aging pig," *Exp. Gerontol.*, vol. 6, no. 6, pp. 447–452, 1971, doi: https://doi.org/10.1016/0531-5565(71)90023-4.

[395] A. B. Curtis, R. Karki, A. Hattoum, and U. C. Sharma, "Arrhythmias in Patients ≥80 Years of Age: Pathophysiology, Management, and Outcomes.," *J. Am. Coll. Cardiol.*, vol. 71, no. 18, pp. 2041–2057, May 2018, doi: 10.1016/j.jacc.2018.03.019.

[396] E. G. Lakatta and D. Levy, "Arterial and Cardiac Aging: Major Shareholders in Cardiovascular Disease Enterprises Part II: The Aging Heart in Health: Links to Heart Disease," *Circulation*, vol. 107, no. 2, pp. 346–354, 2003, doi: 10.1161/01.CIR.0000048893.62841.F7.

[397] V. M. Almaas *et al.*, "Increased amount of interstitial fibrosis predicts ventricular arrhythmias, and is associated with reduced myocardial septal function in patients with obstructive hypertrophic cardiomyopathy.," *Europace*, vol. 15, no. 9, pp. 1319–1327, Sep. 2013, doi: 10.1093/europace/eut028.

[398] C. Sohns and N. F. Marrouche, "Atrial fibrillation and cardiac fibrosis," *Eur. Heart J.*, vol. 41, no. 10, pp. 1123–1131, 2020, doi: 10.1093/eurheartj/ehz786.

[399] N. Morita, W. J. Mandel, Y. Kobayashi, and H. S. Karagueuzian, "Cardiac fibrosis as a determinant of ventricular tachyarrhythmias," *J. Arrhythmia*, vol. 30, no. 6, pp. 389–394, 2014, doi: 10.1016/j.joa.2013.12.008.

[400] M. Shenasa, "Fibrosis and Ventricular Arrhythmogenesis: Role of Cardiac MRI," *Card. Electrophysiol. Clin.*, vol. 11, no. 3, pp. 551–562, 2019, doi: 10.1016/j.ccep.2019.06.002.

[401] C. Spadaccio *et al.*, "The role of extracellular matrix in age-related conduction disorders: A forgotten player?," *J. Geriatr. Cardiol.*, vol. 12, no. 1, pp. 76–82, 2015, doi: 10.11909/j.issn.1671-5411.2015.01.009.

[402] A. K. Heikhmakhtiar, A. A. Tekle, and K. M. Lim, "Influence of Fibrosis Amount and Patterns on Ventricular Arrhythmogenesis and Pumping Efficacy: Computational Study.," *Front. Physiol.*, vol. 12, p. 644473, 2021, doi: 10.3389/fphys.2021.644473.

[403] J. F. Gomez, K. Cardona, L. Martinez, J. Saiz, and B. Trenor, "Electrophysiological and structural remodeling in heart failure modulate arrhythmogenesis. 2D simulation study," *PLoS One*, vol. 9, no. 7, p. e103273, 2014, doi: 10.1371/journal.pone.0103273.

[404] K. H. W. J. Ten Tusscher and A. V Panfilov, "Influence of diffuse fibrosis on wave propagation in human ventricular tissue.," *Europace*, vol. 9 Suppl 6, pp. vi38-45, Nov. 2007, doi: 10.1093/europace/eum206.

[405] N. Morita *et al.*, "Increased susceptibility of aged hearts to ventricular fibrillation during oxidative stress," *Am. J. Physiol. Heart Circ. Physiol.*, vol. 297, no. 5, pp. H1594–H1605, Nov. 2009, doi: 10.1152/ajpheart.00579.2009.

[406] L. García-Mendívil *et al.*, "Inter-individual age-independent differences in human CX43 impact ventricular arrhythmic risk," 2023.

[407] P. Michela, V. Velia, P. Aldo, and P. Ada, "Role of connexin 43 in cardiovascular diseases," *Eur. J. Pharmacol.*, vol. 768, pp. 71–76, 2015, doi: https://doi.org/10.1016/j.ejphar.2015.10.030.

[408] S. Kostin *et al.*, "Gap junction remodeling and altered connexin43 expression in the failing human heart.," *Mol. Cell. Biochem.*, vol. 242, no. 1–2, pp. 135–144, Jan. 2003.

[409] G. E. Morley, D. Vaidya, F. H. Samie, C. Lo, M. Delmar, and J. Jalife, "Characterization of conduction in the ventricles of normal and heterozygous Cx43 knockout mice using optical mapping.," *J. Cardiovasc. Electrophysiol.*, vol. 10, no. 10, pp. 1361–1375, Oct. 1999, doi: 10.1111/j.1540-8167.1999.tb00192.x.

[410] M. Stein, T. A. B. van Veen, R. N. W. Hauer, J. M. T. de Bakker, and H. V. M. van Rijen, “A 50% reduction of excitability but not of intercellular coupling affects conduction velocity restitution and activation delay in the mouse heart.,” *PLoS One*, vol. 6, no. 6, p. e20310, 2011, doi: 10.1371/journal.pone.0020310.

[411] B. C. Eloff, D. L. Lerner, K. A. Yamada, R. B. Schuessler, J. E. Saffitz, and D. S. Rosenbaum, “High resolution optical mapping reveals conduction slowing in connexin43 deficient mice.,” *Cardiovasc. Res.*, vol. 51, no. 4, pp. 681–690, Sep. 2001, doi: 10.1016/s0008-6363(01)00341-8.

[412] S. A. Thomas *et al.*, “Disparate effects of deficient expression of connexin43 on atrial and ventricular conduction: evidence for chamber-specific molecular determinants of conduction.,” *Circulation*, vol. 97, no. 7, pp. 686–691, Feb. 1998, doi: 10.1161/01.cir.97.7.686.

[413] D. E. Gutstein *et al.*, “Heterogeneous expression of Gap junction channels in the heart leads to conduction defects and ventricular dysfunction.,” *Circulation*, vol. 104, no. 10, pp. 1194–1199, Sep. 2001, doi: 10.1161/hc3601.093990.

[414] S. B. Danik *et al.*, “Modulation of cardiac gap junction expression and arrhythmic susceptibility.,” *Circ. Res.*, vol. 95, no. 10, pp. 1035–1041, Nov. 2004, doi: 10.1161/01.RES.0000148664.33695.2a.

[415] M. Boulaksil *et al.*, “Heterogeneous Connexin43 distribution in heart failure is associated with dispersed conduction and enhanced susceptibility to ventricular arrhythmias.,” *Eur. J. Heart Fail.*, vol. 12, no. 9, pp. 913–921, Sep. 2010, doi: 10.1093/eurjhf/hfq092.

[416] H. Kitamura *et al.*, “Heterogeneous loss of connexin43 protein in nonischemic dilated cardiomyopathy with ventricular tachycardia.,” *J. Cardiovasc. Electrophysiol.*, vol. 13, no. 9, pp. 865–870, Sep. 2002, doi: 10.1046/j.1540-8167.2002.00865.x.

[417] J. E. Saffitz, “Arrhythmogenic cardiomyopathy and abnormalities of cell-to-cell coupling.,” *Hear. Rhythm*, vol. 6, no. 8 Suppl, pp. S62-5, Aug. 2009, doi: 10.1016/j.hrthm.2009.03.003.

[418] Y. Zhang *et al.*, “Connexin43 expression levels influence intercellular coupling and cell proliferation of native murine cardiac fibroblasts.,” *Cell Commun. Adhes.*, vol. 15, no. 3, pp. 289–303, Sep. 2008, doi: 10.1080/15419060802198736.

[419] J. A. Jansen *et al.*, “Reduced Cx43 expression triggers increased fibrosis due to enhanced fibroblast activity.,” *Circ. Arrhythm. Electrophysiol.*, vol. 5, no. 2, pp. 380–390, Apr. 2012, doi: 10.1161/CIRCEP.111.966580.

[420] M. S. C. Fontes, T. A. B. van Veen, J. M. T. de Bakker, and H. V. M. van Rijen, “Functional consequences of abnormal Cx43 expression in the heart.,” *Biochim. Biophys. Acta*, vol. 1818, no. 8, pp. 2020–2029, Aug. 2012, doi: 10.1016/j.bbamem.2011.07.039.

[421] T. J. Wu *et al.*, “Characteristics of wave fronts during ventricular fibrillation in human hearts with dilated cardiomyopathy: role of increased fibrosis in the generation of reentry.,” *J. Am. Coll. Cardiol.*, vol. 32, no. 1, pp. 187–196, Jul. 1998, doi: 10.1016/s0735-1097(98)00184-3.

[422] T. A. B. van Veen *et al.*, “Impaired impulse propagation in Scn5a-knockout mice: combined contribution of excitability, connexin expression, and tissue architecture in relation to aging.,” *Circulation*, vol. 112, no. 13, pp. 1927–1935, Sep. 2005, doi: 10.1161/CIRCULATIONAHA.105.539072.

[423] H. V. M. van Rijen *et al.*, “Slow conduction and enhanced anisotropy increase the propensity for ventricular tachyarrhythmias in adult mice with induced deletion of connexin43.,” *Circulation*, vol. 109, no. 8, pp. 1048–1055, Mar. 2004, doi: 10.1161/01.CIR.0000117402.70689.75.

[424] B. Emde, A. Heinen, A. Gödecke, and K. Bottermann, “Wheat germ agglutinin staining as a suitable method for detection and quantification of fibrosis in cardiac tissue after myocardial infarction,” *Eur. J. Histochem.*, vol. 58, no. 4, pp. 315–319, 2014, doi: 10.4081/ejh.2014.2448.

[425] D. J. Fiegle *et al.*, “Severe T-System Remodeling in Pediatric Viral Myocarditis.,” *Front. Cardiovasc. Med.*, vol. 7, p. 624776, 2020, doi: 10.3389/fcvm.2020.624776.

[426] P. V Bayly, B. H. KenKnight, J. M. Rogers, R. E. Hillsley, R. E. Ideker, and W. M. Smith, “Estimation of conduction velocity vector fields from epicardial mapping data.,” *IEEE Trans. Biomed. Eng.*, vol. 45, no. 5, pp. 563–571, May 1998, doi: 10.1109/10.668746.

[427] C. Mendonca Costa *et al.*, “Pacing in proximity to scar during cardiac resynchronization therapy increases local dispersion of repolarization and susceptibility to ventricular arrhythmogenesis.,” *Hear. Rhythm*, vol. 16, no. 10, pp. 1475–1483, Oct. 2019, doi: 10.1016/j.hrthm.2019.03.027.

[428] K. R. Laurita and D. S. Rosenbaum, “Interdependence of modulated dispersion and tissue structure in the mechanism of unidirectional block.,” *Circ. Res.*, vol. 87, no. 10, pp. 922–928, Nov. 2000, doi: 10.1161/01.res.87.10.922.

[429] F. G. Akar and D. S. Rosenbaum, “Transmural electrophysiological heterogeneities underlying arrhythmogenesis in heart failure.,” *Circ. Res.*, vol. 93, no. 7, pp. 638–645, Oct. 2003, doi: 10.1161/01.RES.0000092248.59479.AE.

[430] J. Patin *et al.*, “Gap-134, a Connexin43 activator, prevents age-related development of ventricular fibrosis in Scn5a(+/)(-) mice.,” *Pharmacol. Res.*, vol. 159, p. 104922, Sep. 2020, doi: 10.1016/j.phrs.2020.104922.

[431] P. Taggart *et al.*, “Inhomogeneous transmural conduction during early ischaemia in patients with coronary artery disease.,” *J. Mol. Cell. Cardiol.*, vol. 32, no. 4, pp. 621–630, Apr. 2000, doi: 10.1006/jmcc.2000.1105.

[432] J. Fannin *et al.*, “Age-associated alterations of cardiac structure and function in the female F344xBN rat heart.,” *Age (Dordr).*, vol. 36, no. 4, p. 9684, 2014, doi: 10.1007/s11357-014-9684-6.

[433] S. S. Khan, B. D. Singer, and D. E. Vaughan, “Molecular and physiological manifestations and measurement of aging in humans,” *Aging Cell*, vol. 16, no. 4, pp. 624–633, Aug. 2017, doi: 10.1111/ACEL.12601.

[434] S. Dhein *et al.*, “Effects of metoprolol therapy on cardiac gap junction remodelling and conduction in human chronic atrial fibrillation.,” *Br. J. Pharmacol.*, vol. 164, no. 2b, pp. 607–616, Sep. 2011, doi: 10.1111/j.1476-5381.2011.01460.x.

[435] M. T. Mora, J. M. Ferrero, J. F. Gomez, E. A. Sobie, and B. Trenor, “Ca(2+) Cycling Impairment in Heart Failure Is Exacerbated by Fibrosis: Insights Gained From Mechanistic Simulations.,” *Front. Physiol.*, vol. 9, p. 1194, 2018, doi: 10.3389/fphys.2018.01194.

[436] J. F. Gomez, K. Cardona, L. Romero, J. M. J. Ferrero, and B. Trenor, “Electrophysiological and structural remodeling in heart failure modulate arrhythmogenesis. 1D simulation study.,” *PLoS One*, vol. 9, no. 9, p. e106602, 2014, doi: 10.1371/journal.pone.0106602.

[437] C. Mendonca Costa, G. Plank, C. A. Rinaldi, S. A. Niederer, and M. J. Bishop, “Modeling the Electrophysiological Properties of the Infarct Border Zone.,” *Front. Physiol.*, vol. 9, p. 356, 2018, doi: 10.3389/fphys.2018.00356.

[438] F. G. Akar *et al.*, “Dynamic changes in conduction velocity and gap junction properties during development of pacing-induced heart failure,” *Am. J. Physiol. Heart Circ. Physiol.*, vol. 293, no. 2, Aug. 2007, doi: 10.1152/AJPHEART.00079.2007.

[439] A. Nygren, M. L. Olson, K. Y. Chen, T. Emmett, G. Kargacin, and Y. Shimoni, “Propagation of the cardiac impulse in the diabetic rat heart: reduced conduction reserve,” *J. Physiol.*, vol. 580, no. Pt 2, p. 543, Apr. 2007, doi: 10.1113/JPHYSIOL.2006.123729.